Simulating quasi-brittle failure in structures using Sequentially Linear Methods
Studies on non-proportional loading, constitutive modelling, and computational efficiency

Pari, M.

Important note
To cite this publication, please use the final published version (if applicable).
Please check the document version above.

SIMULATING QUASI-BRITTLE FAILURE IN STRUCTURES USING SEQUENTIALLY LINEAR METHODS

STUDIES ON NON-PROPORTIONAL LOADING, CONSTITUTIVE MODELLING, AND COMPUTATIONAL EFFICIENCY

SIMULATING QUASI-BRITTLE FAILURE IN STRUCTURES USING SEQUENTIALLY LINEAR METHODS

STUDIES ON NON-PROPORTIONAL LOADING, CONSTITUTIVE MODELLING, AND COMPUTATIONAL EFFICIENCY

Dissertation

for the purpose of obtaining the degree of doctor
at Delft University of Technology,
by the authority of the Rector Magnificus, Prof. dr. ir. T.H.J.J. van der Hagen,
chair of the Board for Doctorates,
to be defended publicly on
Friday 04 December 2020 at 10:00 o'clock

by

Manimaran PARI

Master of Science in Civil Engineering,
Delft University of Technology, The Netherlands
born in Chennai, India.

This dissertation has been approved by the promotors:

Prof. dr. ir. J.G. Rots
Prof. dr. ir. M.A.N. Hendriks

Composition of the doctoral committee:

Rector Magnificus	Chairman
Prof. dr. ir. J.G. Rots	Delft University of Technology, Promotor
Prof. dr. ir. M.A.N. Hendriks	Delft University of Technology, Promotor

Independent members:

Prof. dr. ir. L.J. Sluys	Delft University of Technology
Prof. dr. A. Scarpas	Delft University of Technology
	& Khalifa University, United Arab Emirates
Prof. dr. ing. K.V. Høiseth	Norwegian University of Science & Technology
	(NTNU), Norway
Prof. dr. G.P.A.G. van Zijl	Stellenbosch University, South Africa
Dr. ing. J. Eliáš	Brno University of Technology, Czech Republic

Keywords:	Sequentially Linear Analysis, Quasi-brittle fracture, Non-proportional loading, Pushover Analysis, Force-Release method, 3D Fixed smeared crack model, Composite interface model, Direct & Iterative linear solvers.

Printed by:	Ipskamp Printing, The Netherlands.
Cover design:	Manimaran Pari

An electronic version of this dissertation is available at
http://repository.tudelft.nl/.

கேடில் விழுச்செல்வம் கல்வி யொருவற்கு மாடல்ல மற்றை யவை.

<div align="right">திருக்குறள் 400:   திருவள்ளுவர்</div>

<div align="center">Education is the only imperishable riches a man can ever acquire</div>

<div align="right">Couplet 400:   Thiruvalluvar</div>

SUMMARY

Sequentially Linear Analysis (SLA) is a proven alternative to incremental-iterative solution methods in nonlinear finite element analysis (NLFEA) of quasi-brittle specimen. The core of the method is in its departure from a load, displacement or arc-length driven incremental approach, aided by internal iterations to establish equilibrium, to a damage driven event-by-event approach that approximates the nonlinear response by a sequence of scaled linear analyses. The constitutive relations are discretised into secant-stiffness–based *saw-tooth laws*, with successively reducing strengths and stiffnesses. In each linear analysis, the global load is scaled such that the *critical integration point*, with the largest stress, jumps to its next saw-tooth representing locally applied damage increments. Despite the advantages of simplicity and numerical robustness in comparison to NLFEA, SLA as a solution procedure still needs significant developments to be used in engineering practice as a numerical tool for structural applications, such as the pushover analysis of a masonry structure or the capacity assessment of a shear-critical reinforced concrete slab. To this end, the following scientific contributions are made in this dissertation.

Real structures are subject to loading schemes that are characterised by multiple loads. These loads act on the structure non-proportionally which proves to be complicated in a sequentially linear framework. The first contribution in the thesis is of two novel strategies, an analytical and an optimisation based approach, to deduce the critical integration point and the corresponding load multiplier under non-proportional loading conditions in an undamaged 3D continuum stress state. These are essentially two ways of solving the characteristic cubic equation in the load multiplier, to establish the 3D orthotropic damage directions in a smeared fixed crack/crush framework. Subsequently, the damage propagation along the fixed directions is carried out based on uniaxial saw-teeth laws. The analytical approach is preferred over the optimisation one for computational efficiency and accuracy reasons. Validations are made using an experimental benchmark of a reinforced concrete slab subject to axial and shear loads, and academic cases of notched beams subject to combined prestress and bending loads. The SLA simulation of the slab case appropriately exhibits 3D multi-directional fixed cracking leading to brittle shear failure, and one of the notched beam cases with a skewed notch exhibits 3D non-planar curved cracking. The results demonstrate the effectiveness of the proposed approach, and thereby extend SLA to real-life 3D continuum applications with non-proportional loads.

The second contribution is the extension of the discretised tension-shear criterion for 2D line interfaces (using the step-wise secant relations for discrete cracking and Coulomb friction) with a compression failure criterion. This discretised composite interface model makes it possible to analyse quasi-brittle structures in a sequentially linear framework using predefined interfaces as potential discrete cracks, shear or crush planes. This is elaborated herein for masonry, with the simplified micro-modelling strategy, to simulate cracking-shearing-crushing failures typical of masonry damage until structural collapse. The model uses a tension gap criterion coupled with a uniaxial tensile softening law, a

compression cut-off criterion coupled with a compressive parabolic hardening-softening law, and an uncoupled step-wise Coulomb friction formulation with cohesion softening and without dilatancy effects. The model is validated using a pushover experiment of a masonry wall subject to precompression followed by an in-plane lateral load, and is shown to ably reproduce the force-displacement curves and the brittle diagonal shear failure followed by toe-crushing due to the compressive strut action. Furthermore, the formulation is also extended to the 3D case of planar interfaces, and validated using the same case study thereby enabling 3D masonry applications with SLA. The extension to include dilatancy and a more advanced cap-type model for compression are features to be investigated in the future.

The third contribution of the thesis is the proposal of two tailor-made solvers which efficiently use the favourable event-by-event approach of SLA. Both solvers factorise the global stiffness matrix intermittently at only a certain number of linear analyses. The solution for the remaining intermediate linear analyses is found for low-rank corrections to the factorised stiffness matrix, which is possible using additional matrix-vector manipulations. The first is a direct solver based on the Woodbury-Identity matrix to find the inverse of an arbitrary rank-r corrected matrix. The second is a Preconditioned Conjugate Gradient (PCG) solver that uses the factorised stiffness matrix as the preconditioner for the remaining analyses. When the elapsed time in these intermediate analyses grows, a restart step is prescribed wherein a new factorisation is calculated. These points of restart are deduced such that the total analysis times are minimised. The performance of the solvers are analysed using a 2D and 3D case study, including additional saw-teeth and mesh sensitivity studies. Both solvers perform better than a traditional direct solver like Intel's Parallel Direct Sparse Solver (PARDISO), especially for large 3D problems, and the Woodbury-Identity based direct solver is more efficient among the two. Additionally, some branches of the workflow of SLA are computed in parallel, using multi-threading, to further improve the computational performance.

These aside, all through the thesis, the fundamental problem of using a static approach to model an intrinsically dynamic phenomenon like cracking or crushing is investigated at structural level and under non-proportional loading conditions. To this end, in a first of its kind, several experimental benchmarks that exhibit structural collapse are simulated both using SLA and an incremental sequentially linear approach, the Force-Release method. It is exemplified that SLA realises the sequence of damage events, typical of a sudden dynamic damage propagation, in successive equilibrium states by temporary release of all previously applied loads. This is deemed acceptable while simulating a truly quasi-static experiment with snap-backs. On the other hand, the Force-Release method realises the dynamic propagation of damage through disequilibrium states while retaining all previously applied loads, and is suitable for displacement controlled experiments. The difference lies in SLA releasing the stresses due to a damage event instantaneously, while Force-Release doing so gradually. Despite the differences in the approaches, the damage patterns are similar in the considered continuum studies, as opposed to previous lattice modelling examples wherein more abrupt changes in stiffnesses led to larger differences.

In conclusion, the SLA approach has been extended to 3D structural applications involving cracking, crushing, and shear failures, both in a smeared and discrete manner. Furthermore, the method in general has been made relatively efficient. Nevertheless, the

approach still needs to be extended on important topics such as crack-closure effects, which requires a dedicated event & an algorithm and is possibly difficult to incorporate in the total framework, and the computational performance to make it a practical alternative to NLFEA in engineering practice. The latter could be addressed using smart damage tracking algorithms that distinguish the potential elements to be damaged in order to reduce the computational time. Furthermore, other topics for future research include influence of tension-compression interactions for damage initiation and propagation in 2D and 3D stress states, and the extension to anisotropic failure surfaces.

SAMENVATTING

Sequentieel-lineaire analyse (SLA) is een bewezen alternatief voor incrementeel-iteratieve oplossingsmethoden in niet-lineaire eindige-elementenanalyses (NLEEA) voor constructies van quasi-brosse materialen. De kern van de methode is om het concept van een door belasting, verplaatsing of booglengte gestuurde incrementele benadering geholpen door interne iteraties om een evenwicht tot stand te brengen, te verlaten en te vervangen door een door schade-gestuurdebenadering die de niet-lineaire respons benadert met een reeks geschaalde lineaire analyses. De constitutieve relaties worden gediscretiseerd tot secant-stijfheid gebaseerde zaagtandmodellen met afnemende sterktes en stijfheden. Bij elke lineaire analyse wordt de globale belasting zodanig geschaald dat het kritieke integratiepunt met de grootste spanning naar de volgende zaagtand springt, wat neerkomt op lokaal aangebrachte schade-toenames. Ondanks de voordelen van eenvoud en numerieke robuustheid in vergelijking met NLEEA, behoeft SLA als oplossingsprocedure nog belangrijke uitbreidingen om het toepasbaar te maken voor constructieberekeningen in de ingenieurspraktijk, zoals pushover berekeningen van een metselwerkconstructie of het bepalen van de capaciteit van een dwarskracht-kritische plaat van gewapend beton. Daartoe worden in dit proefschrift de volgende wetenschappelijke bijdragen geleverd.

In de praktijk zijn constructies onderworpen aan belastingschema's met meerdere belastingen. Deze belastingen worden niet-proportioneel op de constructie aangebracht, wat een complicerende factor blijkt te zijn in een sequentieel-lineair raamwerk. De eerste bijdrage in het proefschrift bestaat uit twee nieuwe strategieën, een analytische en een optimalisatie-gebaseerde benadering, om het kritieke integratiepunt en de bijbehorende belastingfactor af te leiden voor een onbeschadigd 3D-continuüm met niet-proportionele belastingen. Dit zijn in wezen twee manieren om de karakteristieke derdegraads-vergelijking in de belastingfactor op te lossen, om zo de 3D orthotrope beschadigingsrichtingen in een uitgesmeerd scheur- en verbrijzelingsraamwerk vast te stellen. Vervolgens wordt de toename van schade langs vaste richtingen aangebracht op basis van eendimensionale zaagtandwetten. De analytische benadering heeft de voorkeur boven de optimalisatie om redenen van rekenefficiëntie en nauwkeurigheid, en wordt vervolgens gevalideerd met behulp van een experimentele benchmark van een gewapend-betonnen plaat die onderhevig is aan normaal- en dwarskracht, en meer academische studies van gekerfde balken die onderhevig zijn aan gecombineerde voorspanning en buiging. De SLA-simulatie van de plaat vertoont realistische 3D-scheurvorming met bros bezwijken onder dwarskracht; een balk met een scheve kerf vertoont scheurvorming in een 3D-gebogen vlak. De resultaten tonen de effectiviteit van de voorgestelde aanpak aan en breiden daarmee SLA uit naar realistische 3D continuümtoepassingen met niet-proportionele belastingen.

De tweede bijdrage is de uitbreiding van het afschuif-trek-criterium voor interfaces met een druk-criterium. Dit model maakt het mogelijk om quasi-brosse constructies met vooraf gedefinieerde interfaces als potentiële scheuren, afschuifvlakken of verbrij-zelvlakken te analyseren in een sequentieel lineair raamwerk. In eerste instantie wordt

voortgebouwd op de 2D formulering voor lijn-interfaces met stapsgewijze secant-relaties voor discrete scheurvorming en Coulombse wrijving, aangevuld met secant-relaties voor druk-bezwijken. Dit wordt uitgewerkt voor metselwerk met een vereenvoudigde micro-modelleringsstrategie om scheur-afschuif-verbrijzeling-gedrag te simuleren, dat typisch is voor metselwerk, tot en met het bezwijken van de constructie. Het model gebruikt een trekcriterium in combinatie met een een-assige softeningrelatie, een drukcriterium in combinatie met een parabolische hardening/softeningrelatie en een ontkoppelde formulering voor Coulombse wrijving met cohesie-softening en zonder dilatantie-effecten, alles in een discreet/stapsgewijs formaat. Het model is in staat om de experimentele schadepatronen en kracht-verplaatsingscurven van een metselwerkmuur die onderhevig is aan bovenbelasting gevolgd door laterale belasting in het vlak adequaat te reproduceren, met bros en diagonaal afschuifbezwijken gevolgd door bezwijken op druk van de drukdiagonaal. Bovendien wordt de formulering ook uitgebreid naar 3D vlakvormige interfaces en gevalideerd voor dezelfde case-study, waardoor SLA beschikbaar is gekomen voor 3D-metselwerktoepassingen. De uitbreiding met dilatantie en een geavanceerde druk-kap zijn aangemerkt voor toekomstig onderzoek.

De derde bijdrage van het proefschrift is het uitwerken van twee op maat gemaakte lineaire oplosprocedures, die efficiënt gebruik maken van de gunstige event-by-event benadering van SLA door de globale stijfheidsmatrix slechts een beperkt aantal keren te factoriseren. De oplossing voor de resterende analyses wordt gevonden met lage-rangcorrecties op de gefactoriseerde stijfheidsmatrix, wat mogelijk is met behulp van aanvullende matrix-vectormanipulaties. De eerste is een directe oplosprocedure op basis van de Woodbury-eenheidsmatrix om de inverse van een willekeurige rang-gecorrigeerde matrix te vinden. De tweede oplosprocedure is een Preconditioned Conjugate Gradient (PCG) procedure die de gefactoriseerde stijfheidsmatrix gebruikt als preconditioneerder voor de overige analyses. Wanneer de rekentijd in deze tussentijdse analyses toeneemt, wordt een herstart gedaan waarbij een nieuwe ontbinding wordt berekend. Deze herstartpunten worden zo afgeleid dat de totale analysetijden worden geminimaliseerd. De prestaties van de oplosprocedures worden geanalyseerd met behulp van een 2D- en een 3D-casestudy, aangevuld met zaagtand- en mesh-gevoeligheidsstudies. Beide oplosprocedures presteren beter dan een traditionele directe oplosser zoals Intel's Parallel Direct Sparse Solver (PARDISO), terwijl de op de Woodbury-eenheidsmatrix gebaseerde oplosprocedure de meest efficiënte is, vooral voor grote 3D-problemen. Bovendien worden sommige delen van de workflow van SLA parallel berekend met behulp van multi-threading om de rekenprestaties verder te verbeteren.

Een rode draad in het hele proefschrift is de fundamentele zoektocht naar het gebruik van een passende statische benadering voor een intrinsiek dynamisch fenomeen zoals scheurvorming, en dat op constructie-niveau en voor niet-proportionele belastingen. Daartoe worden voor het eerst verschillende experimentele benchmarks tot en met bezwijken van de constructie gesimuleerd, zowel met behulp van SLA als met een incrementele sequentieel-lineaire benadering, de Force-Release-methode. Gedemonstreerd wordt dat SLA de opeenvolging van schadegebeurtenissen, kenmerkend voor plotselinge dynamische voortplanting van schade, realiseert in opeenvolgende evenwichtstoestanden door tijdelijke vrijgave van alle eerder aangebrachte belastingen. Dit is geschikt voor het simuleren van een echt quasi-statisch experiment. Aan de andere

kant realiseert de Force-Release-methode de dynamische voortplanting van schade door niet-evenwichtstoestanden met behoud van alle eerder aangebrachte belastingen. Deze methode is geschikt voor verplaatsingsgestuurde experimenten. Het verschil ligt in het feit dat SLA de spanningen als gevolg van een schade onmiddellijk opheft, terwijl Force-Release dit geleidelijk doet. Ondanks de verschillen in de benaderingen zijn de schadepatronen in de beschouwde continuümstudies behoorlijk gelijkwaardig, in tegenstelling tot eerdere voorbeelden met lattice-modellen waar de meer abrupte stijfheidsveranderingen tot grote verschillen leidden.

Concluderend is de SLA-benadering uitgebreid naar constructieve 3D-toepassingen met scheur-, verbrijzel- en afschuif-faalgedrag, zowel op een uitgesmeerde als discrete manier. Bovendien is de methode in het algemeen relatief efficiënt gemaakt. Desalniettemin moet de aanpak nog worden uitgebreid met belangrijke onderwerpen zoals het sluiten scheuren, waarvoor een speciaal algoritme nodig zal zijn dat mogelijk lastig in het raamwerk van totale benaderingen kan worden opgenomen, en het verder verbeteren van de rekenprestaties om het een alternatief te maken voor NLEEA in de praktijk. Dit laatste kan worden aangepakt met behulp van slimme algoritmen voor het voorspellen van schade in potentiële elementen, om zo de rekentijd te verminderen. Andere onderwerpen voor verder onderzoek zijn de invloed van trek-druk interacties bij de initiatie en voortplanting van schade in 2D- en 3D-spanningstoestanden en de uitbreiding tot anisotrope bezwijkcriteria.

SYMBOLS AND ABBREVIATIONS

The dissertation uses the following general notations and abbreviations as much as possible for consistency. In general the notations are introduced, anew with explanations, in the main body for additional clarity. This is also done for the exceptional or non-generic cases which do not conform to the notations listed herein.

Roman Symbols	
a_t	Discretisation factor for shear displacement increments in interfaces
c_0, c	Undamaged and mobilised cohesion
$\mathbf{C}$	Lower triangular matrix in the Cholesky decomposition
d_{ipl}	Last successful prescribed displacement combination during Intermittent Proportional Loading
$\mathbf{D}$ or $\mathbf{D}_{\mathrm{sec}}$	Secant-stiffness matrix
$\mathbf{D}_{nt}$	2D Orthotropic Secant-stiffness matrix
$\mathbf{D}_{nst}$	3D Orthotropic Secant-stiffness matrix
$\mathbf{D}_{\mathrm{tan}}$	Tangent-stiffness matrix
E_0	Undamaged Young's modulus
E_k	Damaged Young's modulus at k^{th} saw-teeth
E_x, E_y, E_z	Young's modulus along x, y, z global directions
E_n, E_s, E_t	Young's modulus along n, s, t crack/crush directions
$\mathbf{f}, \mathbf{f}_{\mathrm{ext}}$	External force vector
$\mathbf{f}_{\mathrm{int}}$	Internal force vector
$f, f_{\mathrm{t}}, f_{\mathrm{c}}$	General, tensile and compressive strengths
$\mathbf{g}$	Out-of-balance force vector
G_{xy}, G_{yz}, G_{zx}	Shear modulus along x, y, z global directions
G_{ns}, G_{st}, G_{ts}	Shear modulus along n, s, t crack/crush directions
$G_{\mathrm{c}}, G_{\mathrm{f}}^{\mathrm{I}}, G_{\mathrm{f}}^{\mathrm{II}}$	Compressive, Mode-I (tensile) and Mode-II (shear) fracture energies
h	Crack/crush bandwidth
I_1, I_2, I_3	Stress Invariants
$k_{n,0},\ k_{t,0},\ k_{s,0}$	Undamaged normal (n) & shear (t, s) interface stiffnesses
k_n, k_t, k_s	Damaged normal (n) & shear (t, s) interface stiffnesses
$\mathbf{K}$	Global (system) stiffness matrix
l, m, n	Directional cosines
$L, L_{\mathrm{con}}, L_{\mathrm{var}}, \Delta L_p$	Loads (in general), constant loads, variable loads, and piece-wise proportional load increments
L_{ipl}	Last successful load combination during Intermittent Proportional Loading
$\mathbf{L}, \mathbf{U}$	Lower & Upper triangular matrices in the standard LU decomposition

p	Saw-teeth discretisation factor (Band width ripple approach)
$\mathbf{R}, \Delta\mathbf{R}$	Total reaction force vector and
	reaction force vector due to a load increment
$\mathbf{S}$	Disequilibrium force vector
t_p	Variable to track history along
	piece-wise proportional load increments
t_n, t_t, t_s	Normal (n) & shear (t, s) tractions in interfaces
$\tan(\phi)$	Friction coefficient
$\mathbf{u}, \Delta\mathbf{u}, \delta\mathbf{u}$	Unknown displacement field, the displacement increment
	per step and per iteration respectively
u_n, u_t, u_s	Normal (n) & shear (t, s) relative displacements in interfaces
$\delta u_n, \delta u_t, \delta u_s$	Normal (n) & shear (t, s) relative displacement
	increments in interfaces
$u_n^{\mathrm{pl}}, u_t^{\mathrm{pl}}$	Normal and shear plastic relative displacements

Greek Symbols

α	Threshold crack rotation
β	Shear retention factor
$\gamma_{xy}, \gamma_{yz}, \gamma_{zx}$	Shear strain components along x, y, z global directions
$\gamma_{ns}, \gamma_{st}, \gamma_{ts}$	Shear strain components along n, s, t crack/crush directions
$\Delta\gamma, \Delta\gamma_{\max}$	Change in crack rotation and its largest change
$\boldsymbol{\varepsilon}, \boldsymbol{\varepsilon}_{nt}, \boldsymbol{\varepsilon}_{nst}$	Undamaged, 2D orthotropic and 3D Orthotropic strain tensors
$\varepsilon_{xx}, \varepsilon_{yy}, \varepsilon_{zz}$	Normal strain components along x, y, z global directions
$\varepsilon_{nn}, \varepsilon_{ss}, \varepsilon_{tt}$	Normal strain components along n, s, t crack/crush directions
κ	plasticity parameter
$\lambda, \lambda_{\mathrm{con}}, \lambda_{\mathrm{var}}$	Load multiplier in SLA (in general) and
	those for constant and variable loads
Λ_i	Load multiplier sets per integration point
Λ_{model}	Load multiplier set for the FE model
λ_{crit}	Critical load multiplier per analysis step in SLA
ν_0	Initial Poisson's ratio
$\nu_{xy}, \nu_{yz}, \nu_{zx}$	Poisson's ratio along x, y, z global directions
$\nu_{ns}, \nu_{st}, \nu_{ts}$	Poisson's ratio along n, s, t crack/crush directions
ρ	Density
$\boldsymbol{\sigma}, \boldsymbol{\sigma}_{nt}, \boldsymbol{\sigma}_{nst}$	Undamaged, 2D orthotropic and 3D Orthotropic stress tensors
$\Delta\boldsymbol{\sigma}, \Delta\boldsymbol{\sigma}_{\mathrm{L}}, \Delta\boldsymbol{\sigma}_{\mathrm{S}}$	Incremental quantities of stresses (in general) and those due to
	external loads, and disequilibrium forces respectively
σ_{gov}	Governing stress
$\sigma_1, \sigma_2, \sigma_3$	Principal stresses
$\sigma_{xx}, \sigma_{yy}, \sigma_{zz}$	Normal stress components along x, y, z global directions
$\sigma_{xy}, \sigma_{yz}, \sigma_{zx}$	Shear stress components along x, y, z global directions
$\sigma_{nn}, \sigma_{ss}, \sigma_{tt}$	Normal stress components along n, s, t crack/crush directions
$\sigma_{ns}, \sigma_{st}, \sigma_{tn}$	Shear stress components along n, s, t crack/crush directions

Subscripts	
con	*Constant* load component of the said quantity
crit	*Critical* components of the said quantity
e_i	Element number
i	Integration point number
ipl	Intermittent Proportional Loading
k	Saw-teeth index (Continuum laws)
max	*Maximum* components of the said quantity
min	*Minimum* components of the said quantity
n	Normal direction of crack coordinate system
r	Saw-teeth index (Interface laws)
s	Secondary shear direction of crack coordinate system
t	Tertiary shear direction of crack coordinate system
var	*Variable* load component of the said quantity

Superscripts	
c or cmp	*Compressive* component of the said quantity
j	Analysis number (step)
shr	*Shear* component of the said quantity
t or ten	*Tensile* component of the said quantity

Abbreviations	
2D, 3D	2-Dimensional, 3-Dimensional
BiCG, PCG, CG	Bi-, Preconditioned-, Conjugate Gradient methods
CITA	Continuous Incremental-only Tangent Analysis
CMOD	Crack Mouth Opening Displacement
DOF	Degrees Of Freedom
FE	Finite Element
F-R	Force-Release method
GMRES, MINRES	Generalised-, Minimal residual method
ILU	Incomplete L-U factorisation
IMPL-EX	Implicit-Explicit solution method
IPL	Intermittent Proportional Loading
LATIN	LArge Time INcrement method
MUMPS	MUltifrontal Massively Parallel sparse direct Solver
NAM	Nederlandse Aardolie Maatschappij
NIEM	Non-Iterative Energy-based Method
NLFEA	Nonlinear Finite Element Analysis
NLPO	Nonlinear Pushover Analysis
PARDISO	PARallel DIrect Sparse SOlver
RC	Reinforced Concrete
SLA	Sequentially Linear Analysis
SLM	Sequentially Linear Methods
SDA	Strong Discontinuity Approaches
SPD	Symmetric Positive Definite
SUR	Smooth Unloading-Reloading approach
URM	Un-Reinforced Masonry

CONTENTS

CHAPTER 1
INTRODUCTION

1.1. BACKGROUND

The Netherlands, a low-lying nation in Western Europe, is not known to be prone to tectonic earthquakes. However, extensive extraction of natural gas from fields in the northern province of Groningen, over several decades since the 1960s, has led to induced seismic events in the region. There has been a number of small magnitude earthquakes, with a maximum of 120 events occurring in the year 2013 as shown in Figure 1.1(b), and the trend has shown a growth in seismic activity with increasing gas extraction [148]. Although the earthquakes are of small magnitude, with the largest reported one being 3.6 on the Richter scale in 2013, the predominantly unreinforced masonry (URM) building stock in the region (Figure 1.2) makes it a problem that requires immediate attention considering the risk involved. The problem is compounded by the fact that these buildings are not designed for seismic loads and have characteristics such as slender cavity walls, with large openings and limited cooperation between orthogonal components, which limit their seismic capacities.
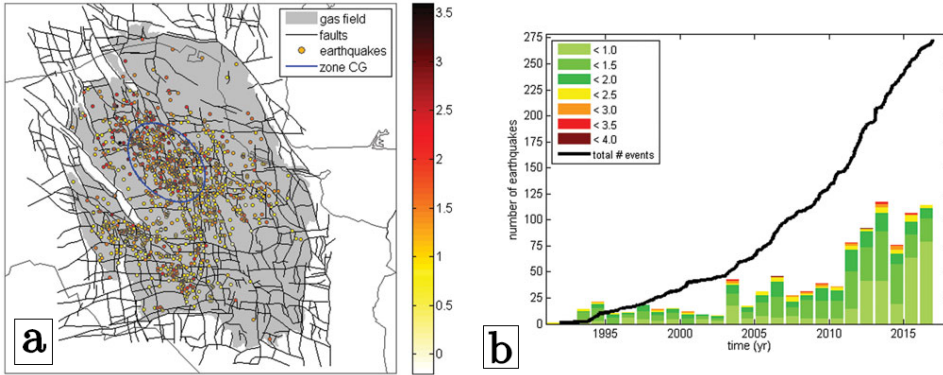
Figure 1.1: (a) The Groningen gas field and the induced seismicity in the region, as reported by the Dutch Meteorological Institute (KNMI), with the colour code indicating the magnitude of the events on the Richter scale, and (b) the growth of the cumulative number of events of magnitude 1.4 & higher (solid line) on the Richter scale, and the overall annual number of earthquakes in different magnitude classes (histogram) [91]

In this regard, Nederlandse Aardolie Maatschappij (NAM), an exploration and production company composed of a joint venture of Shell & Exxon, and the Dutch government initiated a comprehensive research program in 2014 combining experimental testing and computational modelling approaches (Figure 1.2) to assess the seismic behaviour of

1

these URM buildings [87, 124]. An elaborate experimental campaign ranging from material/element level (bricks, mortar, steel ties, timber) to component level (walls, floors) and finally structural level testing (full scale building) was carried out to characterise the building stock of the region and assess the potential damage. However, simultaneously, numerical models were crucial as they not only help in understanding the structural behaviour but also contribute to design measures towards mitigating the problem. The goal was to first cross validate these models against existing and upcoming lab structural tests, to reveal possible conservativeness in existing approaches, and then to predict the capacity of the Groningen building stock under seismic action, in the current state and post-strengthening.

UNREINFORCED MASONRY BUILDING TYPOLOGIES: GRONINGEN, NETHERLANDS
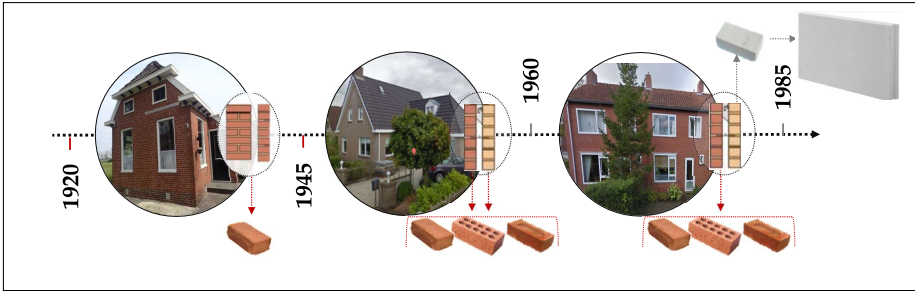
RESEARCH CAMPAIGN
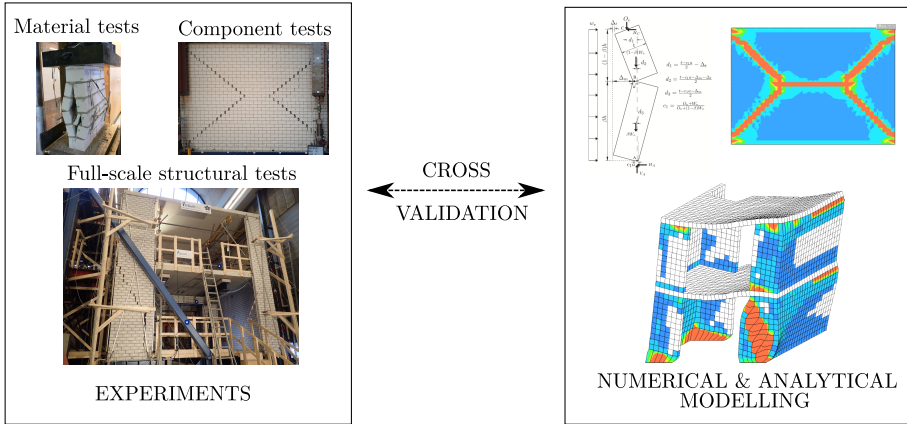
Figure 1.2: The typical unreinforced masonry building typologies in the Groningen area (top), and the research campaign to address the induced seismicity in the region using a combination of a multi-scale experimental program and numerical & analytical modelling approaches [87].

The impact of seismic loads on a structure, in general, can be calculated using one of the following methods: 1) lateral force analysis, which is a static and linear (material)

approach, wherein the load is applied as a concentrated force at the center of mass of each floor, 2) Response spectrum analysis, which is a linear dynamic analysis with loads applied as a spectrum, 3) Pushover analysis, which is a nonlinear static analysis taking into account the material nonlinearity and with sub-variants depending on the shape of loading on the structure [46], and finally, 4) Nonlinear time history analysis, which is a nonlinear dynamic analysis, wherein the load is applied as an accelerogram. Among the alternatives, the Nonlinear Pushover Analysis (NLPO) is the simplest yet most efficient way to obtain information about a structure's response to earthquakes, by verifying the seismic load paths and the performance of the contributing (structural) components. It is computationally less intensive than the more elaborate nonlinear dynamic analysis. Finite element (FE) models, the most widely used class of numerical methods in engineering practice, are often the framework of choice for such pushover applications [88]. However, the numerical prediction of damage in this context is a challenging task since unreinforced masonry, the material under consideration, fails in a rather brittle manner.

Another application of FE models lies in the domain of reinforced concrete structures. Nonlinear finite element analyses (NLFEA) are used in engineering practice towards the assessment of flexural and shear capacity of existing reinforced concretes structures and components, such as bridges & viaducts [13, 62] and slabs in nuclear reactors [20, 93]. Current design standards indicate that those of the past were mostly conservative with respect to shear failure. Elaborate NLFEA simulations could help exploit reserves in the existing design of structures, before venturing towards more expensive options such as strengthening or replacement. However, these simulations are generally characterised by cracking which is often diffused due to the presence of reinforcements, and particularly, in case of the shear critical structures, result in a rather brittle and explosive mechanism.

Quasi-brittle materials, including concrete and unreinforced masonry, appear cracked or damaged to the naked-eye only when the micro-damage coalesces to the macroscopic level. Upon loading beyond their elastic limit, such materials exhibit a degradation of stiffness and strength which is also called post-peak softening. Although it may seem as a material characteristic, it is regarded as a structural phenomenon resulting from micro-cracking [141]. This post-peak softening behaviour poses challenges to nonlinear finite element simulations, as in the pushover analyses and reinforced concrete applications, in firstly, obtaining mesh-objective results and secondly, ensuring robust solutions. Both these issues arise due to the loss of ellipticity of the governing partial differential equations [35], when the increase of damage results in localisation of strains, and the stiffness matrix becomes non-positive definite. The issue of mesh objectivity has been addressed by several researchers using regularisation procedures [12, 109, 11, 36, 108], embedded strong discontinuity approaches (SDA) [42, 76] or the extended finite element method [136, 89, 14, 153] to name a few, all of which are briefly described in Chapter 2. However, the solution procedure in use for such applications, the standard incremental-iterative technique, could lead to solutions that are not converged i.e. do not represent the true equilibrium path.

The incremental-iterative (implicit) solution procedure solves the nonlinear system of equations in stages or the so-called load steps, each of which are discretisations of the total load to be applied on the model. With each load increment, the iterative part of the procedure makes successive predictions for displacements such that the unbal-

1

anced forces (between external and internal forces) are reduced and global equilibrium is reached. In obtaining such a converged solution, the procedure could run into trouble when structural softening results in rapid damage propagation at several locations. This could be seen as multiple cracks trying to survive and that the simulation is at a potential bifurcation point [123]. At such a juncture, the simulation leads to the propagation of some cracks while other unload. Several remedies including using smaller steps, alternate iteration schemes, displacement controlled loading, path following approaches like arc-length control [30, 34, 147] and line search algorithms [29, 35] help only partially because they are not completely robust and additionally, in general, require user expertise.

To address this issue of stability in NLFEA, several alternate approaches were proposed one of which is the Sequentially Linear Analysis (SLA) conceived by Rots [117]. Originally inspired by lattice modelling applications [128], the method was secant stiffness-based and developed for continuum problems to simulate the failure process in quasi-brittle materials by allowing for one damage event at a time. Thus, the nonlinear modelling of quasi brittle fracture was alleviated of multiple cracks attempting to survive and the use of secant stiffness made the procedure robust. The approach involves running linear analyses sequentially, each of which identifies a critical integration point in the FE model with the maximum stress. The strength and stiffness of this point are degraded based on a discretised step-wise constitutive relation called the *saw-tooth law*. The linear analysis results are scaled using a load multiplier corresponding to the identified critical point and the analysis proceeds. Each linear analysis corresponds to a damage event, and therefore, the approach is damage driven as against the load, displacement or arc-length driven approach in traditional implicit NLFEA. There exist other robust solution procedures as well in literature like the IMPL-EX method (combination of the implicit and explicit methods) [100], Non-Iterative Energy-based Method (NIEM)[57], Continuous Incremental-only Tangent Method (CITA)[2] etc., which are discussed in detail in Section 2.2.2. However, SLA, owing to the combined advantage of its simplicity and robustness, is chosen as the solution procedure to address the numerical (FE) prediction/assessment tasks in consideration for the thesis.

1.2. RESEARCH OBJECTIVES & SCOPE

The main objective of the work is to enhance Sequentially Linear Analysis to make general 3D FE applications such as pushover analysis on structures possible. Real life structural analyses involves two key aspects: specimen of large magnitude, and real loading schemes characterised by multiple loads. The latter refers to the presence of constant loads on structures like dead weight and the subsequent application of variable loads like the lateral seismic load. This kind of **non-proportional loading** makes the damage driven SLA procedure less straightforward, and also, invokes the need for redistribution procedures to allow for dynamic failure propagation, which in turn needs more insight at structural level [139]. Furthermore, the SLA procedure has only had 2D modelling applications, under plane stress assumptions, for concrete and masonry specimens in the past [131, 139, 55]. The constitutive models generally used, thus far, for such examples in SLA are the total strain-based orthogonal fixed smeared cracking model [116], discrete cracking [140], and Coulomb friction interface models [139]. These models need to be extended to

three dimensional (3D) stress states, in order to enable structural masonry and concrete illustrations. Finally, the **computational efficiency** of SLA is one of concern as pointed out by many researchers [139, 151, 4, 1]. The system of linear equations to be solved only changes locally between analyses in SLA due to the event-by-event nature of the approach. This is not utilised effectively by traditional direct solvers, thereby compounding analysis times.

In conclusion, the SLA method needs to be improved and extended from the non-proportional loading, constitutive modelling and computational efficiency aspects which translate to the following specific objectives:

- To develop a better understanding of the redistribution mechanism involved in sequentially linear analysis under non-proportional loading conditions

- To extend the constitutive models in SLA and develop the non-proportional loading strategy for full 3D stress states

- To develop tailor-made solvers in order to efficiently solve the system of linear equations in an SLA setup

The studies in this dissertation involve masonry and concrete examples. Masonry can be represented in FE models using micro, meso and macro modelling approaches depending on the required level of accuracy (local or global behavior of the structure) [82]. Macro-modelling, which considers masonry as a homogeneous continuum, is used predominantly in this work because it is advantageous owing to reduced computational time and memory requirements, as well as the user-friendly mesh generation. The material behaviour of the continuum is then described using uniaxial constitutive laws in combination with a fixed smeared crack/crush framework and/or discrete cracking/sliding interfaces [139], where necessary. Concrete has also been represented using these formulations adequately thus far [116, 35] and is therefore used in this study.

The novelty of the work lies in the improvements to these formulations within the SLA setup and in broadening the range of applications, while simultaneously improving the computational efficiency without loss of accuracy. The thesis primarily extends on the aforementioned formulations to allow for 3D cracking/crushing and sliding problems. With regard to damage in the continuum, a simple Rankine-type failure surface is used for both crack and crush initiation. This is followed by uniaxial linear tension softening and parabolic compression softening [51] relations for damage propagation along the orthogonal directions of 3D fixed crack/crush system. Compressive nonlinearities which were previously not considered in the smeared fixed system in an SLA set-up are incorporated in this thesis. However, the effects of lateral confinement or cracking on the compressive behaviour are currently under investigation (for the SLA framework) and therefore, discarded in this study. Additionally, the anisotropic behaviour of masonry is not taken into account in the developments of the constitutive models since the focus of the study is more on the robustness of the SLA procedure for the post peak part of NLFEA simulations. Furthermore, a composite interface model is also proposed, both for line (2D) and planar (3D) formulations, allowing for combined cracking-shearing-crushing failures in discrete interfaces under the domain of micro-modelling approach for masonry analysis. Finally, experimental benchmarks of both concrete and masonry, exhibiting

1

brittle failures, are used for the illustration of each of the said developments, thereby serving as validation studies.

1.3. Thesis Outline

The dissertation is organised as follows:

Chapter 2 presents an extensive literature review on FE modelling of quasi-brittle fracture, ranging from discretisation methods to solution procedures and the problems involved therein. Thereafter, the SLA approach and the latest contributions on the topic are summarised, with a final outlook on the developments needed for this thesis.

Chapter 3 contains an overview on the different classes of sequentially linear methods and their approaches to the non-proportional loading problem. Furthermore, a qualitative discussion on the approaches is presented.

Chapter 4 presents a comparative study between two sequentially linear methods: SLA and the Force-Release approach, using continuum models of structural case studies like pushover analyses on walls and a masonry facade. This chapter illustrates the inherent differences in the redistribution mechanism of the methods.

Chapter 5 presents the 3D total-strain based orthogonal fixed smeared cracking model and proposes two possible solutions for damage initiation under non-proportional loading for a full 3D stress state in the continuum. The concept is then validated using two academic case studies of prestressed beams subject to flexure, with straight and skewed notches to study the effect of planar and non-planar 3D curved cracking respectively. Additionally, the chapter contains the simulation of a real-life experimental benchmark of a reinforced concrete (RC) slab, subject to axial loads followed by a concentrated shear load, that results in a one-way brittle shear failure.

Chapter 6 proposes an extension of the Coulomb friction formulation for interfaces in SLA to a general multi-surface model, including tensile and compression failure options. This is then validated using pushover analyses on 2D and 3D micro-models of a squat masonry wall which exhibits diagonal shear failure.

Chapter 7 proposes two novel tailor-made linear equation solvers to improve the computational efficiency of SLA, solely from the point of view of solving the system of equations more efficiently, in comparison to a direct solution method. Thereafter, using two benchmark cases, one of a pushover analysis on a masonry wall and the RC slab example from Chapter 5, the proposed solvers are examined for improvement in performances, additionally with parametric studies on saw-teeth and mesh refinements.

Chapter 8 summarises the main contributions of this work, the limitations of the SLA approach at this juncture, and presents an outlook for further research on the topic.

Problem identification

Chapter 2
Literature Review

Assessment of methods

Chapter 3

Analysis of approaches to
non-proportional loading in
Sequentially Linear Methods

Chapter 4

Redistribution mechanism in
Sequentially Linear Methods:
SLA vs Force-Release method

Developments   **Applications**

Chapter 5

One-Way shear failure
in RC Slabs

Non-proportional loading
for 3D stress state
(3D Fixed crack model)

Chapter 6

Diagonal shear failure
in masonry walls

Composite Interface model
for masonry analysis:
Line & Surface interfaces
(Cracking+Sliding+Crushing)

Chapter 7

Improved solver times
for increasing problem sizes

Two Tailor made solvers for SLA:
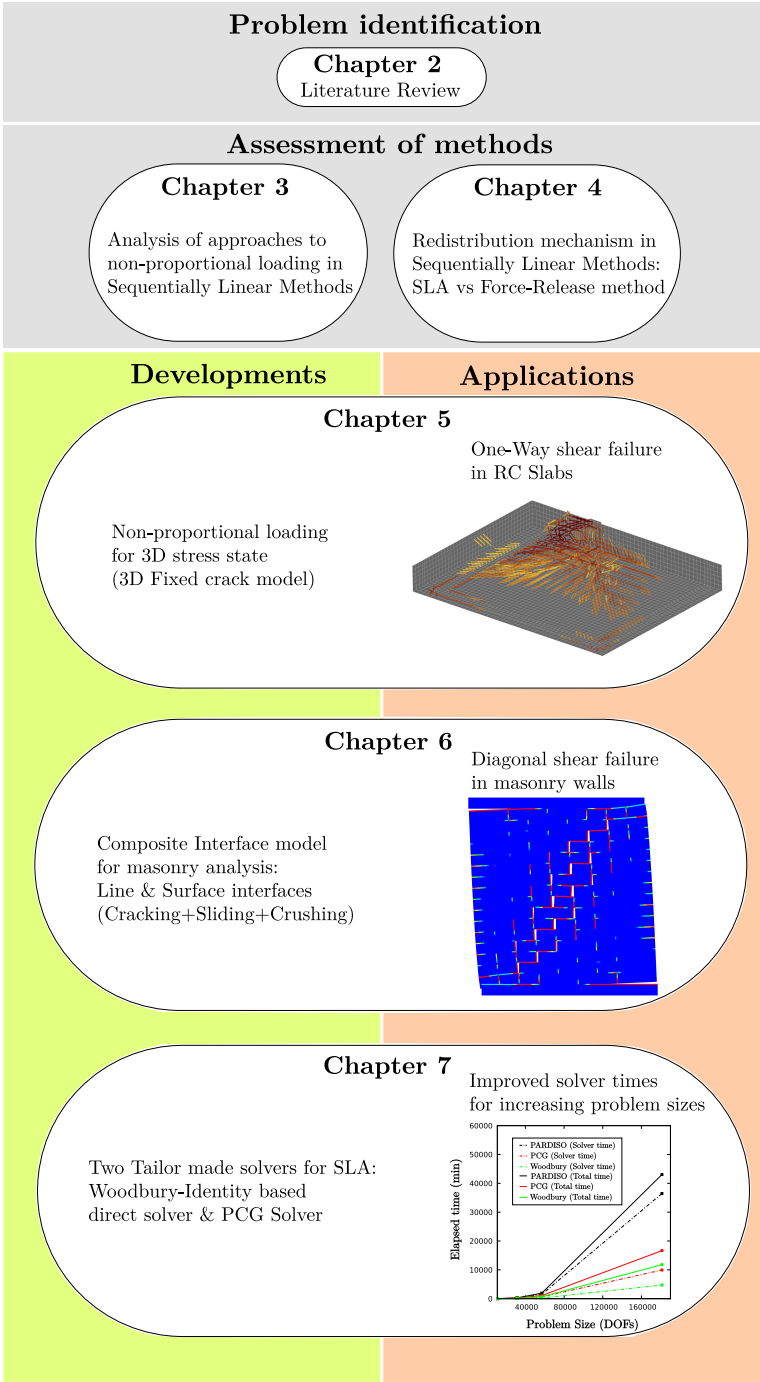Woodbury-Identity based
direct solver & PCG Solver

Figure 1.3: Thesis outline

CHAPTER 2
LITERATURE REVIEW

This chapter presents the background theory necessary to take upon the research objectives briefed in the first chapter. Section 2.1 provides a brief introduction to the available methodologies and constitutive frameworks involved in standard & advanced finite element formulations, with regard to the modelling of quasi-brittle fracture. Section 2.2 sheds light on the numerical solution strategies used in the finite element method, for linear and nonlinear problems, to solve the system of equations. The discussion motivates the need for robust solution procedures in nonlinear finite element analysis. Section 2.3 delves into Sequentially Linear Analysis (SLA), the non-incremental non-iterative solution procedure to be used in this study, and provides an extensive overview on its workflow and constitutive modelling. The chapter is summarised in Section 2.4

2.1. FINITE ELEMENT MODELLING OF QUASI-BRITTLE FRACTURE

Nonlinear analysis of a quasi-brittle structure or specimen using the finite element (FE) method has been in practice for almost 60 years. The development of cracks is a successive physical process that begins with the formation of the so-called *fracture process zone*, which involves micro cracking, and results in its coalescence into a stress-free macro-crack. This is commonly represented mathematically using the cohesive zone model, originally developed for elastic-perfectly plastic material behaviour [8, 41], and later adapted for quasi-brittle materials by Hillerborg et al. [65] as the *fictitious crack model*. Herein, the crack initiation is governed by the exceedance of the principal stress at the tip of the process zone. The cohesive force transfer is then described as a function of the crack width, commonly referred to as tension softening curves [66, 115], and is lumped into a fictitious line or plane.

Finite element representation of such behaviour is usually characterised by localisation of strain and damage into a narrow band of elements. These narrow zones are referred to as *shear bands* in ductile (metals) and granular materials (gravel, sands, soils etc.), and as *kink bands* in fibre-reinforced composites undergoing compressive loading [73]. In case of quasi-brittle materials, the FE representation of these localised damage zones can be classified based on two perspectives as follows.

Kinematic perspective Depending on the regularity of the displacement field **u**, three types of kinematic descriptions are found in literature as shown in Figure 2.1.

- *Strong discontinuities*: This type exhibits jumps in the displacement field across a discontinuity in the specimen and thus, has a singularity in the strain field. It physically corresponds to a crack or slip line. In a finite element sense, these can be

represented in continuum models as discontinuities, commonly referred to as the *discrete crack* approach, in the following manner:

- Using interface elements :
  - ◇ at predefined locations in the mesh, along existing continuum element boundaries, that are known to be prone to cracking. This could be based on a mechanics perspective or on information from the experiments. However, this results in strong mesh-dependence when these element boundaries are not chosen with care [23]
  - ◇ in new locations, as the simulation proceeds, by allowing for remeshing of the model along the propagating crack tip [67, 68, 152, 138]. This is done by continuously changing element topologies and subsequently, enabling crack propagation when either the stress intensity factor, energy release rate or crack opening displacement exceeds a critical value [154]. Although this helps avoid mesh dependence, the complexity of the code, the need to map the previous stress state on the new mesh, and a relatively high computational cost [22, 96] prove to be bottlenecks.
- Using elements with embedded strong discontinuities [42, 76] or the extended finite elements [136, 89, 14, 153], that allow displacement jumps across a sequence of segments with arbitrary positions and orientations with respect to the basic finite element. These approaches depend on enriching the standard shape functions by special discontinuous functions. The relatively large computational demand, and the complications involved in describing crack branching, coalescence and curved crack boundaries in three dimensions, tend to not favour the use of these methods [129, 37] in comparison to the more widely used *smeared crack approach* described in the following.

- *Weak discontinuities*: This type represents damage as a small but finite band of elements separated from those of the undamaged material. The displacement field herein is continuous, while the strain field has two jumps or discontinuities. It physically represents the damage process zone with an almost constant density of micro-damage. The thickness of the band, approximated using standard continuum finite elements, is thus bound by weak discontinuities. It can be seen as a regularisation of the models with strong discontinuities. The *smeared crack approach* [22, 23] and the approach of elements with *embedded localisation bands* [15, 72] fall in this category. The former approach, considering the simplicity and suitability to the traditional displacement-based finite element framework, continues to find popularity in the engineering community for large-scale structural applications. However, it is known to suffer from spurious mesh dependency: both with regard to the fineness and orientation of the elements in the mesh [10]. The crack-band theory [12] with an orientation dependent element characteristic length [99, 149, 131], and additional crack tracking algorithms [24, 134], relieve the approach of such problems, although not fully but satisfactorily. The latter approach permits modelling of the band to be independent of the two issues related to mesh dependency, and the thickness of the band can be considered to be a part of the constitutive model.

- *No discontinuities*: This type describes the damage zone as a continuously differentiable displacement field using localisation limiters, which in turn makes the strain field continuous. This physically reflects a damage process zone with higher concentration of damage near its center. The approaches under this category are referred to as *regularised* models, wherein the enrichment involves a parameter with a characteristic length related to the size and spacing of heterogeneities in the material. This class includes *integral-type non-local* models [109, 11], *gradient enriched* models [36, 108] and the *thick level set* approach [90] to name a few. These methods require extremely fine meshes with multiple elements over the width of the fracture process zone, which hampers use for large-scale structural practice. Furthermore, there are rate-dependent models [142] which also regularise the continuum description of localisation, and additionally, address the time-scale in quasi-static cracking.

The first approach is commonly referred to as the '*discrete crack approach*' while the last two approaches could be considered as '*smeared crack approaches*' together, purely in the sense that cracks are diffused or 'smeared' in the continuum (irrespective of the sophistication of the regularisation technique).

Constitutive framework   All the aforementioned kinematic descriptions inherently require a constitutive framework to describe the behaviour of the material undergoing fracture. The constitutive model describes the macroscopic features of the material using a stress-strain relation, as illustrated in Figure 2.1. These fall broadly into three categories: *damage*, *plasticity* and *combined damage-plasticity* models, all of which can adequately describe both the discrete and smeared crack approaches.

The *damage mechanics* framework, first conceived by Kachanov [75], is based on the concept of progressive reduction of the elastic stiffness. The damage accumulated is considered irreversible and could be isotropic, represented by one or two scalar multiples [27, 86], or anisotropic, using a family of vectors [77] or 2nd [92] or 4th order tensors [25], depending on the model used. The loading and unloading is done using the secant stiffness. These models are suitable to simulate stiffness degradation due to cracking or crushing, and also crack-closure or stiffness recovery, but not irreversible deformations. The *plasticity* framework [60] is based on simulating irreversible inelastic strains since the elastic stiffness is assumed to remain constant. The total strain is decomposed into an elastic part and a plastic part. The principal features of the framework are the yield function which bounds an elastic region in stress space, a hardening law which defines the evolution of the yield surface, and a flow rule. Plasticity models vary depending on the types of these features. But these models, in general, fail to describe the stiffness degradation due to cracking, as well as other related effects like stiffness recovery upon crack closure [27, 59]. In *combined damage-plasticity* models, the positive features of the first two classes of models are combined. The damage theory is used to model the stiffness deterioration caused by micro-cracks propagation, while the permanent deformations are captured using plasticity theory [94, 95]. Variations exist depending on whether the plasticity model is combined with the isotropic [58, 101] or the anisotropic damage model

2

KINEMATIC PERSPECTIVE
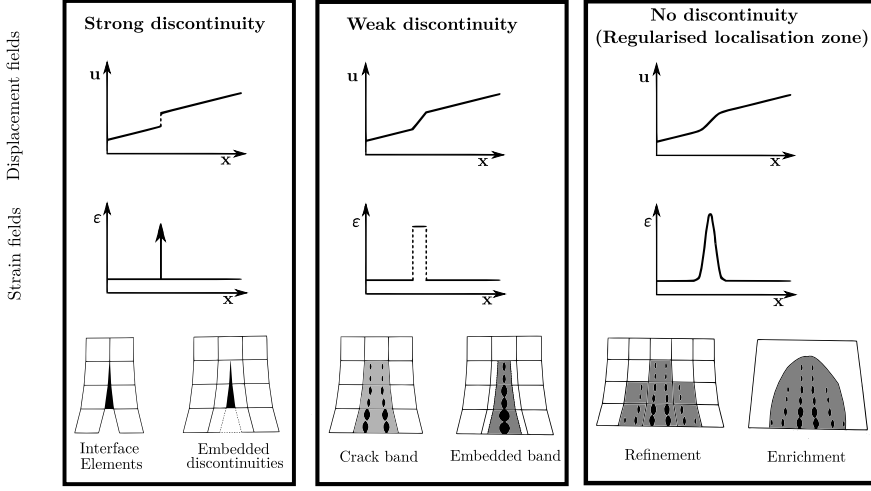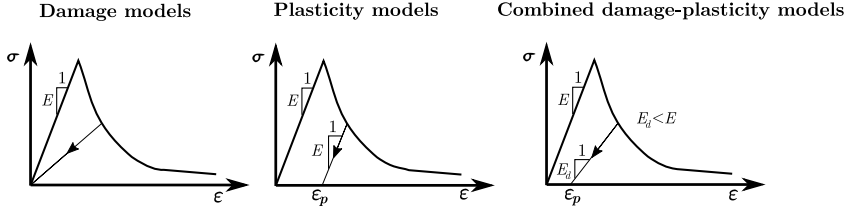

CONSTITUTIVE FRAMEWORKS

Figure 2.1: Classification of crack representations according to: Kinematic perspective (top) [73] and constitutive frameworks (bottom) [94]

[70, 59], with the former being preferred for practical applications (like for concrete) due to the latter's algorithmic complexity .

Apart from the three broad classes of constitutive models, there exists another class of models, specifically for continuum applications, which shares the common features of both the damage and plasticity models. This class is referred to as the *smeared crack models* [116], which are not to be confused with the broader 'smeared crack approaches'. The latter refers to the general idea of diffusing cracks over a band of elements in a continuum. Similar to plasticity models, the smeared crack models can decompose the total strain into an elastic and a plastic part, herein the crack strain. Instead of the yield condition and the flow rule, this model relates the crack strain directly to the traction transferred across the crack. Similar to damage models, the elastic stiffness is damaged progressively and is taken into account in the unloading mode. Such *decomposed strain based* models allow for multi-directional fixed cracks [119]. Alternatively, *total strain based* variations of the smeared crack models relate the material stress to the total strain [50]. The first sub-variant of this type is the *fixed crack model*, wherein the crack direction

is assumed to fixed upon crack initiation, and the shear tractions that develop across the crack face are controlled by the so-called shear retention factor. The second sub-variant is the *rotating crack model* based on the coaxial stress-strain concept, in which the stress-strain relationships are evaluated along the principal directions of the strain vector, thereby alleviating the need for an explicit shear retention function [119]. Hybrid sub-variations which transition from rotating to fixed also exist [112]. This class of total strain based smeared crack models predominate the applications illustrated in this thesis (with secant unloading-reloading) and is described further in Section 2.3.1 from a sequentially linear analysis point of view (described elaborately in Section 2.3).

Furthermore, for continuum representation of fracture, there exists another class of models which are based on the relationship between the vectors obtained by projecting the stress and strain tensors on a plane of a given orientation, as against using the tensorial stress-strain relationship like all other classes of models described herein. The tensorial stress-strain relations are then obtained by averaging over all possible orientations of a finite number of potential damage planes (called *microplanes*). These models are called *microplane models* [21, 102] and are similar to the multi-directional fixed crack concept, except that the macroscopic strain is not decomposed.

2.2. SOLUTION PROCEDURES

2.2.1. SPARSE LINEAR SYSTEMS

For linear elastic problems, the system of equations to be solved in the standard displacement based finite element analysis is as shown in the following

$$\mathbf{Ku} = \mathbf{f} \qquad (2.1)$$

where $\mathbf{K}$ is the system stiffness matrix, $\mathbf{u}$ is a vector of the unknown nodal degrees of freedom (i.e. displacements and rotations. All studies in this dissertation deal with the former.) and $\mathbf{f}$ is the vector of the nodal forces corresponding to the degrees of freedom $\mathbf{u}$. For practical structural applications, the assembled global stiffness matrix $\mathbf{K}$ is square, sparse, and in most formulations, symmetric. Sparse linear systems in typical finite element simulations have a large number of equations and unknowns. Therefore, solving them efficiently is important. The solution methods for such systems are broadly split in two main categories.

First is the traditional direct solution method to solve the system of linear equations, also commonly referred to as *Direct solvers*, which involves a factorisation of the stiffness matrix $\mathbf{K}$ and calculation of the displacements $\mathbf{u}$ by forward and backward substitution. The factorisation takes a lot of time and memory, and is therefore computationally expensive. This is usually done by expressing $\mathbf{K}$ matrix as $\mathbf{K} = \mathbf{LU}$, where $\mathbf{L}$ and $\mathbf{U}$ are lower and upper triangular matrices respectively. Commonly referred to as the LU factorisation, this reduces to the more favourable Cholesky factorisation $\mathbf{K} = \mathbf{CC^T}$ for symmetric positive definite (SPD) stiffness matrices, where $\mathbf{C}$ is a lower triangular matrix. Once factorised, the system can be efficiently solved for any number of right-hand sides and the approach is rather straightforward. Two state-of-the-art direct solvers which provide the additional option of parallelisation are the MUltifrontal Massively Parallel sparse

direct Solver (MUMPS) [5] and the PARallel DIrect sparse SOlver (PARDISO) [127]. The implementation of the direct solution method in DIANA [51], the commercial software used for FE simulations in this thesis, uses Intel's PARDISO interface which enables high-performance serial and parallel solving of sparse linear system of equations. PARDISO is popular for its parallel scaling, where speed ups of a factor of 7 have been realised when running on 8 threads [7].

The second type is the iterative solution method, commonly referred to as *Iterative solvers*, which involves no, or at most a partial factorisation, and deduces the solution using inner-products, vector updates, scalar-vector and matrix-vector products. As a result, these methods require a relatively small amount of memory to solve the problem compared to direct solution methods. Consequently, they are more suitable to problems where **K** is large, typical of structural engineering FE applications. Krylov subspace methods, a class of iterative methods, is described more in detail in Section 7.2.2. There are many types of iterative solvers [125] and the choice is heavily system dependent. Conjugate Gradient method (CG) [64] is suitable for symmetric positive-definite matrices and the MINimal RESidual method (MINRES) [125] for symmetric (and possibly indefinite) matrices. For non-symmetric matrices, there are approaches such as the Generalised Minimal RESidual method (GMRES) [126] and the Bi-Conjugate Gradient method (BiCG) [53]. For information on other solvers like the class of multigrid methods, the reader is referred to References [7, 56].

2.2.2. NONLINEAR SYSTEMS

In the case of nonlinear finite element analysis (NLFEA), similar to linear analysis, the unknown displacements are calculated such that the internal and external forces are in equilibrium. However, the internal force vector may vary nonlinearly on the displacements (nonlinear elasticity - physical nonlinearity), or also depend on displacements from previous increments (plasticity - physical nonlinearity). Furthermore, the external force vector can also become dependent on the displacements when they are large enough to change the direction or magnitude of the loads, thereby forcing to revisit the equilibrium equations (geometric nonlinearity). Alternatively, the stiffness matrix in itself may change with deformation owing to contact involving the interaction of parts of the system (contact nonlinearity). There are several numerical techniques to solve such varied nonlinear problems and these are discussed briefly in this section.

Implicit and Explicit methods   In the displacement based finite element formulation, in addition to discretising the problem in space using finite elements, the problem is discretised in time. This may be the *real*-time as in a dynamic analysis but could also be considered *pseudo*-time that numerically reflects a sequence of situations as in a quasi-static analysis. The solution is then obtained by direct time integration of the equations of motion (EOMs) of the system in the time domain t, such that they are satisfied at discrete time intervals Δt [9]. Depending on the time integration, there exist two types of methods.

The *Implicit methods*, also alternatively known as incremental-iterative methods, achieve equilibrium at the end of each increment by using an iterative solution algorithm like a full or modified Newton-Raphson, Quasi-Newton, the linear or constant stiffness method. For details on the types of iterative methods, the reader is referred to References

[9, 34]. The external load, applied either as forces or prescribed displacements, is discretised into smaller steps (referred to as load control or displacement control) resulting in total displacement increments $\Delta\mathbf{u}$ per step. The iterative displacement increment within each step $\delta\mathbf{u}$ is first computed by using a linearised form of the stiffness matrix $\mathbf{K}$. The internal forces $\mathbf{f}_{\text{int}}$ are then deduced for the corresponding displacement increment, and the out-of-balance force vector $\mathbf{g}$ is calculated as the difference between the external $\mathbf{f}_{\text{ext}}$ and the internal forces $\mathbf{f}_{\text{int}}$. Convergence is considered to be obtained when one or both of the out-of-balance force and the iterative displacement increments measured (for instance, by Euclidean norms (L2)) are within a specified tolerance. For ongoing iterations, the iterative displacements are re-evaluated for the new or existing stiffness matrix (depending on the iterative scheme), and subsequently, out-of-balance forces are rechecked and the process continues until the problem converges. Additionally, line search methods [29, 35] which adapt the size of the displacement increment for a given stiffness matrix and minimise the residuals, instead of computing new search directions with a new stiffness matrix, prove beneficial for faster convergence. However, the performance of line search depends on the smoothness of the relation between the out of balance forces and the displacements, and also on the quality of the current search direction [35]. Furthermore, to capture responses that have snap-throughs and snap-backs, path following methods like the arc-length and crack-mouth opening displacement control are available. The crux of the arc-length method [30, 34, 147] is in forcing the solution path to remain close to the last converged equilibrium point, which is done by introducing an additional constraint equation for the incremental load multiplier that plays the role of an extra degree of freedom in the global linearised equilibrium equations. Various constraint methods have been proposed, such as the direct or indirect displacement control methods, and the choice is crucial since it affects the convergence properties [35]. In summary, implicit methods solve the system of equations involving both the current state of the system at time t and the subsequent one at $t + \Delta t$. They are unconditionally stable, and the size of time increments in solving the system of equations does not significantly affect the accuracy of the solution as long as it is converged to an appropriately small tolerance.

The *Explicit methods*, also alternatively known as incremental tangent methods, solve the system of equations at time $t + \Delta t$ from the ones at time t. The use of such a purely incremental behaviour (without internal iterations) results in numerical instability with the use of large time-steps. It could also result in the drift of the solution from the true equilibrium path due to lack of internal iterations. The time step in explicit analyses must be less than the *Courant time step* (time taken by a sound wave to travel across an element) for numerical stability [9, 35]. Nevertheless, due to the fact that there is no need to solve the matrix system (factorisation) repeatedly, the explicit methods are generally computationally less intensive than the implicit methods [135, 26]. Also, they are more favourable for large deformation and contact problems [26]. The choice between the two methods may be made based on the time-scale of the problem. Explicit methods are suitable for short transient problems such as those with impact loads, while the implicit methods are superior for quasi-static problems.

2

Sequentially linear methods   NLFEA of civil engineering structures/specimens made of quasi-brittle materials, characterised by strain-softening, can suffer from the so-called *convergence troubles*. The incremental-iterative nature of the solution procedure could push multiple integration points into softening simultaneously in a single load step. This can affect the positive definite nature of the global stiffness matrix, resulting in the ill-conditioning of the finite element formulation [31, 57, 35]. As a consequence, numerical instability and divergence may occur at these instances possibly leading to inaccurate results due to deviations into alternative equilibrium paths. Additionally, simulations of such strain softening materials like concrete and masonry, often encounter problems related to snap back, bifurcation points and sudden jumps in the response [123, 139, 131]. Several path-following techniques like the Arc-length control, Crack mouth opening displacement control, energy release control [61, 147] etc. address this problem, but are sophisticated techniques requiring user expertise in NLFEA (also knowledge of crack locations a priori) and do not always guarantee the true response.

This gave rise to several alternate methods, one of which is the Sequentially Linear Analysis (SLA) wherein the nonlinear response is approximated as a sequence of scaled linear analyses with gradually increasing damage (damage-driven). It is a non-incremental (*total*) [117, 121, 118], secant stiffness-based event-by-event approach, wherein one linear analysis is performed at a time to identify and damage the *critical* integration point in the FE model. The definition of the load multiplier per analysis step j for each integration point i, over all elements in the FE model, is shown below in a general sense, where f_i^j and $\sigma_{\mathrm{gov},i}$ are the corresponding allowable strengths and governing stresses respectively. The critical integration point is identified as the one with the minimum of all such positive load multipliers, the critical load multiplier λ_{crit}.

$$\lambda_i^j = \frac{f_i^j}{\sigma_{\mathrm{gov},i}^j}, \quad \lambda_{\mathrm{crit}}^j = \min_i\left(\lambda_{\mathrm{crit},i}^j\right) \quad \forall \quad \lambda_{\mathrm{crit},i}^j > 0. \tag{2.2}$$

The linear analysis results i.e. displacements, forces, stresses and strains are then scaled using the critical load multiplier λ_{crit}. Subsequently, the strength and stiffness of this integration point are reduced in a step-wise manner based on a discretised constitutive relation, with successively reducing secant stiffnesses and allowable strengths, called the *saw-tooth law*. This process of identifying critical events and load scaling is repeated until a user-defined stop criteria is reached or possibly when all elements in the FE model are completely damaged. The method avoids multiple integration points being pushed simultaneously into failure, as in an incremental-iterative approach, and is therefore robust. In other words, SLA traces through every event, i.e. a jump or snap back, that may occur in the response of the structure. The combination of a *total* (load-unload) approach and the saw-tooth laws forms the crux of the method. A detailed overview of the SLA framework, with respect to the constitutive modelling and workflow aspects, is presented in Section 2.3.

The approach has been under development from the early 2000s and successfully used for structural NLFEA in the past [117, 121, 118]. It is a proven alternative for applications in masonry [55], reinforced concrete [139] and glass [69]. Advancements in SLA include

contributions to make the procedure mesh-objective [118, 139], saw-tooth laws for extremely brittle materials like glass (with snap-back at constitutive level) [69], extensions to non-proportional loading situations [40, 44, 57, 43], extensions to interface elements with discrete cracking [140], bond-slip [47] and step-wise secant Coulomb friction laws [139], creep induced cracking [63], combined incremental-total approaches like Non-Iterative Energy based Method (NIEM) and the automatic method [57], SLA in a stochastic setting [54], combining SLA with crack tracking technique [131], and mesh free SLA [1].

SLA is a feature, as a part or whole, of several state-of-the-art solution methods which are hereon referred to as *Sequentially Linear Methods* (SLM), although alternatively referred to as non-iterative methods in literature [57]. These methods, comprehensively reviewed and discussed in Chapter 3, can be classified into three categories: purely *total* approaches [40, 139, 3] wherein unloading and reloading are done non-proportionally, purely *incremental* approaches [44, 43, 57] wherein the stress and loading history is explicitly tracked, and finally, a class of *combined incremental-total* approaches [57].

Other methods   Another approach towards robust simulations in NLFEA is the IMPL-EX method [100] which, as the name suggests, combines the implicit and explicit methods. For a given strain in the current time step, the approach computes the stresses and internal variables in a two-staged process. In the first stage, the stresses and internal variables (like the damage evolution parameter in an isotropic damage model) are explicitly extrapolated, using the implicitly integrated stresses and extrapolated values of the strain-like internal variable obtained in the previous time step. This is used to compute the so-called IMPL-EX algorithmic tangent matrix and then determine the internal forces. Subsequently, nodal displacements are obtained by fulfilling a momentum balance equation in terms of the extrapolated stresses. In the second stage, implicitly integrated stresses and internal variables for the current step are obtained by a standard implicit backward Euler integration scheme of the constitutive model. A point of interest is that the length of the time step affects the accuracy of the solution obtained using the IMPL-EX strategy, where the order of accuracy varies linearly with the size of the time step. The approach has also been extended to the 'modified' IMPL-EX approach [110] for elasto-plastic problems, wherein the internal variables are updated in terms of the explicit evaluation of the plastic strain tensor components, instead of the explicit evaluation of the plastic multiplier.

The Ladevese's LArge Time INcrement method (LATIN) [18], another robust solution procedure developed for nonlinear evolution problems, is a purely iterative approach to derive the solution in a single time increment. The main principle of the method is to split the equations of the problem into two groups, to avoid simultaneously solving the global and the coupled problem. The first is a set of linear equations: the equilibrium and compatibility equations, and the state equations, which are decoupled and applied globally over the entire structure. The second is a group of local equations in space variables, which are constitutive (possibly nonlinear) and also contain initial conditions. The whole loading process is iteratively calculated in a single time increment, wherein each iteration is a two stage process corresponding to the global and local stages. The method's application in modelling softening materials is limited [145] although it helps track snap backs adequately. Additionally, since the *total* approach is used for non-proportional loading, it has limitations similar to SLA wherein reloading of constant loads

on a damaged state causes premature failure problems (addressed in detail in Chapter 3).

Another robust incremental-iterative alternative is the Smooth Unloading-Reloading (SUR) approach [4], that was applied for an isotropic damage model. The approach uses a target function, which replaces the softening function, and gives the equivalent uniaxial stress. This function depends on the damage evolution parameter that is directly proportional to the maximum strain. Additionally, the approach uses a smooth unloading–reloading function to compute an approximate positive-definite tangent matrix. The SUR function also depends on the damage evolution parameter, which is updated every iteration based on the last converged load increment. Although the approximated matrix is not the exact tangent, when there is loading with respect to the damage function, the results obtained were better in terms of efficiency and robustness as against the secant unloading-reloading method. Three acceleration approaches were also proposed [4] to further improve the convergence properties of the SUR method.

More recently, the Continuous Incremental-only Tangential Analysis (CITA) method, was proposed [2]. Similar to SLA, damage is introduced in steps in this incremental approach but the nonlinear stress-strain curve is discretised into piece-wise linear branches. The crux of the method is in using the tangent elasticity modulus to calculate the structural stiffness, despite the fact that some elements may have negative stiffness, using an appropriate linear equation solver with the ability to solve indefinite matrices. Every event is traced by the calculation of a critical load factor to find the smallest change in incremental load which causes the next damage occurrence, i.e. the smallest load for which the end of the current piece-wise branch in the constitutive relation is reached for some integration point. The approach is shown to successfully simulate simple concrete beam tests and claims to improve over the computational intensity of SLA since it requires lesser number of events. But this may not necessarily be the case if the number of branches in the *saw-tooth law* were the same as the number of piece-wise linear branches in CITA. Additionally, although the approach is damage driven, the ability to handle bifurcations and snap backs is unclear since any stress point is allowed only to either move up or down a piece-wise linear branch of the nonlinear curve. Furthermore, the method could potentially fail in case a singularity is reached and this is yet to be investigated.

2.3. SEQUENTIALLY LINEAR ANALYSIS (SLA) FRAMEWORK

2.3.1. CONSTITUTIVE RELATIONS

SLA is different from the traditional incremental-iterative approaches with regard to the constitutive framework in some aspects and these are presented in this section.

Uniaxial laws   The crux of the method is in discretising the uniaxial softening constitutive relation into an equivalent step wise secant material law, also known as the saw-tooth law. In principle, the material law is described as a series of successively reducing secant stiffnesses, starting from the initial elastic branch with the original Young's modulus of the material (E_0). Whenever there is breach of the stress limit in an integration point and it becomes the most critical in the FE model, the load is scaled with the critical load multiplier, and the next secant relation with reduced strength and stiffness properties

takes over from the previous secant branch. This process of tracing the critical point, reducing its stiffness upon attaining a stress limit and load scaling is repeated until the stiffness of the structure has vanished, which corresponds to a state of complete damage.
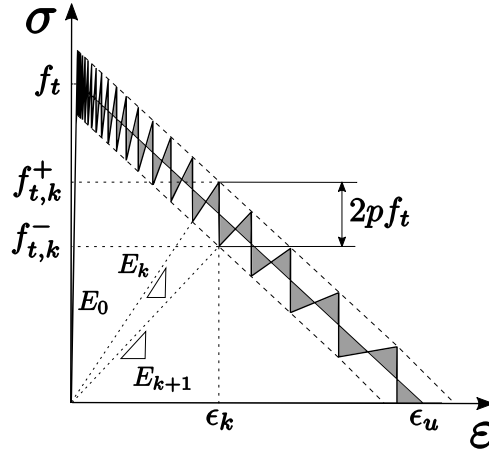

Figure 2.2: Linear tension softening saw tooth law, with p the saw-teeth discretisation factor, based on the band width ripple approach

Initially, the saw-tooth laws were generated by consecutively reducing Young's modulus and/or strength. But these proved to generate mesh objectivity problems with respect to capacity and energy dissipation, and consequently, a simple regularisation procedure was applied wherein the strength or the ultimate strain or even both are updated to keep the energy invariant, with the latter being reported as the most effective [121]. Eventually moving towards a more general approach to achieve mesh objective results, a *band width ripple* concept was introduced [118]. In this approach, a strength range p is defined as a percentage of the undamaged material strength, and a band is introduced into the softening part of the base curve, enclosing it such that the upper and lower triangles cancel each other out and eventually yield the same fracture energy (refer Figure 2.2). More recently, an *improved band width ripple* approach was presented pointing out that the vertical shifts from the base material law that define the original band width ripple approach need not necessarily be equal [139]. However, in complete contrast to the idea of regularising uniaxial saw-tooth laws, Alfaiate et al. [3] claim that a coarse saw-teeth type response in the force-displacement curves is as a result of an incorrect stiffness guess due to many points lying below their respective capacities and not due to mesh-objectivity issues with respect to fracture energy. This is in principle true since SLA is intrinsically a linear elastic load-unload method, and therefore there cannot be any energy dissipation as such. However, the progressive damage in the SLA approach could be interpreted as energy being consumed, which also manifests as the area underneath the sequence of load-displacement points. In summary, the topic of saw-teeth refinement needs further investigation and the illustrations in this study use linear tension softening and parabolic compressive softening relations with the original ripple band approach, unless specified otherwise.

Continuum frameworks

Fixed Smeared Crack Approach   The fixed crack model, a type of total strain based smeared cracking model, considered in most illustrations of the thesis, allows for orthogonal cracking (e.g. Reference [50]) and describes the cracking/crushing that arises in the fracture zone to be smeared over the continuum. It is rather straightforward to use since it describes the tensile and compressive behaviour of a material along orthogonal directions, that are fixed upon crack/crush initiation governed by the principal stress criterion, with uniaxial tensile and compressive saw-tooth laws. For a 2D plane stress situation, as soon as the principal stress violates the allowable strength in tension or compression at an integration point, the isotropic stress-strain relation $\boldsymbol{\sigma} = \mathbf{D}\boldsymbol{\varepsilon}$ transforms into an orthotropic relation as $\boldsymbol{\sigma}_{nt} = \mathbf{D}_{nt}\boldsymbol{\varepsilon}_{nt}$ with nt denoting the fixed cracked/crushed coordinate system. The primary principal stress direction's Young's modulus and strength are damaged according to the uniaxial saw-tooth law of the appropriate failure mode. In the event that normal stresses in the orthogonal direction (secondary) violates the corresponding allowable strength, caused by stress rotations or redistribution of stresses or application of another load non-proportionally, damage is introduced in that direction similarly. So every integration point essentially requires two uniaxial saw-tooth laws each for tension and compression in the 2D stress state, and three in the case of a 3D stress state.
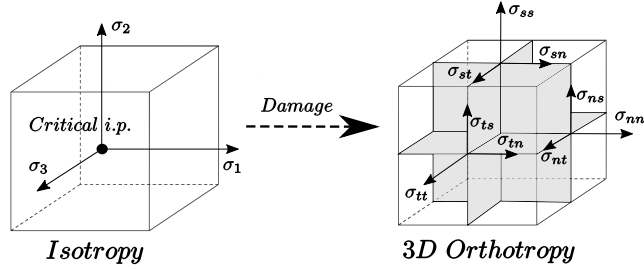

Figure 2.3: The change in isotropic to orthotropic formulation (*nst* crack coordinate system) upon damage initiation in a fixed crack framework for 3D stress states [150]

Furthermore, the model uses the crack band approach proposed by Bazant and Oh [12], which states that fracture energy is spread over the cracked area characterised by a certain crack band length h, to ensure that the constitutive curve depends on the size of the crack band. This, therefore, triggers the energy consumed due to smeared cracking in the fixed crack model to be mesh independent. Alternative projection based crack band approaches are also available [99, 149, 133]. The shear behaviour in the fixed cracking model is represented using a variable shear retention function that reduces with increasing damage in normal directions of the cracked/crushed plane [132]. Also, the Poisson's ratio is reduced at the same rate as the associated Young's modulus. The 3D Orthotropic fixed crack/crush model used in SLA is presented in Section 5.1 in detail, and therefore is not elaborated upon any further here. The full description of the formulation for 2D plane stress state can be found in Reference [139] and the one for shell elements in Reference [38], while detailed description of the fixed crack model in general can be found in Reference [116].

2

Rotating Smeared Crack Approach   The second type of total strain based smeared cracking model is based on the coaxial stress-strain concept, in which the stress-strain relationships are evaluated in the principal directions of the strain vector. This approach, also known as the Rotating crack model, is well suited to the the constitutive modeling of reinforced concrete structures. One of the disadvantages of the fixed crack models is the stress locking phenomenon. The shear forces generated due to the rotation of principal stress directions result in accumulation of shear stresses on the cracked plane, which can be controlled using the shear retention functions [116], but still may result in spurious stress states. Nevertheless, the fixed crack approach is more favourable for an SLA setup since it is more straightforward to implement. This is because the crack coordinate system is fixed upon damage initiation, and the same transformation matrix can be retrieved for a cracked integration point in assessing damage due to further events. On the other hand, although the stress locking problem is not so significant in the case of rotating crack models, combination with SLA is difficult because the rotation of the principal strain is not known a priori. There have been some rotating crack models in the context of SLA with simplifications, wherein the load multiplier is calculated with respect to the last equilibrated direction of a damaged integration point. This is an assumption that stands true only if no rotation of principal strains were to occur. Furthermore, since SLA allows one event at a time, rotation of the crack systems of non-critical damaged integration points are restricted. This is in principle incorrect and would lead to build up of shear stresses in such integration points, but is ignored since it would necessitate an iterative process to arrive at equilibrium. Nevertheless, the available rotating crack approaches for SLA with their assumptions are presented in the following.

- *Slobbe's approach*: Slobbe [130] proposed the first variation of a rotating crack model for SLA, wherein a new type of event, a certain degree of rotation of a crack for a damaged integration point, was introduced. The choice for the critical event is then made between damaging an undamaged point and the rotation of an existing crack. Since a continuous chain of crack rotation events (local stress redistributions resulting in stiffness changes that affect neighbouring cracked elements) would lead to an enormous number of events, a certain threshold angle α is defined. If the change in crack direction $|\Delta\gamma|$ in a cracked integration point is larger than α, it becomes an event, and the integration point with the largest change in crack direction $|\Delta\gamma_{\mathrm{max}}|$ becomes the critical event. The updating of crack direction also results in a stiffness change because of the orthogonal set-up of the model. On the contrary, if the rotation of crack direction $|\Delta\gamma|$ is smaller than α, the standard SLA procedure is followed to find the critical integration point. Tests were carried out for proportional loading conditions, and accordingly small threshold angles were not recommended considering the high computational intensity. In summary, the approach of Slobbe for rotating crack model in SLA is purely rotating only for the critical integration points, while the rest of the damaged points continue to follow the fixed crack model which may develop spurious stresses despite using shear retention formulations.

- *Vorel's approach*: Vorel and Boshoff [151] developed a rotating crack model that can be used within the framework of SLA to analyse structures with strain hardening

cement based composites (SHCC). The Force-Release (F-R) approach by Eliáš et al. [44], an incremental sequentially linear approach described in detail in Section 3.2, was used as the solution procedure in their framework. In this model, the principal direction of the critical integration point is updated after each stress redistribution. Since the loading procedure is incremental and because the rotation of the principal directions is not known beforehand (also depends on the scaling factor), it is assumed that the load multiplier can be evaluated with respect to the last equilibrated principal direction of the considered integration point. When the principal directions do not change within one increment, the procedure turns out to be exact. The crack directions of only the critical integration point is updated thereafter, just as in Slobbe's approach, and therefore this can also be considered only a *partial* rotating crack model. The method has been applied to three-point bending tests on beams, and also on shear beam specimens reinforced with SHCC.

- *Cook's multi-directional fixed crack approach*: Cook et al. [28] developed a multi-directional fixed crack model to be used in conjunction with SLA. The idea was to define a priori a number of potential damage planes per integration point (around 180). Contrary to SLA, evaluations are made along all potential planes for crack initiation, and damage is introduced perpendicular to the critical plane based on typical saw-tooth laws. The element containing the critical crack plane becomes the critical element. In order to narrow down the probable damage planes in the model, a crack tracking algorithm was also introduced wherein three types of elements are defined. This includes a *cracked element*, an *intersected element* which shares boundaries with a cracked element, and finally, pre-defined *isolated elements* wherein cracking can occur without the presence of adjacent cracked elements. This algorithm helps avoid spurious cracks in the structure elsewhere and alleviates stress locking, and also reduces the computational intensity of the procedure reasonably. A simple orthographic projection-based crack band approach is used for all potential crack planes assuming that constant strain, three-noded, triangular finite elements are used. Since multiple cracks are allowed per element, it may be interpreted as a kind of a rotating crack model that releases the locked stresses. Although developed originally for cracking in heterogeneous materials, the approach can also be used for FE modelling of concrete structures and shows promising results for the Double edged notched beam test [98] of mixed mode fracture.

- *Elastic perfectly brittle fraction model*: Hendriks and Rots [120] developed the Elastic-brittle fraction approach in order to simulate the effects of rotational cracking within sequentially linear analysis. This model divides each element in a set of N parallel fractions, each of which is elastic-perfectly brittle with tensile strength, stiffness and thickness chosen appropriately to represent the continuum's constitutive law. The total behaviour is found by the superposition of the stresses and strains of the perfectly brittle fractions, all of whose strains are the same (refer Figure 2.4).

Each fraction, denoted by the subscript k, essentially is isotropic to begin with and as soon as the principal stress violates the allowable strength at an integration point, the isotropic stress-strain relation $\boldsymbol{\sigma}_k = \mathbf{D}_k \boldsymbol{\varepsilon}$ transforms into an orthotropic relation as $\boldsymbol{\sigma}_{k,nt} = \mathbf{D}_{k,nt} \boldsymbol{\varepsilon}_{k,nt}$ with nt denoting the fixed cracked coordinate system.

The fraction is fully cracked but still retains strength in the tangential direction which can also be damaged upon rotation of stresses. Once the fraction is lost, the next layers are damaged and the model thereby describes softening as a gradual reduction of the cross-sectional area, which is physically in accordance with the micro-cracking coalescing to form a macro-crack as in the fictitious crack model [65]. The superposition of fixed crack fractions results in a rotating effect of the crack as shown in Figure 2.4. Since the fractions may also be seen as sublayers, the model is alternatively referred to as the *sublayer model*. A recent study [19] shows that the sublayer model consistently exhibits sharper crack localisation, lesser stress-locking, generally more flexible behaviour for several experimental plain-concrete benchmarks, and sometimes overcomes bifurcations that may be missed with regular SLA using the fixed crack model. The approach was also extended to 3D fractions in the same study [19] with appreciable results.
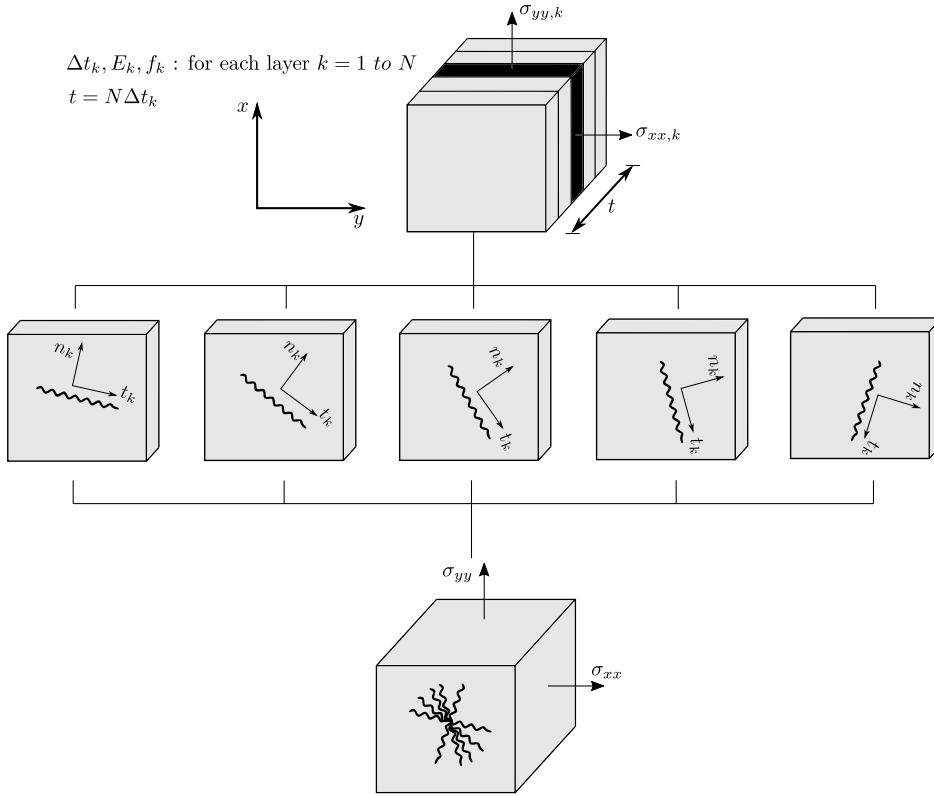

Figure 2.4: Schematic representation of the elastic perfectly-brittle fraction model [19]

The sublayer model is similar to the approaches of Slobbe [130] and Vorel [151] in the sense that only the critical point undergoes crack rotation but there are differences. Slobbe's approach differentiates damage and crack rotation as two different events, while the sublayer model introduces crack rotation with each damage. In

2

comparison to Vorel's approach which explicitly allows for redistribution by gradual release of forces due to damage (avalanche of ruptures using the force-release approach), the redistribution in the sublayer model is implicit with each event. The sublayer model also shows similarities with the approach of Cook et al. [28] in the sense that both approaches allow for multiple cracking planes per integration point. The difference lies in the fact that the orientation of the cracking planes are predefined in Cook's approach while each of the fractions in the sublayer model can have their own cracking direction depending on the principal stress. More recently, Liu [79] proposed the *sub-element* method which is fundamentally similar to the sublayer model but is applied for lattice problems.

INTERFACE ELEMENT FRAMEWORKS

Interface elements, used in standard FE analysis to represent displacement discontinuities, have thus far been used in SLA simulations as well [139]. In this section, the applications of interface elements for discrete cracking [140], Coulomb friction [139] and bond slip models [47] are revisited, using the 2-dimensional interface formulation with a normal stiffness k_n and a shear stiffness k_t. To avoid spurious displacements in the undamaged state, dummy initial stiffnesses $k_{n,0}$ and $k_{t,0}$ which are approximately 1000 times stiffer than the normal stiffness of adjacent continuum elements are used. For the elastic stage, the interface tractions t_n and t_t depend on the corresponding normal and shear relative displacements u_n and u_t as follows

$$\begin{bmatrix} t_n \\ t_t \end{bmatrix} = \begin{bmatrix} k_{n,0} & 0 \\ 0 & k_{t,0} \end{bmatrix} \begin{bmatrix} u_n \\ u_t \end{bmatrix} \tag{2.3}$$

Discrete cracking   In the case of discrete cracking, Eq. 2.4 is enforced to determine the critical integration point i for crack initiation, given the tensile strength f_t. Following crack initiation, the saw-tooth law of a typical linear or exponential tension softening relation is used as the traction-separation law (t_n–u_n) [140]. The normal and shear stiffnesses can then be updated based on such a law, which is in principle a damage formulation with $k_n = (1 - d_n)k_n$ and $k_t = (1 - d_t)k_t$, where d_n and d_t are damage variables.

$$t_{n,i}(\lambda) = f_t \ \wedge \ \forall i \neq k : t_{n,k}(\lambda) < f_t \tag{2.4}$$

Bond Slip   Interface elements have been used to demonstrate a simple bond slip model for SLA [47, 139]. Eq. 2.5 is enforced to determine the critical integration point i for debonding, given the ultimate bond stress $t_{t,\text{ult}}$. Following debonding, the discretised form of a simple bi-linear law between bond stress and slip was considered (t_t–u_t) and only the shear stiffness was updated as the slip evolved, while retaining the undamaged normal stiffness.

$$t_{t,i}(\lambda) = t_{t,\text{ult}} \ \wedge \ \forall i \neq k : t_{t,k}(\lambda) < t_{t,\text{ult}} \tag{2.5}$$

The Δ symbol, commonly used to denote *relative* displacements in interface formulations, is dropped herein to avoid ambiguity with the variations of the said relative displacements as in Eq. 2.8.

Coulomb friction   Coulomb friction formulations in interface elements were not as straightforward as smeared crack models or discrete cracking because of the multiple stress components involved. Additionally, it was not possible to predefine saw-tooth laws since the evolution of the internal variables is not known a priori. The first Coulomb friction formulation for SLA was presented in two variations, depending on how the secant $\mathbf{D}_{\text{sec}}$ matrix is updated: A *coupled* formulation considering dilatancy effects and an *uncoupled* one without it [139].

For proportional loading conditions, the critical integration point is determined based on Eq. 2.6 subject to the traction vector being non-zero and additionally Eq. 2.7 being false, where c and $\tan(\phi)$ are the mobilised cohesion and the friction coefficient. When cohesion softening is taken into account, the mobilised cohesion which only depends on the plasticity parameter (κ) additionally becomes dependent on the load multiplier. Therefore, the load multiplier is deduced iteratively using a local Newton-Raphson scheme. This is explained in detail in Chapter 6.

$$\left(t_{n,i}\tan(\phi) + |t_{t,i}|\right)(\lambda) = c \ \wedge \ \forall i \neq k : \left(t_{n,k}\tan(\phi) + |t_{t,k}|\right)(\lambda) < c \tag{2.6}$$

$$\frac{t_{t,i}}{t_{n,i}} \leq \tan(\phi) \text{ and } t_{n,i} < 0 \tag{2.7}$$

Contrary to the saw-tooth laws defined a priori, each shear stiffness reduction in this approach is computed during the analysis. The update to the stiffness matrix $\mathbf{D}_{\text{sec}}$ in the uncoupled version of the model for analysis step j is computed using the critical shear traction $t_{t,\text{crit}}^{(j-1)}$, the critical relative shear displacement $u_{t,\text{crit}}^{(j-1)}$ of the completed $(j-1)^{th}$ step and a specified relative displacement increment $\delta u_t^{(j-1)}$ which is based on a user defined factor a_t. The updated shear stiffness corresponds to the increased shear displacement and the normal displacement, and this approximation turns out exact if the actual shear displacement equals the specified increased shear displacement.

$$k_t^{(j)} = \frac{t_{t,\text{crit}}^{(j-1)}}{u_{t,\text{crit}}^{(j-1)} + \delta u_t^{(j-1)}} \text{ with } \delta u_t^{(j-1)} = a_t u_{t,\text{crit}}^{(j-1)} \tag{2.8}$$

The update to the secant stiffness matrix $\mathbf{D}_{\text{sec}}$ is more complicated in the coupled version of the Coulomb friction model, and is therefore left out of the scope of this discussion and the thesis. The uncoupled version will be used in the rest of the thesis, in combination with a tension and compression failure criterion to enforce multi-surface failure possibilities, refer Chapter 6 for detailed information.

2.3.2. WORK FLOW: PROPORTIONAL LOADING

The SLA procedure was initially developed for a proportional loading scheme, where the rate of change of all loads is the same. Firstly, the saw-tooth laws are defined as shown in Figure 2.2. Thereafter, the finite element model is loaded by a unit value of the total imposed load (L) which could either be forces or prescribed displacements (or a combination thereof). Subsequently, a linear analysis is performed and a load factor is calculated for each integration point as the ratio of the allowable strength to that of the governing stress as shown in the following.
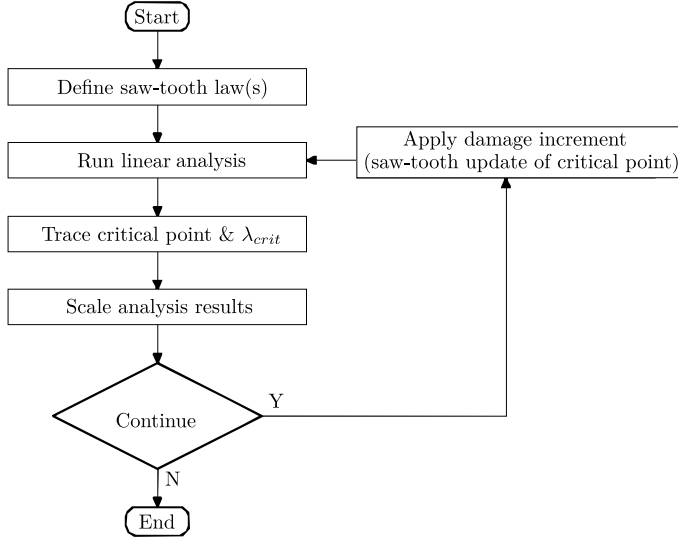
Figure 2.5: SLA workflow for proportional loading conditions [139]

$$\lambda_i^j = \frac{f_i^j}{\sigma_{\text{gov},i}^j} \qquad (2.9)$$

where j refers to the analysis step, and i either denotes an integration point number for an undamaged situation or alternatively upon damage, denotes events corresponding to tension/compression failure criteria along the 2 or 3 fixed damage directions (depending on the stress state). $\sigma_{\text{gov},i}^j$ is the governing stress component (for e.g. the principal stresses for damage initiation in a smeared fixed crack approach) for integration point i, f_i^j is the peak stress limit as defined by the current secant branch of the saw-tooth law, and λ_i^j is the associated load multiplier. The minimum of all load factors is referred to as the critical load factor, and the applied load is then defined as

$$\lambda_{\text{crit}}^j = \min_i \left(\lambda_{\text{crit},i}^j \right) \quad \forall \quad \lambda_{\text{crit},i}^j > 0$$
$$L^j = \lambda_{\text{crit}}^j L \qquad (2.10)$$

This means that the global load is scaled such that only a single integration point, the critical point, just reaches its current peak in its local saw-tooth diagram. The results of the linear analysis; the stresses, strains and displacements, are scaled using the critical load multiplier. Finally, the strength and stiffness of this critical integration point are reduced based on the saw-tooth laws, before the process is repeated.

Unlike NLFEA which is considered as *one analysis* containing several *steps*, SLA comprises several linear analysis which are referred hereon interchangeably throughout the thesis as *'analysis steps'* or *'steps'* as such.

Real-life loading schemes, however, are not proportional and consist of loads that are *constant* on structures like dead weight, followed by *variable* ones like wind, seismic or traffic loads. Such schemes are referred to as *non-proportional* loading conditions (Figure 2.6(b)) where the rate of change of the applied loads is not the same, and they prove to be more complicated in an SLA framework. Although the process of damage propagation and localisation is often sudden and dynamic in nature, the SLA simulation being quasi-static poses a fundamental problem in addressing redistributions, which involve a sequence of damage events, and more so under non-proportional loading conditions. This aspect of SLA needs better understanding, despite previous contributions, especially at structural level. Furthermore, another important feature/disadvantage of the SLA framework is the stress reversal problem that occurs due to redistributions under non-proportional loading conditions. That is, upon reversal of stress along a direction, the damaged stiffness in tension or compression, depending upon the failure mode, is carried onto the opposite regime (Figure 2.6(a)). The need for a crack closure algorithm to address this has been previously pointed out [139, 103] but not addressed in this work. This may result in incorrect strains but in line with previous SLA studies [55, 139, 33], this is accepted as an artifact/limitation for the studies in the thesis.
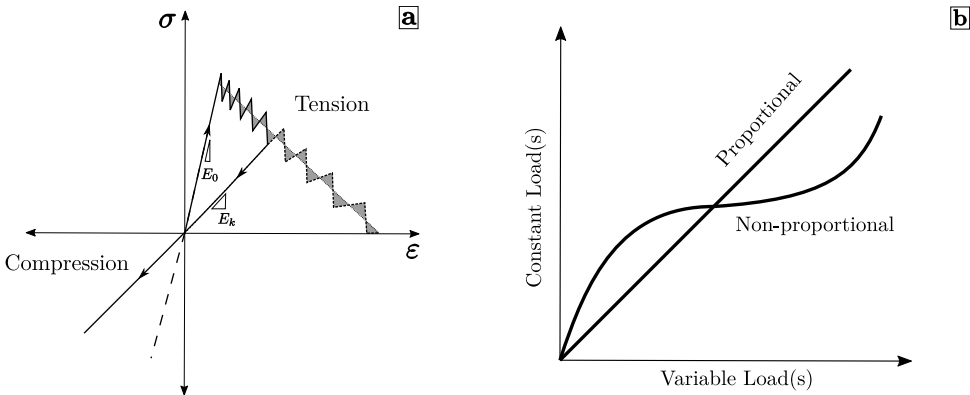

Figure 2.6: (a) stress reversal problem in SLA, and (b) loading schemes assuming constant & variable loads [139]

2.4. CONCLUDING REMARKS

This Chapter reviews finite element formulations, constitutive modelling, and the linear & nonlinear solvers used in the simulation of quasi brittle fracture. A comprehensive overview on available implicit, explicit, sequentially linear and alternative solution methods for NLFEA reinforces the importance of sequentially linear analysis, especially from simplicity and robustness points of view. But with view to structural FE applications of the sequentially linear method, the approach needs to be addressed with regard to the following topics, which in turn translate into the core chapters of this thesis.

2

- **Redistribution mechanism in SLA type procedures requires further understanding for non-proportional loading problems**. The redistribution mechanism involved in SLA under non-proportional loading problems is more prominent in real-life quasi-brittle experiments, at component or structural level, rather than in simple experimental benchmarks. Such redistributions, for instance previously observed with a masonry facade settlement example [139], were attributed to the lack of crack closure algorithm in SLA but there is a lack of complete understanding on this topic. To this end, Chapter 3 presents an extensive overview on all available sequentially linear methods in literature alongside their approaches to the non-proportional loading problem. Additionally, a qualitative discussion and analysis of the methods is included. Subsequently, in Chapter 4, it is sought to truly understand the mechanism of redistribution in Sequentially Linear Methods (SLM) for continuum FE simulations of real-life benchmarks or case studies. Herein, the redistribution mechanism in SLA and an incremental SLM, the Force-Release method, are compared. The validity of unloading and reloading all previously applied loads as in SLA is compared to the gradual static stress redistribution in a Force-Release simulation, and conclusions on suitability of either methods are drawn.

- **Structural simulations require extension of the constitutive model in SLA to 3D stress states and a 3D non-proportional loading strategy**. All existing constitutive formulations in SLA are in 2D, except the one for shell elements (made with an approximation for calculating the critical load multiplier) [38]. Structural level simulations motivate the need for combining a 3D smeared cracking model: either fixed or rotating, with a solution strategy to deduce the load multiplier for damage initiation in a full 3D stress state under non-proportional loading conditions. This is addressed in Chapter 5 alongside validation studies. Additionally, Coulomb friction formulations for planar interface elements in SLA would also be essential for 3D sliding problems. This is addressed in Chapter 6.

- **Structural simulations of SLA are currently extremely computationally intensive**. Computational intensity has been pointed out previously to be one of SLA's major bottlenecks [139, 151, 4, 1]. For instance, considering an SLA simulation to predict tensile failure in an FE model with x truss elements, there can be a maximum of $x \times y \times z$ linear analyses or damage events, where y & z correspond to the number of integration points per truss element, and the number of saw-teeth in tension per integration point respectively. This would become 2 or 3 times larger in case of 2D or 3D elements considering the appropriate directions of the orthogonal smeared cracking model, and possibly even more if compression nonlinearities were to be considered. This indicates the need for an extremely high number of linear analyses (each corresponding to a unique damage location) to bring about an equivalent nonlinear response as in traditional NLFEA (damaging multiple locations). A departure from the event-by-event nature of SLA into multiple failures per analysis could be considered, but the robustness may be lost in the process in attempting to establish equilibrium using internal iterations.

Under such a premise where the event-by-event nature of SLA is not compromised, the time taken to solve the system of linear equations using direct solvers could

be targeted, which is the most dominant part of the computing time in each SLA step. Since only one element is effectively damaged at a time, the system of linear equations to be solved actually changes locally between these analyses. Traditional direct solution techniques, such as those reviewed in Section 2.2, do not exploit this property and calculate a rather expensive stiffness matrix factorisation every step, resulting in high computational times. Smart tailor made solvers are required to make SLA studies more conducive to research, before considering possibilities of being a truly attractive alternative to implicit NLFEA. This is addressed in Chapter 7.

2

CHAPTER 3

ANALYSIS OF APPROACHES TO NON-PROPORTIONAL LOADING IN SEQUENTIALLY LINEAR METHODS[*]

In order to extend sequentially linear analysis to real-world structural examples in civil infrastructure and building structures, which are not only huge in magnitude but are also subject to real loading schemes which often have multiple loads, the approach to non-proportional loading becomes crucial. The simplest and most common case of non-proportional loading is when there are constant loads on the structure like dead loads, precompression, overburden etc., and the structure is subsequently subject to variable loads like earthquake, wind or vehicle loads. Under such loading conditions, problems arise due to considerable stress rotations and consequently, finding the critical load multiplier and integration point in SLA is not as straightforward anymore. SLA is a feature, as a part or whole, of several state-of-the-art solution methods referred to as Sequentially Linear Methods. The extension to non-proportional loading was intended to make the SLA procedure more suitable to wider applications, and the various strategies that have been proposed to incorporate this aspect in different sequentially linear methods, which are generally classed into three categories, are presented in this Chapter. Firstly, purely total approaches wherein unloading and reloading are done non-proportionally are presented in Section 3.1. This is followed by purely incremental approaches in Section 3.2, wherein the stress and loading history is explicitly tracked. Subsequently, a class of combined incremental-total approaches is presented in Section 3.3. Finally, a discussion on the methods is outlined in Section 3.4.

3.1. TOTAL METHODS

This class of sequentially linear methods relies on unloading and reloading a specimen, of all previously applied loads, while undergoing damage propagation. In line with this nature, they are also alternatively referred to as *load-unload* methods in literature [44, 81]. Each of them trace the critical event differently but are all similar with respect to non-proportional loading.

DeJong's method The method of DeJong et al. [40] was proposed for the smeared cracking approach, involving tensile failure only, under plane stress assumptions. For a system loaded by constant loads (L_{con}) and a unit variable load (L_{var}), the global stresses

---

[*]This Chapter is based on the author's article published in *Engineering Fracture Mechanics 2020* [105]. Minor modifications are made to suit the thesis.

31

are expressed as the superposition of the stresses due to the constant and scaled variable loads ($\boldsymbol{\sigma}_{\text{con}}$ and $\boldsymbol{\sigma}_{\text{var}}$ respectively) as shown in Eq. 3.1. These are then substituted in the expression for the principal stress, to be limited by the tensile strength (f_t), which is a function of the load multiplier for the variable load λ as shown in Eq. 3.2.

$$\boldsymbol{\sigma} = \boldsymbol{\sigma}_{\text{con}} + \lambda \, \boldsymbol{\sigma}_{\text{var}} \tag{3.1}$$

$$\sigma_{1,2} \, (\lambda) = f_t \tag{3.2}$$

The closed form solution for λ of Eq. 3.2 corresponds to crack or damage initiation for an integration point. For already damaged integration points, linear equations are solved along the orthogonal directions of the crack coordinate system, n and t, as shown in Eq. 3.3.

$$\begin{aligned} \sigma_{nn} \, (\lambda) &= f_{t,nn} \\ \sigma_{tt} \, (\lambda) &= f_{t,tt} \end{aligned} \tag{3.3}$$

The selection criteria for the critical load multiplier are based on the stress caused by the variable load. In case the variable load causes tension, considering the crack opening effect, the associated λ^t is considered a 'maximum' load multiplier (in which the superscript j indicating the analysis step is dropped for readability). In case the variable load causes compression, considering the crack closing effect, the associated λ^c is considered as a 'minimum' load multiplier. The minimum of all λ^t from the integration points is denoted λ^t_{min}, and the maximum of all λ^c from the integration points is denoted λ^c_{max}. In the scenario that $\lambda^t_{\text{min}} > \lambda^c_{\text{max}}$, λ^t_{min} is chosen as λ_{crit}, and the corresponding integration point is damaged based on the saw-tooth law ensuring that all other integration points adhere to the constitutive law. However, when $\lambda^t_{\text{min}} < \lambda^c_{\text{max}}$, no λ_{crit} can be selected such that all integration points in the finite element model adhere to their respective constitutive relations. This situation hereon is referred to as *limit point*, wherein no *constitutively admissible*[†] λ_{crit} can be found. This *limit point* is not to be confused with the traditional limit point encountered in an NLFEA response. DeJong's approach in such a situation proceeds forward by selecting λ^c_{max} as the critical load multiplier. Therefore, it allows for temporary violation of the constitutive law in one or more integration points, which may lead to rupture under invalid stress fields as has been pointed out in References [139, 44].

Constrained maximisation analogy The constrained maximisation approach proposed by Van de Graaf [139] follows the basics of the non-proportional loading concepts proposed by DeJong et al., with regard to the principal of superposition of stresses, the use of principal stresses for damage initiation, and the calculation of the closed form solution for the critical load multiplier. The difference lies in the selection criteria for the critical load multiplier which herein is based on a constrained maximisation approach, and sets of admissible load multipliers are deduced. Damage initiation involves solving quadratic (2D) or cubic inequalities (3D) in the load multiplier depending on the stress state [104],

---

[†]A constitutively admissible critical load multiplier refers to one which limits the stresses of each integration point in the FE Model, including the critical one, to be less than or equal to the current strength of their respective saw-tooth laws, considering tension and compression criteria in all relevant directions.

while damage propagation involves solving linear inequalities per direction of the orthogonal cracked system. The common global subset of these local sets would then reflect the set of constitutively admissible load multipliers for the entire FE model, the maximum of which is chosen as the critical load multiplier.

$$L_{ipl} = L_{con} + \lambda_{crit}^{j-1} \, L_{var} \tag{3.4}$$

$$L_{ipl}^{j} = \lambda_{crit}^{j} \, L_{ipl} \tag{3.5}$$

In the event that this common subset is empty in a certain analysis step j, the approach runs into the aforementioned *limit point*. In order to adhere to the constitutive law, Van de Graaf proposed the double load multiplier strategy which includes an *intermittent proportional loading* (IPL), wherein the last successful load combination L_{ipl} of step $(j-1)$ (Eq. 3.4) is scaled proportionally as shown in Eq. 3.5. It allows for redistribution by implicitly allowing for the reduction of the constant load, and is deemed acceptable when the redistribution is followed by full recovery of the constant load. Chenjie et al. [155] also proposed an algorithm for the non-proportional loading problem but confined their applications to problems wherein the determination of the critical load multiplier was not affected significantly by the constant loads. This class of problems was referred to as *weakly nonlinear* problems. The work flow for the constrained maximisation analogy is described in detail as follows for a 2D plane stress state.

1. Set up the saw-tooth laws as shown in Figure 2.2.

2. Run a linear analysis with the full value of the constant load.

3. In case of damage already in this stage (nonlinearity):

    (a) Identify the critical integration point with the least ratio of (f/σ_{gov}), where σ_{gov} is the governing principal stress and f is the allowable strength (Eq. 2.9).

    (b) Scale the constant load with the critical load multiplier (i.e the ratio from above)(Eq. 2.10)

    (c) Reduce the strength and stiffness of the critical integration point based on the saw-tooth law.

    (d) Return to step 2 and repeat until the scaled value of the constant load is the same as the original full value.

4. Once the constant load is fully applied, perform a linear analysis with the two load cases - one for the full constant load and the variable load applied as a unit load.

5. Construct the global stresses as a superposition of the stresses due to the constant and variable loads (indicated with indices 'con' and 'var' respectively) and express the resulting principal stress as a function of the load multiplier for the variable load (λ) as shown below:

$$\sigma_{xx} = \sigma_{xx,con} + \lambda\sigma_{xx,var}$$
$$\sigma_{yy} = \sigma_{yy,con} + \lambda\sigma_{yy,var} \tag{3.6}$$
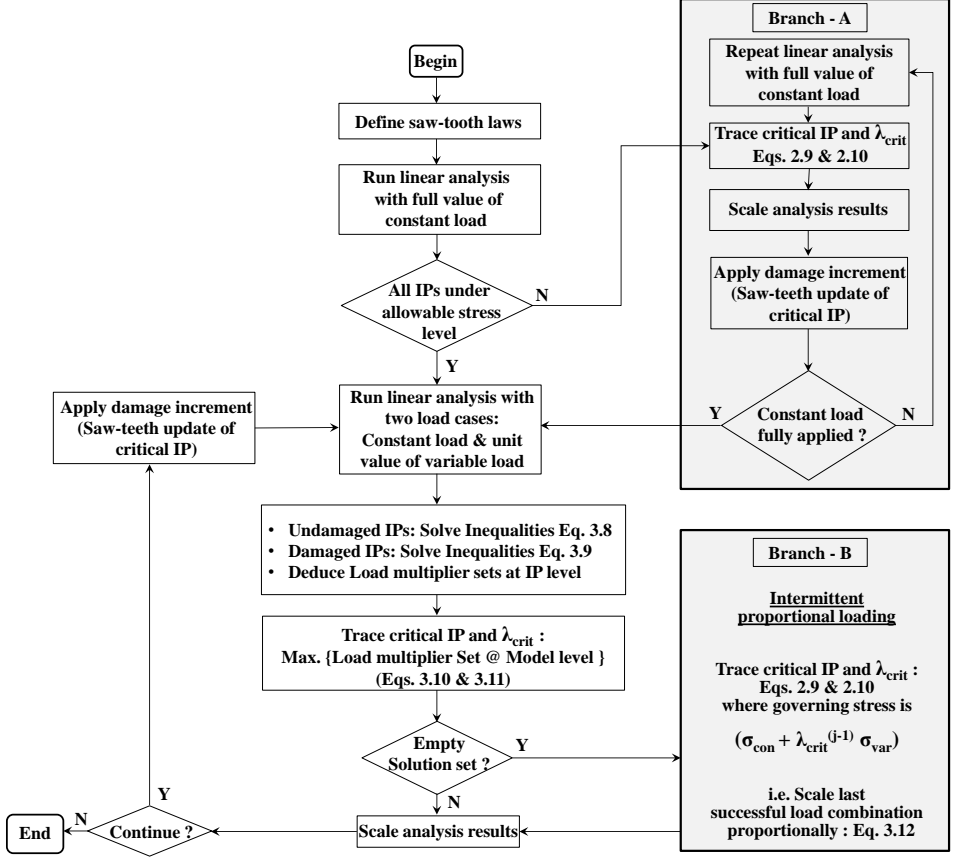$$\sigma_{xy} = \sigma_{xy,con} + \lambda\sigma_{xy,var}$$

3

Figure 3.1: The general workflow in SLA for a plane stress state - with additional branches 'A' for the the case when damage occurs before the full application of constant loads, and 'B' for addressing redistribution. (IP refers to integration point)

$$\sigma_{1,2}(\lambda) = \frac{1}{2}(\sigma_{xx} + \sigma_{yy}) \pm \sqrt{\frac{1}{4}(\sigma_{xx} - \sigma_{yy})^2 + (\sigma_{xy})^2} \tag{3.7}$$

6. Subsequently, two scenarios have to be considered.

   (a) Damage initiation: For integration points that are *undamaged*, the principal stresses are limited to the tensile and compressive strengths (f_t and f_c) resulting in quadratic inequalities in the load multiplier λ. Solving these as equations instead would yield a closed form solution in λ for each governing principal stress. The resulting load multiplier would either be a maximum or minimum value corresponding to solving for the inequality $\sigma_{1,2}(\lambda) \leq f$, and eventually sets of values of λ per integration point i, Λ_i^t and Λ_i^c, for tension

and compression failures respectively, are found.

$$\sigma_1(\lambda) \leq f_t \text{ resulting in } \Lambda_i^t \tag{3.8a}$$

$$\sigma_2(\lambda) \geq -f_c \text{ resulting in } \Lambda_i^c \tag{3.8b}$$

(b) Damage propagation: For integration points that are already *damaged*, the fixed crack system *nt* is already known. For such points, the scaled combination of constant and variable loads is limited to the current allowable strength on the saw-tooth, along each of the orthogonal failure directions *n* and *t*, resulting in linear inequalities. Again, solving for these inequalities results in sets of values of λ per integration point per failure direction. For simplicity, only the tensile failure relations are shown below.

$$\sigma_{nn,\text{con}} + \lambda_{nn}\sigma_{nn,\text{var}} \leq f_{t,nn} \tag{3.9a}$$

$$\sigma_{tt,\text{con}} + \lambda_{tt}\sigma_{tt,\text{var}} \leq f_{t,tt} \tag{3.9b}$$

7. The sets of constitutively admissible range of λ values from the damaged and undamaged integration points are subsequently assembled to find a common subset that would reflect the constitutively admissible range of load multipliers at the model level for the current analysis j. This would yield two scenarios as listed below.

(a) Non-zero solution set: The maximum of the common subset is denoted as the critical load multiplier λ_{crit} for N number of events.

$$\Lambda_{\text{model}}^j = \bigcap_{i=1}^{N} \Lambda_i^j \tag{3.10a}$$

$$\lambda_{\text{crit}}^j = \max(\Lambda_{\text{model}}^j) \tag{3.10b}$$

$$L_{\text{crit}}^j = \lambda_{\text{con}} L_{\text{con}} + \lambda_{\text{var}} L_{\text{var}} \quad \text{where} \quad \lambda_{\text{con}} = 1 \text{ and } \lambda_{\text{var}} = \lambda_{\text{crit}} \tag{3.11}$$

(b) Empty solution set: When the stress states in two or more integration points do not allow for a common set of constitutively admissible scaled combination of the constant and variable loads, a return to an *intermittent proportional loading* is done. The *last successful load combination* is scaled in a proportional way thereby reducing the constant load temporarily and also partly retaining the scaled variable load [139]. The integration point for which the load multiplier λ is critical (least positive) is then identified.

$$L_{\text{crit}}^j = \overline{\lambda}_{\text{crit}}^j (\lambda_{\text{con}}^{j-1} L_{\text{con}}^{j-1} + \lambda_{\text{var}}^{j-1} L_{\text{var}}^{j-1}) \quad \text{where} \quad \overline{\lambda}_{\text{crit}}^j = \lambda_{\text{crit}}^j \tag{3.12}$$

8. Once the critical integration point and load multiplier are determined, scale the stresses and strains accordingly, and obtain the new state.

9. Remove all loads, update the strength and stiffness of the critical integration point based on the saw tooth law, return to step 4, and repeat until the element/structure is completely damaged.

Improved total analysis   The inherent feature of unloading and reloading non-proportionally is the main cause for the problems associated with non-proportional loading in total methods, and to supposedly overcome this, Alfaiate et al. proposed the Improved total analysis [3]. Considering a non-proportional loading case of loads L_1 and L_2 applied sequentially, the improved total analysis proposes an initial load close to the last successful applied load instead of reloading again sequentially as L_1 and L_2. So, at analysis step j, the load is determined based on the preceding load combination as follows.

$$L^{j-1} = L_1 + \lambda^{j-1} L_2 \qquad (3.13)$$

$$L^j = L_1 + (\lambda^{j-1} + \Delta\lambda^j) L_2 \qquad (3.14)$$

The term $\Delta\lambda^j$ could be negative or positive but the total second load L_2 applied remains positive. In principle, the approach claims to allow for partial unloading and thereby avoid reloading non-proportionally. However, it seems clear from a prestressed beam example in their work that the stress history is not kept in memory. The stress state corresponding to each load is indeed recomputed for the damaged state, the representation of using about 75% of the last successful load multiplier is only mathematical, and the approach does not truly adhere to the physical loading history like in an incremental approach. The approach is therefore purely total, and equivalent to the previously described constrained maximisation analogy. Additionally, the approach does not indicate its take on the limit point situation where there is no possible load multiplier. However, simultaneously, Alfaiate et al. [3] proposed an incremental version, allowing for partial unloading, called the *secant-incremental analysis* which is described in the following section.

3.2. INCREMENTAL METHODS

Force-Release method   Elias et al. [44] also pointed out that DeJong's approach essentially did not incorporate the correct loading history, and additionally, that an event may lead to a series of subsequent failures in the vicinity of a damaged element without increasing the prescribed displacement or forces. These regions normally appear as instabilities in a displacement controlled experiment which look smoothed out. However, in principle, these are snap backs which are referred to as avalanche of ruptures by Elias at al., driven by redistribution of the elastic energy released from damaged elements into their vicinity. Addressing this fundamental problem of using a quasi-static approach in simulating a dynamic phenomenon like an avalanche of ruptures due to damage (cracking or crushing), Elias et al. [44] proposed the Force-Release method.

This method is a purely incremental approach wherein the non-proportional load path is discretised into a series of piece-wise proportional loading paths. They proposed to discretise each load into a series of n_p load vectors with magnitudes L_p, with $p = 1, 2, .. n_p$, ensured to be non-decreasing, so that the proper loading/stress history is taken care of. For force loads, the magnitude is based on the euclidean norm of the prescribed forces. The variable t_p, ranging from 0 to 1, represents how far the simulation has proceeded along a certain load magnitude L_p, and is essentially a fraction of the prescribed load. It

is expressed as in Eq. 3.17, where ΔL_p are reference load increments analogous to the unit load in SLA. The stiffness matrix, displacements, reactions, and stresses are denoted as **K, u, R,** and $\boldsymbol{\sigma}$ respectively. Linear analyses are performed either with the *reference load increments*, which would represent regions of static equilibrium in the response, or with *disequilibrium forces* representing the intermediate redistribution region. After each load increment or event, all quantities are updated with their incremental parts and stored.

The work flow is summarised as follows. To begin, linear analysis is performed with the reference load increment of the first load ΔL_1 to compute the reactions $\Delta\mathbf{R}$, displacements $\Delta\mathbf{u}$, and stresses $\Delta\boldsymbol{\sigma}$. Thereafter the critical element, i, is deduced such that the following holds.

$$(\sigma_i + \lambda\Delta\sigma_i) = f \ \wedge \ \forall i \neq k : (\sigma_k + \lambda\Delta\sigma_k) < f \tag{3.15}$$

In Eq. 3.15, all quantities with Δ are their corresponding incremental values caused by the load increment ΔL_1, and f is the allowable strength. Once the critical element is evaluated, a decision between damage & redistribution or proceeding to the next load's increment ΔL_2 is made based on the following (with appropriate values of the load sequence p).

$$0 < \lambda \leq (1 - t_p)\frac{L_p}{\Delta L_p} \tag{3.16}$$

$$t_p = t_p + \lambda\frac{L_p}{\Delta L_p} \tag{3.17}$$

On the one hand, if the inequalities of Eq. 3.16 are true, the critical element i is damaged. The stiffness matrix, reactions, displacements, and stresses are updated with their corresponding scaled incremental quantities. The variable t_p is also updated with its scaled increment as shown in Eq. 3.17. Subsequently, the system is loaded by disequilibrium forces, **S = R - Ku** that arise due to the previous event. This region represents a state of disequilibrium, and a new potential critical element is deduced based on Eq. 3.15. $0 < \lambda \leq 1$ indicates that the unbalanced forces generated by the previous damage event i need to be redistributed in its vicinity, by another rupture. The newly identified critical element is damaged, and the stiffness matrix, reactions, displacements and stresses are again updated. Thereafter, the system is loaded by the newly computed disequilibrium forces to determine if there needs to be yet another rupture due to the redistribution. Thereby, the avalanche of ruptures or the so-called redistribution loop continues, as long as $0 < \lambda \leq 1$, through several disequilibrium states before returning to static equilibrium. Once the avalanche finishes, the simulation moves to the next load L_{p+1}.

On the other hand, if the inequalities of Eq. 3.16 do not hold, $\lambda = (1 - t_p)(L_p/\Delta L_p)$ and it indicates no damage possibilities until the end of the load ΔL_p. In other words, the system is in equilibrium and further external load is added. The internal state parameters are updated and the simulation moves to the next load L_{p+1}, similar to the continuation at the end of the avalanche. The entire workflow is shown in Figure 3.2.

The Force-Release method, in summary, uses the constitutive model as in SLA while performing linear analyses with reference load increments which are fractions of the total prescribed load. Each reference load increment corresponds to an analysis which may or may not lead to damage. Upon damage, the stress from a damaged element

is released gradually through a sequentially linear redistribution loop wherein other elements may be damaged. The approach is suitable for non-proportional loading paths but cannot handle snap backs because of its incremental nature. Additionally, although it is claimed that these imposed loads could either be forces or prescribed displacements, for simulations involving global softening, the Force-Release procedure would work only under prescribed displacements since imposed forces cannot reduce in magnitude.
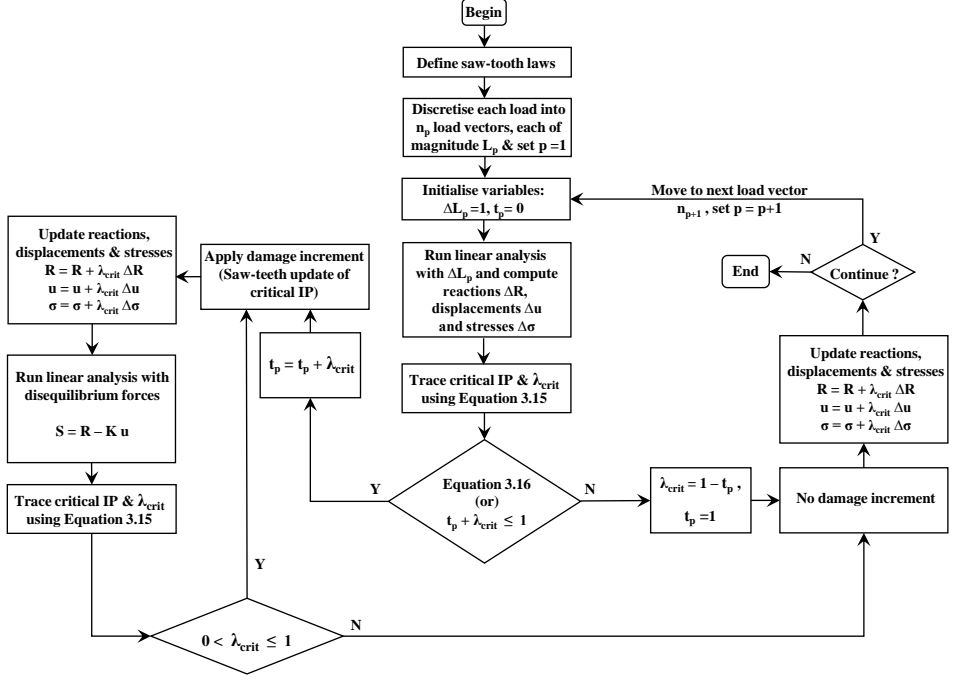

Figure 3.2: The general workflow in the Force-Release method (IP refers to integration point)

General method   This approach is shown to be a generalisation, of which the load-unload and the Force-Release methods are extreme cases [43]. It also overcomes the problems of non-observance of snap back in the Force-Release method and the lack of avalanche of ruptures due to a single damage event in the load-unload method. The *general method* is based on the redistribution of stresses from damaged elements as is done in the Force-Release method and the simultaneous scaling of external load characteristic of the load-unload method.

The formulation involves defining two reference stress variables $\Delta\boldsymbol{\sigma}_L$ and $\Delta\boldsymbol{\sigma}_S$ corresponding to the external load increment and the disequilibrium forces. The method is suited to either force or displacement loading or both (depending upon appropriate boundary conditions). The total reference stress state is expressed as the sum of the two reference stress variables, enhanced by a slight modification of the external load by a

parameter ω, as shown in Eq. 3.18. ω determines the ratio between the effects of the external load and the disequilibrium forces to the reference stress. Substituting this in the governing equation of the Force-Release method, Eq. 3.15, the expression for the general method is deduced (Eq. 3.19).

$$\Delta\boldsymbol{\sigma} = \Delta\boldsymbol{\sigma}_{\mathrm{S}} + \omega\Delta\boldsymbol{\sigma}_{\mathrm{L}} \tag{3.18}$$

$$(\sigma_i + \lambda(\Delta\sigma_{\mathrm{S},i} + \omega\Delta\sigma_{\mathrm{L},i})) = f \ \wedge \ \forall i \neq k : (\sigma_k + \lambda(\Delta\sigma_{\mathrm{S},k} + \omega\Delta\sigma_{\mathrm{L},k})) < f \tag{3.19}$$

3

The method now is *general* because the choice of the parameter ω allows the process to be steered as desired. By setting $\omega = 0$, the external load is kept constant which would be equivalent to the Force-Release method. It can also be led to alternate equilibrium states by choosing values for ω arbitrarily. If the ω is set such that the redistribution finishes exactly when the external load diminishes to zero, the path would lead back towards the origin and this corresponds to the load-unload method. The choice of the parameter to control the external load is direct while indirect controls like the Crack Mouth Opening Displacements (CMOD), which are often used to steer experiments, are also possible in this set-up of the general method. The approach in shown to be suited to both proportional and non-proportional loads [43].

Simultaneously, Liu and Sayed [81] proposed another general approach which also treats the load-unload and Force-Release methods as special cases. However, this is based on a simple linear interpolation of the trial displacement fields of both the methods, as against the scaled combination of the reference stress states due to the external load and residual forces in Elias' general approach [43]. Elias claims that the latter seems a more reasonable formulation considering the underlying physics of the problem since the displacement field interpolation lacks a strong physical motivation [43].

Secant-incremental analysis   In addition to the previously described Improved total analysis, a purely incremental procedure referred to as the secant incremental solution was proposed by Alfaiate et al. [3]. Inspired from the former, the latter approach allows for partial unloading with the secant stiffness $\mathbf{K}^{j-1}$ of the previous step thereby avoiding sudden load drops as in SLA. The load is kept close to the previously applied load, a reloading secant-incremental stiffness $\mathbf{K}^*$ is determined based on a heuristically evaluated local constitutive $\mathbf{D}^*$ matrix, and the minimum load factor is determined to reach the envelope using the defined stiffness relation. The new secant stiffness $\mathbf{K}^j$ is then determined a posteriori. Additionally, the approach is shown to allow for non-secant unloading, without allowing the damage to increase, by discretising the unloading path using intermediate multi-linear branches. Unlike the improved total analysis, this approach is incremental in principle and therefore overcomes the non-proportional loading problem naturally. The approach, however, is computationally intensive owing to the need of evaluating the global stiffness matrix twice per analysis, and there is also no proof that there always exists an admissible solution for λ.

3.3. MIXED FORMULATIONS

Combined incremental-total approaches   Two combined incremental-total approaches were first presented by Graca-e-Costa et al. and were called the *Automatic Method* and the *NIEM (Non-Iterative Energy based method)* [57]. Both approaches, in contrast to SLA, use multi-linear material laws to ensure that all nonlinearities are due to loading or unloading. The idea of both these methods it to employ a non-iterative *incremental* solution, and then to shift to the *total* approach intermediately when bifurcation points arise, to guarantee a unique admissible path which may not be traced otherwise. The incremental part is controlled by the increment of loads leading to the largest energy release at the structural level in the FE model, in line with the Energy release control proposed by Gutierrez et al. [61]. Locally, at the integration point level, for a certain load increment ΔL, the evolution of the constitutive law is forced to follow the valid path, either positive (loading) or negative (unloading), that ensures the release of the largest amount of energy. To begin with, the critical load factor λ_{crit} is evaluated in a trial step, which corresponds to reaching the nearest point in the multi-linear law for an integration point. Subsequently, the true step ensuring $\Delta L_{\text{true}} = \lambda_{\text{crit}}\Delta L_{\text{trial}}$ is performed, and the material stiffness is updated. This carries on as long as bifurcation points do not arise. When they do, the *total* approach takes over. The stiffness update in each *total* step could be done in two ways, and accordingly two approaches were deduced.

In the first approach, referred to as the *Automatic Method*, similar to SLA, the secant stiffness is reduced by a predefined factor as in the saw-tooth law. Subsequently, only one of the points becomes critical and reaches the original envelope, while all others are on their respective current secant paths. After intermediately traversing through this region, the method shifts back to the incremental approach using tangent stiffness matrix $\mathbf{D}_{\text{tan}}$. In the second approach, referred to as the *NIEM (Non-Iterative Energy based method)*, the a priori definition of the secant stiffness reductions is avoided. When an integration point encounters a bifurcation, a true incremental step is performed, although it is incorrect. This is done to determine the new updated stiffness for all non-critical points that may be on the envelope or unloading, and compute their secant stiffnesses as:

$$K^j = \frac{\sigma^j}{\varepsilon^{j-1} + \Delta\varepsilon^{j-1}_{\text{trial}}} \tag{3.20}$$

while keeping the secant stiffness fixed for the critical bifurcation points. This step in any case is deemed null, and the total approach is adopted with the computed secant stiffnesses. Eventually, the approach reverts back to the incremental part in a similar way to the Automatic Method.

Although the material loading history is taken care of in the incremental part, the total part of both approaches still required a non-proportional loading approach which in turn was based on DeJong's approach of the principle of superposition of stresses, followed by the determination of load factors. However, the authors mention that the adopted procedure overcomes the development of new nonlinearities during the initial loading (non-proportional reloading) due to the preferential usage of the incremental solution. Both methods have been validated against several benchmarks, concluding that the NIEM leads to more consistent results in terms of energy dissipated, peak capacity

and the consistency condition. Both methods were able to properly track the material loading history as against a total method like SLA due to the inherent incremental nature. Additionally, no material parameters were to be regularised, as in SLA to ensure mesh objectivity, due to the use of multi-linear constitutive relations.

Incremental Sequentially linear analysis   The Incremental Sequential Linear Analysis (ISLA) was proposed recently [156], in which an incremental procedure is used in combination with internal iterations intermittently. In contrast to the traditional incremental-iterative methods, this approach uses the secant stiffness relation globally and therefore the solution path will have jumps similar to the combined incremental-total approaches. The imposed load is either force or displacement controlled. In general, for a non-proportional loading case with two loads L_1 and L_2, for each load step the loading and stress history in stored because of the incremental nature. Three variations namely: *load control*, *damage control* and *load & damage control* were proposed depending on the method of stiffness reductions, and how the corresponding loading factors λ_1, λ_2 are treated.

In the *load control*, the λ_1 corresponding to L_1 is fixed for all load steps (once fully applied), and the λ_2 corresponding to L_2 is fixed in a certain load step $j-1$. A critical element is identified based on the ratio of the strength to the total governing stress accumulated thus far. For the subsequent step j, the second load factor λ_2 is increased and if the stress in the critical point exceeds the allowable strength, damage is increased based on the saw-teeth definition and the stiffness matrix is updated. The displacements and other system variables of the previous step $j-1$ are restored, and the internal forces are calculated to check for equilibrium. If not, damage is again induced to the same structure-state as in step $j-1$, for the same or another critical element, until the algorithm reaches a temporary equilibrium state using Newton-Raphson (N-R) iterations. In the *damage control* method, once a critical element is damaged, the damage is kept constant and the load multiplier λ_2 corresponding to L_2 is repeatedly reduced based on a constant reduction value or a function, using N-R iterations to arrive at an equilibrium state. In the *load & damage control* method, once a critical element is damaged, the damage is also varied (in the same or different critical elements) along with the load multiplier λ_2 corresponding to L_2, which is also iteratively reduced, to arrive at an equilibrium state.

The load control method in ISLA can be seen as an equivalent of the Force-Release method which also traverses through disequilibrium states to arrive at equilibrium. Additionally, they are similar in the sense that post peak softening behaviour can be realised only if the imposed loads are prescribed displacements.

3

Table 3.1: Constitutive modelling and applications of the discussed approaches

METHOD	CONSTITUTIVE MODELS & ILLUSTRATIONS
DeJong's method [40]	Continuum models - Smeared fixed crack model and discrete cracking interfaces using uniaxial saw-teeth relations
Force-Release (F-R) method [44]	Lattice models - elastic brittle relations, Continuum models - Smeared rotating crack model [151]
General method [43]	Lattice models with meso-level internal definition - Mohr Coulomb surface with tension cut-off
Constrained maximisation analogy [139]	In addition to the illustrations by DeJong [40], bond-slip relations for reinforcement, Coulomb friction model for interfaces
Automatic method [57]	Similar to the illustrations by DeJong [40] except using uniaxial multi-linear relations
NIEM method [57]	Similar to the illustrations by DeJong [40] except using uniaxial multi-linear relations
Improved total analysis [3]	Mixed mode traction based model - discrete cracking
Secant-Incremental analysis [3]	Mixed mode traction based model - discrete cracking
Incremental sequentially linear analysis (ISLA) [3]	Continuum & discrete models - with softening, plasticity etc.

3.4. DISCUSSION ON THE METHODS

Sequentially linear methods, thus, differ on two main accounts. Firstly, the application of load and the tracking of its history are different under a non-proportional loading situation. The class of *total* approaches unload and reload non-proportionally. However, as long as the current damage situation allows for all previously applied loads (or the so called constant loads) to be applied without new failures, the constant loads are truly kept constant and this can be interpreted as unloading only until the beginning of the variable load. When the limit point situation arises, previously described in Section 3.1, the constant load could potentially cause premature failure problems which brings about the need for an explicit redistribution[‡]. Of all the *total* approaches, only the constrained maximisation analogy with the double load multiplier strategy [139] provides an alternative in such a situation by allowing to unload and reload from the beginning of the constant load. Or, in other words, an intermittent proportional loading is performed to allow for redistribution by scaling the last successful load combination proportionally, and potentially reach a damage state which allows for full recovery of the constant loads. For simplicity, the constrained maximisation variant of SLA with the double load multiplier strategy [139] is referred to as SLA in the remainder of the thesis. In case of the class of *incremental* methods, the inherent incremental nature keeps track of the loading history thereby avoiding the problems with regard to non-proportional loading.

Secondly, the avalanche of ruptures or multiple failure events is addressed differently by both classes of approaches. In case of the *total* approaches like SLA, these manifest as sharp snap backs or sudden decay of loads. SLA brings about an instantaneous stiffness reduction in the damaged element thereby relieving it of the stress. However, the neighbouring elements that are almost loaded up to their respective strengths are unable to take over the released stress. In such a scenario, the SLA set-up allows for a reduction in load factor as the *only* option to redistribute, which brings about a snap back in the response. This happens multiple times, inducing failures in the surrounding elements, before allowing for a full recovery of the load factor close to the true equilibrium path. While in the case of the *incremental* approaches like the Force-Release method, the load is kept constant and the avalanche of ruptures are achieved in states of disequilibrium using a sequentially linear redistribution loop. Herein, the unbalanced forces that may arise due to a damage event are gradually reduced. Thus, both the approaches address the time scales of redistribution differently as has been previously pointed out by Liu and Sayed [80]. It is understood that when the internal forces of the damaged elements are released instantaneously, the *total* methods are preferable. Contrarily, when the internal forces are released gradually, the elemental failure sequence becomes crucial, and the Force-Release method becomes suitable. These time scales for release of internal forces, either instantaneously or gradually, due to a damage event are in reference to the loading rate [43]. That is, when the loading protocol can react fast enough to a rupture, total methods are suitable and on the other hand, when the load stays constant, the incremental methods are suitable. Liu and Sayed [80] conclude from their illustrations with lattice models that damage evolution in the Force-Release method ensures compatibility

---

[‡]These premature failure problems due to unloading and reloading non-proportionally affects the LATIN method as well, described in Section 2.2.2 under the *Other methods* subsection.

of controlled displacement loadings throughout the analysis, and that the area under the force displacement curve is the exact amount of work done by the external loads and the released internal forces.

There exists another minor difference between the approaches. With respect to constitutive relations, *incremental* formulations allow for discretised laws with elastic stiffnesses for evolving stress points. This means unloading under arbitrary stiffness is possible which allows for plastic strains unlike the *total* approaches which rely purely on damage mechanics. Furthermore, such modified constitutive models would make it possible for *incremental* approaches to be applied to cyclic loading problems. On the other hand, *total* approaches unload to zero-stress-strain state and plastic strains cannot be captured in principle. However, there exists an alternative for allowing plastic strains in a total set-up by defining and discretising a non-secant unloading branch using several saw-teeth. This is in principle possible but is not investigated in this thesis.

Both the aforementioned major differences, between the total and incremental approaches to the sequentially linear method, are investigated in Chapter 4 using continuum FE models of experimental benchmarks that exhibit true brittle collapse.
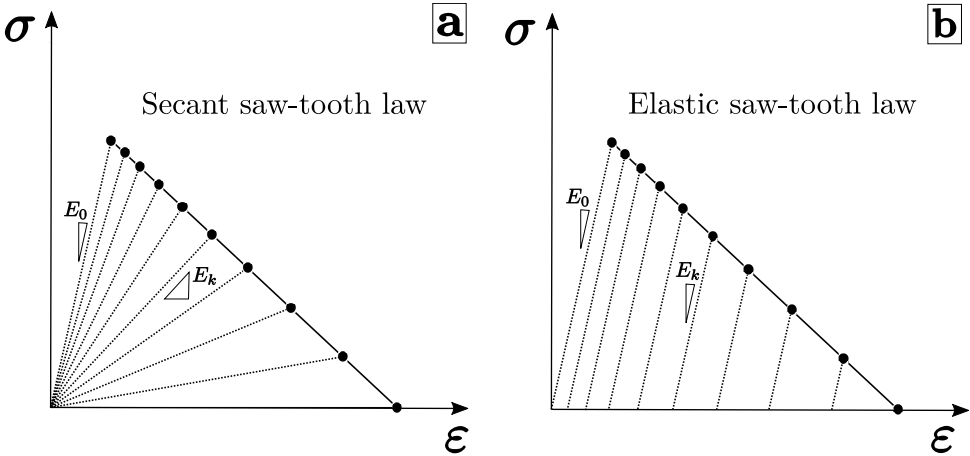
Figure 3.3: (a) Secant Saw-tooth laws applicable to both *total* and *incremental* sequentially linear methods, and (b) elastic saw-tooth laws applicable to the *incremental* ones.

REDISTRIBUTION MECHANISM IN SEQUENTIALLY LINEAR METHODS[*]

The topic of non-proportional loading in SLA and similar Sequentially Linear Methods (SLM) continues to be a debated one. This chapter illustrates the necessity for stress redistribution in the quasi-static set up of SLM to simulate the dynamic[†] phenomenon of cracking/crushing, and elucidates the differences between a purely-total and an incremental approach for continuum finite element problems. Firstly, in Section 4.1, the inherent differences between SLA with the double load multiplier strategy using a constrained maximisation approach (total) and the Force-Release method (incremental), are illustrated using three case studies involving non-proportional loading. These include a prestressed concrete beam example, and two in-plane pushover analysis examples of a slender cantilever masonry wall and a squat cantilever reinforced concrete (RC) wall. Thereafter, in Section 4.2, the difference between prescribed forces and prescribed displacements during the intermittent proportional loading phase in sequentially linear analysis is illustrated. Finally, Section 4.3 presents the conclusions of the work.

4.1. COMPARATIVE STUDY: SLA VS FORCE-RELEASE METHOD

The difference in the mechanism of stress redistribution between a total and an incremental SLM is illustrated in this section using structural continuum finite element models. All FE simulations in this study are performed in 2D under plane stress assumptions. The constitutive model is that of the smeared fixed crack/crush model using a simple Rankine-type failure surface for crack/crush initiation. The shear retention is damage based [132], and the uniaxial saw-tooth relations are of the ripple band type illustrated as in Figure 2.2, with p the saw-teeth discretisation factor, unless stated otherwise. In the presence of interfaces, similar ripple band saw-teeth relations are used to simulate discrete cracking, and for reinforcements, a ripple band saw teeth with constant residual stress resembling ideal plastic response is used to simulate yielding. The latter is kept damage based as in Reference [139] for suitability to SLA. Alternatively, for the Force-Release method, a discretised elasto-plastic constitutive law can be made with elastic stiffnesses to attain true plastic unloading but this is not considered herein. Pure sliding failures, which are possible in typical masonry mechanism, may not be relevant for masonry walls which fail in rocking as in Sections 4.1.2 & 4.1.3. Therefore, the modelling approach is restricted to

---

[*]This Chapter is based on the author's article published in *Engineering Fracture Mechanics 2020* [105]. Minor modifications are made to suit the thesis.

[†]The word 'dynamic' in this Chapter/Thesis, used at several locations, refers to the dynamic nature of the fracture process. It is reiterated that all studies herein are performed under quasi-static assumptions with no inertial effects.

macro-modelling, and not the detailed micro or meso-modelling in combination with Coulomb friction interface formulation for SLA as in Reference [139] and Chapter 6.

The loading condition for all the chosen examples is non-proportional and is composed of two stages: firstly, a precompression or prestress is added as force loads, followed by a second stage of imposed/prescribed displacements. The force loads and prescribed displacements are depicted in orange and green/yellow colours respectively in the FE model descriptions for consistency.

4.1.1. PRESTRESSED BEAMS

Experiment   Several three-point bending tests were performed on plain concrete beams in an experimental campaign by Zhao et al. [157]. These were previously analysed using SLA with plane stress assumptions [139]. Of these beams, SG2-B1, of span 600 mm, 150 mm depth, and 120 mm thickness is chosen as reference for this study. The beam is tested in three point bending with a notch of depth 60 mm and 2 mm width, and a schematic representation of the experiment is shown in Figure 4.1(a). The middle of the beam is in pure bending, and if such a beam were to be subject to axial loads (purely for an academic purpose) like a prestress force, the loading would become non-proportional. The effect of compressive axial loads will increase the capacity of a beam and has been a proven benchmark study for testing non-proportional loading strategies in SLA thus far [40]. This simple case study is used to compare the performance of SLA and the Force-Release method.

Finite Element Model   The simply supported beam is modelled with geometry as shown in Figure 4.1(a), except that the notch width is assumed to spread over an entire element length. The FE model is made using linear 4-noded iso-parametric plane stress elements, with 2 translational degrees of freedom per node and a regular 2×2 Gaussian integration scheme. All elements are square and approximately 10 mm in size. Concrete has been modelled as a linear-elastic material everywhere except the notched column of gray coloured elements, refer Figure 4.1(b), where all the physical nonlinearity is lumped (only tensile). A linear tensile softening saw-tooth law with material parameters mentioned in Table 4.1 is used. Two cases are considered in this section. First, the three point bending test of SG2-B1 beam as in the experiment is simulated. Since the notch extends over one whole linear element, the point load is assumed to be equivalent to two prescribed displacements applied either side of the central element at the top of the notch as shown in Figure 4.1(b). Second, the beam is firstly assumed to be subject to a uniform compressive prestress, of magnitude 0.42 MPa, at the ends of the beam before proceeding to the three point bending.

Results & Discussion   The force displacement curves from SLA and the Force-Release method, for the first case without axial loads, match up well with those from the experiment. Furthermore, both simulations show the propagation of the tensile crack through the height of the notch, resulting in the reduction of effective cross section of the beam. This behaviour results in the loss of flexural capacity, and is eventually observed as the global softening in the force displacement curves shown in Figure 4.1(c). Furthermore, the

Table 4.1: Modelling and Material parameters - Prestressed beam

Parameters	Values
Young's Modulus E_0 [GPa]	16
Poisson's ratio ν_0	0.15
Tensile strength f_t [MPa]	3.78
Mode I fracture energy G_f^I [N/mm]	0.224
Tension softening relation	Linear
Saw-teeth discretisation factor - tensile (p)	0.15
No. of saw teeth	16
Compressive behaviour	Linear elastic
Crack bandwidth h [mm]	10
Shear retention factor β	10^{-4}

Figure 4.1: (a) Schematic diagram of the 3-point bending test on beam SG2-B1 by Zhao et al. [157], (b) FE model of the set-up with axial force loads and prescribed displacements for the bending, and (c) load-displacement curves for the 3-point bending case, with and without axial loads, simulated as in SLA and Force-Release method

SLA and Force-Release responses are similar for the non-proportional case of axial loads followed by the bending load as well. The presence of axial loads like the compressive prestress tends to delay the cracking and consequently, results in a higher capacity.

However, there are small variations between SLA and Force-Release in both sets of responses with and without the prestress force. The SLA shows small snap backs in the response which is indicative of the load-unload nature of the approach, and the way multiple failure events are handled. Since one event occurs at a time, a potential event in a neighboring integration point occurs only by allowing for a reduction of the load in the next linear analysis. Conversely, in case of the Force-Release method, vertical drops are observed in the force displacement response rather than snap-backs. Since the previously applied load can not be modified, for a constant prescribed displacement, an additional event or more occurs due to the gradually released unbalanced forces from the previous event. This denotes a region of disequilibrium, and is referred to as the *avalanche of ruptures* (previously described in Section 3.2). Additionally, since the constant load i.e the compressive axial load is not too high, SLA does not run into the

intermittent proportional loading and the associated redistribution. That is, SLA could keep the prestress load (constant) throughout the entire simulation, while fully satisfying the constitutive laws. This case study shows the inherent difference in load application between the two approaches. The small differences in element failure sequence is not apparent due to the problem definition, wherein the overall final crack is confined to a single band of the elements, and is therefore not deliberated upon.

4.1.2. PUSHOVER ANALYSIS OF A SLENDER MASONRY WALL

Experiment   TUDCOMP-20 was one of the several quasi-static in-plane cyclic tests performed recently at the TU Delft laboratories. This was part of an extensive experimental campaign to characterise the response of unreinforced Dutch masonry buildings to induced seismicity [87]. The specimen was a calcium-silicate brick masonry wall, roughly 2.7 m high and 1.1 m long, with a thickness of 102 mm. The wall was tested under cantilever boundary conditions, i.e. it was clamped at the bottom and free to rotate at the top. Firstly, an overburden stress of 0.63 MPa was applied on the wall through a combination of actuators and a steel beam as shown in Figure 4.2(a). This load was maintained constant throughout the experiment while allowing for the rotation of the top of the wall. Subsequently, a cyclic lateral displacement was applied to the top of the wall using a horizontal actuator connected to the top steel beam. This wall exhibited pure rocking movement and for large displacements, splitting cracks were observed at the bottom-left and bottom-right corner of the wall, refer Figure 4.4(a). This was followed by the phenomenon of toe crushing, when the base shear force dropped substantially for the same imposed displacement, starting at the red dot in the experimental response, refer Figure 4.2(b). Considering the scope of this study/chapter, the explosive failure in this non-proportionally loaded experiment makes for an interesting case to be investigated using the SLA and Force-Release methods. The explosive failure led to instability of the wall and its eventual collapse (refer Figure 4.4). For further information about the experiment, the reader is referred to Reference [48].

Table 4.2: Modelling parameters - TUDCOMP20: identifed by sensitivity studies based on material properties obtained from the experiments [87, 48]

| Material	Parameters	Continuum	Interface
MASONRY	Young's Modulus E_0 [GPa]	4.972	-
	Normal & Shear stiffness [N/mm^3]	-	10^4
	Poisson's ratio v_0	0.16	-
	Tensile strength f_t [MPa]	-	0.13
	Mode I fracture energy G_f^I [N/mm]	-	0.15
	Saw-teeth discretisation factor - tensile (p)	-	0.1
	Tension softening relation	-	linear
	Compressive strength f_c [MPa]	6.35	-
	Compressive fracture energy G_c [N/mm]	20	-
	Compressive softening relation	parabolic	-
	Saw-teeth discretisation factor - compressive (p)	0.1	-
	Crush bandwidth h [mm]	55	-
	Shear retention factor β	Damage-based [132]	10^{-2}
STEEL BEAM	Young's Modulus E_0 [GPa]	210	-
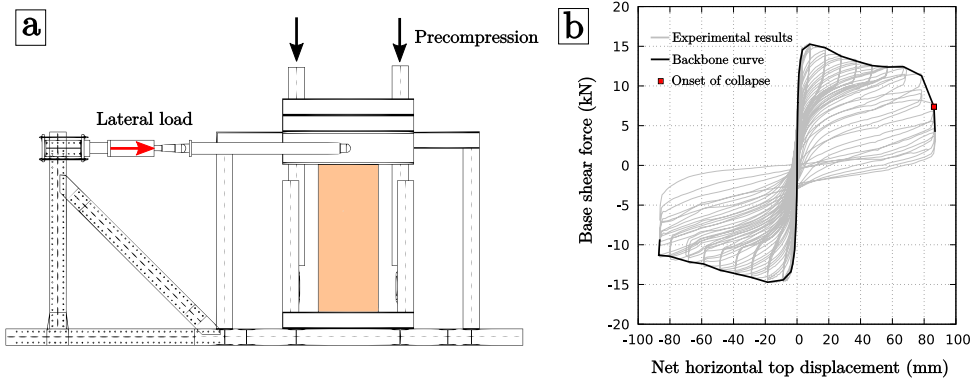
Figure 4.2: (a) Experimental set-up to apply precompression followed by a prescribed cyclic lateral displacement to the top of a cantilever wall, and (b) the experimental response of base shear against the net top horizontal displacement, additionally, showing the point of onset of collapse [48]

Finite element model Since cyclic loading applications are not yet possible in the SLA framework, the loading is kept monotonic and the results from the simulation are compared to the backbone/envelope curve of the experimental cyclic response as shown in Figure 4.3(b). The finite element model of the wall, as shown in Figure 4.3(a), is made with 4-noded iso-parametric plane stress elements, roughly 55×55 mm in size, with linear interpolation shape functions and a 2×2 Gaussian integration scheme. The compressive nonlinearities are in these continuum elements and are described by a smeared fixed crush framework, while behaving linearly in tension. The uniaxial saw-tooth compressive softening law is of a parabolic type [51] with material parameters as described in Table 4.2. Additionally, a zero-thickness interface (shown in green in Figure 4.3(a)) is provided at the bottom of the wall to simulate the discrete cracking leading to the rocking behaviour. This is made using 2+2 noded interface elements, roughly 55 mm in length each, with linear interpolation shape functions and a 2 point Newton-Cotes integration scheme. The tensile nonlinearities in these interface elements are described using a linear tension softening type saw-teeth law with material parameters mentioned in Table 4.2. The FE model also includes another row of continuum elements at the top of the wall (not shown herein) with stiffer properties behaving linear elastically. This is to ensure the cantilever boundary conditions. The bottom of the wall is fixed as shown in Figure 4.3(a). The overburden load is applied first as force loads at the top edge of the wall, and subsequently, a prescribed displacement is applied at the left top corner. The assumption in the FE model to separate tensile nonlinearities into the discrete cracking interface and the compressive ones into the continuum membrane elements is made to simplify the problem while accurately capturing the failure mode.

Results & Discussion Firstly, both the SLA and Force-Release simulations exhibit the rocking behaviour, which is localised in the discrete cracking interface, followed by compressive softening in the toe region of the wall. This leads to dissipation of energy resulting in a rather ductile response as shown in Figure 4.3(b). It is clear that both responses show

reasonable qualitative agreement to the experiment in terms of the load-deformation curve and the failure modes. Although the two simulations are rather identical, there are minor differences (similar to those observed in the prestressed beam case, Section 4.1.1).
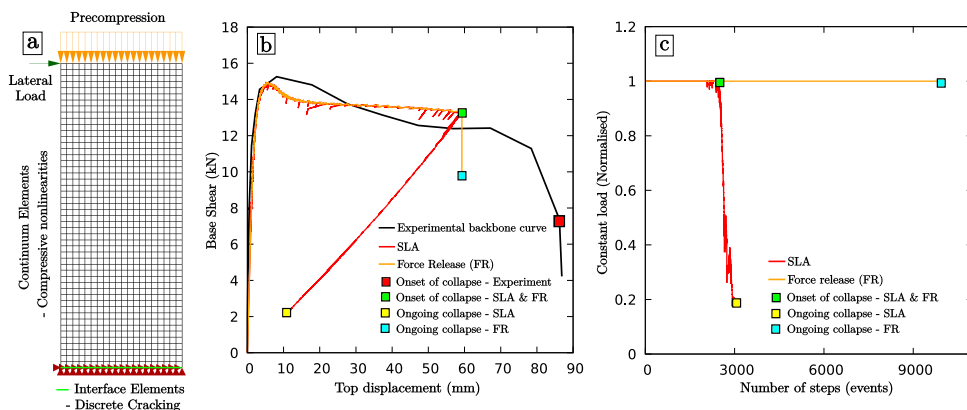

Figure 4.3: (a) FE model of the TUDCOMP20 test, (b) the base shear vs top displacement response for SLA & Force-Release methods compared against the experimental backbone curve - including the reference points during the collapse mechanism, and (c) evolution of the precompression load (normalised) during the simulations

Figure 4.4: Failure pattern of masonry wall in the TUDCOMP20 experiment before collapse (left) and after collapse (right) [48]

The explosive failure is captured adequately by both methods, but the mechanism of redistribution differs. The point of onset of the mechanism is denoted by a green mark in the Figure 4.3(b), and it occurs around the same imposed displacement for both simulations. The damage patterns are also identical as seen in Figure 4.5(a) where DmSS is the amount of damage accumulated in the discrete cracking interface and the crushing continuum. DmSS ranges from 0 to 1, which corresponds to undamaged and
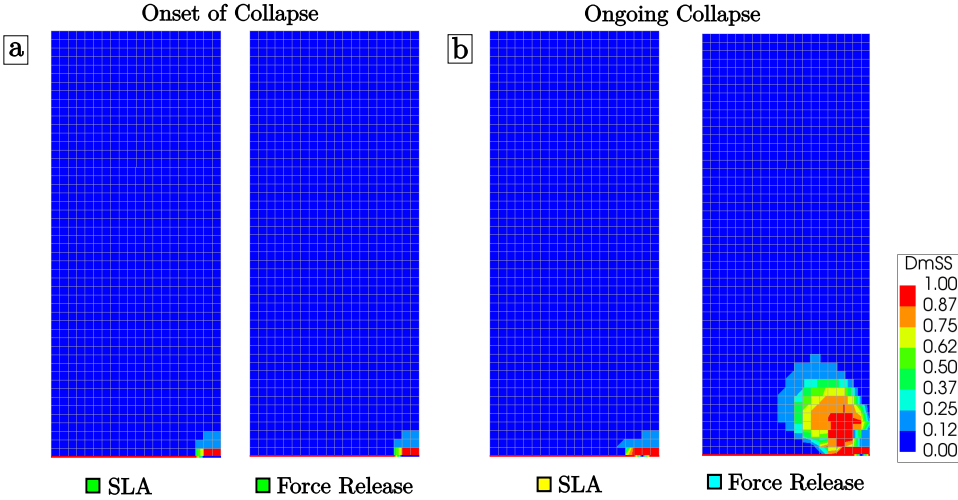
Figure 4.5: Failure patterns of SLA & Force-Release simulations of the TUDCOMP20 experiment: (a) at the onset of collapse, and (b) during collapse, in relation to Figure 4.3

fully damaged conditions. It is clear that the two continuum elements at the bottom right corner of the wall are fully crushed and that all interface elements to the left of this region are completely cracked, leaving a tiny portion which effectively supports the wall. The ensuing mechanism is described by both approaches differently. On the one hand, SLA runs into the limit point situation described previously in Section 3.1, where there is no constitutively admissible critical load multiplier. The intermittent proportional loading (IPL) commences and the last successful load combination is scaled proportionally. Firstly, the IPL occurs a little before the onset of collapse as well but recovers back to the conventional non-proportional loading. However, once the collapse begins, the IPL never recovers which is evident from the amount of precompression, the first load applied (constant), that remains on the structure in the rest of the simulation, refer Figure 4.3(c). The IPL implicitly reduces the constant load, thereby describing the entire dynamic brittle collapse mechanism while maintaining equilibrium. On the other hand, the Force-Release method runs into an avalanche of ruptures while going through disequilibrium states. Since the previously applied load can not be altered, for the same imposed displacement and the full value of precompression, the Force-Release method attempts to allow for redistribution due to successive failure events by gradually releasing the stresses. The ongoing failure is therefore captured differently by both approaches as seen in Figure 4.5(b).

The difference between the approaches in describing collapse may be interpreted as two extremes of the time scales for a dynamic redistribution process [43]. SLA in this situation is essentially assuming that the loading equipment is fast enough to react to the collapse mechanism, alter the load and consequently, release the stresses quickly to avoid further failures. This is clear as the eventual failure pattern additionally only involves the crushing of the tiny effective portion supporting the wall before the onset of collapse. The crush zone appears to be more realistic, in a quasi-static sense, wherein SLA gives room for

damage propagation while quasi-statically releasing the loads. The Force-Release method, on the other hand, stays true to the displacement controlled experiment, and realises the full collapse by gradually releasing the stresses in a sequentially linear redistribution loop. Although the process is dynamic, the Force-Release method effectively neglects all inertial forces. Since vertical equilibrium is not possible anymore, the simulation could be interpreted to have been completed, and the wider crush-zone is indicative of this instability. In summary, both approaches adequately describe a real non-proportionally loaded experiment involving true brittle collapse, in terms of the failure patterns and the eventual mechanism, differing only in their respective approaches to the latter.

4.1.3. PUSHOVER ANALYSIS OF A SQUAT REINFORCED CONCRETE WALL

Experiment The third benchmark is a reinforced concrete shear wall, named SW13, from the experiments of Lefas et al. [78]. Figure 4.6 shows the experimental set-up, the geometry, and reinforcement layout of the wall. The vertical and horizontal reinforcement bars were of 8 mm and 6.25 mm diameter respectively. Additionally, mild steel stirrups of 4 mm diameter were used to confine the wall edges. An axial load of 355 kN was first applied through a spreader beam to the top edge of the walls, and the horizontal load was then applied to the header beam at a rate of 0.04 kN/sec. The crack progression began with the first flexural cracks near the bottom third of the tensile edge at around 15% of the horizontal load (49.5 kN). At 40% of the horizontal load (130 kN), the first inclined crack appeared, and simultaneously, the flexural cracks had already spread at a slight inclination within the wall web. This was followed by growth in the flexural and inclined cracks, almost reaching the compressive edge. The first yielding of the tensile reinforcement occurred at 75% of the horizontal load (250 kN), which was followed by the failure. Figure 4.7(b) shows the failure that occurred by way of near-vertical splitting of the compressive zone at a peak load of 330 kN. For further information on the experiment, the reader is referred to Reference [78].
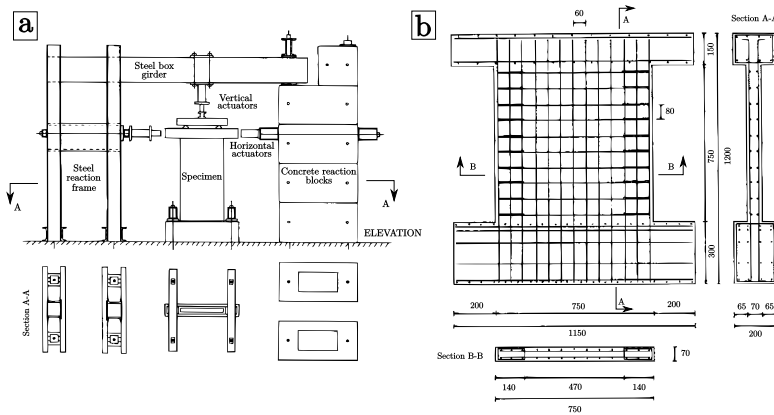

Figure 4.6: (a) Experimental set-up of the shear wall test by Lefas et al. [78], and (b) geometry & reinforcement detailing of the wall [78]
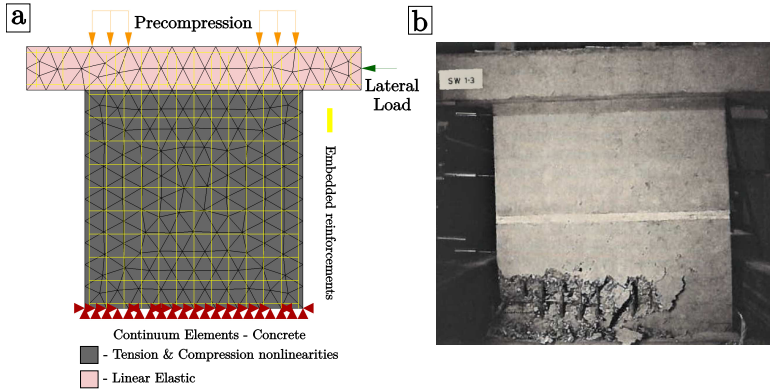
Figure 4.7: (a) FE Model of the RC shear wall test (reinforcements in yellow), and (b) the final failure pattern of the experiment [78]

Table 4.3: Modelling parameters - RC Shear-Wall: identified by studies from the work of References [33, 97]

Material	Parameters	General	Compression	Tension
CONCRETE	Young's Modulus E_0 [GPa]	28.537	-	-
	Poisson's ratio v_0	0.16	-	-
	Strength f_c, f_t [MPa]	-	34.5	2.67
	Fracture energy G_c, G_f^I [N/mm]	-	34.5	0.138
	Saw-teeth discretisation factor (p)	-	0.1	0.1
	Softening relation	-	Parabolic	Linear
	Crush/Crack bandwidth h [mm]	-	75	75
	Shear retention factor β	-	Damage-based [132]	Damage-based [132]
REINFORCEMENTS	Young's Modulus E_0 [GPa]	210	-	-
	Saw-teeth discretisation factor (p)	-	0.1	0.1
	Ultimate strain	-	-0.02	0.02
8 mm ϕ	Yield Strength [MPa]	-	-470	470
6.25 mm ϕ	Yield Strength [MPa]	-	-520	520
4 mm ϕ	Yield Strength [MPa]	-	-420	420

Finite element model Figure 4.7(a) shows the discretised model of the shear wall used in the SLA and Force-Release simulations. 6 noded iso-parametric triangular continuum elements of 75 mm, with quadratic interpolation shape functions and a 3-point Gaussian integration scheme, are used. Reinforcements are modelled as embedded units and are shown in yellow in Figure 4.7(a). The constant vertical load of 355 kN is applied as two uniformly distributed loads over a distance of 125 mm on the top edge of the wall, to replicate the the load application to the spreader beam as in the experiment. The horizontal load is applied to the right side of the header beam at mid-height as a prescribed displacement. The foot of the wall is not modelled because its influence was found to be negligible [33]. Instead, the base of the wall is fixed with translational restraints in both directions to model the clamped wall base. Table 4.3 shows the material parameters used in the simulations for concrete, according to the *fib* Model Code 2010 [16], and reinforcement properties obtained from the experiment.
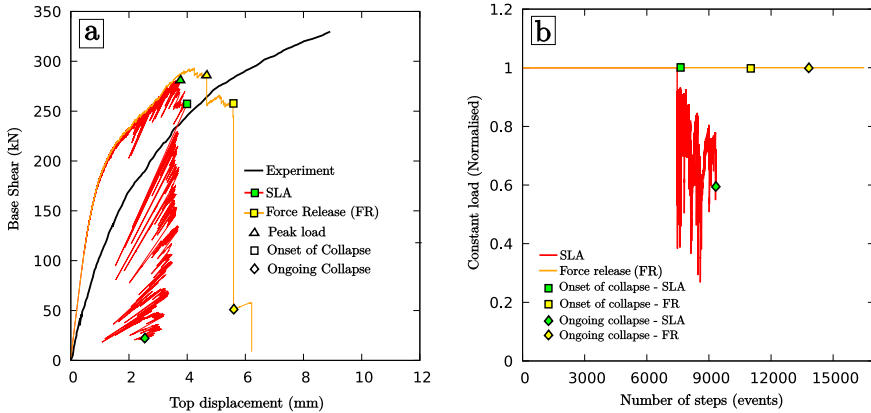
Figure 4.8: (a) Base shear vs top displacement response for SLA & Force-Release methods compared against the experimental response - including the reference points during the collapse mechanism, and (b) evolution of the precompression load (normalised) during the simulations

Results & Discussion   The results from the SLA and Force-Release simulations for the RC shear wall test, shown in Figure 4.8, exhibit the decisive failure as a drop of load. Although the response from both the approaches is stiffer than the experiment, have a delayed onset of cracking and exhibit a lower peak load, the qualitative behaviour is consistent with the experiment. These problems are not a feature of the SLA or the Force-Release methods, but also arose in previous NLFEA simulations, and is more a feature of the constitutive modelling used [97, 33]. The material parameters in Table 4.3 are based on previously done NLFEA studies [97, 33] to obtain the best fit. The flexural crack progression is followed by the inclined cracks until the peak load (Figure 4.11). Eventually, the toe crushing combined with yielding of reinforcements is captured well. The toe region of this wall undergoes crushing of the concrete (refer Figure 4.9), compressive yielding of the reinforcements (refer Figure 4.10), and additionally, exhibits splitting cracks at the onset of collapse (Figure 4.12). The splitting cracks in this region are due to the lateral compressive softening, in addition to the presence of the yielding vertical reinforcements that are close to rupture.

The collapse mechanism begins with the crushing of concrete at the toe and the yielding of the reinforcement as seen in Figures 4.9&4.10, which further propagates through the simulation. Both approaches capture this adequately. However, the drop of load corresponding to the eventual instability is described by the SLA and Force-Release methods in diametrically opposite ways with regard to the time scales for the redistribution. This is in line with the differences observed between the approaches to the explosive failure in the previous case study, and is clear from how the loading is modified in case of SLA (Figure 4.8(b)) during collapse. SLA again describes the collapse mechanism while maintaining equilibrium by reducing the constant load, while the Force-Release method addresses it using the avalanche of ruptures in disequilibrium. Furthermore, as the complex stress state in this zone evolves and undergoes redistribution, SLA experiences stress reversal problems. The evolving splitting cracks (due to lateral compression softening) in this complex zone causes unloading in surrounding elements, resulting in

crack closure in some elements with incorrect damaged stiffness. This is a characteristic to the approach, wherein damaged stiffness is carried onto tension or compression upon stress reversal due to redistribution. This therefore hinders the splitting crack formation at the peak and close to the onset of collapse in the case of SLA, refer Figures 4.11 & 4.12. On the other hand, at a similar stage in the simulation, Force-Release captures the splitting cracks better as observed in Figure 4.12. This is because the stress reversal problem is less accentuated in case of the Force-Release method, which is in turn due to the inherent incremental nature of the approach in keeping track of the stress history. Nevertheless, a dedicated stress reversal event and a corresponding load multiplier should be incorporated in line with previous proposals for SLA in continuum models [103] and the Force-Release method in lattice models [45].
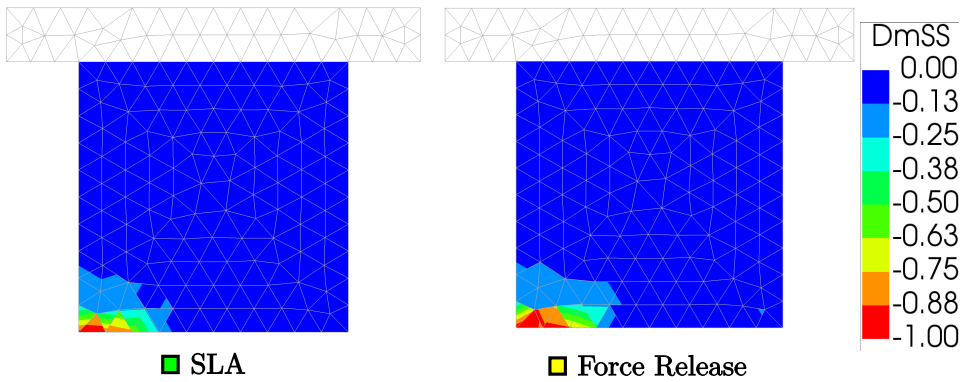
Figure 4.9: Damage patterns of SLA & Force-Release simulations of the RC shear wall experiment indicating toe crushing at the onset of collapse (refer Figure 4.8). DmSS ranging from 0 to -1 indicates undamaged to fully crushed situation.
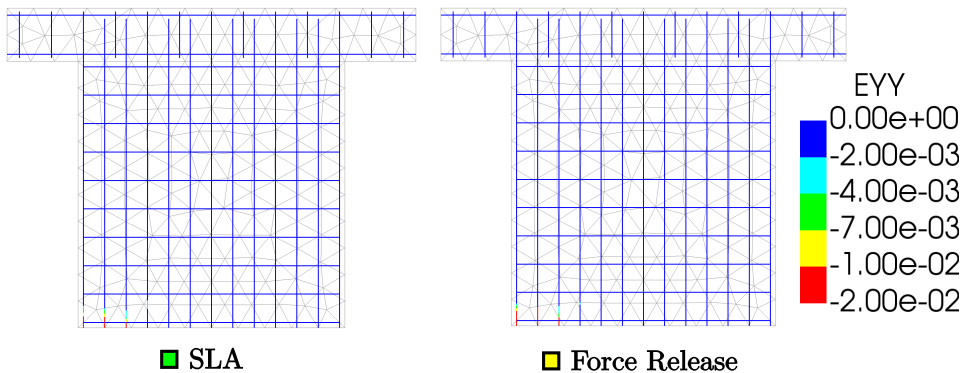
Figure 4.10: Reinforcement vertical strain patterns of SLA & Force-Release simulations of the RC shear wall experiment indicating compressive yielding and rupture (at the toe region) at the onset of collapse (refer Figure 4.8)
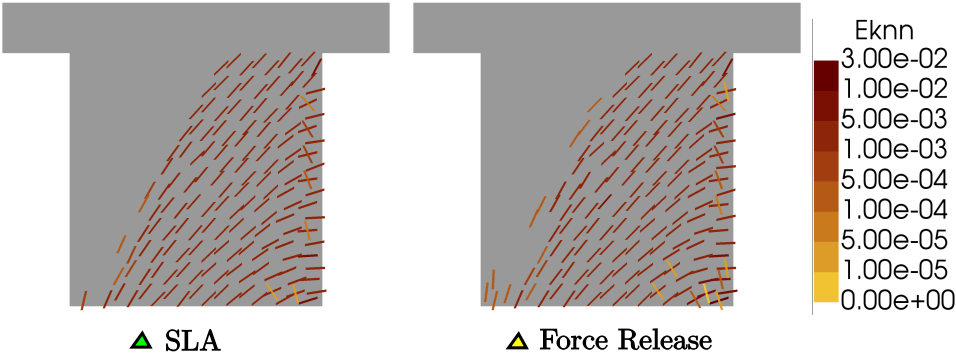
Figure 4.11: Crack pattern plots (Eknn denotes the normal crack strain) of SLA & Force-Release simulations of the RC shear wall experiment around the corresponding peak loads (refer Figure 4.8)
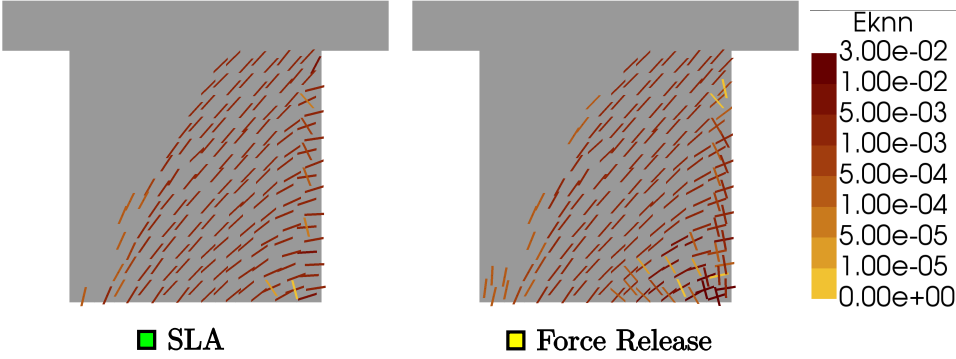

Figure 4.12: Crack pattern plots (Eknn denotes the normal crack strain) of SLA & Force-Release simulations of the RC shear wall experiment at the onset of collapse. (refer Figure 4.8) (Splitting cracks at the toe captured better in Force-Release compared to SLA)
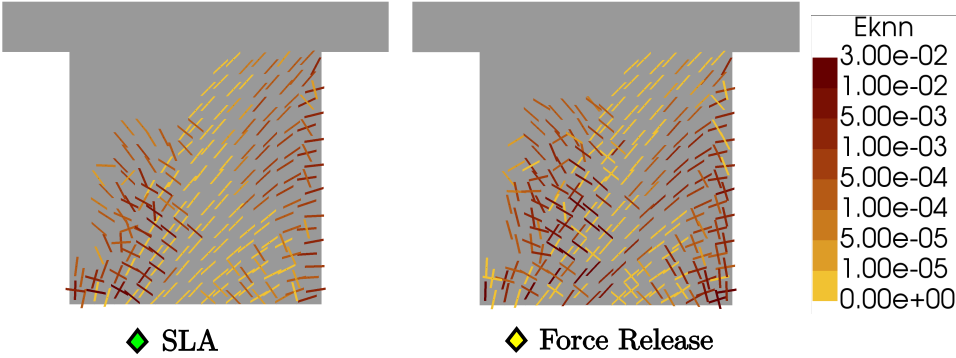

Figure 4.13: Crack pattern plots (Eknn denotes the normal crack strain) of SLA & Force-Release simulations of the RC shear wall experiment during collapse (refer Figure 4.8)

4.1.4. PUSHOVER ANALYSIS ON A 2D MASONRY FACADE

Experiment A full scale solid clay-brick masonry building tested by Magenes et al. [85] is a well known benchmark study to investigate the seismic response of masonry buildings [38]. It consists of four walls: walls A + B + C which are connected by an interlocking brick pattern around the corner, and wall D which is disconnected from perpendicular walls A and C (Figure 4.14(a)). This detached wall can be simulated using 2D plane stress elements. Although the experiment was a cyclic test, this benchmark is herein simulated with monotonically increasing lateral loads, and the backbone curve of the cyclic response is used as reference for comparison.
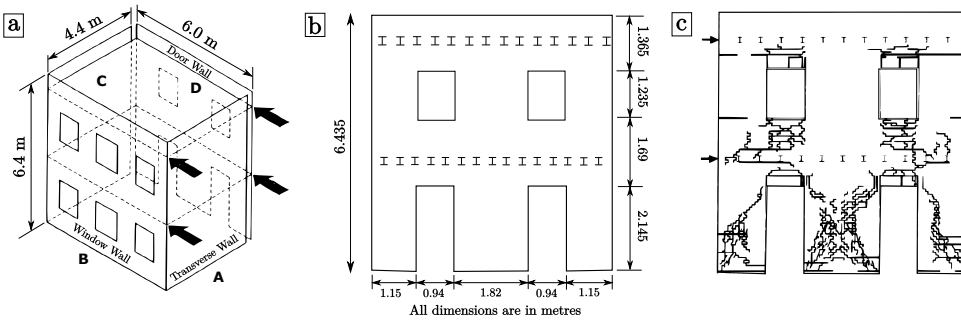
Figure 4.14: (a) The experimental scheme of the quasi-static cyclic pushover test on a 2-storey house, (b) the dimensions of Wall D of the house, and (c) the cyclic experimental crack pattern of Wall-D at ultimate displacement [85]

The geometry of the facade is shown in Figure 4.14(b) and has a thickness of 0.25 m. The facade is loaded in two stages: First, the floors are loaded by a distributed load of 10 kN/m^2, resulting in total vertical loads of 248.4 kN and 236.8 kN at the first and second floor respectively. The floors rest on beams, which are connected to walls B and D, such that half of the floor load is carried by each facade. Second, the building is loaded by a monotonically increasing lateral load at both floors to simulate the static equivalence of seismic action. The damage pattern corresponding to the cyclic test at an ultimate displacement of 23 mm is as shown in Figure 4.14(c).

CONTINUUM MODEL

The FE model of wall D is made of 8 noded iso-parametric quadrilateral plane stress elements, with quadratic interpolation shape functions and 2×2 Gaussian integration scheme. All elements in white, representing masonry, are provided tensile and compressive nonlinearities with parameters mentioned in Table 4.4. The ones of the lintel and those along the floor levels (in gray) are kept linear elastic since cracks are not expected here [38]. All elements are of size 230 mm. Loading of the first stage contains vertical loads applied as line loads along the height of the two stories, and additionally, gravity loads. The second stage involves applying prescribed displacements to an auxiliary frame, as shown in Figure 4.15, such that equal monotonically increasing lateral forces are applied at both floors (using the master-slave connection) to simulate the static equivalence of seismic action. This is in line with a mass-proportional pushover analysis (assuming

Table 4.4: Modelling parameters - Masonry Facade: identified by studies from the work of Reference [38]

Material	Parameters	General	Compression	Tension
MASONRY	Young's Modulus E_0 [MPa]	1410	-	-
	Poisson's ratio v_0	0.2	-	-
	Density ρ [Kg/m^3]	1800	-	-
	Strength f_c, f_t [MPa]	-	-3.0	0.1
	Fracture energy G_c, G_f^I [N/mm]	-	10	0.05
	Saw-teeth discretisation factor	-	0.11	0.11
	Softening relation	-	Parabolic	Linear
	Crush/Crack bandwidth h [mm]	-	230	230
	Shear retention factor β	-	Damage-based [132]	Damage-based [132]

the floors have the lumped mass), contrary to a modal pushover analysis. The facade is supported at the bottom in both horizontal and vertical directions to simulate the fixed boundary condition. This study involves the diagonal shear failure mechanism in piers, and in principle, requires pure-sliding failure possibilities. This is possible using a meso-model in combination with the Coulomb friction interface formulation for SLA as in Reference [139], but considering the scale of the facade, the study is limited to the orthogonal fixed smeared cracking/crushing approach under macro modelling as previously done in Reference [38].
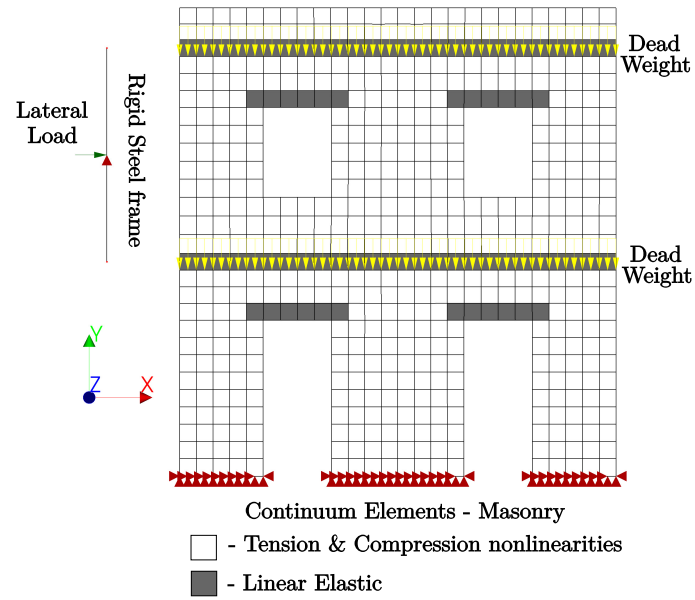

Figure 4.15: FE Model of wall D of the pushover test on the building, simulated using a stiff auxiliary frame to impose equal forces on both floors

Results & Discussion   The results of the SLA and Force-Release simulations of the pushover test are shown in Figure 4.16. The results show reasonable qualitative agreement
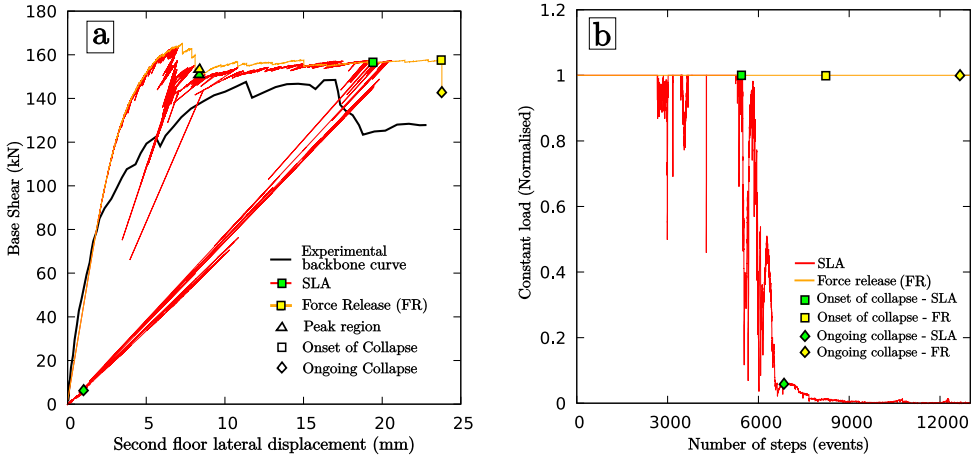
Figure 4.16: (a) Base shear vs lateral second floor displacement response for SLA & Force-Release methods compared against the backbone curve of the cyclic experimental response - including the reference points during the collapse mechanism, and (b) evolution of the precompression+gravity loads (normalised) during the simulations

with the experimental backbone curve. Since the experiment was cyclic in nature, the damage accumulation over the test, i.e. the progressive degradation in stiffness, affects the peak load achieved as against a monotonic counterpart. Accordingly, the simulations show a slightly higher peak load. However, the first stage of the rocking of the piers, followed by diagonal splitting type cracks in the center and right piers, is in accordance to the experimentally observed damage crack patterns. Around peak load, the first drop of load corresponds to the development of the diagonal cracks in the central and right piers. This is shown in Figure 4.17. SLA and Force-Release methods differ slightly in the crack patterns and this corresponds to minor differences in the elemental sequence failure that is characteristic of both approaches. However, around this first drop of load, SLA requires the intermittent proportional loading for redistribution due to the dynamic crack propagation in the central and right piers. These are also seen as drops of the constant load between the 2000th and 4000th steps (linear analysis) in Figure 4.16(b). Although such a redistribution driven by the intermittent proportional loading is premature, i.e. much ahead of the actual structural collapse observed in previous case studies, it allows for recovery of the full magnitude of the constant loads and is therefore acceptable. Force-Release, on the contrary, goes through three large avalanche of ruptures for corresponding constant imposed displacements through this region. This again illustrates the inherent differences in the approaches (Figures 4.18 & 4.19).

At an ultimate displacement of around 18 mm, SLA runs again into the intermittent proportional loading. However, this time the actual collapse begins with the right pier completely failing by diagonal splitting failure, and also lateral splitting near the toe region due to the compression softening. Force-Release, owing to the inherent incremental approach and the manner of redistribution, proceeds further to an ultimate displacement of 24 mm leading to the collapse, while going through disequilibrium states. However,
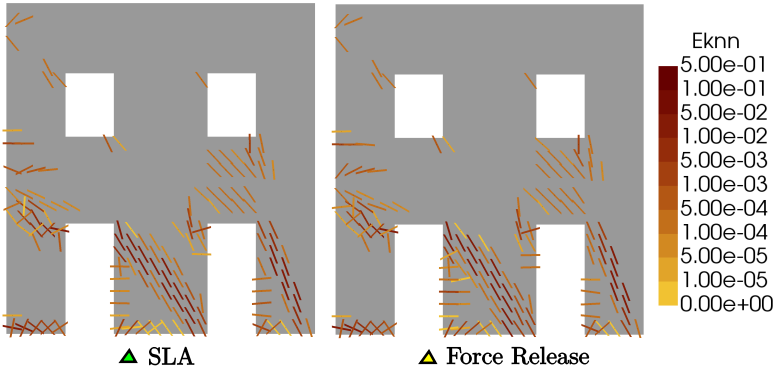
Figure 4.17: Crack pattern plots (Eknn denotes the normal crack strain) of SLA & Force-Release simulations of the pushover test around the peak region after the first drop of load (refer Figure 4.16)
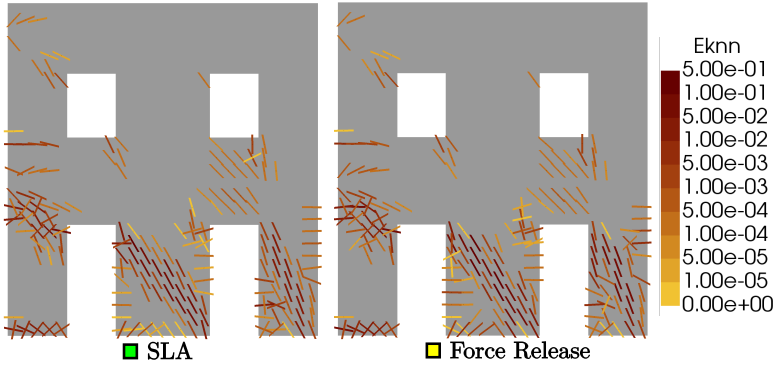

Figure 4.18: Crack pattern plots (Eknn denotes the normal crack strain) of SLA & Force-Release simulations of the pushover test at onset of collapse (refer Figure 4.16)

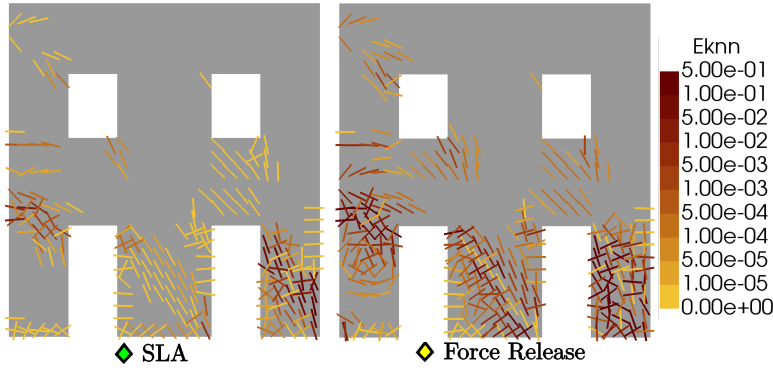Figure 4.19: Crack pattern plots (Eknn denotes the normal crack strain) of SLA & Force-Release simulations of the pushover test showing ongoing collapse (refer Figure 4.16)

the collapse mechanism is captured similarly by both approaches varying again only in the manner of load modification. SLA, once again, enforces a relaxed failure mechanism in equilibrium while Force-Release describes the explosive failure as an instability.

4.2. INTERMITTENT PROPORTIONAL LOADING IN SLA: PRESCRIBED DISPLACEMENTS VS FORCE LOADS

The Intermittent Proportional Loading (IPL), that drives the redistribution mechanism in SLA upon reaching the limit point of no constitutively admissible load multiplier under non-proportional loading, leads to differences depending on the type of external loading. That is, the response during IPL in SLA differs if the variable load is applied as a force or as a prescribed displacement.

Case Study   The aforementioned influence of loading on IPL in SLA is illustrated herein using an in-plane pushover experiment on a solid clay brick squat shear wall [6] (described also in Section 7.3). The experiment on the masonry wall subject to overburden followed by quasi-static cyclic lateral load is said to show a brittle failure due to diagonal shear cracking [6]. Although the test is cyclic in nature, the test can be used under monotonic loading as a benchmark for 2D (plane stress) SLA simulations by making qualitative comparisons between the response and the envelope of the experimental curve. This is simulated using a 2D finite element model, shown in Figure 4.20(b), made of 8 noded iso-parametric quadrilateral plane stress elements (of size 55 mm) with quadratic interpolation shape functions and a 2×2 Gaussian integration scheme. These elements are provided with material properties listed in Table 4.5, and are described using a fixed crack/crush constitutive framework. However, Mode-I fracture energy G_f^I of 0.1 N/mm, as mentioned in the Table 4.5, applies only for the elements along the bottom and top edges in the model. The rest of the elements are provided $G_f^I = 0.15$ N/mm to mimic the larger dissipation of energy observed in a diagonal shear crack, as against the flexural crack in the extreme elements. Furthermore, the FE model is fixed at the bottom while the rotation at top is restrained to ensure a straight edge, using a master-slave connection. This is to comply with the double-clamped boundary condition of the experiment.

Table 4.5: Modelling parameters - Masonry shear wall [6]

| Parameters	Values
Young's Modulus E_0 [GPa]	1.491
Poisson's ratio v_0	0.15
Tensile strength f_t [MPa]	0.17
Mode I fracture energy G_f^I [N/mm]	0.1
Saw-teeth discretisation factor - tensile & compressive	0.1
Tension softening relation	linear
No. of saw-teeth	32
Compressive strength f_c [MPa]	6.2
Compressive fracture energy G_c [N/mm]	40
Compressive softening relation	parabolic
No. of saw-teeth	24
Crack bandwidth h [mm]	Elem. size
Shear retention factor β	10^{-2}
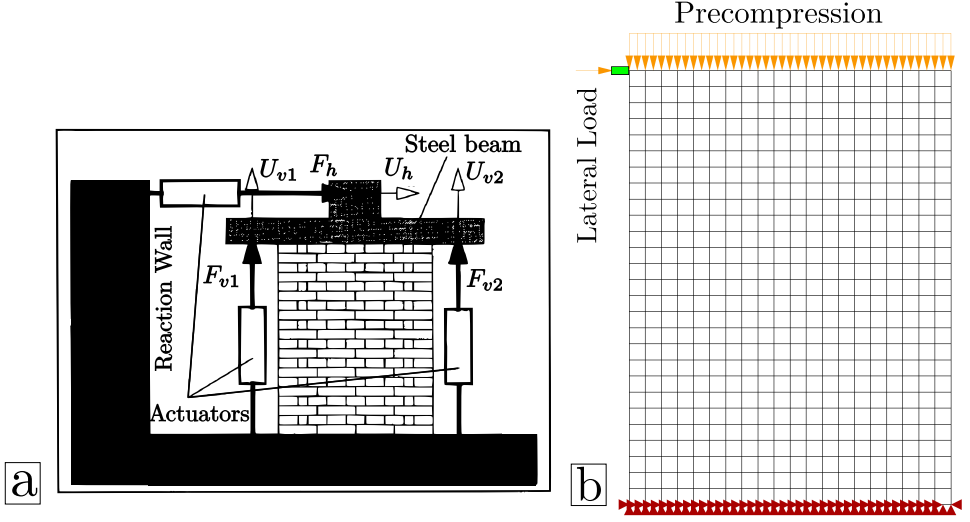
Figure 4.20: (a) Experimental setup, and (b) the FE model of the quasi-static cyclic pushover test [6]

The overburden/precompression load of 0.5 MPa is applied as distributed force load. The FE model is first simulated using an implicit NLFEA, to serve as reference, since the experimental crack patterns are not available [6]. The lateral load is applied in displacement control over 100 equal sized steps of magnitude 0.1 mm each, on a single node as shown in Figure 4.20(b). The implicit scheme uses a Newton-Raphson method that converges to either a force or displacement norm of 0.0001. Thereafter, two simulations are run using SLA. The first run is with the lateral load applied as a force, while the second one is with a prescribed displacement (hereon, for simplicity, referred to as force-controlled and displacement controlled SLA respectively). In principle, both should yield the same result since SLA is damage driven. Additionally, a force-release simulation, which also uses prescribed displacements by default, is run to get a more comprehensive outlook.
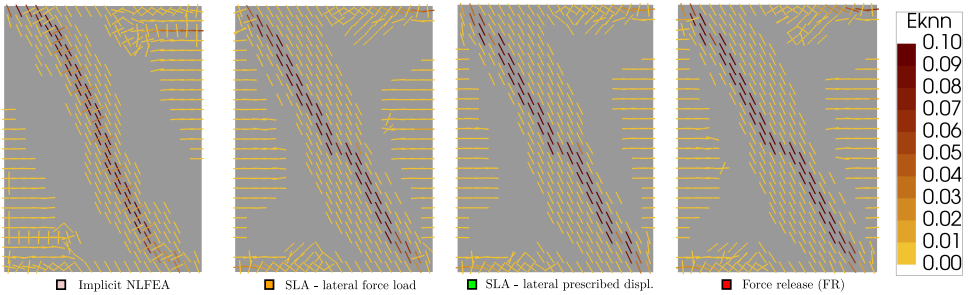

Figure 4.21: Crack pattern plots (Eknn denotes the normal crack strain) of the implicit NLFEA, SLA (lateral load applied as force loads or prescribed displacements) & Force-Release simulations at the reference points shown in Figure 4.22(a) around 7.2 mm lateral top displacement.
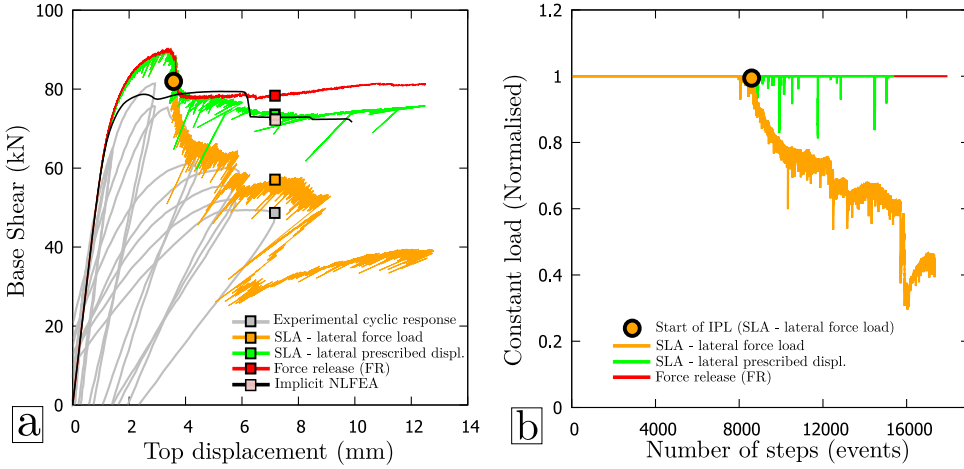
Figure 4.22: (a) Base shear vs top displacement response from SLA (lateral load non-proportionally applied either as force loads or prescribed displacements), Force-Release method & an implicit NLFEA simulation compared against the experimental cyclic response (only 1st quadrant shown) - including the reference points for comparison of damage, and (b) the evolution of the precompression load (normalised) during the SLA & Force release simulations

Discussion The result from the implicit NLFEA confirms the diagonal localised shear cracking behaviour, which is in good agreement with the three responses of force and displacement controlled SLA, and the Force-release case, as seen in the crack pattern plots around 7.2 mm lateral top displacement (refer Figure 4.21). There are some minor differences as well but, in general, the patterns are similar. However, the force displacement response of the force controlled SLA appears brittle in comparison to the rest of the three cases, all of which are qualitatively similar and more ductile as shown in Figure 4.22(a).

$$L_{\text{ipl}} = L_{\text{con}} + \lambda_{\text{crit}}^{j-1} L_{\text{var}} \tag{4.1}$$

$$L_{\text{ipl}}^{j} = \lambda_{\text{crit}}^{j} L_{\text{ipl}} \tag{4.2}$$

In case of the force controlled SLA, the response is rather brittle because the recovery of constant load becomes almost impossible when global softening is imminent or ongoing beyond the circular marker as seen in Figure 4.22. It is clear from Eqs. 4.1-4.2 that constant load is recovered in the IPL *only* when the load factor for the variable load simultaneously reaches $\lambda_{\text{crit}}^{j-1}$ (which is larger in magnitude) corresponding to the last successful load combination L_{ipl}. Attempting to reach such a higher load factor during global softening is not possible unless some redistribution allows for it, refer Figure 4.23. This is similar to expecting a reduction of load in a force controlled implicit NLFEA upon reaching the traditional limit point situation [35]. In conclusion, once a force-controlled SLA simulation runs into IPL in the global softening region of the response, the simulation shows a gradual reduction of constant load to extremely low values which is not truly reflective of the experiment. The response is under loading conditions different to that of

the experiment, and therefore could be interpreted as an alternate equilibrium path. This kind of redistribution is hereon referred to as *premature* IPL.

In the other case of a displacement controlled SLA, the analysis moves forward and the constant load is recovered. This is possible herein because the IPL for a displacement controlled SLA is a little different. In this case, the last successful load combination is also the prescribed displacement, and therefore in subsequent steps the IPL attempts to reach a higher displacement d_{ipl}^j that is greater than or equal to d_{ipl}, refer Eq. 4.3 and Figure 4.23.

$$d_{ipl}^j = \lambda_{crit}^j \, d_{ipl} \tag{4.3}$$

However, even this case becomes impossible for a typical instability in the force-displacement response wherein the tangent is infinite (as in a brittle collapse). Attempting to reach a higher load factor for the variable load (in this case the prescribed displacements) during local instabilities is not possible unless some redistribution allows for it. In case of collapse, it becomes impossible. Such a response has been previously observed during the collapse mechanisms in SLA studies of Sections 4.1.2, 4.1.3 & 4.1.4. This is similar to expecting a reduction of the prescribed displacement in the displacement controlled implicit NLFEA upon reaching the traditional turning point situation [35].
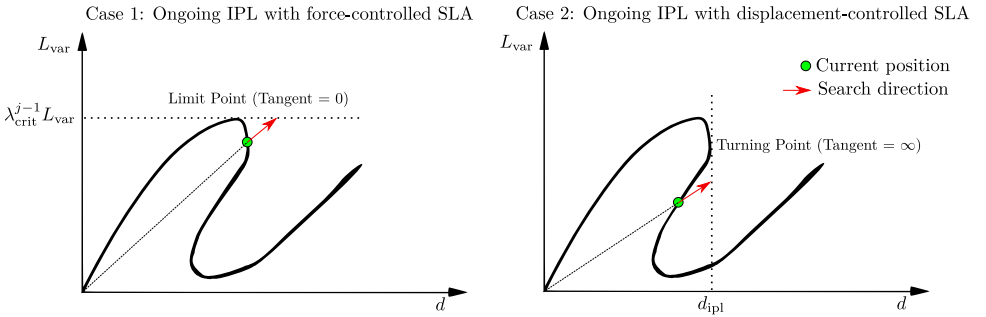

Figure 4.23: SLA during intermittent proportional loading with prescribed forces (left) and displacements (right)

Modelling prescribed displacements for SLA in DIANA   In DIANA, the nodes with prescribed displacements are constrained along the corresponding degrees of freedom in general. Additionally, in the attempt to reduce analysis times for problems typified by multiple load cases (non-proportional loading), the set of constrained and unconstrained variables for any FE model is forced to be the same for all load cases by default [51]. As a consequence, the stiffness matrix is decomposed only once, and for every load case the solution is obtained using the backward and forward substitutions. However, this efficient approach becomes a problem in the case of SLA since it relies on identification of the critical integration point by superposition of stresses from different load cases. When one of the loads is a prescribed displacement, the presence of the constraint at all times in the FE model will affect the stress field due to the other load case. These manifest as

small stress concentrations which are, in principle, incorrect. This particularly becomes a problem in a non-proportional case where the variable load is applied as a prescribed displacement along the same direction as the constant load. The problem actually calls for the use of an incremental approach instead of the total approach. Nevertheless, it can be addressed in a total set-up using a *phased* analysis, wherein the supports for prescribed displacement is added to the FE model only while considering the corresponding load and is discarded for other load(s). This requires extensive implementation within the DIANA framework, and is therefore not considered in this study.

However, it has been observed over several examples in this chapter and further in the thesis, that the effect of this feature is not significant as long as the damage zones in the simulation are not close to the constraint like for instance in the cases described in Sections 4.1.2, 4.1.3 & 4.1.4. The exception to this is the study described in this section, and therefore, both the forces and displacements are applied to the wall through a stiff small steel beam, shown in green in Figure 4.20(b).

4.3. CONCLUDING REMARKS

Finite element simulation of quasi-brittle materials using incremental-iterative methods often suffers from robustness issues. Consequently, several sequentially linear methods were devised to address this problem [139, 57, 3, 44, 43, 156]. Although several studies have been made in the lattice modelling community to elucidate the inherent differences between two classes of methods: namely the *total* and *incremental* approaches [44, 81], their suitability to structural applications has been touched upon sparsely. Of all the available total approaches in literature, only the constrained maximisation analogy [139] addresses the *limit point* situation wherein no constitutively admissible critical load multiplier can be found. This method is, therefore, chosen as the reference *total* approach to be compared in this chapter against an *incremental* counterpart, the Force-Release method.

The inherent differences between these methods are illustrated using continuum FE models of structural examples involving non-proportional loading in this chapter. To this end, an academic example of a prestressed beam and three experimental benchmarks: a slender masonry wall, a squat reinforced concrete wall and a full-scale 2D masonry facade, all subject to different magnitudes of precompression followed by a pushover load are studied. In general, it is observed in all three case studies that the non-proportional loading strategy in a total approach like SLA is almost equivalent to the incremental solution obtained using a Force-Release method, in terms of force-displacement curves and damage patterns, until the *limit point* situation is reached. Prior to this, although the unloading and reloading are both done non-proportionally in SLA, it is acceptable to interpret that unloading happens only until the beginning of the variable load (i.e. partial unloading) since all the previously applied (constant) loads can be reloaded fully without causing new damage. It is also interesting to note that the differences in the sequences of events, which can significantly affect the eventual failure mechanism in the case of lattice modelling examples [81], do not greatly affect the eventual results at continuum level for all the presented case studies.

However, upon reaching the *limit point*, which denotes an oncoming dynamic failure propagation region in the true response, the process needs to be driven by a sudden release of energy which inherently requires multiple failure events or the so called avalanche of ruptures. The SLA and Force-Release approaches differ in the redistribution mechanism at this juncture. On the one hand, SLA allows for such multiple failures sequentially, by reduction of all previously applied loads which brings about snap-backs. Since every damaged element's stress is released instantaneously, the neighbouring elements whose stresses are close to their respective allowable strengths subsequently become critical in SLA at a considerably lower load. This is done by scaling the last successful load proportionally which in turn still allows for damage propagation by reduction of forces, unlike *complete unloading*, thereby giving the structure the time to relax. In other words, SLA lets the damage progress quasi-statically by load reduction during a dynamic event. This is acceptable under proportional loading situations, and also under non-proportional loading conditions if the experiments are controlled truly quasi-statically. In case of SLA, the system as whole is allowed for *an overall* quasi-static damage propagation which may be interpreted to be equivalent to a CMOD controlled experiment as in Reference [122], which involves a unique damage process zone. However, in case of multiple cracks developing in the system, SLA does not control *a specific damage process zone* as in a CMOD experiment and may incorrectly decrease it. Force-Release method, contrarily, may increase the CMOD due to the redistribution. In a quasi-static sequentially linear setup, a truly CMOD controlled experiment with multiple evolving damage zones can be appropriately simulated by the general method [43]. This is traditionally simulated using arc-length control procedures in an implicit NLFEA set-up. On the other hand, the Force-Release method keeps track of the load history incrementally, and allows for multiple failure events by gradual redistribution of stresses through disequilibrium states. The Force-Release method is suitable for typical displacement controlled experiments which actually exhibit instabilities, but is not suitable for physical processes which exhibit snap backs or for truly quasi-static experiments.

Thus, both approaches are essentially extremes with regard to time scales for redistribution, which is more apparent only in major dynamic failure processes in the case of continuum models. These dynamic failure processes can either be *intermediate* in the entire process of damage evolution (local instabilities) or the final *collapse* mechanism in itself. In the former case of an *intermediate* failure process, with regard to SLA, if the simulation allows for a full recovery of all previously applied loads, the results are deemed acceptable. Such an instance was observed around the first drop of load after the peak in the pushover case study of a 2D masonry facade [105] (also refer Section 4.1.4). However, during these *intermediate* failure processes, if all previously applied loads have to be gradually reduced to extremely low values to simulate the failure process, then the results of SLA correspond to alternate equilibrium paths of damage propagation that do not culminate in the actual expected collapse mechanism. Such an instance of *premature* IPL was observed in the SLA study of the pushover analysis on a squat masonry wall, refer Section 4.2, wherein the lateral load was applied as force loads. Or, in other words, premature loss of previously applied loads much ahead of the actual mechanism is not equivalent to simulating the experiment truly. In the latter case where the dynamic failure is the actual *collapse* mechanism as observed in the pushover case studies of the masonry

and reinforced concrete walls, and the masonry facade (Sections 4.1.2, 4.1.3 & 4.1.4), SLA tries to enforce equilibrium by load reduction and allows for a relaxed failure mechanism. The Force-Release method, on the other hand, describes both the *intermediate* and the explosive *collapses* through avalanches of events that are states of disequilibrium. The Force release method stays true to the instability in the experiment but excessive damage propagation at collapse, such as those observed in the wider-crush zone of the slender masonry wall case study (Section 4.1.2), needs further deliberation including a localisation analysis. In summary, complex dynamic failure processes which cause robustness issues in incremental iterative methods also affect sequentially linear methods under non-proportional loading, and are addressed differently by the two sub-classes: the total and incremental approaches, with their suitability depending on the type of experiment/structure being simulated.

4

NON-PROPORTIONAL LOADING FOR 3D STRESS STATE IN CONTINUUM[*]

Applications in SLA, thus far, have been restricted to 2D and 3D continuum problems for proportional loading and solely 2D problems for non-proportional loading situations, using the total-strain based fixed smeared crack constitutive framework. To this end, this chapter contributes to the extension of SLA to 3D stress states, under non-proportional loading conditions, which in turn would enable structural level applications. For 3D stress states under non-proportional loading conditions, the lack of a closed form solution for the critical load multiplier, with regard to damage initiation, was the hindrance to the identification of the critical integration point. Accordingly, two solutions strategies are proposed to address the issue. Firstly, the fixed smeared cracking constitutive model for solid elements (3D stress state) in elaborated in Section 5.1. Then, the motivation for the 3D non-proportional loading strategy is briefed upon in Section 5.2. Subsequently, in Sections 5.3.1 & 5.3.2, the two new methodologies enabling extension to 3D stress states in non-proportional loading are detailed upon, including a qualitative discussion in Section 5.3.3 corroborating the choice of the first method for further studies. In the first approach, the cubic function in the load multiplier is analytically solved for real roots using trigonometric solutions or the Cardano method. In the second approach, the load multiplier is expressed as a function of the inclination of a potential damage plane and is deduced using a constrained optimisation approach. Section 5.4 presents the 3D validation studies. This includes two academic cases of 3-point bending tests of a beam (with and without prestress loads): one with a straight and the other with a skewed notch, and a more complex case of RC slabs subject to shear loads in combination with axial loads [20].

5.1. ORTHOTROPIC 3D FIXED SMEARED CRACK MODEL

SLA for continuum problems is based on a total strain based smeared cracking/crushing model with the fixed crack/crush approach. In this section, the fixed crack/crush model extended to 3D stress states [150] is elaborated upon. The word *crush(ing)* is dropped hereon for simplicity. As soon as the principal stress violates the allowable strength at an integration point in tension or compression, the isotropic stress-strain relation $\sigma = D\varepsilon$ transforms into a 3D orthotropic relation as $\sigma_{nst} = D_{nst}\varepsilon_{nst}$, and the cracked coordinate system denoted by *nst* is fixed along the directions of the principal stresses. A simple Rankine type failure surface is used to initiate damage for tension or compression failures in the fixed crack set-up. In the primary principal stress direction, the Young's modulus

---

and strength are reduced according to the uniaxial saw tooth law. Subsequently, in the event of principal stress rotations, redistribution of stresses, or application of another load non-proportionally; the normal stresses in the orthogonal directions of the fixed crack system (secondary or tertiary) may violate the allowable strength, and damage is introduced accordingly in the corresponding directions. So every integration point essentially requires three uniaxial saw tooth laws each for tension and compression in the 3D stress state. Furthermore, the shear behaviour in the fixed cracking model is represented using a variable shear retention function that considers the reduction of shear stiffness with increasing damage in the normal direction of the cracked plane. Similarly, the Poisson's ratio is reduced at the same rate as the associated Young's modulus.

The 3D orthotropic compliance relation deduced from the isotropic relation $\boldsymbol{\varepsilon} = \mathbf{C}\boldsymbol{\sigma}$, using the individual uniaxial stress-strain relations based on Hooke's law in Voigt notation, is given by:

$$
\begin{bmatrix} \varepsilon_{xx} \\ \varepsilon_{yy} \\ \varepsilon_{zz} \\ \gamma_{xy} \\ \gamma_{yz} \\ \gamma_{zx} \end{bmatrix} = \begin{bmatrix} \frac{1}{E_x} & \frac{-\nu_{xy}}{E_y} & \frac{-\nu_{xz}}{E_z} & 0 & 0 & 0 \\ \frac{-\nu_{yx}}{E_x} & \frac{1}{E_y} & \frac{-\nu_{yz}}{E_z} & 0 & 0 & 0 \\ \frac{-\nu_{zx}}{E_x} & \frac{-\nu_{zy}}{E_y} & \frac{1}{E_z} & 0 & 0 & 0 \\ 0 & 0 & 0 & \frac{1}{G_{xy}} & 0 & 0 \\ 0 & 0 & 0 & 0 & \frac{1}{G_{yz}} & 0 \\ 0 & 0 & 0 & 0 & 0 & \frac{1}{G_{zx}} \end{bmatrix} \begin{bmatrix} \sigma_{xx} \\ \sigma_{yy} \\ \sigma_{zz} \\ \sigma_{xy} \\ \sigma_{yz} \\ \sigma_{zx} \end{bmatrix}
\tag{5.1}
$$

Due to the symmetry of the compliance matrix $\mathbf{C}$, the Poisson's ratios should be interrelated as well. Inverting the compliance matrix, the following stiffness matrix $\mathbf{D}$ is obtained.

$$
\mathbf{D} = A \begin{bmatrix} (\nu_{yz}^2 \frac{E_y}{E_z} - 1)E_x & -(\nu_{xy} + \nu_{yz}\nu_{zx}\frac{E_y}{E_x})E_x & -(\nu_{xy}\nu_{yz} + \nu_{zx}\frac{E_z}{E_x})E_x & 0 & 0 & 0 \\ -(\nu_{yz}\nu_{zx} + \nu_{xy}\frac{E_x}{E_y})E_y & (\nu_{zx}^2 \frac{E_z}{E_x} - 1)E_y & -(\nu_{yz} + \nu_{xy}\nu_{zx}\frac{E_z}{E_y})E_y & 0 & 0 & 0 \\ -(\nu_{zx} + \nu_{xy}\nu_{yz}\frac{E_x}{E_z})E_z & -(\nu_{xy}\nu_{zx} + \nu_{yz}\frac{E_y}{E_z})E_z & (\nu_{xy}^2 \frac{E_x}{E_y} - 1)E_z & 0 & 0 & 0 \\ 0 & 0 & 0 & \frac{G_{xy}}{A} & 0 & 0 \\ 0 & 0 & 0 & 0 & \frac{G_{yz}}{A} & 0 \\ 0 & 0 & 0 & 0 & 0 & \frac{G_{zx}}{A} \end{bmatrix}
\tag{5.2}
$$

where

$$
A = \frac{E_x E_y E_z}{-E_x E_y E_z + \nu_{xy}^2 E_x^2 E_z + \nu_{zx}^2 E_z^2 E_y + \nu_{yz}^2 E_y^2 E_x + 2\nu_{xy}\nu_{yz}\nu_{zx}E_x E_y E_z}
\tag{5.3}
$$

For the initial uncracked stage, denoted by subscript 0

$$
E_x = E_y = E_z = E_0; \ \nu_{xy} = \nu_{xz} = \nu_{yx} = \nu_{yz} = \nu_{zx} = \nu_{zy} = \nu_0; \ G_{xy} = G_{yz} = G_{zx} = G_0 = \frac{E_0}{2(1+\nu_0)}
\tag{5.4}
$$

Upon crack initiation, the three axes of the orthotropic *nst* coordinate system are fixed. The *n*-axis is aligned with σ_1 and is perpendicular to the primary crack plane. The *st*

plane covers the tangential crack directions, for which the directions are aligned with the principal stress directions σ_2 and σ_3, respectively, at the onset of damage. Similarly, when the failure type is compressive, the primary direction is that of the minimum principal stress. In conclusion, the orthotropic relation upon damage becomes

$$
\begin{bmatrix}
\sigma_{nn} \\
\sigma_{ss} \\
\sigma_{tt} \\
\sigma_{ns} \\
\sigma_{st} \\
\sigma_{tn}
\end{bmatrix}
= \mathbf{D}_{nst}
\begin{bmatrix}
\varepsilon_{nn} \\
\varepsilon_{ss} \\
\varepsilon_{tt} \\
\gamma_{ns} \\
\gamma_{st} \\
\gamma_{tn}
\end{bmatrix}
\tag{5.5}
$$

where the orthotropic stiffness matrix is similar to the aforementioned $\mathbf{D}$ matrix with subscripts n, s, t instead of x, y, z.

In this formulation, Poisson effects and shear behaviour can also be made damage based. That is, the shear stiffness is reduced in a step-wise fashion, directly dependent on the minimum of the corresponding Young's moduli. This variable shear retention approach is comparable to the ones adopted for plane stress [139] and shell elements [38]. Similarly, the Poisson's ratios are reduced depending on their corresponding Young's modulus, as shown in the following. The orthotropic degradation i.e. the crux of the fixed crack set up necessitates the simultaneous reduction of Poisson behavior during damage to avoid spurious lateral cracking/crushing. Furthermore, this yields a favourable symmetric reduced stress-strain relationship in which the orthotropic degradation is solely dependent on the reduced moduli of elasticity.

$$
\nu_{sn} = \nu_{tn} = \nu_0 \frac{E_n}{E_0} \qquad \nu_{ns} = \nu_{ts} = \nu_0 \frac{E_s}{E_0} \qquad \nu_{nt} = \nu_{st} = \nu_0 \frac{E_t}{E_0}
\tag{5.6}
$$

$$
G_{ns} = \frac{\min(E_n, E_s)}{2(1 + \nu_0 \frac{\min(E_n, E_s)}{E_0})} \quad G_{st} = \frac{\min(E_s, E_t)}{2(1 + \nu_0 \frac{\min(E_s, E_t)}{E_0})} \quad G_{tn} = \frac{\min(E_t, E_n)}{2(1 + \nu_0 \frac{\min(E_t, E_n)}{E_0})}
\tag{5.7}
$$

Alternatively, Poisson's ratios could be set to zero at the onset of damage thereby decoupling the orthogonal behaviour, and the traditional constant shear retention could be used. Higher values of $\beta = 0.01$ or 0.1, a constant shear retention factor, are generally used for standard NLFEA applications in concrete to simulate the aggregate interlock, while lower values are used to avoid stress locking problems. In the illustrations presented in this chapter, at onset of damage, $\nu_{ij} = 0$ and a constant shear retention factor $\beta = 0.0001$ are used, unless specified otherwise. Both choices could influence the crack propagation phase and the interaction of multiple cracks, however, considering the motivation to solely address the crack/damage initiation problem in a 3D stress state for non-proportional SLA (detailed further in Section 5.2), the choices are deemed reasonable.

Furthermore, in the current framework, immediately upon violation of the allowable strengths either along the maximum or minimum principal stress direction, the transition from an isotropic to orthotropic formulation is made, and the 3D orthogonal fixed

crack system (*nst*) is established. Alternatively, the fixing of the secondary and tertiary directions of the crack system could be postponed until failure in the secondary direction, due to violation of the allowable strength by the principal stress (computed anew) in that direction. This is a more realistic representation of the multi-directional cracking phenomenon in comparison to the simplified former approach, but it is not investigated in this study.

5.2. MOTIVATION

Structural level applications of SLA, for instance a pushover analysis of a masonry or reinforced concrete building, would only be possible if the non-proportional loading strategy could be extended to 3D stress states. The principle of superposition of stresses due to non-proportional loads and the total strain based fixed crack approach, with the use of principal stresses for damage initiation, has formed the basis of 2D continuum applications of SLA thus far. This approach relied on a closed form solution for the critical load multiplier (for damage initiation) which, in turn, depended on the existence of a rather simple expression for the principal stress like the one in Eq. 3.7 for the plane stress state. In an earlier attempt to extend SLA to 3D applications, DeJong et al. [38] made a simplification to at least enable the use of shell elements. The formulation is similar to layered membrane elements spaced over the thickness of the shell, introduced through a 2D mesh, with additional integration points in the thickness direction. These assumptions fix the crack plane to be perpendicular to the plane of the shell element, and the shell mid-surface is aligned with the *n-s* coordinate plane. However, this membrane approach does not take into account the two out-of-plane shears in the calculation of the critical load multiplier. In conclusion, it was clear that deducing a similar expression for principal stresses from the characteristic cubic equation for a full 3D stress state was not as straightforward, and thus had to be addressed. This motivation has previously been touched upon leading to an alternate non-proportional loading strategy called the Sequentially linear *theta*-based non-proportional strategy (SLTHNP) [103], which was first validated for the 2D plane stress state. The characteristic equation in a 3D stress state is given by the following equations:

$$det(\Sigma - \Lambda \mathbf{I}) = 0 \tag{5.8}$$

$$\begin{vmatrix} \sigma_{xx} - \Lambda & \sigma_{xy} & \sigma_{zx} \\ \sigma_{xy} & \sigma_{yy} - \Lambda & \sigma_{yz} \\ \sigma_{zx} & \sigma_{yz} & \sigma_{zz} - \Lambda \end{vmatrix} = 0 \tag{5.9}$$

$$\Lambda^3 - I_1 \Lambda^2 + I_2 \Lambda - I_3 = 0 \tag{5.10}$$

where Σ is the 3D stress tensor in matrix notation, Λ are the principal values - σ_1, σ_2, and σ_3, $\mathbf{I}$ is the Identity matrix, and I_1, I_2 and I_3 are the stress invariants. Mathematical procedures like the Cardano's method [17], involving a transformation to get reduced cubic equations (a monic trinomial wherein the quadratic term is zero) and subsequent deduction of analytical solutions using trigonometric identities, are well documented in

literature. This forms the crux of the first method for 3D non-proportional SLA presented in the following section. Alternatively, the SLTHNP strategy suitable for the 3D stress states was introduced [103] wherein the problem statement was reformulated as a two-dimensional optimisation case, with respect to the directional cosines of a potential damage plane, and this is the second approach described in the next section.

Therefore, for undamaged integration points, analogous to Eqs. 3.8, cubic inequalities have to be solved for both tension and compression failure, and immediately establish the 3D orthogonal fixed crack system *nst* along the directions of the principal stresses at the onset of damage. This is as shown in the following.

$$\sigma_1(\lambda) \leq f_t \text{ resulting in } \Lambda_i^t \tag{5.11a}$$

$$\sigma_3(\lambda) \geq f_c \text{ resulting in } \Lambda_i^c \tag{5.11b}$$

In case of the damaged integration points, analogous to Eqs. 3.9, linear inequalities have to be solved per direction of the *nst* crack coordinate system for both tensile and compressive failures, of which only the ones corresponding to tensile failure are shown below for simplicity. These, however, are rather straightforward to solve unlike Eq. 5.11.

$$\sigma_{nn,\text{con}} + \lambda_{nn}\sigma_{nn,\text{var}} \leq f_{t,nn} \tag{5.12a}$$

$$\sigma_{ss,\text{con}} + \lambda_{ss}\sigma_{ss,\text{var}} \leq f_{t,ss} \tag{5.12b}$$

$$\sigma_{tt,\text{con}} + \lambda_{tt}\sigma_{tt,\text{var}} \leq f_{t,tt} \tag{5.12c}$$

Finally, the rest of the workflow is similar to that in the plane stress case (Section 3.1, Figure 3.1), with respect to deducing the critical load multiplier as the maximum of the common subset of the constitutively admissible range of load multiplier values at the model level. In the event of an empty solution set, the procedure returns to the *Intermittent Proportional Loading* (IPL).

5.3. SOLUTION METHODS

5.3.1. ANALYTICAL APPROACH

This section elaborates on the analytical solution to find the critical load multiplier for 3D stress states, for undamaged integration points (refer Eqs. 5.11,) in a fixed smeared crack set-up. In line with the principle of superposition of stresses, the global stresses (shown in a general index notation in Eq. 5.13) are first expressed as a scaled combination of those due to the non-proportional loads (constant loads depicted by subscript con and variable loads by subscript var) analogous to Eq. 3.6 .

$$\sigma_{ij} = \sigma_{ij,\text{con}} + \lambda\sigma_{ij,\text{var}} \tag{5.13}$$

$$I_1 = \sigma_{xx} + \sigma_{yy} + \sigma_{zz}$$
$$I_2 = \sigma_{xx}\sigma_{yy} + \sigma_{yy}\sigma_{zz} + \sigma_{zz}\sigma_{xx} - \sigma_{xy}^2 - \sigma_{yz}^2 - \sigma_{zx}^2 \tag{5.14}$$
$$I_3 = \sigma_{xx}\sigma_{yy}\sigma_{zz} + 2\sigma_{xy}\sigma_{yz}\sigma_{zx} - \sigma_{xx}\sigma_{yz}^2 - \sigma_{yy}\sigma_{zx}^2 - \sigma_{zz}\sigma_{xy}^2$$

$$f_t^3 - I_1 f_t^2 + I_2 f_t - I_3 = 0 \tag{5.15a}$$

$$f_c^3 - I_1 f_c^2 + I_2 f_c - I_3 = 0 \tag{5.15b}$$

These global stresses in Eq. 5.13 are subsequently substituted in the invariants I_1, I_2 and I_3 of the 3D stress tensor shown in Eq. 5.14. Since both tension and compression failures are considered, principal stresses σ_1 and σ_3 will be relevant. Accordingly, two separate cubic equations can be obtained by substituting the invariants of the stress tensor, containing the superposed global stresses, into Eq. 5.10: one with $\Lambda = \sigma_1 = f_t$ and another with $\Lambda = \sigma_3 = f_c$, where f_t and f_c are the tensile and compressive strengths. The resulting equations, shown in Eq. 5.15 in a rather shortened sense, obtained by substitution of Eq. 5.13 in Eq. 5.14 and subsequently in Eq. 5.10, are actually standard cubic equations in the load multiplier λ as shown in the following:

$$a\lambda^3 + b\lambda^2 + c\lambda + d = 0 \tag{5.16}$$

Without loss of generality, Eq. 5.16 can be written as Eq. 5.17 by manipulating the function to have coefficient $a = 1$ (dividing equation by a), with coefficients $\hat{b}, \hat{c}$ and $\hat{d}$ that are detailed upon in Appendix-A.

$$\lambda^3 + \hat{b}\lambda^2 + \hat{c}\lambda + \hat{d} = 0 \tag{5.17}$$

Subsequently, Eq. 5.17 is transformed into a monic trinomial (or a depressed cubic equation) in a new variable α by substituting $\lambda = \alpha - \hat{b}/3$ as shown in the following:

$$\alpha^3 + P\alpha + Q = 0$$

$$\text{where} \quad P = \frac{3\hat{c} - \hat{b}^2}{3} \quad \& \quad Q = \frac{2\hat{b}^3 - 9\hat{b}\hat{c} + 27\hat{d}}{27} \tag{5.18}$$

The solution strategy is then chosen based on the discriminant D of Eq. 5.18. If the discriminant shown in Eq. 5.19 is less than or equal to zero, the depressed cubic equation would yield three real roots (of which at least two roots would be equal if $D = 0$), else if the discriminant is greater than zero, the cubic equation would yield only one real solution.

$$D = \left(\frac{P}{3}\right)^3 + \left(\frac{Q}{2}\right)^2 \tag{5.19}$$

In the former case, the three real solutions are obtained using trigonometric functions and the formulae [17] as shown in the following:

$$\alpha_k = 2\sqrt{-\frac{P}{3}} \cos\left(\frac{1}{3}\arccos\left(\frac{3Q}{2P}\sqrt{-\frac{3}{P}}\right) - \frac{2\pi k}{3}\right) \text{ for } k = 0, 1, 2. \tag{5.20}$$

In the latter case, with the discriminant less than zero, the *Cardano* method [17] is used to find the real root. The complex roots are not of concern for our application; however, the

physical meaning of the nature of the roots is discussed at the end of this section. This method involves introducing two new variables u and v, linked by the condition $\alpha = u + v$, in the depressed cubic presented in Eq. 5.18. This is followed by imposing a condition $3uv + P = 0$ and eventually, solving a quadratic equation of which u^3 and v^3 are roots. For further details, the reader is referred to the work of Birkhoff and Maclane [17].

$$u^3 = -\frac{Q}{2} + \sqrt{\frac{Q^2}{4} + \frac{P3}{27}} \quad v^3 = -\frac{Q}{2} - \sqrt{\frac{Q^2}{4} + \frac{P3}{27}} \tag{5.21}$$

$$\alpha_{\text{real}} = u + v$$

$$\alpha_{\text{complex1}} = -\frac{(u+v)}{2} + i(u-v)\frac{\sqrt{3}}{2}$$

$$\alpha_{\text{complex2}} = -\frac{(u+v)}{2} - i(u-v)\frac{\sqrt{3}}{2} \tag{5.22}$$

Once the real roots from the depressed cubic equation in α are determined, the actual load multipliers λ are obtained using $\lambda = \alpha - \hat{b}/3$. The minimum positive value of the obtained real roots is subsequently tested on its possibility to be a maximum or a minimum load multiplier to satisfy the inequalities as in Eq. 5.11, additionally, subject to the condition that $\sigma_1 > \sigma_2 > \sigma_3$. This in turn will help deduce sets of the load multiplier λ values per undamaged integration point (Λ_i^t or Λ_i^c as is the case), and thus the critical load multiplier of an undamaged integration point is determined. Once an integration point is damaged, the crack coordinate system nst is set up. In subsequent SLA cycles for damaged integration points, three possible load multipliers are evaluated per analysis as shown in inequalities of Eq. 5.12, corresponding to the three existing fixed failure directions (additionally for tension and compression damage possibilities per direction for triaxial failures), and eventually the load multiplier sets per integration point are set up for both damaged and undamaged integration points. The critical load multiplier λ_{crit} for the system would be the maximum of the common subset of constitutively admissible load multipliers for both damaged and undamaged integration points, or, in other words, the least positive of all maximum load multipliers from the individual sets. This is the constrained maximisation approach as detailed in Section 3.1 which returns to the *intermittent proportional loading* in case of an empty solution set.

5.3.2. OPTIMISATION APPROACH

This section presents an alternative new approach for damage initiation in 3D non-proportional loading, wherein the problem is reformulated as a constrained optimisation case. For an undamaged integration point, the critical plane for crack/crush initiation is now identified by expressing the load multiplier λ as a function of the inclination of an arbitrary potential plane of damage, defined by θ for 2D plane stress states and by the two directional cosines l and m for 3D stress states, with respect to the reference coordinate system. The critical points of the function are deduced using optimisation techniques and subsequently, the critical load multiplier is established. This approach was referred to as the Sequentially linear *theta*-based non-proportional (SLTHNP) loading strategy, and has been previously validated for plane stress state using benchmark studies in the work

of Pari et al. [106]. The obtained solution was shown to match up to the corresponding closed form solution elaborated in Section 3.1.

Instead of resorting to the closed form expressions of the eigenstresses from the principal stress theory to subsequently find the closed-form solution for λ, the normal stress on an arbitrary potential plane of damage is now expressed as a function of its inclination. In the 3D stress state, an arbitrary plane may be related to the reference coordinate system by means of the directional cosines l, m and n, of which only two may be considered independent variables since they are related as $l^2 + m^2 + n^2 = 1$. The normal stresses acting on this plane due to the constant and variable loads can thus be expressed in terms of the directional cosines, and the load multiplier is now deduced as a function of two of these directional cosines, rewriting the third as $n = \sqrt{(1 - l^2 - m^2)}$ whose two solutions (positive and negative) are considered herein. The resulting optimisation problem is as shown in the following.

$$\max_{l,m} \quad \lambda(l, m) \tag{5.23}$$

$$\text{subject to} \quad \sigma_{nn}(l, m) \leq f_{\text{t}} \tag{5.24}$$

$$\sigma_{nn}(l, m) \geq -f_{\text{c}} \tag{5.25}$$

where

$$\sigma_{nn}(l, m) = \sigma_{nn,\text{con}}(l, m) + \lambda(l, m)\sigma_{nn,\text{var}}(l, m)$$

$$\sigma_{nn,\text{con}}(l, m) = \sigma_{xx,\text{con}}l^2 + \sigma_{yy,\text{con}}m^2 + \sigma_{zz,\text{con}}n^2 + 2\sigma_{xy,\text{con}}lm$$

$$+2\sigma_{yz,\text{con}}mn + +2\sigma_{xz,\text{con}}nl \tag{5.26}$$

$$\sigma_{nn,\text{var}}(l, m) = \sigma_{xx,\text{var}}l^2 + \sigma_{yy,\text{var}}m^2 + \sigma_{zz,\text{var}}n^2 + 2\sigma_{xy,\text{var}}lm$$

$$+2\sigma_{yz,\text{var}}mn + +2\sigma_{xz,\text{var}}nl$$

The idea is to find the values of λ, at which the slope of the function is zero, denoting the critical points of the function (namely the maxima, minima and the saddle point), and the corresponding inclination of the plane defined by the directional cosines l, m, n will be representative of the plane of failure (cracking/crushing). This helps establish the 3D orthogonal smeared fixed crack directions (*nst*). The function of the load multiplier may be continuous or discontinuous for different stress states, and typical functions of the load multiplier look like those shown in Figure 5.1. Firstly, the critical points of the functions are found per integration point, using optimisation techniques, which are the bounds of the solution to the superposition of the non-proportional loads. These correspond to the limits of the admissible range of values of λ per integration point as determined in Section 3.1, and the maximum λ of the common subset of all the integration points is chosen as the critical load multiplier for the system. Additionally, for the critical damage plane at an inclination l, m and n, with respect to the reference coordinate system, there will also be normal stresses σ_{tt} and σ_{ss} along tangential directions which are to be considered. For the critical λ evaluated by finding the optimum l, m and n, with respect to σ_{nn}, the corresponding σ_{tt} and σ_{ss} should be such that $\sigma_1 > \sigma_2 > \sigma_3$.

For the 2D plane stress state, the extrema (bounds) of the critical load multiplier were determined numerically using a one-dimensional optimisation routine, since the load multiplier was a function of the inclination of the damage plane, θ. It was easier to handle discontinuous functions at the 2D level because one-dimensional (θ) optimisation allows for bracketing of critical points, before using optimisation techniques like the Brent's method (in combination with inverse quadratic interpolation) or the Golden search methods [111] for subsequent isolation of the critical points. However, in the reformulated 3D non-proportional loading case, the optimisation has to be done with respect to 2 variables l and m. Consequently, a multidimensional optimisation routine is required, and preliminary investigations were made with the rather basic downhill simplex method (Nelder-Mead algorithm) [111]. The limitation, however, in multidimensional optimisation is that the initial bracketing of the extremum or critical points is not possible anymore, and emphasis has to be laid on possibly restarting the optimisation routine from a 'converged solution' repeatedly to ensure that the extremum is indeed the one sought for. The critical locations to be searched for in each function are points of zero slope i.e. the minima, maxima and saddle point, which indicate the possible combinations of the load multiplier and potential failure planes. In a plane stress state, every stress state corresponded to two critical points in the range of $-\pi$ to π, and the least positive value of all minima (points of positive second derivate) corresponded to the upper bound solution, and the maximum positive value of all maxima (points of negative second derivate) corresponded to the lower bound. Along the same lines, the bounds of the solution can be obtained from the sets of three possible combinations per integration point in the 3D stress state, and eventually arrive at the critical load multiplier for damage initiation. Once a point is damaged, the approach is similar to solving inequalities in Eq. 5.12, and the rest of the workflow is as described in Section 5.2.

5.3.3. COMPARISON OF THE APPROACHES

In order to illustrate the two approaches described in Sections 5.3.1 and 5.3.2, three different stress states as shown in Table 5.1 are considered. The choice of these stress states is arbitrary, and serves to only elucidate the possible combinations of the one/three real roots case from the analytical approach and the smooth/non-smooth functions from the optimisation approach. The stress states as such have no significance. The analytical approach either yields one or three real roots depending on the discriminant of the depressed cubic function (Eq. 5.18) in the load multiplier λ. If and only if $4P^3 + 27Q^2 \leq 0$, three real roots are obtained. When the discriminant $4P^3 + 27Q^2 > 0$, one would expect to have one real and two complex roots. However, only the real roots are of concern in determining the critical load multiplier as mentioned before. Although the complex roots for the scaling multiplier would result in one of the principal stresses (σ_1 or σ_3) being equal to the allowable strength, the other two principal stresses would result in complex values which are not representative of stress states in the case of classical continuum mechanics. Therefore, such roots are discarded. The analytical solution to the 3 illustrative stress states are shown in Table 5.2. It has been observed in the validation studies of Section 5.4 that the case of three real roots dominate and that there are very few instances of the 'one real root' case.

Table 5.1: Stress components (in MPa) used for comparison of the two approaches

Stress state	Strength	σ_{xx}		σ_{yy}		σ_{zz}		σ_{xy}		σ_{yz}		σ_{zx}	
		$\sigma_{xx,con}$	$\sigma_{xx,var}$	$\sigma_{yy,con}$	$\sigma_{yy,var}$	$\sigma_{zz,con}$	$\sigma_{zz,var}$	$\sigma_{xy,con}$	$\sigma_{xy,var}$	$\sigma_{yz,con}$	$\sigma_{yz,var}$	$\sigma_{zx,con}$	$\sigma_{zx,var}$
I	0.25	4	2	-2.5	2	0.2	0.3	1	0.2	0.5	0.05	0.1	0.1
II	0.25	1	-2	0.5	2	0.2	0.3	1	0.2	0.5	1.25	0.1	0.1
III	0.25	4	2	2.5	-2	0.2	0.3	1	0.2	0.5	0.05	0.1	-0.1

Table 5.2: Solutions to the illustrative stress states of Table 5.1

Stress state	Analytical solutions			SLTHNP optimisation
	1st root	2nd root	3rd root	
I	1.803	-0.061	-1.906	Continuous function (Figure 5.1a) with maxima, saddle and minima corresponding to 3 real roots
II	0.235	-0.092	-1.166	Discontinuous function (Figure 5.1b) with local critical points corresponding to 3 real roots
III	-1.89	$0.521 + 0.522i$	$0.521 - 0.522i$	Discontinuous function (Figure. 5.1c) with one real root

5
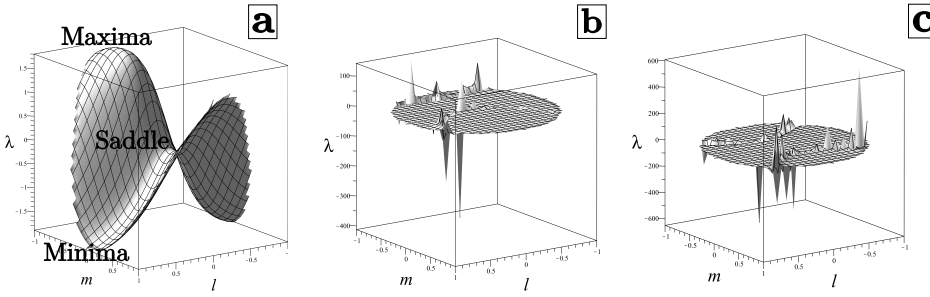
Figure 5.1: Typical continuous and discontinuous functions of the load multiplier dependent on the directional cosines of a potential failure plane: (a), (b) and (c) corresponding to stress states I, II and III mentioned in Table 5.1

With regard to the optimisation approach for the three stress states considered, the corresponding load multiplier λ functions, with respect to the directional cosines l, m of the potential damage plane, are shown in Figure 5.1. The smooth function illustrated in Figure 5.1a, corresponding to Stress state I in Table 5.1, could be representative of a local region in the discontinuous function displayed in Figure 5.1(b),(c). The critical points in the discontinuous functions shown in Figure 5.1(b),(c), corresponding to stress states II and III, are not visible owing to the large range in values of λ, and also the rather non-smooth nature of the function. Accordingly, it is difficult to deduce these points using optimisation techniques. There seems to be no real correlation between the type/form of the discontinuous function and the nature of roots from the analytical approach vis-a-vis one or three real root cases. This is also reflected in the similarity of plots for the discontinuous functions in Figure 5.1(b),(c). Furthermore, the extreme peaks, which are not of concern for the current study, possibly refer to inclination of failure planes that are potentially not critical, for the stress state caused by the scaled combination of the constant and variable loads. This is because the bounds/limits for the solution are sought, which are the least positive of all minima (the upper bound) and the maximum positive of all maxima (the lower bounds). Consequently, extremely large negative and positive values of the load multipliers are not of concern as they would be farther from the solution bounds. With regard to the optimisation approach, discontinuous functions like the ones shown in Figure 5.1(b),(c) are typical and account for 99 % of all stress states observed in the validation studies that follow in Section 5.4. However, since the success of such an approach relies heavily on the smoothness of the function, which is the case for most optimisation methods, and non-smooth functions are often hard to handle, the SLTHNP approach could be cumbersome.

In conclusion, owing to the following reasons, the analytical approach is preferred over the optimisation approach for all validation studies in Section 5.4.

- Discontinuous functions are hard to optimise for critical points because

   - Such methods may converge to points that are not necessarily the local critical points being sought for. This necessitates the need for multiple restarts to

validate the converged solution, or alternatively, a good first guess

– Bracketing of critical points is not possible in multi-dimensional optimisation methods unlike in the case one-dimensional methods like the Golden section search or Brent's methods [111].

Consequently, the computational intensity of the optimisation approach is higher than the analytical approach.

• Despite the computational effort, the solutions from the optimisation approach may still not be accurate enough, and therefore the solution may trace through alternate equilibrium paths.

5.4. ILLUSTRATIONS

In order to verify the presented concept for 3D non-proportional loading, validation studies are carried out using 3D solid element FE models. A notched concrete beam tested in 3 point bending with and without the effect of axial loads, a more complex case of a simply supported RC slab subjected to concentrated load near the supports with and without the effect of axial load, and finally, a skewed notch concrete beam tested in 3 point bending with additional prestress (to simulate 3D non-planar curved cracks), are considered.

5.4.1. PRESTRESSED BEAMS[*]

Several three-point bending tests performed by Zhao et al. [157], were previously analysed using SLA with plane stress assumptions [139]. Of these beams, SG2-B1, of span 600 mm, 150 mm depth, and 120 mm thickness is chosen as reference for this study but now in a 3D context. The beam is tested in three point bending with a notch of depth 60 mm and 2 mm width, and a schematic representation of the experiment is shown in Figure 5.2. The load F results in a mid-span deflection u, which was measured at the load application point.

The middle of the beam is in pure bending (no shear), and therefore, the governing principal stress at the mid-section will align exactly with the longitudinal axis of the beam. If such a beam were to be subject to axial loads (purely for an investigation purpose) like a tensile or compressive prestress, the loading would become non-proportional. The effect of axial loads will either increase or decrease the capacity of a beam, and has been a proven benchmark study for testing non-proportional loading strategy in SLA for the plane stress state thus far [40]. Although the case study does not represent a truly 3D stress state that might result in 3D multi-directional cracking, considering its simplicity and the fact that SLA introduces asymmetric failure propagation in FEM unlike traditional incremental iterative techniques (in this case with respect to an XY plane at the middle of the beam along its thickness, refer Figure 5.2); which in turn could yield stress situations that do not exactly resemble the perfectly symmetric 2D stress situation; the SG2-B1 beam specimen subject to additional axial loads makes for a good case study to be investigated for validation purposes of the 3D non-proportional loading strategy.

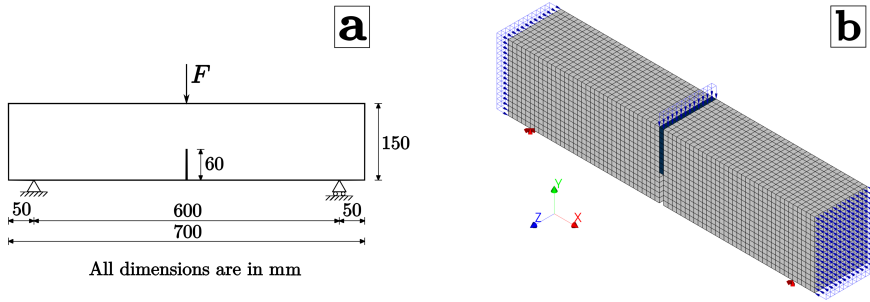[*]This case study is the same as the one used in Section 4.1.1.

Figure 5.2: (a) Schematic representation of experiment Beam SG2-B1 [157],
and (b) FE Model of the same with axial loads

Finite Element Model   The simply supported beam is modelled with geometry as shown in Figure 5.2, except that the notch width is assumed to spread over an entire element length. The FE model is made using linear 8-noded iso-parametric solid (brick) elements, with translational degrees of freedom and a reduced 1-point Gaussian integration scheme. All elements are approximately 10 mm in size. Linear elements (i.e elements with linear interpolation shape functions) are used in order to ensure constant strain distribution over the entire element. This helps in symmetric assessment of the crack bandwidth which is then equal to the length of the element. Concrete has been modelled as a linear-elastic material everywhere except the notched column of elements, where all the physical nonlinearity is lumped. These elements along the notch are provided the possibility of tensile softening failure. The adopted saw-tooth law for these notched column of elements is of linear tension softening type, with material parameters mentioned in Table 5.3. Three cases are considered to address the non-proportional loading problem. First, the three point bending test of SG2-B1 beam as in the experiment is simulated. Since the notch extends over one whole linear element, the point load is assumed to be equivalent to a distributed surface load applied at the top row of the central elements above the notch as shown in Figure 5.2. Second, the beam is additionally assumed to be subject to a uniform compressive prestress, of magnitude 0.25 MPa, at the ends of the beam. Third, the beam is instead subject to a uniform tensile prestress, of magnitude 0.25 MPa.

Results & Discussion   To begin with, the force displacement curves from SLA, on the first case without axial loads, match up well with those from the experiment. Furthermore, the results from all 3 analyses show the propagation of the tensile crack through the height of the notch, resulting in the reduction of effective cross section of the beam. This behaviour results in the loss of flexural capacity, and is eventually observed as the global softening in the force displacement curves shown in Figure 5.3. The qualitative behaviour of all the 3 beams is similar barring the observed ultimate capacity. The presence of axial loads like the compressive prestress tends to delay the cracking and consequently, results in a higher capacity. On the contrary, due to tensile axial loads, a decrease in capacity is observed. The response from the 3 beams, therefore, qualitatively agrees

Table 5.3: Modelling and Material parameters - Prestressed beam

Parameters	Values
Young's Modulus E_0 [GPa]	16
Poisson's ratio ν_0	0.15
Tensile strength f_t [MPa]	3.78
Mode I fracture energy G_f^I [N/mm]	0.224
Tension softening relation	Linear
Saw-teeth discretisation factor - tensile (p)	0.15
No. of saw teeth	16
Compressive behaviour	Linear elastic
Crack bandwidth h [mm]	10
Shear retention factor β	10^{-4}

Figure 5.3: (a) Force displacement curves for the 3-point bending cases using the 3D Model with and without axial loads, and (b) its comparison against 2D plane stress state simulations

to the expected response patterns from prestressed concrete theory. Additionally, it can also be observed that the force displacement curves match up to those obtained through 2D plane stress SLA simulations as shown in Figure 5.3(b), thereby validating the 3D Non-proportional strategy. With regard to the analytical solution of the load multiplier, obtained for undamaged integration points per analysis step, both the non-proportional cases of compressive and tensile axial loads yield 3 real roots always (not all were necessarily positive though). Additionally, the constant load i.e the compressive or tensile axial load in both cases was kept constant throughout the analysis, and there was no need to return to the *intermittent proportional loading* which is *Branch-B* of the workflow in Figure 3.1. The use of a reduced 1-point integration scheme gave symmetry with regard to the YZ plane through the midsection but non-symmetry with respect to the XY plane, as only one integration point can become critical at a time and not two symmetric points (if present) of an element simultaneously.

An interesting point of observation was that while using a regular 2×2×2 Gaussian integration scheme, the development of the crack through the thickness is rather stunted, while it is uniform in the plane stress state or the reduced integration study in the 3D model (Figure 5.4(b)). This is a case of alternating columns of elements, along the thick-
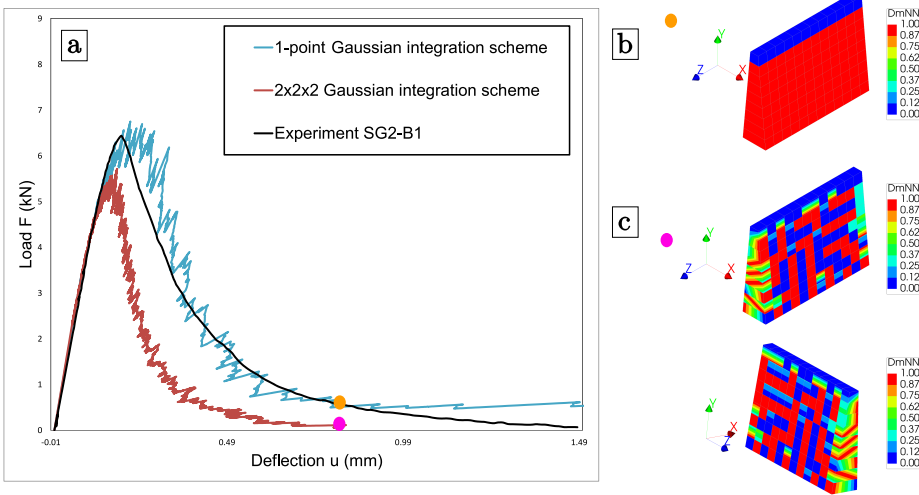
Figure 5.4: (a) Force displacement curves for the 3-point bending beam (proportional loading) for different integration schemes, and (b)-(c) their corresponding crack localisation patterns

ness of the beam, exhibiting crack localisation (within the elements) and propagation in a zig-zag band of integration points (along either side of the notch) over the height of the beam, as shown in Figure 5.4(c). This leaves some integration points of certain elements undamaged, and therefore results in a lower peak capacity and lower dissipation of energy as observed in Figure 5.4(a). The phenomenon is due to the inherent property of SLA in inducing asymmetry in localisation rather than due to the fixed crack approach.

5.4.2. RC Slab in shear failure

In order to corroborate the non-proportional loading strategy for full 3D cracking/failure possibilities, an RC slab case study is chosen, which was tested in shear along with axial loads to study the effect of pre-stressing. A similar RC slab, also tested in shear, was simulated previously [139] using SLA but under proportional loading assumptions. The tests performed by Bui et al. [20], which are considered for this study, include a series of slabs tested in shear with either compressive or tensile axial loads, which would correspond to an increase or decrease in the shear strength of the RC slab respectively. This is analogous to the prestressed beam cases presented in the previous section but will certainly result in more typical 3D cracking patterns. In this section, the experimental details are first described, with regard to the set up, crack patterns and force displacement curves. Subsequently, the SLA simulations for the slabs are presented.

Experiments   An extensive experimental campaign was recently conducted [20] to assess the shear strength of reinforced concrete slabs, subject simultaneously to shear loads and axial tensile or compressive loads. The purpose of the study was to understand the effects of axial loading due to shrinkage, earthquakes etc. on the shear resistance of RC

slabs. To this end, 8 simply supported (on all 4 sides) RC slabs of size 4m x 2.6m x 0.3m were subject to concentrated loads near the supports.
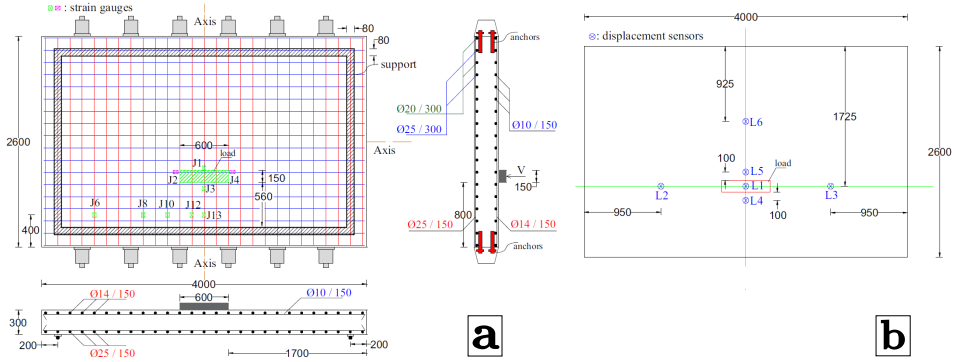

Figure 5.5: (a) Experimental set up: Loading plate, reinforcements, axial load and prestress application setup, and positions of strain gauges J1 - J13 to measure deformations in concrete along the reinforcements, and (b) positions of LVDT transducers L1 - L6

All slabs were cast without shear reinforcement but were provided sufficient longitudinal and transverse reinforcements, to ensure the occurrence of shear failure over flexural failure. One reference slab (S2) was tested without axial forces, 2 slabs were tested with compressive axial loads of magnitude 1 MPa (SC1) and 1.5 MPa (SC2), and 4 slabs were tested with varying magnitudes of tensile axial loads ranging from 0.65 MPa to 1.2 MPa (ST1, ST2, ST3 and ST4). The axial loads were applied by means of 12 in-plane hydraulic jacks, while the concentrated load was applied using an out-of-plane hydraulic jack over a loading plate, at a distance of 560 mm from the nearest line support and 875 mm from the nearest edge. The experimental set up is shown in Figure 5.5. For further information about the experiments pertaining to the experimental setup, material properties etc., the reader is referred to the work of Bui et al. [20]. Slabs S2 (without axial loads), SC2 (with 1.5 MPa compressive axial loads), and ST4 (with 1.2 MPa tensile axial loads) are chosen for this study. These would be analogous to the prestressed beam benchmark comparison and make for an ideal benchmark study to exemplify the newly introduced 3D non-proportional loading strategy.
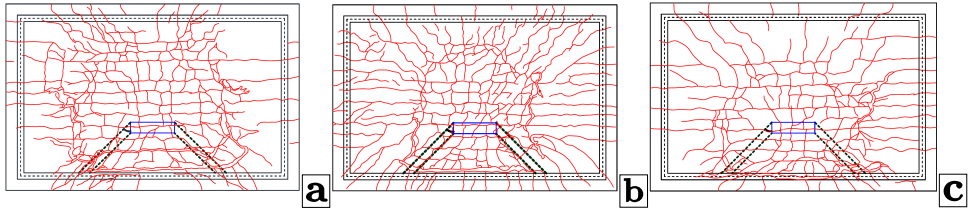
Figure 5.6: Experimental crack patterns of the bottom face of slabs (a) S2, (b) SC2 and (c) ST4. The black dashed lines from the loading plates to the supports denote the diagonal strut that determines the effective width for shear strength estimation [20]
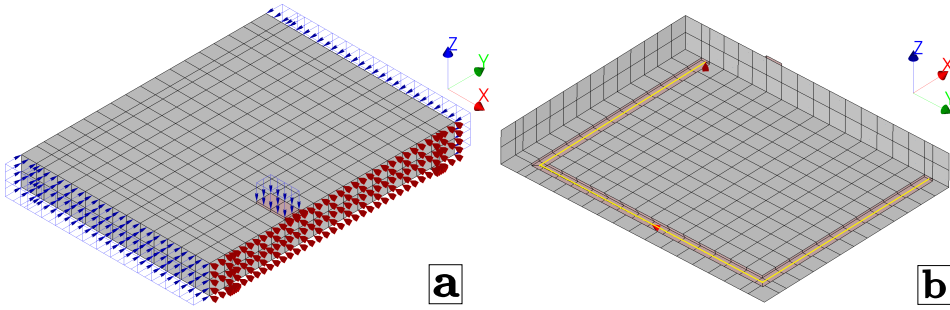
Figure 5.7: FE Model of half of the RC Slabs showing (a) the concentrated load on the loading plate, axial compressive loads and constraints along the axis of symmetry, and (b) the vertical support system

Table 5.4: Modelling and Material parameters - RC Slabs

Material	Parameters	Slab S2	Slab SC-2	Slab ST-4
CONCRETE	Young's Modulus E_0 [GPa]	15.875[a]	15.375[a]	16.2[a]
	Poisson's ratio v_0	0.15	0.15	0.15
	Tensile strength f_t [MPa]	2.87	3.63	3.5
	Mode I fracture energy G_f^I [N/mm]	0.175[b]	0.177[b]	0.178[b]
	Tension softening relation	linear	linear	linear
	Saw-teeth discretisation factor (p)	0.15	0.15	0.15
	No. of saw teeth	9	9	9
	Compressive strength f_c [MPa]	30.91	33.3	30.91
	Compressive fracture energy G_c [N/mm]	43.75	44.25	43.75
	Compressive softening relation	parabolic	parabolic	parabolic
	No. of saw teeth	12	12	12
	Crack bandwidth h [mm]	Elem. size	Elem. size	Elem. size
	Shear retention factor β	10^{-4}	10^{-4}	10^{-4}
REINFORCEMENTS	Young's Modulus E_0 [GPa]	210	210	210
& STEEL PLATES	Poisson's ratio v_0	0.3	0.3	0.3

[a] 50 % of the reported Young's modulus in experiment to account for overly-stiff behaviour
[b] Values deduced by preliminary calibration which are higher than the Mode-I fracture energy prescribed by MC2010 [16]

All slabs were characterised by a similar failure mechanism, wherein firstly flexural cracks appeared at the bottom face along the transverse and longitudinal reinforcements, followed by cracks due to a two way shear slab mechanism (punching shear failure) with a perimeter crack surrounding the loaded area, and eventually, the pure shear failure occured along the line support nearest to the loading plate (refer Figure 5.6). The failure was quite brittle, more so in the case of slab SC2 with compressive prestress, and these aspects of the experiment also fit well with the possibility to observe post peak brittle failures with SLA. Figure 5.8(a) shows the force displacement relations of the applied load at the loading plate vs deflection at LVDT position L5 (as shown in Figure 5.5(b)).

Finite Element Model   FE models of the RC Slab tests are made keeping in mind the constraints of SLA with regard to computational time. Consequently, only half the slabs are modelled because of the symmetry along the longitudinal direction. The loading plate and the support system of plates, to provide simple support all along the 4 sides, are

both of uniform thickness of 20 mm, and are provided linear elastic properties of steel. Both tensile and compressive softening possibilities (cracking and crushing) are provided to the concrete in the RC slab, and the material properties for the same are mentioned in Table 5.4. The steel plates and the slabs are discretised by 20-noded quadratic iso-parametric solid (brick) elements with translational degrees of freedom and a 3×3×3 Gaussian integration scheme. Linear interface elements are provided between the steel plate and the slab to provide uniform contact between the slabs and the support/loading plate, as is done by the neoprene layer in the experimental set-up. The number of elements in the direction of thickness (300 mm) is restricted to two, and the size of most elements in the model is approximately 100-150 mm. The reinforcements are modelled as an embedded system of bars and the constitutive behaviour is kept linear elastic since the reinforcement ratios are quite high to result in flexural failure. This was also confirmed in a sensitivity analysis wherein the stresses in the reinforcements did not exceed ~350 MPa. The FE model is as shown in Figure 5.7. Along the face of symmetry, the displacements along the X direction (longitudinal) are constrained (Figure 5.7(a)). The vertical support along Z axis is modelled using a single master node which is connected to the mid-line of the steel plate system (shown in yellow) using linear constraints as shown in Figure 5.7(b). Also, a node right in the middle of the support plate in the transverse direction is supported along the Y direction to avoid the corresponding rigid body mode. The concentrated load on the loading plate near the support is applied as a unit distributed pressure load, and axial loads of -1.5 MPa or 1.2 MPa (as the case may be) are applied on either ends of the slab. The modelling parameters and material properties pertaining to each of the three analyses (reported by Bui et al. 2017 [20], unless stated otherwise) are summarised in Table 5.4.
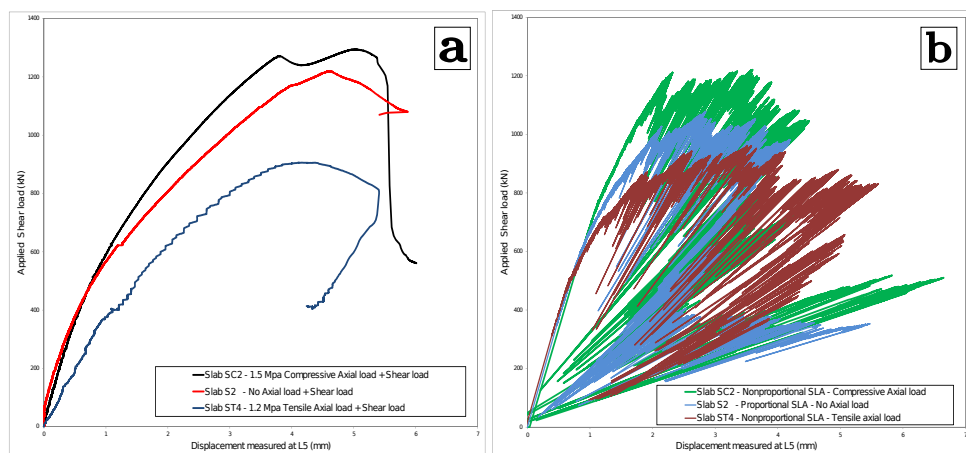

Figure 5.8: (a) Force displacement curves for Slabs S2, SC2 and ST4 from the experiments and (b) monotonic SLA simulations

Results & Discussion   All three considered cases show initial cracking followed by a phase of reduction in stiffness wherein the two way shear mechanism is observed to
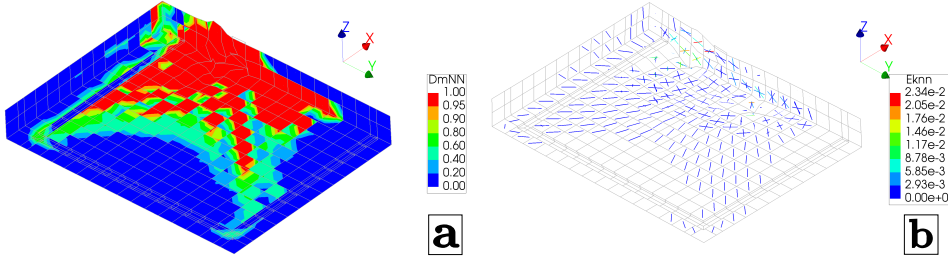
Figure 5.9: (a) Damage plots and (b) crack strain plots of half of slab S2's bottom face at the end of the brittle failure (Eknn denotes the normal crack strain)
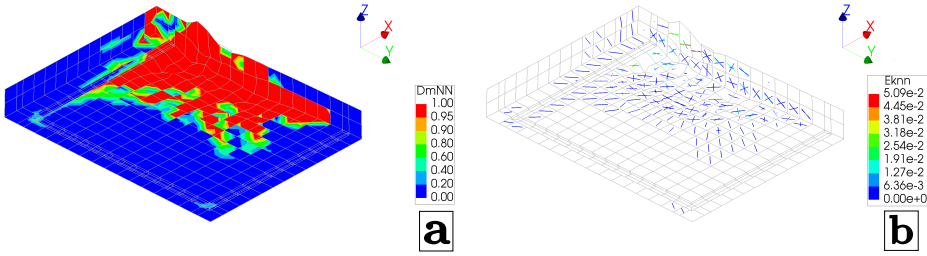

Figure 5.10: (a) Damage plots and (b) crack strain plots of half of slab SC2's bottom face at the end of the brittle failure (Eknn denotes the normal crack strain)
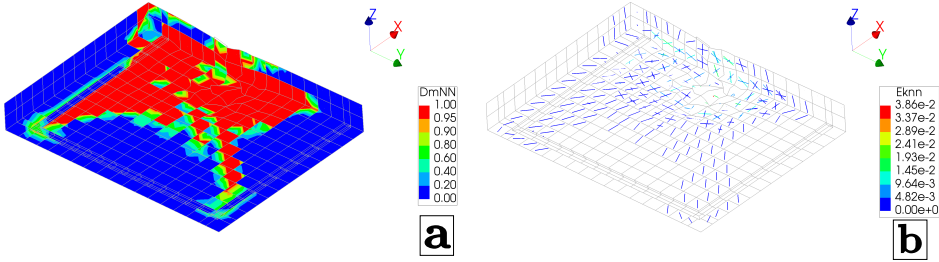

Figure 5.11: (a) Damage plots and (b) crack strain plots of half of slab ST4's bottom face at the end of the brittle failure (Eknn denotes the normal crack strain)

develop, before and around the peak load, culminating in the one way brittle failure beyond the peak load. The numerical results qualitatively agree well with the experiments in terms of increase in load capacity with axial compressive loads and the contrary decrease in load capacity with axial tensile loads, refer Figure 5.8(b). The crack patterns shown in Figures 5.9, 5.10 & 5.11 are all in reasonable agreement to the experimental crack patterns in Figure 5.6 in terms of the development of the shear crack perimeter zone, formed due to the diagonal compression strut from the loading plate. Simultaneously, in the same figures, damage in the first failure direction of the *nst* orthogonal crack

system expressed as $D = 1 - (E_{current}/E_{original})$, is also shown. DmNN = 0 and 1 in these plots refer to undamaged and fully damaged cases, respectively, in the n direction of the orthogonal crack system of an integration point. These plots correspond to the end of the brittle failures in the respective force displacement evolutions (yellow circular dots in Figures 5.12, 5.13 & 5.14).

Furthermore, it has to be pointed out that the Young's moduli of all three specimen have been reduced to 50 % of those reported in the experiments. With the original values of stiffness, an overly-stiff behaviour was observed regardless of the slab. This is also confirmed in the numerical simulations of the authors of the experimental campaign, using a concrete damage plasticity (CDP) model in combination with an explicit solver in the commercial FEA program ABAQUS [93], shown in Figure 5.12(a). The flexible mortar bedding layer between the steel reaction support system and the slab was pointed out to be the source of this discrepancy. The FE Model has an interface between the steel frame and the slab, but this also does not help simulating the flexible behaviour observed in the experiment. Accordingly, the decision to use reduced stiffness values was taken. However, despite reducing the stiffness, the force displacement relation of Slab ST4 in particular seems to still be a lot stiffer than the experimental response.

With regard to the experiments, the reduction in initial stiffness in the ST4 case, in comparison to slabs S2 and SC2, is in line with experimentally observed trend of decreasing initial elastic stiffness for increasing axial tensile loads for cases (Slabs ST1-ST4) [20]. But this lacks clarity and insight. SLA simulations do not show such a decrease in stiffness, as seen in Figure 5.8(b). Furthermore, the choice of two elements over the thickness was made keeping in mind the computational aspects of SLA as has been already mentioned. The mesh objectivity for this case study is illustrated using the SC2 case and is presented in Section 7.3.2, after the completion of the development of a tailor-made linear solver for SLA to circumvent high computation times for finer meshes. Shear locking as expected is not a problem due to the use of a lower shear retention factor.

The results are hereon presented individually (Figures 5.12, 5.13 & 5.14), in terms of damage patterns at the end of the brittle failures in each of the three cases corresponding to the respective force displacement curves. Firstly, the proportional loading case of slab S2 is considered. The monotonic SLA simulation, with only the concentrated load, shows a clear brittle failure post peak. Although the material model allows for compressive failure, 3D orthogonal multi-directional cracking becomes decisive leading up to the brittle failure. This is evident in the development of the diagonal tensile cracking from the loading area toward the support as shown in Figure 5.9(b). Figure 5.12(a) additionally shows two other responses. One of the same FE model (material & modelling parameters as well) simulated using a traditional implicit solver (with a Newton-Raphson iteration scheme that converges to an energy norm of 10^{-4}, and in combination with an arc-length control) in order to highlight the problems of non-convergence, and the other of a rather fine FE model with the CDP material model-based explicit solver response [93]. The post peak behaviour is rather well captured with the SLA procedure compared to the two responses. Similar NLFEA for the non-proportional cases are not done owing to triviality.

The aim of this study is to validate the 3D non-proportional loading in SLA. The performance in terms of delayed cracking in the compressive axial load case (SC2) and the reduced capacity in the tensile axial load case (ST4) exemplifies the approach. Both
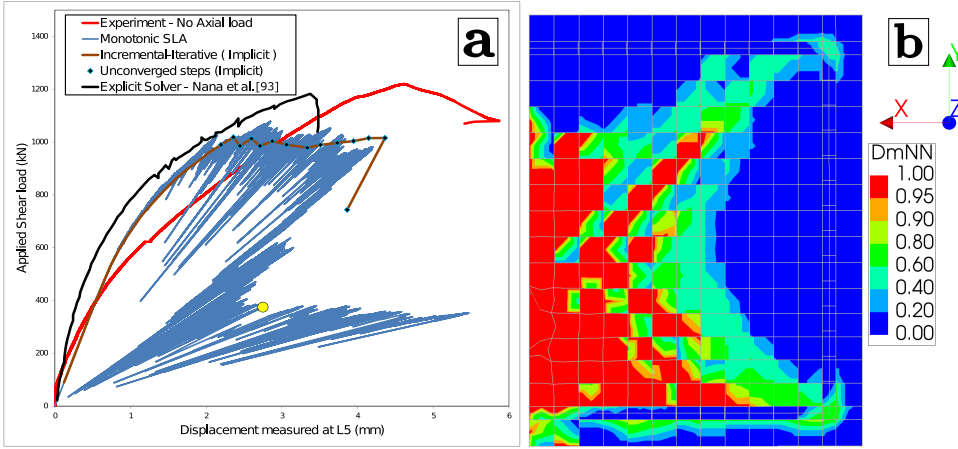
Figure 5.12: (a) Force displacement curves of the experiment vs proportional SLA - Slab S2, additionally also showing the response using the traditional incremental-iterative procedure(implicit) and the explicit solver [93], and a yellow circular dot denoting the reference point for end of brittle failure, and (b) the SLA damage plots of half of the slab at the reference point
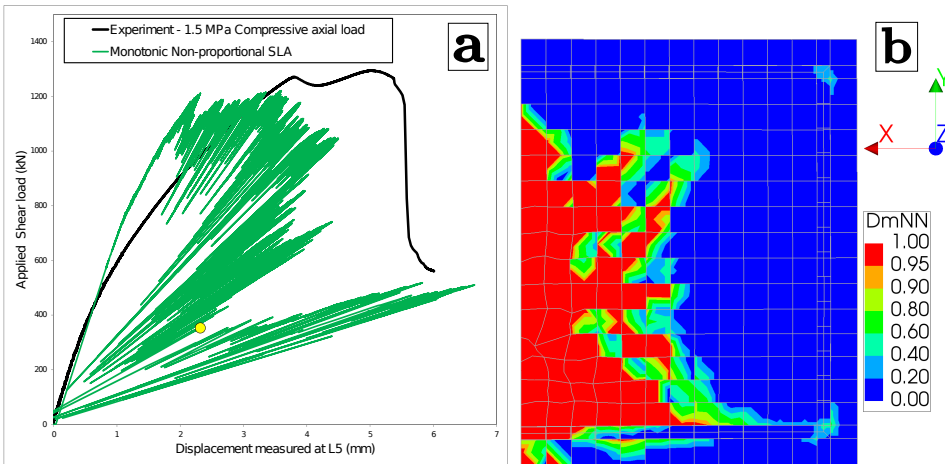
5

Figure 5.13: (a) Force displacement curves of the experiment vs non-proportional SLA (compressive prestress 1.5 MPa) - Slab SC2 and a yellow circular dot denoting the reference point for end of brittle failure, and (b) the SLA damage plots of half of the slab at the reference point

the slabs SC2 and ST4 show the brittle collapse post peak due to the shear failure involving 3D orthogonal multi-directional cracking. The damage plots are shown alongside the force displacement evolutions in Figures 5.13 & 5.14 in relation to the reference point at the end of the brittle failure. Additionally, the corresponding crack strain plots are shown in an isometric view in Figures 5.10(b) & 5.11(b) which show the multi-directional
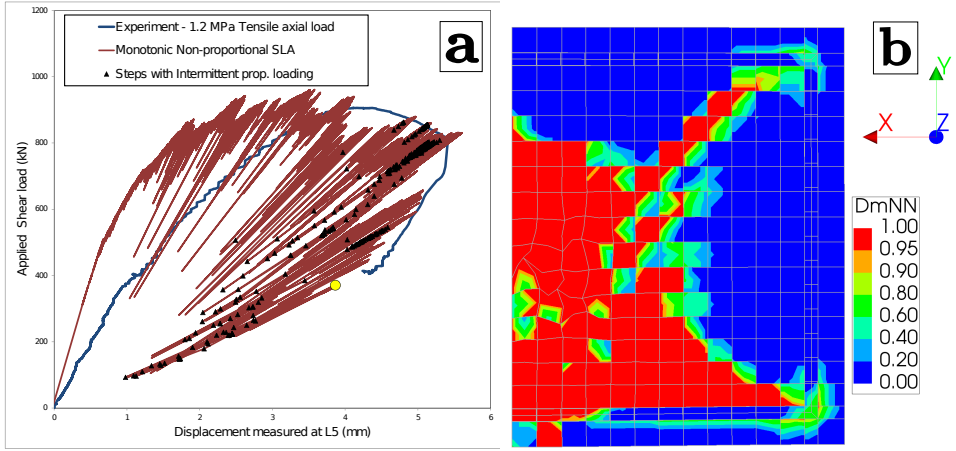
Figure 5.14: (a) Force displacement curves of the experiment vs non-proportional SLA (tensile prestress - 1.2 MPa) - Slab ST4 and a yellow circular dot denoting the reference point for end of brittle failure, and (b) the SLA damage plots of half of the slab at the reference point
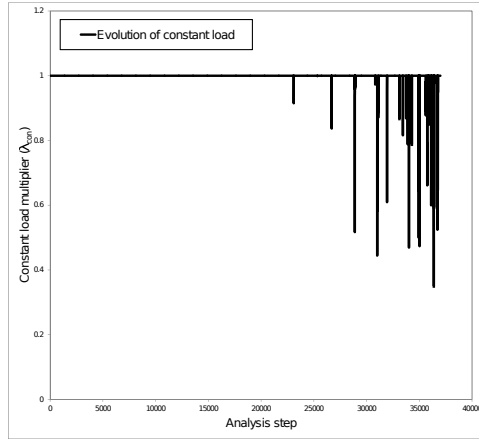

Figure 5.15: Evolution of constant load (tensile axial load - normalised) multiplier for the Slab ST4 case

cracking, the shear perimeter and the highly deformed failing elements. Slab ST4 in particular is reported to have a smaller shear crack perimeter than slabs S2 [20], because of having a steeper diagonal strut due to the applied axial tension, but those from the simulations do not differ much. However, the reported relative increase in the ductility of the slabs in the case of axial tensile loads (ST1-ST4) [20] is well captured in the SLA simulation of ST4.

With regard to the presented root finding algorithm for damage initiation in the 3D orthogonal fixed smeared cracking in this chapter, both slabs exhibit a small difference. Slab SC2, on the one hand, does not show any stress state all through the analysis involving

complex roots. While slab ST4 involves a few analysis steps where one or two of the un-damaged points' stress states yield complex roots. However, as explained in Section 5.3.3, these roots are not of significance, and hence do not affect the non-proportional loading strategy. The slabs SC2 and ST4 also exhibit another difference with respect to the redistribution related to the double-load multiplier approach outlined in Section 3.1. On the one hand, the constant load is maintained at its fullest value all through the analysis in the case of slab SC2, implying no need for redistribution by returning to the *intermittent proportional loading*. Contrarily, slab ST4's SLA simulations involve the redistribution strategy towards the end of the analysis, and this is exemplified in the evolution of the constant load multiplier as seen in Figure 5.15. However, there is no correlation between the observed 'one real root' case and the onset of redistribution in any of the steps resulting in the *intermittent proportional loading*. The need for such a redistribution in the quasi-static set-up of SLA under non-proportional loading has been touched upon in Chapter 4 for cases when the constant load continues to drop gradually to extremely low values, much ahead of the actual structural collapse, indicating alternative equilibrium paths as has been previously interpreted in Section 4.2. Nevertheless, in this case study of ST4, the constant load is restored to its full value after each set of these redistribution steps, happens around the actual expected structural collapse, and is therefore acceptable. Finally, although compressive nonlinearities are allowed in the material model, there were only few critical events involving compressive softening, and is therefore not discussed/shown here since it is not decisive in the development of the mechanism.

5.4.3. NON-PLANAR 3D CURVED CRACK EVOLUTION IN PLAIN CONCRETE: SKEW-NOTCHED PRESTRESSED BEAM

The two validation studies presented thus far illustrate the capability of the methodology to capture 3D cracks in an SLA set up. The smeared distribution of damage, typically observed in reinforced concrete behaviour, would camouflage the characteristic response of plain concrete fracture which is proven to be rather difficult to reproduce numerically. Therefore, modeling of 3D non-planar curved cracks, in unreinforced concrete structures is addressed in this section. 3D non planar crack propagation has been previously simulated by numerical techniques in literature [71, 52] but are mostly validated against experimental benchmarks like beams or cylindrical notched specimen loaded in torsion, 3-point and 4-point bending beams with eccentric/skewed notches, and wedge splitting tests to name a few, all of which are proportional loading cases. Owing to lack of experiments which are performed under non-proportional loading, an academic case study is considered in this section to illustrate the validity of the methodology. A three-point bending test, similar to the one presented in Section 5.4.1, is analysed. The beam measures 600 mm, 150 mm and 120 mm in span, depth and thickness, respectively. However, compared to the beam in Section 5.4.1, the depth of the notch is 30 mm, 5 mm wide and is skewed. The inclination of the notch with longitudinal axis of the beam is $\tan(\theta) = 0.5$, and a schematic representation of the same is shown in Figure 5.16(a). This beam is subject to an additional compressive axial prestress, similar to the first case study. This non-proportional case is used to further validate the proposed methodology by comparing against an NLFEA response (using an implicit solver).
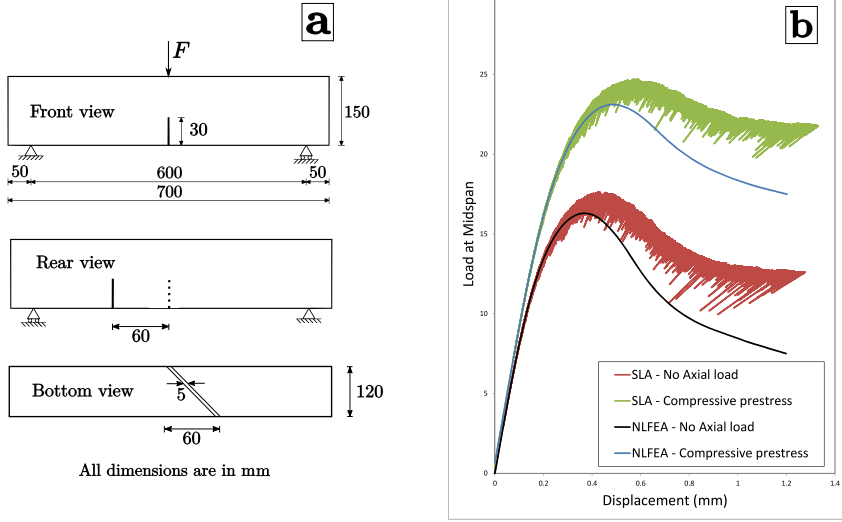
Figure 5.16: (a) Schematic representation of a 3 point bending test with a skewed notch - 30 mm deep and 5 mm wide, and (b) Force displacement curves of the SLA and NLFEA simulations

Finite Element Model   The FE model, shown in Figure 5.17(a), is made using 3-noded triangular iso-parametric solid (brick) elements, with translational degrees of freedom and a reduced 1-point Gaussian integration scheme. The choice of triangular elements was made to avoid mesh induced directional bias that would prove to be critical in achieving the curved non-planar crack. Since the framework is that of smeared cracking, additional crack tracking algorithms [131] could also help but this is not considered for the current study. Concrete has been modelled as a linear-elastic material everywhere except the middle part of the beam, containing the inclined notch, which is shown in dark blue, refer Figure 5.17(a). All elements in this middle region are approximately 7.5 mm in size or lower and are provided the possibility of tensile softening failure. All other elements shown in light blue are approximately 20 mm in size. Linear elements (those with linear interpolation shape functions) are used in order to ensure constant strain distribution over the entire element. The adopted saw-tooth law for the middle part of the beam has the same linear tension softening material model and parameters as mentioned in Table 5.3, except for a couple of differences. The shear retention and Poisson effects are both made damage based as explained in Section 5.1, and the crack bandwidth relates to the size of the element. The point load is assumed to be equivalent to a distributed line load applied as shown in Figure 5.17(a). The beam is additionally subject to a uniform compressive prestress, of magnitude 1.0 MPa, at the ends. Two SLA simulations are performed: One with only the bending load (proportional), and the other in combination with the prestress (non-proportional). The NLFEA simulations use the same parameters as their SLA counterparts except that the bending load is applied in displacement control, over 100 equal sized steps of magnitude 0.012 mm, with a Newton-Raphson iteration scheme that would converge to an energy norm of 0.0001.
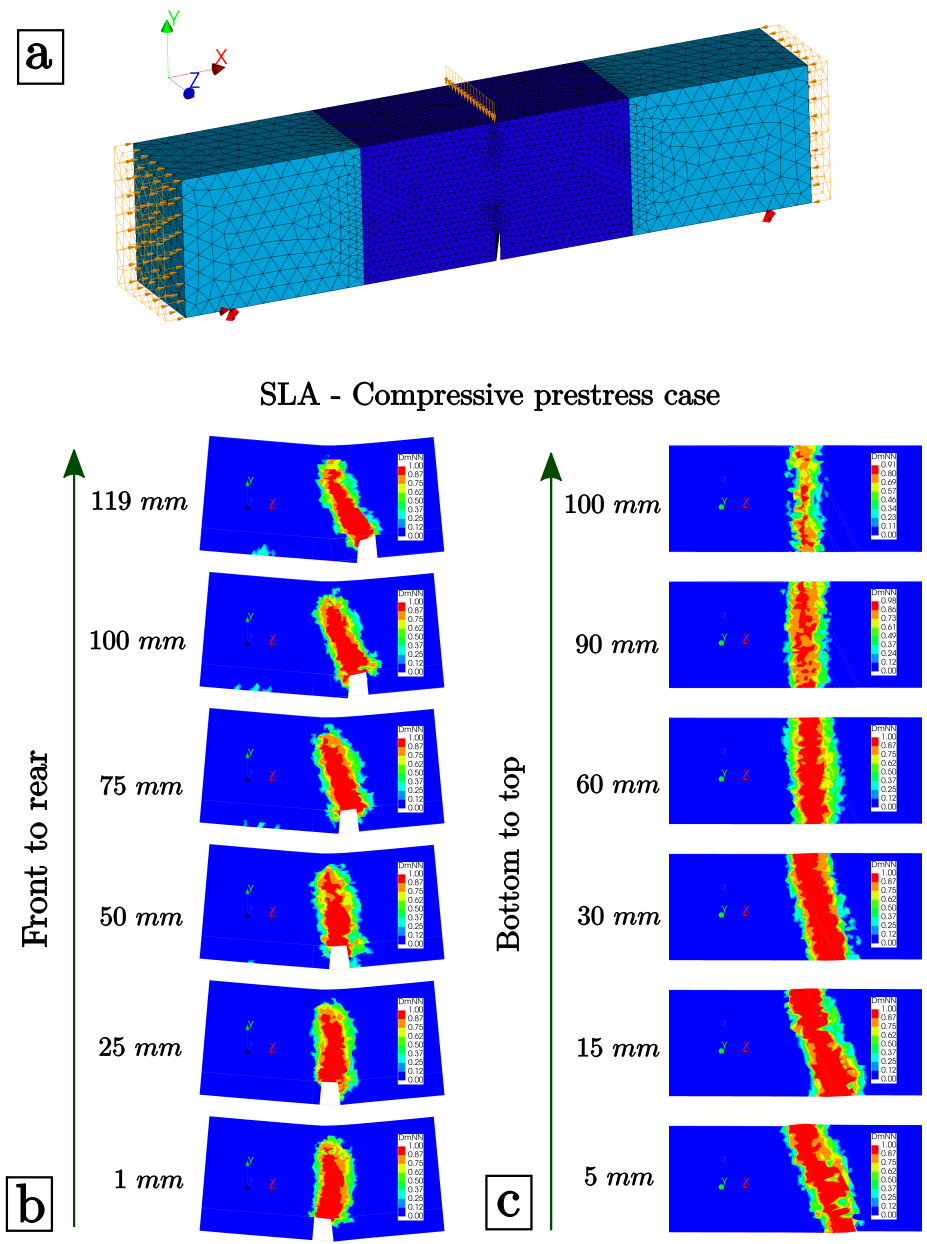
Figure 5.17: (a) FE model of the skew-notched beam case with axial loads, and damage plots for the prestress case using SLA shown as: (b) front views along XY plane slices at several distances from front to rear of the beam (along Z – thickness of the beam) and (c) bottom views along XZ plane slices at several distances top of the notch to top of the beam (along Y – height of the beam)

Results & Discussion   The results from SLA simulations of the both cases, with and without prestress, show the propagation of the 3D-curved tensile crack through the height in a non-planar fashion, resulting in the reduction of effective cross section of the beam. Since the purpose of the study is to validate the non-proportional loading strategy, only the prestress case results from SLA are presented in Figure 5.17(b) & (c). Herein, crack evolution is presented as damage plots for the middle portion of the beam (nonlinear material). In Figure 5.17(b), the plots correspond to the front view along XY plane slices at several distances from front to rear of the beam (along Z axis – thickness of the beam). It is clear how the crack is straight at the front end, and starts to incline towards the rear end indicating non-planarity about Z axis. In Figure 5.17(c), the bottom view along XZ plane splices at several distances from top of the notch to the top of the beam are shown (along Y axis – height of the beam). It is evident that the crack is inclined at the bottom, and starts to straighten towards the top of the beam indicating non-planarity about Y axis. YZ plane sections would not provide any new information. The results from NLFEA are in good agreement with those from SLA in terms of the twisted crack propagation and are therefore not shown.

The loss of cross section due to the crack propagation results in the loss of flexural capacity, and is eventually observed as the global softening in the force displacement curves shown in Figure 5.16(b). The presence of axial loads like the compressive prestress tends to delay the cracking, and consequently results in a higher capacity, which is well captured and qualitatively agrees to the expected response patterns from prestressed concrete theory. Additionally, it can also be observed that both SLA responses (with and without axial loads) match up reasonably well to those obtained from NLFEA as shown in Figure 5.16(b), thereby validating the 3D Non-proportional strategy. The difference in the post peak behavior is due to the higher strength properties used because of the ripple band approach in SLA, and the stress locking typical of fixed cracking. With regard to the solution obtained for undamaged integration points per analysis step, the non-proportional loading case yields 3 real roots always (though not necessarily positive). Additionally, the constant load i.e the compressive axial load, was kept constant throughout the analysis, and there was no need to return to the *intermittent proportional loading*.

5.5. Concluding remarks

This chapter contributes to extending sequentially linear analysis to 3D applications with non-proportional loading. Two approaches have been presented to determine the load multiplier per undamaged integration point, in a 3D stress state, for damage initiation under non-proportional loading in a smeared cracking framework. This in turn brings about a change from an isotropic to a 3D orthogonal damage formulation, with directions along those of the principal stresses at the onset of damage.

- The first approach involves deducing two cubic equations in the load multipliers (tension and compression failures), manipulating the equations into monic

trinomials, and subsequently, solving these depressed cubic equations using the Cardano method or trigonometric solutions, for one or three real roots respectively, depending on the discriminant of the equation.

- The second approach involves a reformulation of the case as an optimisation problem. The load multiplier is now expressed as a function of the inclination of a potential failure plane. The aim is to find solutions to the inclination of the critical plane, i.e the directional cosines, and consequently, determine the critical load multiplier. The second approach has previously been validated for 2D plane stress state. However, for 3D stress state it is shown to be computationally intensive, and also cannot guarantee solutions that match up to the analytical solution. The first approach is, therefore, preferred over the second for the validation studies, due to possibilities of loss of accuracy and computational efficiency reasons, but the validity of the concept as such remains.

The first concept is then validated against three case studies involving 3D stress states under non-proportional loading: A three point bending beam (notched) test example with compression and tensile prestress loads, an experimental campaign on the effect of axial loads on shear strength of RC slabs without shear reinforcement, and a three point bending beam (skewed notch) example with a compressive prestress load. In the first case, the increase and decrease in capacity of the beam with compressive and tensile prestress respectively, was well captured in the simulations. The second case of RC slabs also exhibited a similar trend in the shear strength capacity depending on the axial load applied, and also showed a good-to-reasonable agreement in terms of damage patterns, force displacement curves and the failure mechanism. The post peak brittle failure in all three cases was captured to good degree in SLA. In the third case, the increase in capacity of a bending beam (with a skewed notch) with additional compressive prestress was well captured in the SLA simulation along with a 3D non-planar curved crack. With regard to the analytical solution presented in this chapter, all non-proportional loading cases of the prestressed beam studies and RC slabs, except the tensile axial load case of ST4, always resulted in 3 real roots and the roots were rather easy to find in comparison to the SLTHNP optimisation approach. Even in the case of slab ST4, 99% of all stress states in the analysis yielded 3 real roots analytically. The 'one real root' case was sparsely observed but did not affect the non-proportional loading in any way. With regard to the redistribution strategy in SLA in returning to the *intermittent proportional loading*, all non-proportional case studies involved maintaining the constant load at its fullest value all through the analysis except in the ST4 slab case. But even in that case the redistribution was always followed by recovery of the full magnitude of the constant load and additionally, occured closer to the actual structural collapse which is acceptable. In conclusion, the case studies provide satisfactory results in terms of force displacement response and damage patterns, thereby proving the validity of the proposed 3D non-proportional loading strategy for continuum SLA applications.

COMPOSITE INTERFACE MODEL FOR SEQUENTIALLY LINEAR METHODS*

This Chapter proposes an extension of the discretised tension-shear model for interfaces, suitable for sequentially linear methods [139], with a simplified compression cap criterion. This enables simulation of combined cracking-crushing-shearing failure possibilities typical of damage in masonry. The formulation for two-dimensional (2D) line interfaces including the tension cut-off, Coulomb friction, and compression cap criteria is detailed in Section 6.2.1, followed by the three-dimensional (3D) planar interface formulation in Section 6.2.2. The applicability of the formulations are illustrated using 2D and 3D models of a pushover analysis on a squat unreinforced masonry wall in Section 6.3. The simulations are made using both Sequentially Linear Analysis (SLA) and the Force-Release method.

6.1. MOTIVATION

Zero-thickness interface elements are used in standard finite element (FE) analysis to represent displacement discontinuities, for e.g. in plain and reinforced concrete applications to simulate cracking and bond slip failures. In masonry structures, global failure mechanisms generally comprise rocking, shear sliding, and diagonal shear failures, or combinations thereof, which in turn involve a wide range of local mechanisms including cracking and slipping of joints, cracking under direct or diagonal tension of brick units, and masonry crushing at the toe of a rocking pier. Standard homogenised continuum representation of all such failure possibilities is possible [84] but at the expense of additional assumptions and is, furthermore, known to cause convergence issues in the traditional implicit NLFEA setup. Alternatively, the micro-modelling strategy [32, 82] has been employed by differentiating the continuum into linear elastic bricks and potential failure planes represented by interface elements: along head and bed joints, and additionally, a potential brick cracking plane. These nonlinear failure planes allow for a discontinuous jump in the displacement field from one course of brick to the other which is characteristic of masonry failure. The commonly used constitutive framework is the *composite-interface formulation* [83] under a traditional NLFEA set-up, which allows for combined cracking-crushing-shearing failures in discrete interface elements. However, the ultimate collapse, most often involving crushing, is intrinsically brittle and difficult to simulate due to convergence issues. This could therefore be addressed using numerically robust solution procedures such as the sequentially linear methods. To this end, the step-wise secant Coulomb friction formulation of Van de Graaf [139] needs a compression cap criterion to allow for all 3 failures: cracking, shearing and crushing.

---

*This Chapter is based on the author's article submitted to *Engineering Structures*.

6.2. Constitutive model & workflow

A composite-interface formulation is proposed in this study, shown in Figure 6.1, to be used in conjunction with the sequentially linear framework. The tension-cut-off criterion is coupled with a uniaxial tension softening law. The compression-cap could be given an elliptical shape but is simplified herein as a cut-off criterion, dependent purely on the normal traction, coupled with a uniaxial hardening-softening law (referred to as the parabolic softening law [49, 51] hereon). Step-wise secant saw-tooth laws address these uniaxial material behavior. Finally, the Coulomb friction criterion which involves multiple stress and/or deformation components requires a more sophisticated approach for use in sequentially linear methods such as the SLA. In this regard, step-wise secant Coulomb friction laws proposed by Van de Graaf [139] for SLA, briefly reviewed in Section 2.3.1, are used herein. The sub-variant which decouples the tension and shear modes is the formulation considered in this study. The dilatancy effects are neglected because of no coupling, i.e the dilatancy angle $\psi = 0$, an assumption that yields good results for masonry structures in general [32, 144] and also using SLA [139].

The loading is considered to be non-proportional, and for a system loaded by constant loads (L_{con}) and a unit variable load (L_{var}), the tractions corresponding to normal (subscript n) and shear directions (subscripts t and s) are expressed as the superposition of the tractions due to the constant and scaled variable loads as shown in Eq. 6.1 for each integration point i. The governing stress, as the failure type may be, is then limited by the allowable strength corresponding to the failure criterion.

$$
\begin{aligned}
t_{n,i} &= t_{n,i\,\mathrm{con}} + \lambda \; t_{n,i\,\mathrm{var}} \\
t_{t,i} &= t_{t,i\,\mathrm{con}} + \lambda \; t_{t,i\,\mathrm{var}} \\
t_{s,i} &= t_{s,i\,\mathrm{con}} + \lambda \; t_{s,i\,\mathrm{var}}
\end{aligned}
\tag{6.1}
$$

In this section, both the 2D and 3D formulations are outlined for the different failure types in regard to the following aspects:

- Determination of the load multipliers per integration point in the FE model : λ_i^{shr}, λ_i^{ten} and λ_i^{cmp} corresponding to the shear, tension and compression failures, and the identification of the critical integration point $\lambda_{\mathrm{crit},i}$ and failure mode.

- Updating the stiffness of the critical integration point based on the failure mode.

6.2.1. Line Interfaces formulation (2D)

In the 2D interface formulation, at the linear elastic stage, the interface tractions t_n and t_t are related to the corresponding normal and shear relative displacements $u_n{}^\dagger$ and $u_t{}^\dagger$ by means of the uncoupled constitutive secant matrix $\mathbf{D}_{\mathrm{sec}}$ (with an undamaged normal stiffness $k_{n,0}$ and shear stiffness $k_{t,0}$) in the following way.

$$
\begin{bmatrix} t_n \\ t_t \end{bmatrix} = \begin{bmatrix} k_{n,0} & 0 \\ 0 & k_{t,0} \end{bmatrix} \begin{bmatrix} u_n \\ u_t \end{bmatrix}
\tag{6.2}
$$

---

†The Δ symbol, commonly used to denote *relative* displacements in interface formulations, is dropped herein to avoid ambiguity with the variations of the said relative displacements used in the *stiffness update* subsection

CRITICAL LOAD MULTIPLIER

Shear mode Considering initial cohesion c_0 and the yield criterion $|t_t| = -t_n \tan(\phi) + c_0$, the load multiplier for shearing failure per integration point i is defined as shown in Eq. 6.3, where $\tan(\phi)$ is the friction coefficient.

$$\left(|t_{t,i\,\mathrm{con}} + \lambda_i \; t_{t,i\,\mathrm{var}}| \right) + \left(t_{n,i\,\mathrm{con}} + \lambda_i \; t_{n,i\,\mathrm{var}} \right) \tan(\phi) \leq c_0 \qquad (6.3)$$

Cohesion softening is considered for this study, and therefore the determination of the load multiplier per integration point is not equivalent to solving Eq. 6.3. This is because the mobilised cohesion c, in addition to being dependent on the plasticity parameter κ (assumed to be equal to the largest plastic relative shear displacement in the absolute sense [82]), becomes dependent on the load multiplier λ as shown in Eq. 6.4, where G_f^{II} is the mode-II fracture energy.

$$c(\kappa, \lambda) = c_0 \exp\left(-\frac{c_0}{G_f^{\mathrm{II}}} \kappa \right)$$

$$\kappa = \max |u_t^{\mathrm{pl}}| \qquad (6.4)$$

Therefore, the load multiplier is deduced in the following way:

1. Evaluate load multipliers λ_{c_0} and λ_0, corresponding to states of initial cohesion and zero cohesion, as follows:

$$\left(|t_{t,i\,\mathrm{con}} + \lambda_{c_0} \; t_{t,i\,\mathrm{var}}| \right) + \left(t_{n,i\,\mathrm{con}} + \lambda_{c_0} \; t_{n,i\,\mathrm{var}} \right) \tan(\phi) \leq c_0 \qquad (6.5a)$$

$$\left(|t_{t,i\,\mathrm{con}} + \lambda_0 \; t_{t,i\,\mathrm{var}}| \right) + \left(t_{n,i\,\mathrm{con}} + \lambda_0 \; t_{n,i\,\mathrm{var}} \right) \tan(\phi) \leq 0 \qquad (6.5b)$$

2. Perform a bisection between λ_{c_0} and λ_0 to find an initial root, and then refine it using a Newton-Raphson scheme to arrive at the load multiplier λ_i^{shr} for shear failure, such that the integration point i lies on the shifted Coulomb surface (Figure 6.1), i.e. the normalised yield lies below a user specified tolerance β as shown in Eq. 6.6.

$$\frac{\left(|t_{t,i\,\mathrm{con}} + \lambda_i^{\mathrm{shr}} \; t_{t,i\,\mathrm{var}}| \right) + \left(t_{n,i\,\mathrm{con}} + \lambda_i^{\mathrm{shr}} \; t_{n,i\,\mathrm{var}} \right) \tan(\phi) - c}{c_0} \leq \beta \qquad (6.6)$$

The friction coefficient is assumed to be constant i.e. friction softening is neglected. Note that in case the cohesion softening is absent, λ_i^{shr} can be calculated according to Eq. 6.5(a).

Tension mode The load multiplier for tensile cracking is as shown in Eq. 6.7, where f_t is the current tensile strength based on a predefined saw-tooth law, or on a stress-strain relation evolving during analysis with *user specified* relative displacement increments and the corresponding traction decrements [139] as shown in Figure 6.2(a).

$$\left(t_{n,i\,\mathrm{con}} + \lambda_i^{\mathrm{ten}} \; t_{n,i\,\mathrm{var}} \right) \leq f_t \qquad (6.7)$$
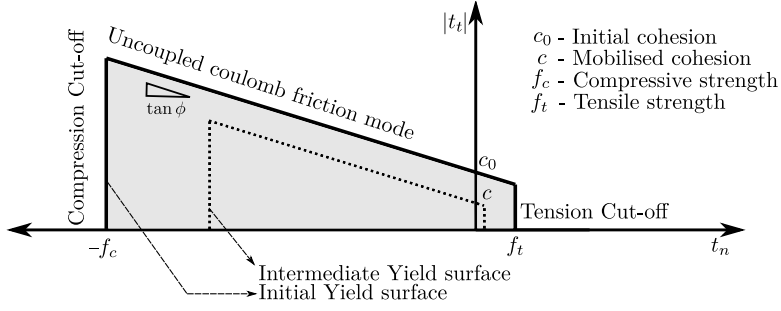
Figure 6.1: Failure surface for the 2D line interfaces

Compression mode   The load multiplier for crushing failure is as shown in Eq. 6.8, where f_c is the current compressive strength based on a predefined parabolic softening saw-tooth law as shown in Figure 6.2(c). The failure criterion for compression in the original composite interface formulation for masonry [82] is an ellipsoid cap model that depends on the normal and shear stresses through a set of material parameters. However, for simplicity, this is herein treated as a straight shear-independent cut-off criterion. This approach is reasonably accurate and also fits well with material parameters such as the compressive strength f_c and fracture energy G_c, which are widely used in engineering practice for e.g. in a simple Rankine-type failure surface for the total strain based smeared cracking models.

$$\left(t_{n,i\,\mathrm{con}} + \lambda_i^{\mathrm{cmp}}\, t_{n,i\,\mathrm{var}} \right) \geq -f_c \tag{6.8}$$

The critical load multiplier is then determined as the minimum of all the load multipliers.

$$\lambda_{\mathrm{crit}} = \min_i \left(\lambda_i^{\mathrm{shr}}, \lambda_i^{\mathrm{ten}}, \lambda_i^{\mathrm{cmp}} \right) \tag{6.9}$$

STIFFNESS UPDATE

Once the critical integration point is identified, the stiffness matrix is degraded based on the failure mode as detailed in the following.

Shear mode   The shear failure involves update to *only* the shear stiffness term of the uncoupled constitutive matrix $\mathbf{D}_{\mathrm{sec}}$, which is defined for the jth linear analysis or step as follows

$$\mathbf{D}_{\mathrm{sec}}^{(j)} = \begin{bmatrix} k_n^{(j)} & 0 \\ 0 & k_t^{(j)} \end{bmatrix} \tag{6.10}$$

$$k_t^{(j)} = \frac{t_{t,\mathrm{crit}}^{(j-1)}}{u_{t,\mathrm{crit}}^{(j-1)} + \delta u_t^{(j-1)}} \ \ \text{with} \ \ \delta u_t^{(j-1)} = a_t u_{t,\mathrm{crit}}^{(j-1)} \tag{6.11}$$

The update to the shear stiffness is computed during the analysis, as shown in Eq. 6.11, with the critical shear traction $t_{t,\text{crit}}^{(j-1)}$ and the critical relative shear displacement $u_{t,\text{crit}}^{(j-1)}$ of the completed $(j-1)^{\text{th}}$ step, and additionally, a specified relative shear displacement increment $\delta u_t^{(j-1)}$ which is based on a user defined factor a_t. This factor is similar to the saw-tooth band width ripple factor p, as in Figure 2.2, and is used for discretising the constitutive behavior. The updated shear stiffness $k_t^{(j)}$ therefore corresponds to the increased shear displacement $(1 + a_t) u_{t,\text{crit}}^{(j-1)}$, and is a prediction that is exact *only* if the actual shear displacement in the subsequent step will equal the specified increased shear displacement. This way of updating stiffness during an ongoing analysis is merely an alternative approach to the a priori definition of saw-tooth laws. This is also shown in the cohesion softening law evolving 'during' analysis in Figure 6.2(b), wherein subscripts r for the shear stiffness k_t refer to the subsequent saw teeth number in the softening law (not to be confused with analysis step j).The effect of larger values of the user defined factor a_t was previously shown to result in a saw-tooth (coarser) type response in the force displacement evolution, due to the approximate stiffness guess, for a shear study on bricks under confinement [139].

Tension and Compression modes   Both the cracking and crushing failures consider the normal traction for damage initiation and propagation. Accordingly, both failures involve update to the normal stiffness term of the uncoupled constitutive matrix $\mathbf{D}_{\text{sec}}$, shown in Eq. 6.10, based on predefined saw-tooth laws. For tensile cracking, linear tension softening relations are approximated as the predefined band width ripple type saw-tooth law shown in Figure 2.2. Alternatively, similar to the cohesion softening law evolving during analysis, the normal stiffness updates can be made on the basis of a specified normal relative displacement increment $\delta u_{n,r}$ and an associated drop in normal traction $\delta t_{n,r}$ for the current saw-teeth number r as shown in Figure 6.2(a). For compressive failures, the band width ripple version of the parabolic hardening-softening relation shown in Figure 6.2(c) is used.

Furthermore, the shear stiffness is also damaged in both cases as shown in Eq. 6.12, where $k_{n,0}$ and $k_{t,0}$ are the undamaged normal and shear stiffnesses. However, if the current shear stiffness $k_t^{(j-1)}$ at the end of the completed analysis step $(j-1)$ is lesser than the computed $k_t^{(j)}$, the shear stiffness is not degraded any further.

$$k_t^{(j)} = k_{t,0} \frac{k_n^{(j)}}{k_{n,0}} \tag{6.12}$$

The original composite interface model [82] was plasticity-based, i.e. with elastic unloading/reloading. In contrast, the proposed model has secant unloading/reloading for all modes. This better fits quasi-brittle materials particularly in relation to discrete cracking. This is because elastic unloading of fully open tensile cracks, as in the original formulation, could result in an overly-stiff behaviour which is not desirable. In this sense, the proposed model is advantageous. However, the use of a total approach may result in inappropriate crack-closure effects under redistribution, with carry over of damaged stiffness between stress regimes.
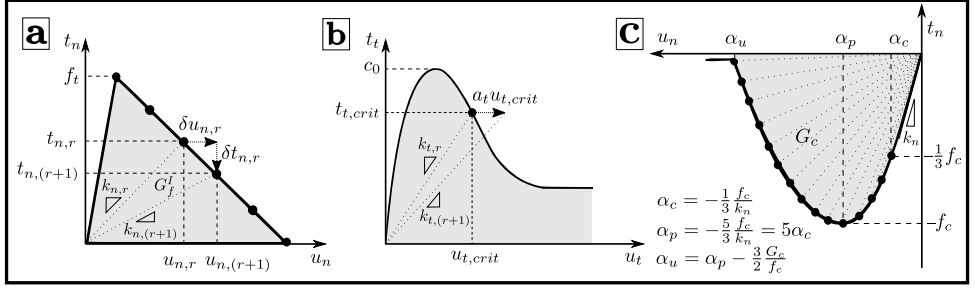
Figure 6.2: (a) Linear tension softening law evolving 'during' analysis with user specified relative normal displacement increments, (b) cohesion softening law deduced 'during' analysis with user specified relative shear displacement increments, and (c) pre-defined parabolic hardening-softening saw-tooth law for compression [49]. Studies in this chapter use (b) as such for the shear mode, while predefined band width ripple versions of (a)&(c) (Figure 2.2) are used for the tension and compression modes.

6.2.2. PLANAR INTERFACES FORMULATION (3D)

In the 3D interface formulation, at the linear elastic stage, the interface tractions t_n, t_t and t_s are related to the corresponding normal and shear relative displacements u_n, u_t and u_s respectively by means of the uncoupled constitutive secant matrix $\mathbf{D}_{\text{sec}}$ (with undamaged normal stiffness $k_{n,0}$ and shear stiffnesses $k_{t,0}$ & $k_{s,0}$) in the following way.

$$\begin{bmatrix} t_n \\ t_t \\ t_s \end{bmatrix} = \begin{bmatrix} k_{n,0} & 0 & 0 \\ 0 & k_{t,0} & 0 \\ 0 & 0 & k_{s,0} \end{bmatrix} \begin{bmatrix} u_n \\ u_t \\ u_s \end{bmatrix} \tag{6.13}$$

CRITICAL LOAD MULTIPLIER

The load multiplier definition for the tension and compression failure modes for the 3D planar interfaces are the same as those for the 2D case, as shown in Eq. 6.7 & 6.8, since the cracking or crushing initiation and propagation depends on the normal traction t_n. However, with regard to the shear failure mode in planar interfaces, the yield criterion for an integration point i is governed by the effective shear stress [143] which is defined as follows.

$$t_{eff} = -t_n \tan(\phi) + c_0$$
$$\text{where} \quad t_{eff} = \sqrt{t_{t,i}^2 + t_{s,i}^2} \tag{6.14}$$

Accordingly, the plasticity parameter κ is also expressed as the effective plastic shear relative displacement in the following manner.

$$u_{t.eff}^{\text{pl}} = \sqrt{u_t^{\text{pl}2} + u_s^{\text{pl}2}} \tag{6.15}$$

Rest of the workflow to determine the load multiplier for shear failure is similar to the 2D formulation, wherein equations Eq. 6.3-6.6 hold with the appropriate effective shear stress and the effective plastic shear relative displacement. The critical load multiplier is

then deduced according to Eq. 6.9, and the stiffness update for the corresponding failure mode is carried out as explained in the following subsection.
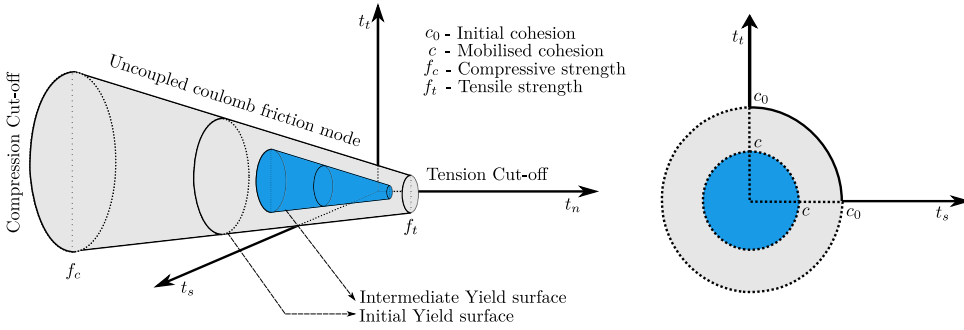

Figure 6.3: Failure surface for the 3D planar interfaces

STIFFNESS UPDATE

Shear mode Similar to the 2D formulation, the shear failure involves update to the shear stiffness terms of the 3D uncoupled constitutive matrix $\mathbf{D}_{\text{sec}}$ in Eq. 6.16. Both the shear stiffnesses are calculated based on user-specified relative shear displacement increments $\delta u_t^{(j-1)}$ and $\delta u_s^{(j-1)}$, which now require two user defined factors a_t and a_s, during an ongoing analysis step j as shown in Eq. 6.17.

$$\mathbf{D}_{\text{sec}}^{(j)} = \begin{bmatrix} k_n^{(j)} & 0 & 0 \\ 0 & k_t^{(j)} & 0 \\ 0 & 0 & k_s^{(j)} \end{bmatrix} \tag{6.16}$$

$$k_t^{(j)} = \frac{t_{t,\text{crit}}^{(j-1)}}{u_{t,\text{crit}}^{(j-1)} + \delta u_t^{(j-1)}} \text{ with } \delta u_t^{(j-1)} = a_t u_{t,\text{crit}}^{(j-1)}$$

$$k_s^{(j)} = \frac{t_{s,\text{crit}}^{(j-1)}}{u_{s,\text{crit}}^{(j-1)} + \delta u_s^{(j-1)}} \text{ with } \delta u_s^{(j-1)} = a_s u_{s,\text{crit}}^{(j-1)} \tag{6.17}$$

Tension and Compression modes The update to the normal stiffness in case of cracking and crushing failures, involves resorting to the predefined or evolving tension and compression softening saw-teeth relations, again similar to the 2D formulation. However, in addition to the update to normal stiffness, the shear stiffness is damaged along both shear directions as shown in Eq. 6.18, unless the current shear stiffnesses $k_t^{(j-1)}$ and $k_s^{(j-1)}$ at the end of the completed analysis step $(j-1)$ are lesser than the newly computed $k_t^{(j)}$ and $k_s^{(j)}$.

$$k_t^{(j)} = k_{t,0} \frac{k_n^{(j)}}{k_{n,0}}$$

$$k_s^{(j)} = k_{s,0} \frac{k_n^{(j)}}{k_{n,0}}$$

(6.18)

6.3. ILLUSTRATION : PUSHOVER ANALYSIS OF A MASONRY WALL

Experiment   In this section, the experiment on a solid clay brick masonry wall tested by Raijmakers and Vermeltfoort [113, 114] is used as a benchmark to validate the 2D and 3D composite interface formulations presented in this chapter. The wall was made of 18 courses of bricks, with dimensions of 210 mm×52 mm×100 mm, and mortar layers of 10 mm thickness. The dimensions of the wall are as shown in Figure 6.4(a), based on the 18 courses of bricks, resulting in an approximate effective width/height ratio of one. The top and bottom courses of bricks were clamped to a steel beam to constrain the rotation along both edges, additionally preventing the free vertical movement of the top edge. The walls were loaded initially by an overburden pressure of 0.30 N/mm$^2 \triangleq$ 30 kN, followed by a monotonically increasing lateral load d applied under displacement control. The force displacement evolution and damage patterns of two such walls (namely J4D and J5D) are shown in Figure 6.6 and Figure 6.4(b),(c) respectively. The damage in both walls begins with a rocking type failure i.e. cracks developing along the top and bottom of the wall. This is followed by a diagonal stepped crack which leads to the failure mechanism, simultaneously with cracks in the bricks and crushing of the compressed toes of the wall. Such a mechanism and the availability of data on material properties, including fracture energies from small-scale companion tests, makes this an ideal benchmark considering the scope of the proposed composite interface formulations.
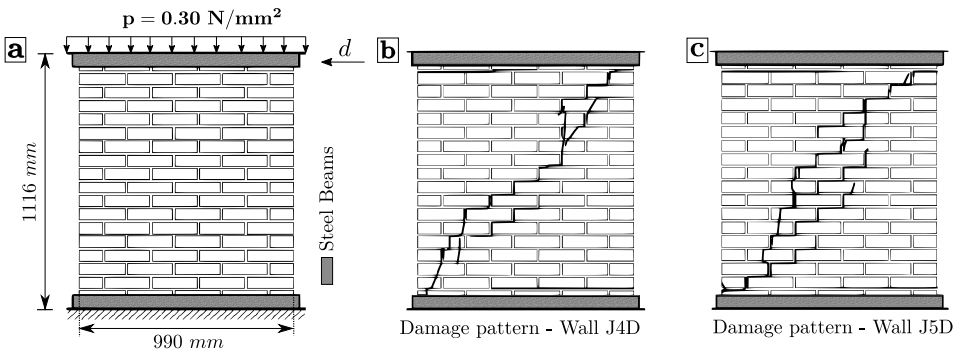

Figure 6.4: (a) Schematic representation of solids clay brick masonry walls (J4D & J5D) loaded firstly by an overburden pressure of 0.30 N/mm^2 followed by a lateral prescribed displacement d, and the experimental crack patterns of the walls (b) J4D and (c) J5D

6.3.1. 2D LINE INTERFACE MICRO-MODEL

Finite Element Model The walls are discretised using the simplified micro-modelling strategy [32, 82], wherein mortar joints and the brick-mortar interfaces are lumped together into a zero-thickness interface, and the bricks are extended to account for the mortar thickness. The bricks are modelled using 4-noded iso-parametric plane stress elements, roughly 27.5 mm×27.5 mm in size, with linear interpolation shape functions and a 2×2 Gaussian integration scheme. The zero-thickness interfaces are modelled using 2+2 noded interface elements, allowing for 2 in-plane translational degrees of freedom (DOFs) per node, in conjunction with a 2-point Newton-Cotes integration scheme. All DOFs along the bottom edge of the wall are fully constrained, while the top edge is prevented against any rotation. The nodes along the top edge of the wall are given an initial vertical displacement 0.083 mm, which is the imposed displacement equivalent to an overburden pressure of 0.30 N/mm^2. Subsequently, a lateral displacement is imposed on the top edge to simulate the lateral load.
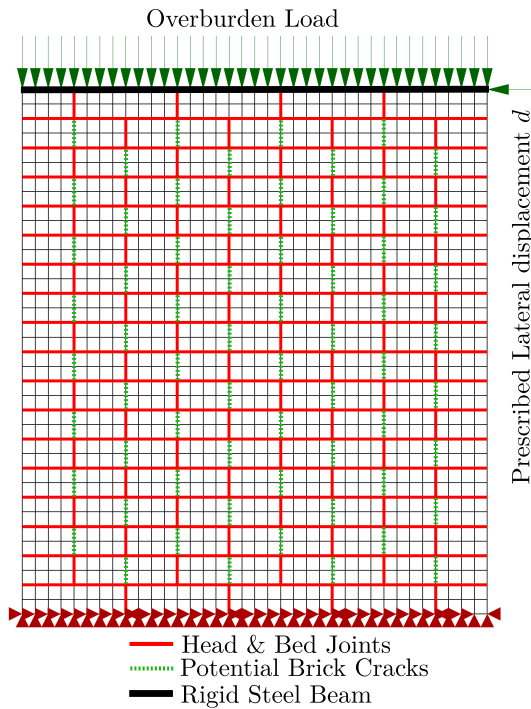
Figure 6.5: 2D Finite element micro model of the solid clay brick wall subject to overburden & pushover loads

The FE model shown in Figure 6.5 includes interfaces along the head and bed joints, and additionally, along the mid-length of bricks to simulate vertical brick cracks. The 2D composite line interface formulation presented in this chapter is the adopted constitutive model, and all head & bed joints are lumped with the nonlinearities of tensile cracking, crushing and shearing, with material parameters as shown in Tables 6.1&6.2. The predefined band width ripple based linear tension softening and parabolic compres-

Table 6.1: Elastic modelling parameters - J4D & J5D walls: based on References [113, 114, 82]

Masonry Units	Parameters	Elastic
Bricks	Young's Modulus E_0 [GPa]	16.7
	Poisson's ratio v_0	0.15
Head & Bed Joints	Normal stiffness k_n [N/mm^3]	82
	Shear stiffness k_t [N/mm^3]	36
Brick Cracks	Normal stiffness k_n [N/mm^3]	10^6
	Shear stiffness k_t [N/mm^3]	10^6

Table 6.2: Inelastic modelling parameters based on References [113, 114, 82] (except compression)

Masonry Units	Parameters	Compression	Tension	Shear
Head & Bed Joints	Strength f_t, f_c, c_0 [MPa]	6.0	0.25	0.35
	Fracture energy G_c, G_f^I, G_f^{II} [N/mm]	1.8	0.018	0.125
	Saw-teeth discretisation factor	0.1	0.15	0.05
	Softening relation	Parabolic	Linear	Exponential
	Shear retention factor β	Damage-based [132]	Damage-based [132]	-
Bricks Cracks	Tensile Strength f_t [MPa]		2	
	Fracture energy G_f^I [N/mm]		0.08	
	Saw-teeth discretisation factor		0.2	
	Softening relation		Linear	
	Shear retention factor β		Damage-based [132]	

6

sion hardening-softening saw-tooth laws are used. The properties for compression are reduced in comparison to those used in Reference [82], by means of a sensitivity study, to fit the experimental results. This is also motivated by the use of a straight cap (cut-off) criterion instead of the elliptical cap for compression failure. For the decoupled Coulomb friction failure mode, a user specified discretisation factor of $a_t = 0.05$ for the specified relative shear displacement, as in Eq. 6.11, is used. Vertical interfaces are included in the middle of the bricks, with only the discrete cracking possibility while omitting the shear & compression failures, in accordance to previous studies in References [83, 139]. Additionally, the overall brick behaviour and the vertical brick-crack joints along the bottom and top-most course of bricks in particular, which are attached to the stiff steel beams, are kept linear elastic with material parameters as shown in Table 6.1.

RESULTS & DISCUSSION

Firstly, the performance of the micro-model with the full composite interface formulation, i.e. discrete cracking, shearing and crushing in the interfaces, is analysed. This is treated as the reference case and is referred to as the *discrete-crushing* model hereon. The force-displacement evolution for this pushover study, shown in Figure 6.6, shows good qualitative agreement with the experimental responses of walls J4D and J5D, in terms of the peak loads, and the global softening behaviour that leads to loss of lateral capacity. The deformed profile and damage propagation in the masonry are summarised for the SLA simulation of this model in Figure 6.7 at 2 mm and 4 mm prescribed lateral top displacements. The damage plots DmTeNN and DmCoNN indicate loss of normal stiffness due to cracking and crushing respectively. The DmTeSS damage plots indicate loss of shear stiffness which is either due to a pure-sliding failure or the damage based shear reduction associated with the cracking/crushing modes. All damage plots herein range
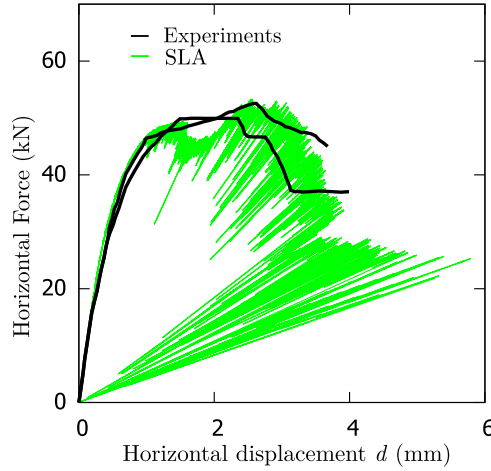
Figure 6.6: Force-displacement curves of the experiments compared against those of SLA for the reference *discrete-crushing* micro model : with discrete cracking, shearing and crushing in interfaces

from 0 to 1 which refer to undamaged and fully damaged cases for the corresponding failure criteria.

The wall firstly exhibits flexural failure which is visible as horizontal cracks along bed joints at the bottom-right and top-left corners of the wall. After the flexural cracks are fully developed (before 2 mm top displacement), compressive strut action results in a staggered step-like crack along the diagonal to the toe (left bottom corner) of the wall. This damage propagation includes both sliding failure along the bed joints, resulting in loss of shear stiffness, and tensile cracking along head joints, resulting in loss of both normal and shear stiffnesses. The fully developed flexural cracks and propagating diagonal step cracks at 2 mm top displacement are shown as tensile cracking and shear failure plots in Figure 6.7. Furthermore, the stress flow into the toe of the wall leads to the onset of the crushing failure, which can be seen as loss of normal stiffness in the crushing plots of Figure 6.7.

Upon further increase of the lateral displacement to 4 mm, the damage along the diagonal shear crack increases and localises, leading to a widening of the head joints and simultaneous sliding along bed joints, along the diagonal of the wall. Furthermore, the stepped crack also involves vertical splitting cracks through the bricks along the courses at mid-height of the wall, which often appear as sudden drops/instabilities in traditional NLFEA [82]. This is adequately captured by SLA. Simultaneously, the toe of the wall is completely crushed along half the length of an entire brick. This results in a clear drop of lateral capacity which is observed in the force-displacement curve, indicating failure.

The performance of the model can also be assessed based on the development of the vertical reaction forces, and its eccentricity with respect to the center line of the wall. The comparison of these aspects with the experiments is shown in Figure 6.11. Firstly, the general trend of the increase in vertical reaction with increasing lateral displacement is captured reasonably well. However, the results are adrift of the experiment. Secondly, the development of eccentricity (x/w) of the effective vertical reaction, where w is half the
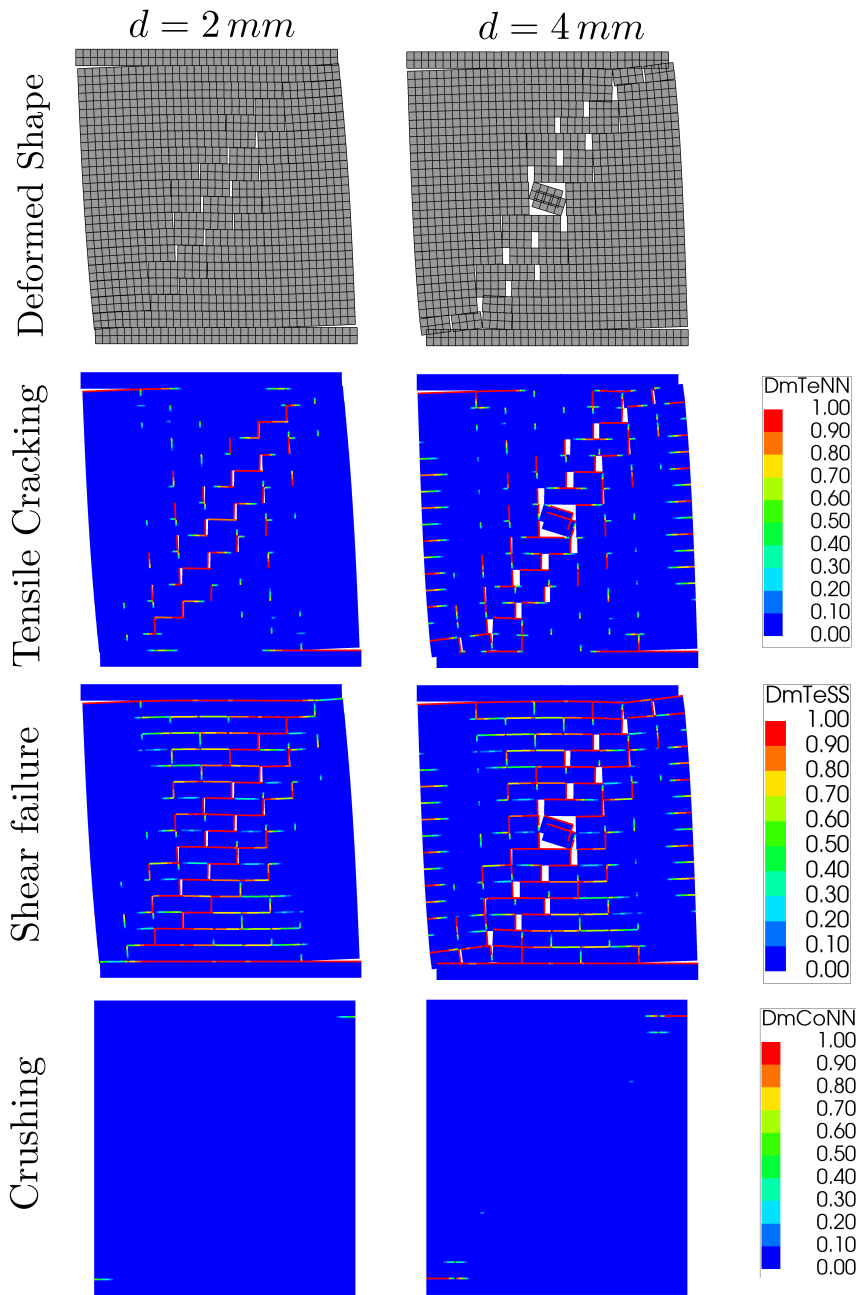
Figure 6.7: The deformed profile, and damage plots indicating tensile, shear and crushing failures for the pushover study of reference *discrete-crushing* model, with discrete cracking-shearing-crushing interfaces, using SLA at 2 mm and 4 mm prescribed lateral displacements

width of the wall and x is the distance of the effect vertical reaction force from the center line of the wall, is analysed. The eccentricity first grows outwards and eventually inwards to the center line of the wall with increasing lateral displacement in the SLA simulation. This is similar to the trends from the experiments, however, once again differences are observed. Despite the two above mentioned artefacts, the force-displacement evolution seems to be captured perfectly and therefore, these are considered acceptable in this study. Furthermore, despite the assumption of zero dilatancy angle, which is a feature of the decoupled Coulomb friction model used herein, the force-displacement response is close to the experiment. This is in line with the findings of previous works [32, 144] on the acceptable use of zero-dilatancy angle in the analysis of masonry structures. Finally, the performance of the non-proportional loading strategy in SLA in fully retaining the constant load until physical failure is remarkable in this case, and this is discussed in detail the following section.

VARIATION STUDIES

The following variations are performed on the benchmark study to analyse the performance of the proposed composite interface formulation. These are additionally summarised in Table 6.3.

- Firstly, the micro-model is run with discrete cracking and shearing failure possibilities in the interfaces excluding compressive nonlinearities, to understand the influence of crushing that is often the primary cause of collapse in masonry units such as shear walls. This case is referred to as the *no-crushing* model hereon.

- Secondly, the reference micro-model with full composite interface failure possibilities, i.e. the *discrete-crushing* model previously analysed using the SLA, is additionally studied using an incremental sequentially linear method, the Force-Release method. This helps to understand the influence of non-proportional loading in SLA, and also the importance of tracking stress history on damage accumulation and the eventual failure mechanism.

- Thirdly, a variation is performed with a micro model which distinguishes only the cracking and shearing failures into the interfaces. The crushing is smeared into the continuum brick elements using an orthogonal fixed smeared crush model. This case is referred to as the *smeared-crushing* model hereon.

Table 6.3: Overview of models studied in this section. 'T', 'S' and 'C' denote tension, shear and compression nonlinearities, while 'El.' denotes elasticity.

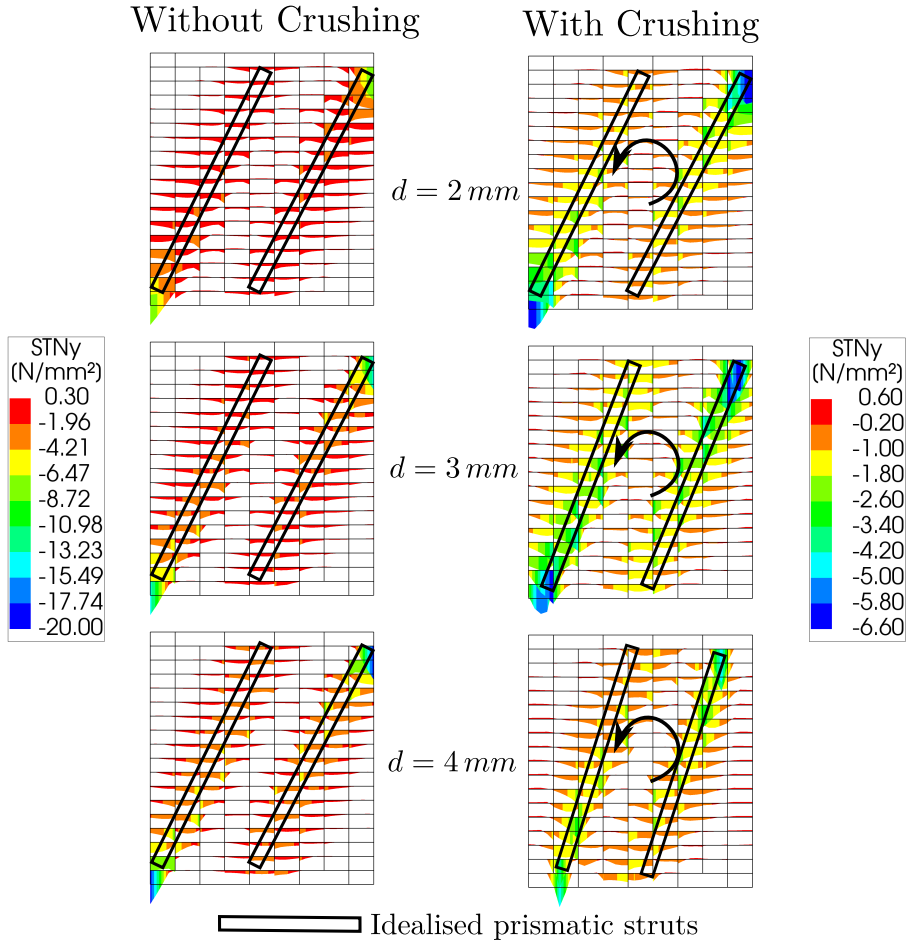| Modelling Units	Influence of crushing		SLA vs Force Release		Interfaces vs Continuum	
	discrete-crushing	no-crushing	discrete-crushing	discrete-crushing	discrete-crushing	smeared-crushing
Head & Bed Joints	T-S-C	T-S	T-S-C	T-S-C	T-S-C	T-S
Potential Brick Cracks	T	T	T	T	T	T
Bricks	El.	El.	El.	El.	El.	C

Figure 6.8: Evolution of compressive tractions along bed joints of the wall, with and without the crushing failure possibility (note the different colour scales), for increasing lateral displacements; & the schematic view of the rotation and movement of two parallel struts in the case of crushing failure possibility, with progressive crushing of the toe region of the wall.

Case 1: Influence of crushing   The force displacement curves of the *no-crushing* model compared against the reference *discrete-crushing* model is shown in Figure 6.9. The importance of crushing nonlinearities is clearly observed in the response of the *no-crushing* model which shows progressive increase in capacity with an increasing prescribed lateral displacement. This is also confirmed by the growing compressive tractions, in the bed joint interface near the toe of the wall, to almost 20 MPa at 4 mm top displacement as seen in Figure 6.8. Contrarily, the response of the reference *discrete-crushing* model shows a nonlinear distribution of compressive tractions along the length of the said bed joints already at 2 mm top displacement. With further increase in lateral displacement, the tractions in the bed joints drop and move inwards towards the center of the wall. This

indicates crushing of the toe. Figure 6.8 shows the formation of two parallel struts which are both rotating and approaching each other, which is also exemplified by the variation of eccentricity of the effective vertical force in Figure 6.11(b). This study validates the proposed simplified cut-off criterion used for crushing in the composite interface formulation. Although an elliptical cap model is used in the original formulation [82], the simplified straight cap (cut-off) criterion, in conjunction with other assumptions for the shear formulation and calibrated properties in compression, performs remarkably well.
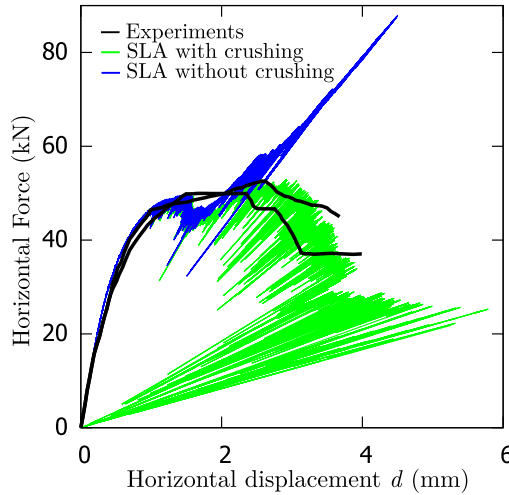
Figure 6.9: Force-displacement curves of the SLA simulation of the micro models with and without crushing nonlinearities: *discrete-* and *no-crushing* models

Case 2: SLA vs Force Release method   The Force-Release method [44] extensively compared against SLA for continuum modelling illustrations in Chapter 4 is now applied for the composite interface formulation. The reader is referred to Chapter 3 for an overview on the method. The composite interface formulation for 2D line interfaces, as outlined in Section 6.2.1, will hold good for the Force-Release method as well, but with the incremental approach in considering the stresses due to all previously applied loads as 'constant'. The force displacement curve for the Force-Release simulation of the pushover study using the reference *discrete-crushing* model is as shown in Figure 6.10(a). It compares well with SLA, and is mostly an envelope of the SLA response. This is corroborated by the close similarity in the damage plots of the SLA and Force-Release simulations at 2 mm prescribed lateral displacement, refer Figures 6.7 & 6.12.

The differences become apparent whenever SLA returns to the *Intermittent Proportional Loading* (IPL), wherein the last successful load combination is scaled proportionally to avoid violation of the constitutive law anywhere in the FE model. Under such conditions, the overburden load in SLA is implicitly reduced to enforce equilibrium during a quasi-static damage driven failure propagation. This becomes significant starting ~ 3.7 mm prescribed lateral displacement, marked as a yellow circle in Figure 6.10, indicating onset of collapse. The constant load drops to extremely low values through this region
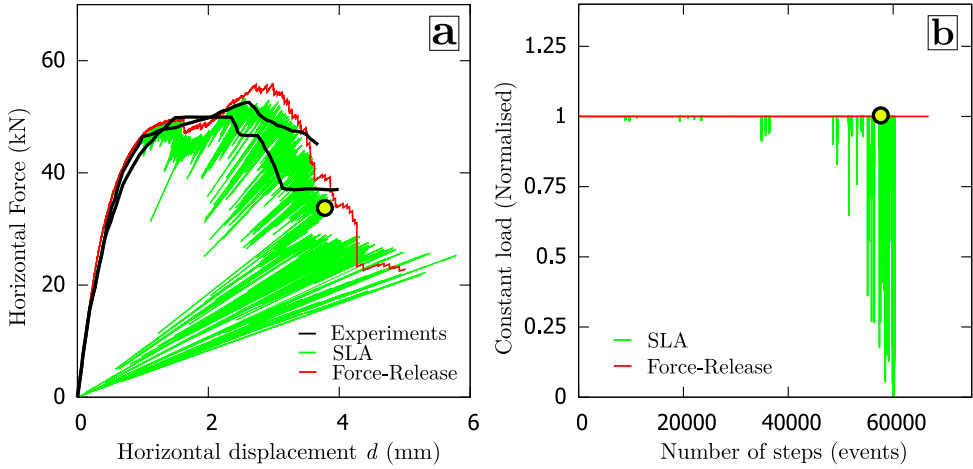
Figure 6.10: Force-displacement curves of the experiments compared against those of the SLA and the Force-Release simulations of the *discrete-crushing* model, and (b) the evolution of constant load of precompression during the simulations
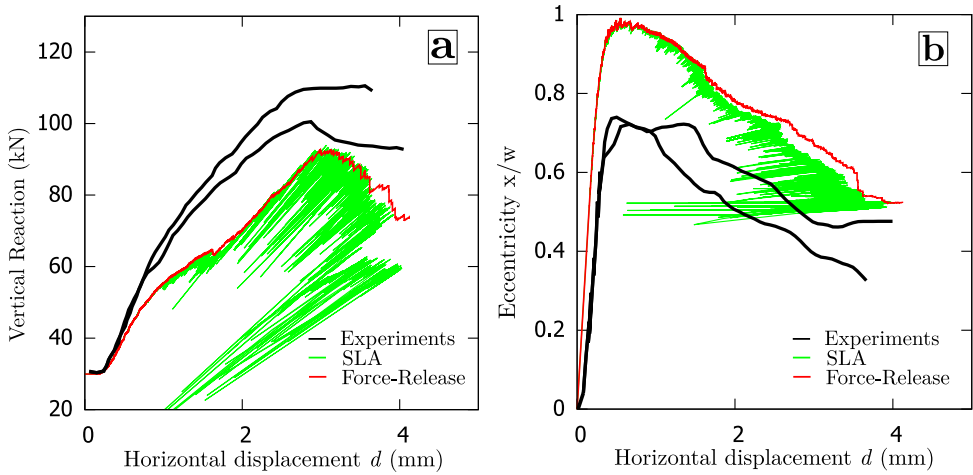

Figure 6.11: (a) Evolution of the vertical reaction forces, and (b) its eccentricity with respect to the center line of the wall, for increasing prescribed lateral displacements in the SLA & Force-Release simulations of the *discrete-crushing* model

but is also recovered immediately, which appear as large snap-backs in the post-collapse region at prescribed lateral displacements around 4 mm. Since every damaged element's stress is released instantaneously in SLA, the neighbouring integration points of the critical integration point whose stresses are close to their respective allowable strengths subsequently become critical at a considerably lower load. In summary, the performance of the non-proportional loading strategy of SLA is successful in this problem leading to collapse, which in turn is described using its inherent redistribution procedure (IPL).
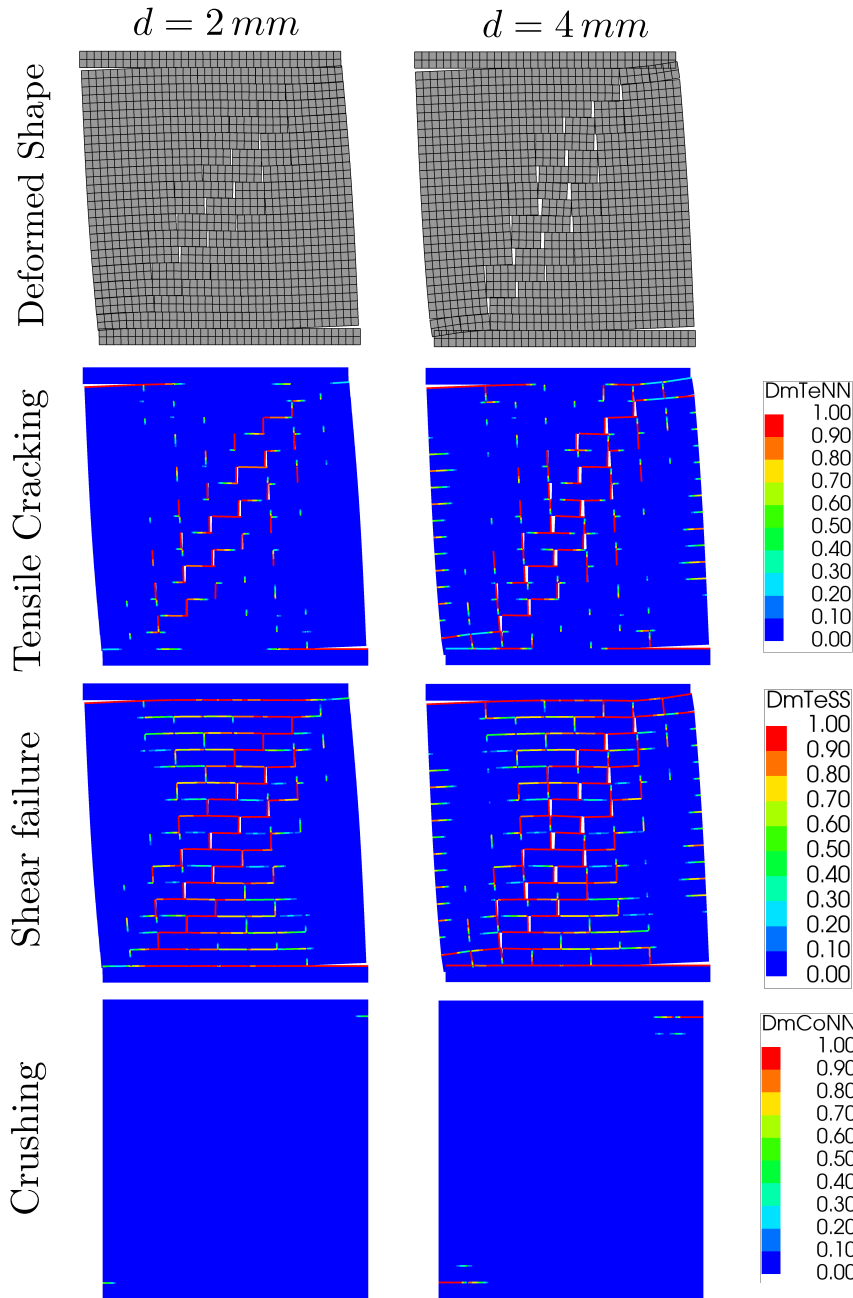
Figure 6.12: The deformed profile, and damage plots indicating tensile, shear and crushing failures for the pushover study of reference *discrete-crushing* model, with discrete cracking-shearing-crushing interfaces, using the Force-Release method at 2 mm and 4 mm prescribed lateral displacements

On the other hand, these regions are simulated in disequilibrium using the Force-Release method appearing as instabilities or *drops* of load for a constant imposed displacement. It is known that the difference in load history results in a different elemental failure sequence in lattice simulations [44], and that for continuum studies as well damage propagation could be different, by a small amount, as confirmed by studies in Chapter 4. This is reiterated by the current case study as well which is evident from damage plots for SLA and Force-Release at 4 mm top displacement, refer Figures 6.7 & 6.12. Although the plots look alike, there are yet notable differences like the through vertical cracks in the middle course of bricks in SLA which appears to be more a stepped crack passing through the head and bed joint in the Force-Release case. Such minor differences are the effect of an accumulation of differences in damage locations over several steps. The IPL is used in SLA often after 50000 events as seen in Figure 6.10(b), while the Force-Release traverses through these regions through several small instabilities. One such prominent region is around 4.25 mm prescribed lateral displacement of both SLA and Force-Release curves in Figure 6.10(a). Furthermore, the evolution of vertical reaction forces and its eccentricity with the imposed displacement in the Force-Release simulation is also similar to that of SLA, refer Figure 6.11. In conclusion, Force-Release simulation (*incremental*) of the composite interface formulation also performs well for the case study and compares well with the *total* version of SLA.
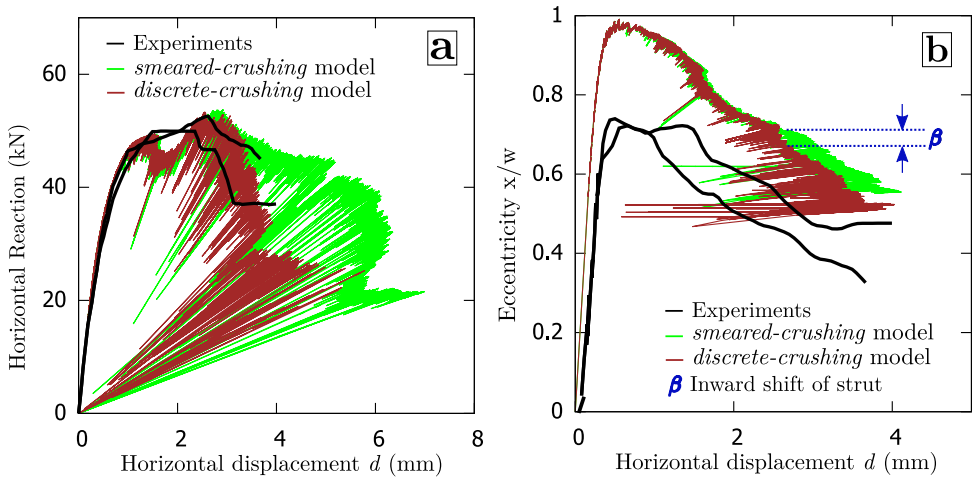

Figure 6.13: (a) SLA simulations of the *discrete-crushing* model, and the *smeared-crushing* model with compression nonlinearity smeared into the continuum, and (b) evolution of eccentricity of vertical reaction forces up to 4 mm horizontal displacement

Case 3: Crushing in Interfaces vs Continuum   The final variation in this 2D study using SLA (and additionally, the Force-Release method) is that of the *smeared-crushing* model that allows for compressive failure in the continuum elements instead of the interfaces as in the reference *discrete-crushing* model. This is done using the 2D orthogonal fixed smeared crush model with a simple bi-axial Rankine-type failure criterion for crush

initiation in the continuum. The nonlinearity parameters for all elements are the same as those in Table 6.2, except that the continuum elements are provided the crushing parameters. Uniaxial parabolic hardening-softening curves, as in Figure 6.2(c), are used but with the band width ripple, for both directions of the 2D crush set-up. The crushing is smeared over a bandwidth of ∼ 40 mm and the shear retention function is kept damage-based [132].
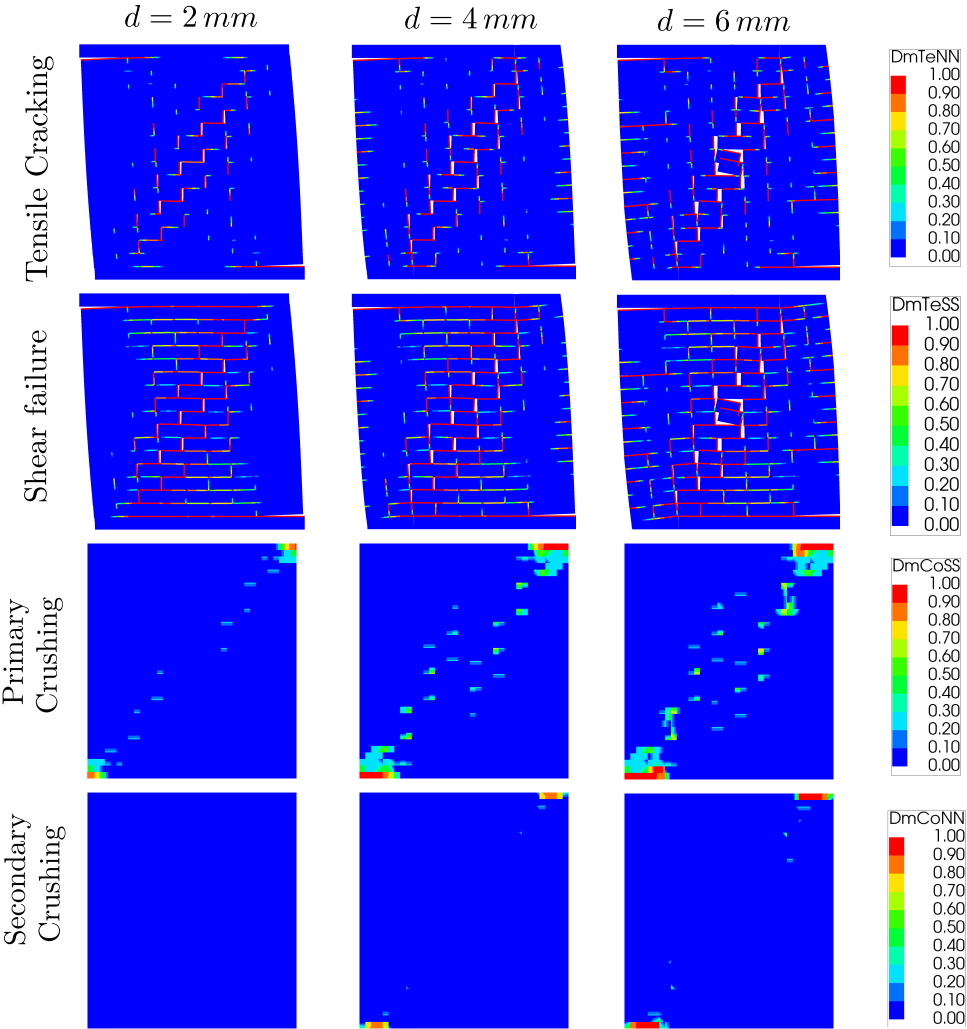

Figure 6.14: Damage plots indicating tensile, shear and crushing failures for the pushover study of the *smeared-crushing* model, with discrete cracking & shearing in interfaces while crushing is smeared in the continuum, using SLA at 2 mm, 4 mm and 6 mm prescribed lateral displacements

The force displacement evolution for the SLA pushover study using the *smeared-crushing* model is as shown in Figure 6.13(a). The evolution of the 'constant' overburden
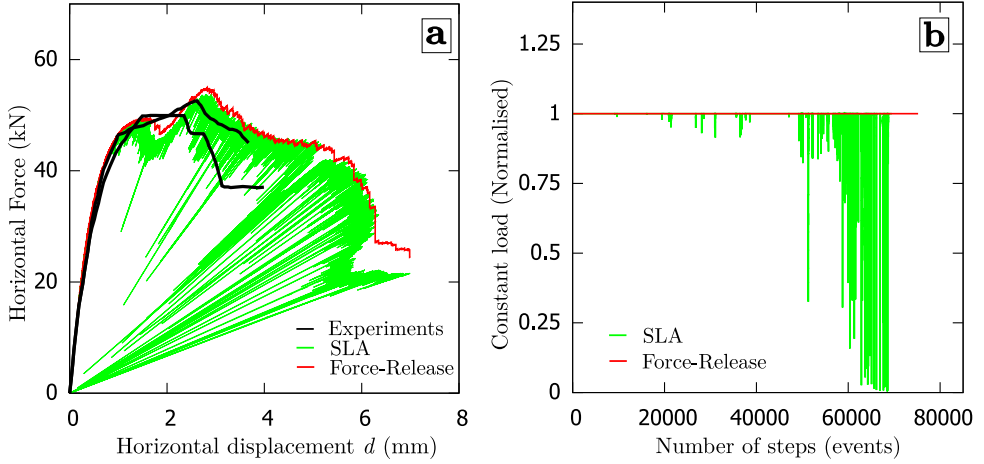
Figure 6.15: Force-displacement curves of SLA and the Force-Release simulations of the *smeared-crushing* model, and (b) the evolution of constant load of precompression during the simulations

load through the analysis is shown in Figure 6.15 alongside a Force-Release simulation of the same model for comparison. Due to the good agreement with Force-Release simulation, only the SLA results are deliberated hereon. The damage initiation with flexural failure, followed by the diagonal stepped cracks culminating in the toe crushing, as observed in the experiments and in the *discrete-crushing* model are captured well by the *smeared-crushing* model as well, refer Figure 6.14.

However, the post-peak response involving crushing of the toe is slightly more ductile in the case of the *smeared-crushing* model. To understand this, the evolution of eccentricity of the effective vertical reaction force with respect to the imposed displacement is analysed. The response of both models match up until an imposed displacement of around 2.5 mm, refer Figure 6.13. Beyond this point, the inward motion of crushing zone towards the center of the wall is more drastic in case of the *discrete-crushing* model, denoted by parameter β in Figure 6.13(b), which indicates complete crushing of the left most part of the toe (roughly half a brick length - Figure 6.7). In accordance with Eq. 6.12, complete crushing also leads to total loss of shear stiffness in this toe region which results in the sliding out of the brick (Figure 6.7). The crush zone thus effectively moves more inwards leading to an earlier collapse. However, in case of the *smeared-crushing* model, the smearing out of crushing into the continuum results in a more diffused damage zone near the toe region as seen in the plots of Figure 6.14. This damage distribution helps delay the inward movement of the crush zone which is decisive for the onset of collapse. That aside, the damage is distinguished into primary and secondary crushing along the directions of the orthogonal fixed crush-coordinate system of an integration point, which is known to have locking issues, despite the use of a shear retention function. There is also some amount of crushing at several locations along the diagonal, due to contact between bricks, which is not observed in the *discrete-crushing* model. The combined effect of these differences results in the slightly more ductile response of the *smeared-crushing* model.

In conclusion, the relatively quicker inward displacement of the crush zone, due to the movement and rotation of the struts, sets off the global softening faster in the case of the reference *discrete-crushing* model as against the *smeared-crushing* model. The ductile response of the latter can be attributed to the larger diffused crush zone coupled with stress locking, which leads to the slower inward propagation of the crush zone, and also more inwards than in the case of the former.

6.3.2. 3D PLANAR INTERFACE MICRO-MODEL

Finite Element Model   The 3D model of the case study presented thus far is made in the same manner as the 2D model, with regard to the micro-modelling approach, and is therefore not shown here owing to triviality. The differences are summarised as follows. The mortar joints and the brick-mortar interfaces are lumped together into a zero-thickness 4+4 noded planar interfaces with a 2×2 Newton-Cotes integration scheme. The extended bricks are modelled using 8 noded iso-parametric solid elements, all approximately 27.5 mm×27.5 mm×27.5 mm in size, with linear interpolation shape functions and a $2 \times 2 \times 2$ Gaussian integration scheme. All DOFs along the bottom faces of wall are fully constrained, while the top face is prevented against any rotation. The nodes along the top face of the wall are given an initial vertical displacement 0.083 mm, which is the imposed displacement equivalent to an overburden pressure of 0.30 N/mm^2. Subsequently, a lateral displacement is imposed on the top edge to simulate the lateral load. The presented planar interface composite interface formulation is the adopted constitutive model and all head & bed joints are lumped with the nonlinearities of tensile cracking,crushing and shearing, with material parameters as shown in Tables 6.1,6.2. However, for the decoupled Coulomb friction failure mode, user specified discretisation factor of $a_t = 0.075$ and $a_s = 0.075$ for the specified relative shear displacement along the two shear directions, as in Eq. 6.17, are used as against $a_t = 0.05$ in the 2D analysis. Also, all saw-teeth discretisation factors for tensile and compressive ripple band relations are set to 0.2 whereas narrower ripple bands were used in the 2D analysis. The above mentioned changes in discretisation factors are made to avoid long computational times.

Results & Discussion   Firstly, the SLA simulation of the 3D micro-model shows good qualitative agreement with the 2D simulation of the reference *discrete-crushing* model (Figure 6.17(a)), and the experimental responses of walls J4D and J5D as well (Figure 6.16), in terms of the peak loads and the global softening behaviour that leads to loss of lateral capacity. The deformed profile and damage propagation in the masonry are summarised for the SLA simulation of the 3D Model in Figure 6.18 at 2 mm and 4 mm prescribed lateral top displacement d. The damage plots DmTeNN and DmCoNN indicate loss of normal stiffness due to cracking and crushing respectively. The DmTeSS and DmTeTT plots indicate loss of shear stiffness along the two shear directions, which are either due to sliding failures or the damaged based shear reduction due to the associated normal cracking/crushing. All damage plots herein range from 0 to 1 which refer to undamaged and fully damaged cases for the corresponding failure criteria.

Similar to the 2D response, the wall firstly exhibits flexural failure which is visible as horizontal cracks along bed joints at the bottom-right and top-left corners of the wall. After the flexural cracks are fully developed, compressive strut action results in a
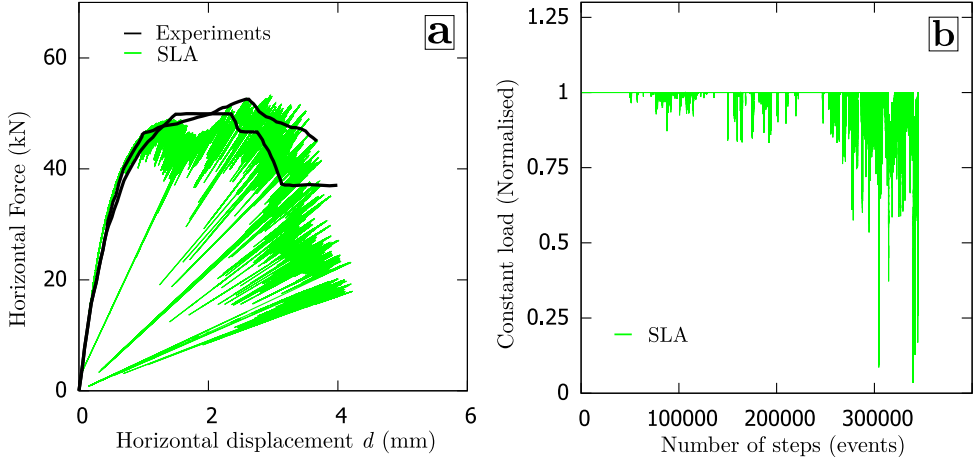
Figure 6.16: Force-displacement curves of the experiments compared against those of the SLA for the 3D model, and (b) the evolution of constant load of precompression during the SLA simulation
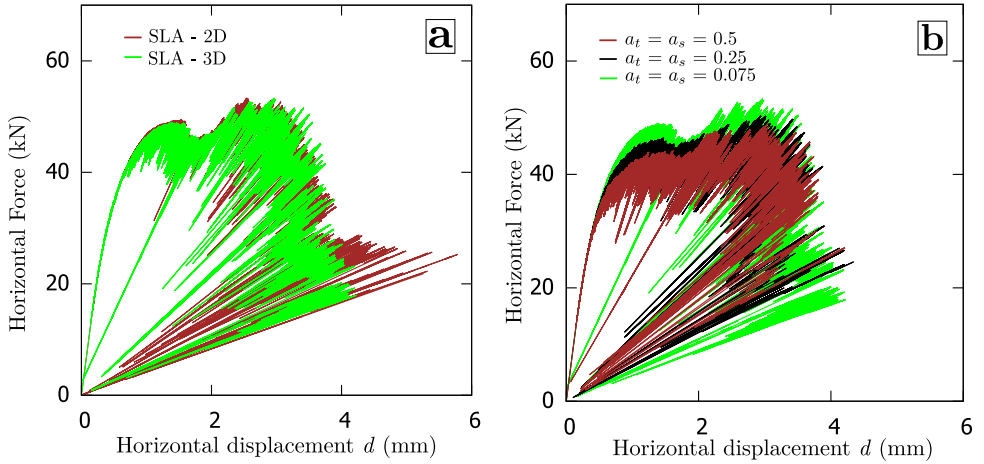

Figure 6.17: Force-displacement curves of the 2D and 3D SLA simulations, and (b) 3D SLA simulations for varying values of user-specified shear displacement increment factors a_t and a_s

staggered diagonal shear crack. This damage propagation includes both sliding failure along the bed joints, resulting in loss of shear stiffness, and tensile cracking along head joints, resulting in loss of both normal and shear stiffness as is observed in the plots of Figure 6.18. Although minor out-of-plane effects were seen along the staggered diagonal crack and also at the top edge of the wall, they are negligible. The case study, in principle, serves as a good starting case for 3D sliding problems and the proposed formulation shows good promise. Since the 2D formulation has been shown to work equally well with both SLA and Force-Release methods, 3D formulation is shown here only with SLA although the Force-Release simulation should be possible in principle.

One key aspect of simulating sliding problems using SLA is the effect of the user-specified shear displacement increment factors a_t or a_s (Eq. 6.17) on the shear capacity. It is most likely that only one of the two has a substantial influence in the present case study since shearing will be dominant in only one direction. However, it is possible in principle to change them simultaneously. Furthermore, it was noted previously that the curves become less smooth upon increasing values of these factors, but that the peak capacity and post-peak behavior were convergent for moderately large values [139]. However, it is found in a sensitivity study for these factors that the effect is important for sliding problems. It is clear from Figure 6.17(b), that values such as $a_t = a_s = 0.5$ or 0.25 result in quicker loss of the mobilised cohesion and lower dissipation of energy. This is because the update in stiffness is rather drastic leading to larger plastic shear displacements than based on the prediction as in Eq. 6.17, and it is therefore recommended to use this factor appropriately.

6.4. CONCLUDING REMARKS

This chapter proposes an extension to the step-wise secant Coulomb friction formulations [139], with a compression failure criterion. This makes it possible to analyse masonry components using the micro-modelling approach in combination with sequentially linear methods until full collapse. The constitutive model is therefore a composite failure criterion, and is described in detail for both line (2D) and planar interfaces (3D) with regard to determining critical load multiplier and the mode of stiffness update. The model is summarised as follows:

- Shear failure is described by the uncoupled Coulomb friction formulation, allowing for cohesion softening, and updating the shear stiffness based on *specified* shear relative displacement increments.

- Discrete cracking is initiated by a tension cut-off criterion coupled with a uniaxial tension softening saw-tooth law.

- Crushing is initiated by a compression cut-off criterion coupled with a hardening-softening saw-tooth law.

The formulations are then validated using a benchmark study of a pushover analysis on a solid clay brick masonry wall. The wall is first subject to precompression followed by an imposed lateral displacement, resulting in a diagonal shear failure typical of squat masonry walls. This benchmark is simulated using both 2D and 3D models, and the results of both compare well to the experiments. Firstly, the agreement between the SLA simulation and the experiment is good with regard to the force-displacement relation and the damage patterns. Toe crushing is captured adequately which leads up to the inward movement of the crush zone, in turn due to the inward movement and rotation of two parallel struts, and results eventually in a brittle failure. Secondly, the non-proportional loading strategy used in SLA works well for the presented case leading up to true-collapse. The constitutive formulation works adequately in combination with the incremental Force-Release method as well. Furthermore, the lack of dilatancy in the Coulomb friction formulation does not seem to affect the force displacement relations, although the

development of vertical reaction forces are adrift of those from the experiment, both in magnitude and in terms of eccentricity. Nevertheless, there is scope to improve the performance of the proposed composite interface formulation, for e.g. by using a compression criterion as in the traditional elliptical cap model proposed by Lourenco [82, 83].
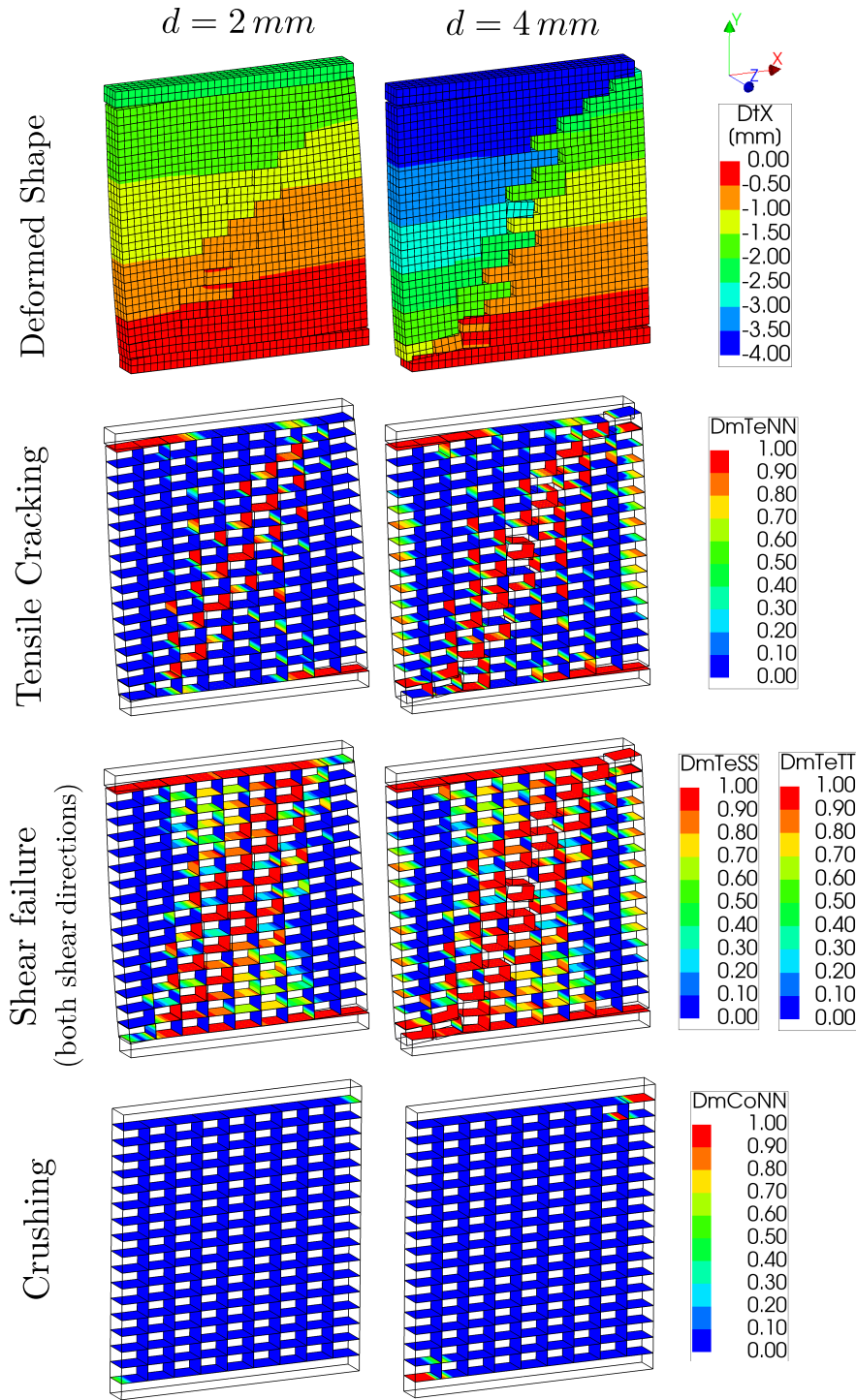
6

Figure 6.18: Deformed profiles, and damage plots indicating tensile, shear and crushing failures for the pushover study of 3D Model using SLA at 2 mm and 4 mm prescribed lateral displacements

COMPUTATIONAL PERFORMANCE
ASPECTS OF SLA[*]

In this Chapter, two tailor-made solvers are proposed to improve the computational performance of Sequentially Linear Analysis. Firstly, the motivation for such dedicated solvers is briefed upon in Section 7.1. Thereafter, an adapted direct solution technique based on the Woodbury matrix identity is proposed in Section 7.2.1. This identity, the generalisation of the Sherman-Morrison formula (to find the inverse of a rank-1 corrected matrix) to a rank-r correction, allows for cheaper numerical computation of the inverse of a low-rank corrected matrix by avoiding the matrix factorisation every analysis step. The old factorisation can be reused with some additional matrix and vector manipulations in order to solve a significantly smaller linear system of equations relatively efficiently. The optimal point of restarting, to start off again with a new factorisation is also deduced. Secondly, an improved preconditioner for the Conjugate Gradient (CG) method [56] is proposed in Section 7.2.2. Instead of an Incomplete LU factorisation (ILU) as a preconditioner, which is more commonly used for solving large systems of equations pertaining to structural applications, the complete factorisation (LU) of a previous analysis step is used as a preconditioner which reduces the number of required CG iterations significantly. The point at which too many CG iterations are required and a new factorisation is necessary, is determined using a restarting strategy similar to that of the first method. The restarting strategy is elaborated upon in Section 7.2.3. Subsequently, in Section 7.3 the proposed solution strategies are compared against a widely used parallel direct sparse solver (PARDISO) [56], from a performance perspective, using two real life benchmarks. The first benchmark is that of a masonry wall tested for a quasi-static lateral load in combination with an overburden load [6], and the second is a reinforced concrete slab tested for a concentrated shear load, along with axial loads at the lateral faces [20] (also previously investigated in Section 5.4.2, Chapter 5). From the numerical studies, it follows that both the proposed methods perform significantly better than the direct solution method, especially for large 3-dimensional problems. Results from the sensitivity studies performed for problem sizes and for the number of steps used to discretise the constitutive model, are detailed in Section 7.3.2. Finally, Section 7.4 summarises the main findings of the presented work and the directions to future work.

7.1. MOTIVATION

Despite active contributions to different topics under SLA by several researchers, the computational performance remains not very conducive to practical applications as has

---

been pointed out previously [139, 151, 4, 1]. It is the event-by-event nature of the SLA approach, which on the one hand instills robustness, contrarily makes the procedure computationally intensive. However, since only one element is effectively damaged at a time, the system of linear equations to be solved only changes locally between these analyses. Traditional direct solution techniques do not exploit this property, and calculate a rather expensive stiffness matrix factorisation every linear analysis, resulting in high computational times per analysis step. Additionally, the need for a high number of linear analyses, to bring about an equivalent nonlinear response as in the traditional approaches, compounds the total analysis time. This motivated the need for a tailor-made solver for SLA, additionally inspired by remarks made in References [45, 74]. To address this issue, and efficiently make use of previous stiffness matrix factorisations and solutions, two solution strategies are proposed in this chapter. Alternative faster methods combining a traditional incremental-iterative technique and the total approach of SLA are also available in literature, addressing the need for a practical alternative [57], but the focus of this work is to solely improve the performance of SLA with regard to solving the system of linear equations. It is reiterated once again that unlike NLFEA, which is considered as *one analysis* containing several *steps*, SLA comprises several linear analyses which are referred herein interchangeably as *'analysis steps'* or *'steps'* as such.
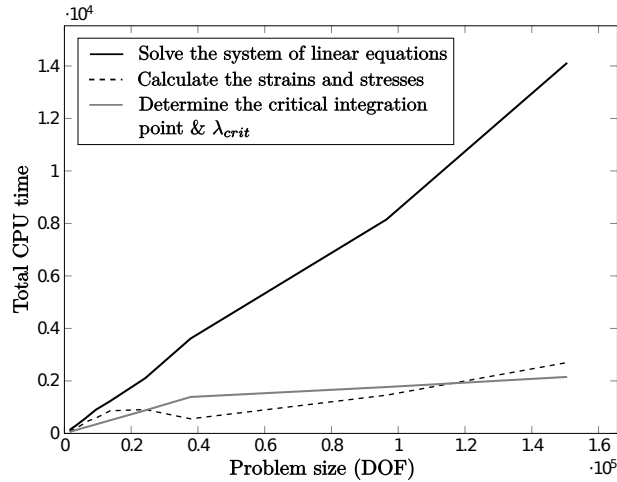

Figure 7.1: Total CPU time (in seconds) for the most dominant processes of SLA in relation to the problem size (number of degrees of freedom (DOFs)) of a 2D shear wall case study [137]

The traditional direct solution method to solve the system of linear equations involves an expensive matrix factorisation of the stiffness matrix K, and calculates the displacements $\mathbf{u}$ by forward and backward substitution.

$$K\mathbf{u} = \mathbf{f} \tag{7.1}$$

Common factorisation techniques, like the LU and Cholesky decomposition methods, become expensive if they have to be computed in every analysis step. As a result, for increasing problem sizes, solving the system of equations becomes the bottleneck for

SLA, and is illustrated by the CPU-time measurements for a 2D shear wall case-study reported in Reference [137], refer Figure 7.1 for the results. The system of equations undergoes a low-rank correction of the global stiffness matrix per analysis step in SLA, and therefore there is a need for efficient solution strategies that exploit this feature, two of which (originally developed by Swart [137][107]) are outlined in the following sections.

7.2. TAILOR-MADE SOLVERS FOR SLA

7.2.1. DIRECT SOLVER USING WOODBURY MATRIX IDENTITY

The inverse of a rank-1 corrected matrix $(A + \mathbf{u}\mathbf{v}^T)$, subject to the inverse A^{-1} being known a priori, can be computed relatively easily using the well known *Sherman-Morrison formula* [56] as against having to perform the inverse operation altogether anew. The rank correction for practical applications in finite element analysis using the SLA, however, is generally of a higher order.

To this end, the *Woodbury matrix identity* [56], which is a generalisation of the *Sherman-Morrison formula* for a rank-r correction of a matrix, is more suitable. The identity states that for matrices $A \in \mathbb{R}^{N \times N}, U \in \mathbb{R}^{N \times r}, C \in \mathbb{R}^{r \times r}, V \in \mathbb{R}^{r \times N}$, assuming A and C are invertible, the inverse of a low-rank corrected matrix is defined as : $(A + UCV)^{-1} = A^{-1} - A^{-1}U(C^{-1} + VA^{-1}U)^{-1}VA^{-1}$. Substituting $r = 1$, it follows directly that the Woodbury identity reduces to the Sherman-Morrison formula. In SLA, additionally, the low-rank correction is symmetric, and therefore UCV can be written as UCU^T with C as a symmetric matrix. In this case, the expression simplifies to the following:

$$\left(A + UCU^T\right)^{-1} = A^{-1} - A^{-1}U\left(C^{-1} + U^T A^{-1} U\right)^{-1} U^T A^{-1} \tag{7.2}$$

Assuming an element e_i is damaged in the nth analysis step, the low-rank corrected system stiffness matrix $K^{(n+1)}$, for the subsequent analysis step can be written as

$$\begin{aligned} K^{(n+1)} &= K^{(n)} + T_{e_i}\left(K_{e_i}^{(n+1)} - K_{e_i}^{(n)}\right) T_{e_i}^T \\ &:= K^{(n)} + T_{e_i} D_{e_i}^{(n)} T_{e_i}^T, \end{aligned} \tag{7.3}$$

where $D_{e_i}^{(n)}$ is the update to the stiffness matrix of element e_i, and T_{e_i} is the transformation matrix which maps the local numbering of the element to the global numbering of the FE model. It is to be noted that the subscripts and superscripts refer to element numbers and the analysis step respectively. Constructing the eigendecomposition of $D_{e_i}^{(n)}$ and substituting it in Eq. 7.3, the following is obtained.

$$\begin{aligned} K^{(n+1)} &= K^{(n)} + T_{e_i} Q_{e_i}^{(n)} \Lambda_{e_i}^{(n)} \left(Q_{e_i}^{(n)}\right)^T T_{e_i}^T \tag{7.4} \\ &= K^{(n)} + \left(T_{e_i} Q_{e_i}^{(n)}\right) \Lambda_{e_i}^{(n)} \left(T_{e_i} Q_{e_i}^{(n)}\right)^T \\ &:= K^{(n)} + U^{(n)} C^{(n)} U^{(n)\,T} \tag{7.5} \end{aligned}$$

wherein the matrix $C^{(n)} = \Lambda_{e_i}^{(n)}$ is a diagonal matrix whose elements are the eigenvalues of $D_{e_i}^{(n)}$, $Q_{e_i}^{(n)}$ contains the corresponding eigenvectors, and $U^{(n)} = T_{e_i} Q_{e_i}^{(n)}$. The eigendecomposition only considers sufficiently large eigenvalues corresponding to dominant features

of the applied damage increment in an SLA step. The basis for this choice and its effect on the convergence of the solution is elaborated upon in Section 7.2.3. It is clear that the rank in every analysis step increases by the number of sufficiently large eigenvalues of the eigendecomposition of $D_{e_i}^{(n)}$, which regardless of the type of analysis (2D or 3D) is at most d, where d is the number of degrees of freedom (DOF) of the element e_i. Rewriting in a suitable form for Woodbury identity, Eq. 7.5 is defined recursively in terms of the initial stiffness matrix $K^{(0)}$ which yields

$$
\begin{aligned}
K^{(n+1)} &= K^{(0)} + \sum_{j=1}^{n} U^{(j)} C^{(j)} U^{(j)\,T} \\
&= K^{(0)} + \begin{bmatrix} U^{(1)} & \cdots & U^{(n)} \end{bmatrix} \begin{bmatrix} C^{(1)} & & \\ & \ddots & \\ & & C^{(n)} \end{bmatrix} \begin{bmatrix} U^{(1)\,T} \\ \vdots \\ U^{(n)\,T} \end{bmatrix} \\
&:= K^{(0)} + U_n C_n U_n^T .
\end{aligned}
\tag{7.6}
$$

Algorithm 1 Direct Solution using the Woodbury matrix identity

1: Solve the system $K^{(0)}\mathbf{x} = \mathbf{f}$, for $\mathbf{x}$ by using the known factorisation of $K^{(0)}$
2: Solve the system $K^{(0)} Z = U_n$, for Z by using the known factorisation of $K^{(0)}$
3: Calculate $E = C_n^{-1} + U_n^T Z$
4: Calculate $\mathbf{y} = U_n^T \mathbf{x}$
5: Solve the system $E\mathbf{z} = \mathbf{y}$, for $\mathbf{z}$ by calculating a factorisation of E, and subsequently applying forward and backward substitutions.
6: Solution to the system of equations: $\mathbf{u} = \mathbf{x} - Z\mathbf{z}$

7

Now, Eq. 7.6 is of the form as required by Eq. 7.2. Once the factorisation of $K^{(0)}$ is known and the above set-up is performed, the solution to the system of equations $K^{(n+1)}\mathbf{u} = \mathbf{f}$ of the $(n + 1)^{th}$ linear analysis step can be calculated by performing the steps in Algorithm 1. In summary, Woodbury identity helps achieve a cheaper computation of the inverse of a low-rank corrected matrix, by avoiding the calculation of an expensive new factorisation every analysis step. Thus, it enables the reuse of an old factorisation, and subsequently, the solution is obtained with additional matrix and vector multiplications. A significantly smaller system of equations is solved for effectively in step 5 of Algorithm 1, as opposed to the direct solution method.

7.2.2. PRECONDITIONED CONJUGATE-GRADIENT ITERATIVE SOLVER

Krylov subspace methods, which belong to an iterative class of solution methods, in contrast to direct solution methods generate a sequence of approximate solutions $\mathbf{u}_i$ to Eq. 7.1. This is done by solving a minimisation problem over the subspace $\mathcal{K}^k$ which contains the solution, and is called the Krylov subspace as defined below in Eq. 7.7. Herein, $\mathbf{r}$ is the residual vector and $\mathbf{r_0} = \mathbf{f} - K\mathbf{u_0}$, where $\mathbf{u_0}$ is the initial guess, and k is the number of iterations.

$$
\mathcal{K}^k(K, \mathbf{r}_0) = \mathrm{span}\left\{ \mathbf{r}_0, K\mathbf{r}_0, \ldots, K^{k-1}\mathbf{r}_0 \right\}
\tag{7.7}
$$

The stiffness matrix is symmetric and positive definite (SPD) for the problems solved using SLA, and for such cases, the Conjugate Gradient (CG) method is the Krylov subspace method of choice. After N iterations, the Krylov subspace spans $\mathbb{R}^N$, and therefore CG terminates (in exact arithmetic) at the exact solution after at most N iterations. A stricter error bound using eigenvalues is also well known, which states that if K (or $P^{-1}K$ for a preconditioned problem) has ρ distinct eigenvalues, convergence is guaranteed in at most ρ iterations [56]. The extreme eigenvalues of K influence the convergence speed of CG, which in turn can be improved using preconditioning to obtain more favourable eigenvalues.

In the preconditioned CG (PCG) method, for a matrix P which is assumed to be non-singular, $P^{-1}K\mathbf{u} = P^{-1}\mathbf{f}$ is solved for, and is shown in Algorithm 2. Since in every iteration the linear system $P\mathbf{z}_{k+1} = \mathbf{r}_{k+1}$ is solved for, P should be chosen such that operations with P^{-1} are cheap to perform. Furthermore, the choice of the preconditioner must ensure that the eigenvalues of $P^{-1}K$ are clustered for a faster rate of convergence. Several choices for the preconditioner P exist, such as the extremes $P = I$ and $P = K$, or the intermediate incomplete LU factorisation.

Algorithm 2 Preconditioned Conjugate Gradient algorithm

1: Set $\mathbf{r}_0 = \mathbf{f} - K\mathbf{u}_0$, $\mathbf{z}_0 = P^{-1}\mathbf{r}_0$, $\mathbf{p}_0 = \mathbf{z}_0$.
2: **for** $k = 0, 1, \dots$ until convergence **do**
3:     $\alpha_k = \mathbf{r}_k^T\mathbf{z}_k / \mathbf{p}_k^T K\mathbf{p}_k$
4:     $\mathbf{u}_{k+1} = \mathbf{u}_k + \alpha_k\mathbf{p}_k$
5:     $\mathbf{r}_{k+1} = \mathbf{r}_k - \alpha_k K\mathbf{p}_k$
6:     $\mathbf{z}_{k+1} = P^{-1}\mathbf{r}_{k+1}$
7:     $\beta_k = \mathbf{r}_{k+1}^T\mathbf{z}_{k+1} / \mathbf{r}_k^T\mathbf{z}_k$
8:     $\mathbf{p}_{k+1} = \mathbf{z}_{k+1} + \beta_k\mathbf{p}_k$
9: **end for**

Due to the event-by-event strategy of SLA, the choice $P = K^{(0)}$ would be appropriate especially when the factorisation is not performed every analysis, in order to have a balance between a cheap computation of P and a reasonable rate of convergence. This suggests the use of the complete factorisation of $K^{(0)}$ as a preconditioner. Taking $P = K^{(0)}$, it follows that in the first analysis step $P^{-1}K^{(0)} = I$, and basically becomes a direct solution method. However, subsequent analysis steps require considerably less iterations due to the event-by-event nature of SLA. That is, the first subsequent system needs at most $(r_1 + 1)$ iterations, with r_1 equal to the rank of the first update. The second system needs at most $(r_1 + r_2 + 1)$ iterations, since $K^{(2)}$ differs from $K^{(0)}$ by at most a rank $r_1 + r_2$ update. This argument can be repeated, which implies that after n SLA steps, at most $(\sum_{i=1}^{n} r_i + 1)$ CG-iterations are needed. The iterative scheme is repeated until the approximate solution is sufficiently converged. This is determined by a stopping criterion, one of which is shown below for some tolerance ε, where $\mathbf{r}$ is the residual vector.

$$\frac{\|\mathbf{r_k}\|}{\|\mathbf{f}\|} \leq \varepsilon \tag{7.8}$$

Therefore, the optimal point at which a new factorisation is calculated should be determined such that the total computing time is minimised. In such an iterative approach, instead of factorisation, the matrix K is only involved in matrix-vector multiplications, and the solution to Eq. 7.1 is determined using inner-products, vector updates, scalar-vector and matrix-vector products, and back- and forward substitutions with the factors of $K^{(0)}$ (the most expensive operations). Krylov subspace methods, in general, require a relatively small amount of memory to solve the problem compared to direct solution methods. However, in SLA's context, more memory is required because of the factorisation being used as preconditioner.

7.2.3. RESTARTING STRATEGY FOR THE SOLVERS

The solution strategies presented in Section 7.2.1 & 7.2.2 are similar to the end that both require an expensive factorisation step followed by a series of significantly faster steps. While solving large linear systems using these strategies, two parameters can be tuned. Firstly, the number of sufficiently large eigenvalues to be considered for the eigendecomposition of the update to the critical element stiffness matrix in Eq. 7.4 has to be chosen, i.e. a decision has to be made to find a balance between performance and accuracy. Secondly, it is also possible to restart which implies that a new factorisation of the stiffness matrix could be computed, resulting in the rank being set back to 0. The penalty in restarting is in having to recompute a costly matrix decomposition, while, on the other hand, the following analysis steps would be considerably cheaper. The restarting point, therefore, has be to be determined such that these effects are balanced.

Eigenvalue Ratio   Numerically calculated eigenvalues of the update to critical element's stiffness matrix, using some iterative scheme, could contain rounding errors which may result in non-zero values, and therefore influence the eventual results. To address this, the absolute value of all eigenvalues during every analysis step was compared to the largest eigenvalue as a ratio, the eigenvalue threshold $\epsilon = |\lambda_i|/\lambda_{\max}$, which in turn helped control the choice of dominant eigenvalues differing from the largest value by a certain order of magnitude. Parametric studies were performed on several test problems, without restarting as proposed in Section 7.2.1, to solely analyse the influence of the choice of an eigenvalue ratio on the accuracy of the solution. Thus, isolating the effect of only the eigenvalue threshold, a choice of $\varepsilon > 10^{-10}$ was made [137]. In general, the solution residuals were observed to increase faster with the Woodbury based solution (without restarting) than those of the direct solution method. This is due to the rounding errors resulting from the numerous intermediate matrix and vector manipulations involved in the former approach. Nevertheless, the residuals of the Woodbury solution were in reasonable agreement to the direct solution method in terms of accuracy (one order of magnitude difference), especially considering the fact that restarting was not *yet* used.

Restarting strategy   After deciding on an eigenvalue threshold based on the performance of the method without loss of any accuracy (residuals differing by one order of magnitude), the next step of determining a restarting strategy was carried out. The optimal point when a new factorisation has to be recalculated for both Woodbury based

and PCG methods, such that the total analysis time is minimised, could possibly be determined using two approaches. Owing to the inherent similarity in the proposed Woodbury based and PCG methods, the restarting ideas are presented using the Woodbury method as reference.

Firstly, a rank-correction based approach was considered. Herein, the theoretical cost estimates for both the direct solution method and the Woodbury identity based approach are derived using the theoretical flop counts for all necessary sub-steps within a linear analysis, which depends on the rank correction r, the lower and upper bandwidths of the stiffness matrix p, q, and also its size $N \times N$. This rank-based optimal restarting strategy determines the point of restarting by minimising the cost function with respect to the rank r. However, since the approach relies heavily on the estimated bandwidths, which cannot be efficiently deduced for complex geometries, and the fact that the direct solution method (PARDISO) being considered here has a fill-in minimising reordering scheme (which does not necessarily minimise the bandwidth), it is highly unlikely that the prediction for the restarting point would be optimal indeed. Detailed information on the rank-based restarting strategy, and the associated cost functions can be found in Reference [137].

Secondly, a time-estimation based approach was deduced. The computing times of the analysis steps are measured, and an estimate is made for the expected total analysis time. The measured time for a direct solution analysis step (t_d) includes those for factorisation, back- and forward substitutions. The subsequent n_r analysis steps, where n_r denotes the next restarting analysis step, yield the solution using Woodbury method in time $t_w(i)$ where $i = 1, \ldots, n_r$. There are two key assumptions to this restarting strategy:

- The maximum number of analysis steps m is known a priori.

- The total computing time is composed of a sequence of repeating measured patterns (times) after every restart.

Restarting after the n_r^{th} analysis step and assuming that the measured sequence of times $\{t_d, t_w(1), \ldots, t_w(n_r)\}$ repeats until the end of the analysis, the total computing time of the analysis can be computed as shown below, where the second term is pre-multiplied by a typical indicator function (to adjust for the remaining analysis steps after the last of several restarts):

$$t(n_r) = \left\lfloor \frac{m}{n_r + 1} \right\rfloor \cdot \left(t_d + \sum_{i=1}^{n_r} t_w(i) \right) + \mathbb{1}_{\left\{ m - \left\lfloor \frac{m}{n_r+1} \right\rfloor \cdot (n_r+1) \neq 0 \right\}} (n_r) \cdot \left(t_d + \sum_{j=1}^{m - \left\lfloor \frac{m}{n_r+1} \right\rfloor \cdot (n_r+1) - 1} t_w(j) \right)$$

(7.9)

In order to corroborate the assumptions to be realistic, simple performance studies were carried out for a coarse mesh of a 3D reinforced concrete (RC) slab problem, reported in Reference [137]. This RC slab subject to concentrated shear load was previously simulated using SLA [139] under proportional loading conditions. Figure 7.2(a) shows the patterns of elapsed time per linear analysis step/event for the standard PARDISO, and Woodbury Identity based direct solvers (with and without the restarts) for 80 steps.

Figure 7.2(b) shows the total time taken for these 3 cases up to 80 steps, and emphasises the need for restarting. The maximum number of analysis steps m does not have any significant effect on the restarting point derived by optimising Eq. 7.9, and this was also observed as closely spaced restarting points for varying values of m, as shown in Figure 7.3(a). This is because m just appears as a multiplicative constant in Eq. 7.9, and for large cases, one could ignore the second term in Eq. 7.9.
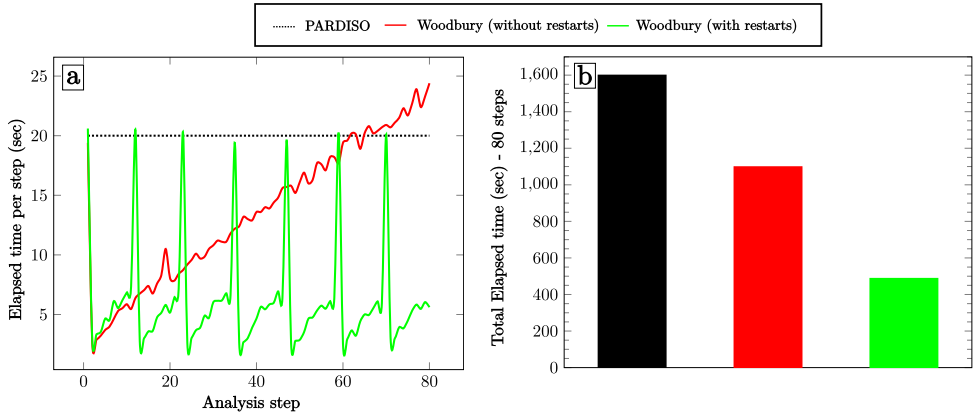

Figure 7.2: (a) Elapsed times per analysis step up to 80 steps of a 3D RC-Slab simulation using the PARDISO and Woodbury Identity based direct solution methods, with and without restarting at the optimal point, and (b) the total elapsed time for the 3 cases up to 80 events
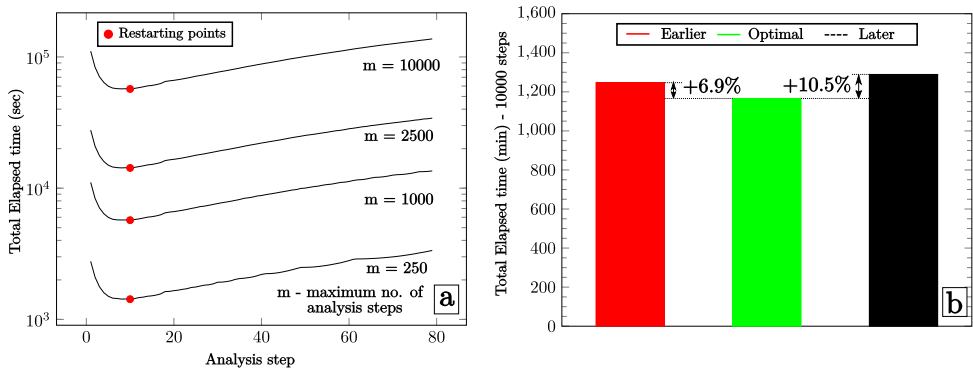
Figure 7.3: (a) Total elapsed times for different values of m i.e. the maximum number of analysis steps illustrating the proximity of restarting points [137], and (b) the total elapsed times until the 10000th analysis step, for the 3D RC-Slab simulation with a finer mesh, comparing the effect of earlier or delayed restarting with respect to the optimal point

Furthermore, the problem was solved with restarting points a few steps before and after the optimal ones, for a finer mesh of the aforementioned case study. Figure 7.3(b)

shows the total analysis times (for 10000 steps in all) for these three cases referred to as *Earlier, Later* and *Optimal*. This study confirmed that continuing longer without restarting results in a performance penalty in the last analysis steps (total analysis time = 1289 mins), while restarting earlier results in too many expensive factorisations (total analysis time = 1247 mins). In comparison, the optimal case takes a total analysis time of 1166 mins. These simple studies validate the assumptions and the restarting strategy by itself. In conclusion, the time-estimation based restarting strategy seems a more reasonable option for the presented solution methods, and is therefore used as reference for the validation and parametric studies presented in Section 7.3. Further information on the time-estimation-based restarting strategy can be found in Reference [137].

7.3. CASE STUDIES

In order to validate the proposed solution strategies, two experimental benchmarks are considered. Firstly, the structural response of both the benchmarks, as simulated using SLA, are briefly touched upon. Thereafter, the computational performance of these reference models (solved with the parallel direct sparse solver) are compared against those solved with the Woodbury identity based method and the PCG. Subsequently, parametric studies are presented in Section 7.3.2.

PUSHOVER ANALYSIS OF A SHEAR WALL (2D)

The first benchmark considered is that of an unreinforced brick masonry wall, 1.35m x 1.1m in size and clamped along the top and bottom edges, firstly subject to an overburden/precompression of 0.6 MPa followed by a quasi-static lateral load. This case study has been previously analysed in Section 4.2. Although the test is cyclic in nature, the test can be used under monotonic loading as a benchmark for 2D (plane stress) SLA simulations by making qualitative comparisons between the response and the envelope of the experimental curve. Diagonal shear failure was observed in the experiment subsequent to reaching the peak force. Further details about the experiment can be found in Reference [6]. The experimental setup and the results of the SLA simulations are shown in Figure 7.4. Modeling and material parameters are given in Table 4.5. Good agreement with the force-displacement curves are observed, however, since the focus of this study/chapter is more on the performance of the solver, further information on the simulation in terms of the 2D finite element model, the agreement between the experimental crack patterns and those from SLA etc., can be found in Section 4.2 or alternatively in Reference [106].

SHEAR TESTING OF A REINFORCED CONCRETE SLAB (3D)

The second benchmark is that of a reinforced concrete (RC) slab (excluding shear reinforcements), 4×2.6×0.3 m in size and simply supported on all 4 sides, firstly subject to an in-plane compressive axial load of 1.5 MPa followed by an out-of-plane concentrated load near one of the line supports. This is the SC2 slab analysed in Section 5.4.2. The axial loads were applied by means of 12 in-plane hydraulic jacks, while the concentrated load was applied at a distance of 560 mm from the line support using an out-of-plane hydraulic jack over a loading plate. The failure mechanism begins with flexural cracks that appeared at
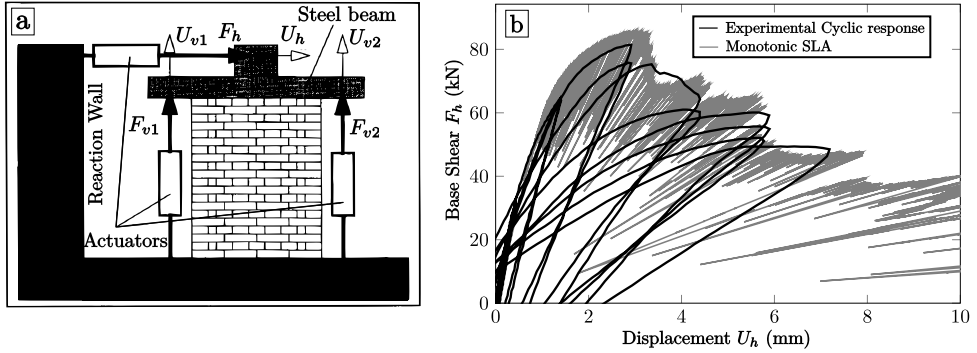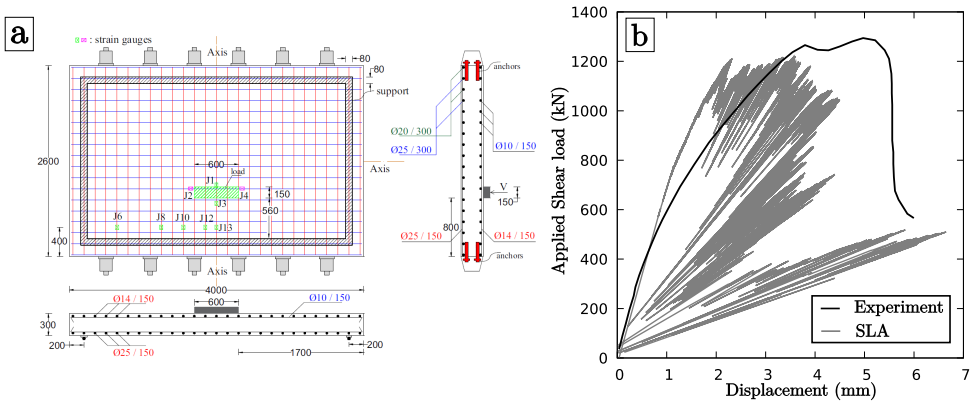
Figure 7.4: (a) Experimental setup of the quasi-static cyclic pushover test, and (b) the comparison of the 2D monotonic SLA results to those of the backbone of the cyclic response [106]

Figure 7.5: (a) Experimental set up of the shear test on reinforced concrete slab: Loading plate, reinforcement layout and axial load application setup [20], and (b) comparison of the SLA & experimental force displacement curves [104]

the bottom face along the transverse and longitudinal reinforcements, followed by cracks due to the two-way shear slab mechanism (punching shear failure) with a perimeter crack surrounding the loading area, and eventually the pure shear failure along the line support which was quite brittle. Further information on the experiment can be found in Section 5.4.2 or in detail in Reference [20]. The experimental setup and the results of the 3D SLA simulations are shown in Figure 7.5. Reasonable agreement is found in terms of the force-displacement curves, and the qualitative brittle behaviour in the simulated failure mechanism. The experimental peak load is predicted reasonably well by the SLA simulation but the ductility is underestimated. However, this is not just a feature of SLA but the smeared crack approach in general, as has been previously observed in another implicit NLFEA simulation [158] and also using a plasticity-based approach in an explicit solver based ABAQUS simulation [93]. Considering the scope of this study/chapter, all information pertaining to the simulation can be found in Section 5.4.2 or alternatively in Reference [104].

7.3.1. DISCUSSION ON PERFORMANCE OF THE SOLUTION METHODS

The Central Processing Unit (CPU) used for this study is an AMD EPYC 7351 processor with 16 cores / 32 threads, a base clock speed of 2.4 GHz, and an all core boost speed of 2.9 GHz. All studies are run on single-threading, unless specified otherwise. CPU time is the exact amount of time spent in processing the data by the CPU for a specific process, while the elapsed time refers to the total time taken for the completion of a process, which is the sum of the CPU and I/O times.

Total analysis times in each SLA step are composed of those for several operations like setting up the element stiffness matrices and assembling the global stiffness matrix (referred to as ELMATR hereon); solving the system of equations for unknown displacements (referred to as SOLVE hereon); calculation of stresses and strains from the displacement field (referred to as STREAC hereon); and determining the critical integration point and the load multiplier, scaling stresses & strains, and finally updating the stiffness & strength of the critical integration point (referred to as SLSCAL hereon). Times per analysis step for all these operations, except SOLVE, would approximately be the same for a simulation run using either the reference parallel direct sparse solver (PARDISO) or the proposed solutions methods presented in Section 7.2.1 & 7.2.2. This is clear from the elapsed times of the Shear wall and RC Slab case studies run on a single-thread of a processor, as shown in Table 7.1.

Table 7.1: Contributions of dominant processes to total elapsed times on a single thread - Shear Wall & RC Slab

Description	PARDISO		Woodbury		PCG	
	Shear Wall	RC Slab	Shear Wall	RC Slab	Shear Wall	RC Slab
SOLVE - Solve system of linear equations	43.57 %	65.69 %	13.70 %	26.86 %	29.56 %	49.08 %
	(10.07 min)	(282.24 min)	(2.15 min)	(54.15 min)	(5.52 min)	(145.57 min)
STREAC - Calculate strains and stresses	20.15 %	11.49 %	30.42 %	24.67 %	24.95 %	17.12 %
from displacement fields	(4.66 min)	(49.39 min)	(4.77 min)	(49.32 min)	(4.69 min)	(50.76 min)
SLSCAL - Determine critical int. point (IP) and λ_{crit},	32.54 %	22.01 %	50.06 %	46.98 %	39.98 %	32.49 %
update stiffness of IP, and scale results	(7.52 min)	(94.58 min)	(7.85 min)	(94.72 min)	(7.51 min)	(96.35 min)
Total elapsed time	23.12 min	429.65 min	15.69 min	201.63 min	18.78 min	296.557 min

Thus, the CPU time per analysis step to solve the system of equations (SOLVE) is chosen as the yardstick to compare the performance of the PARDISO, Woodbury and PCG solvers. The pattern of CPU times for the first 1000 analysis steps is illustrated in Figure 7.6 for the shear wall and RC slab studies. On the one hand, the PARDISO cost as expected is roughly constant throughout the analysis since the stiffness matrix factorisation and the backward and forward eliminations to obtain the solution are repeated every analysis step. On the other hand, Woodbury and PCG gain speed by reusing the factorisation repeatedly until the optimal points of restart are reached. This pattern of an expensive analysis step followed by relatively cheaper steps is clearly seen in Figure 7.6(b).

In the time patterns for the 2D shear wall example shown in Figure 7.6(a), two types of fluctuations are observed regardless of the solver type. One, when there are other
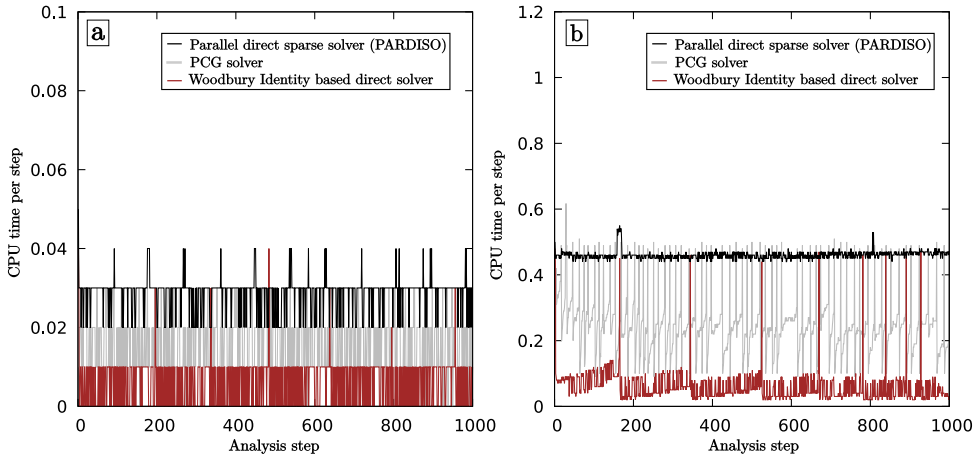
Figure 7.6: Comparison of CPU time taken per analysis step by the SOLVE block of the PARDISO, PCG and Woodbury solvers: for the (a) Shear wall and (b) RC Slab cases, shown for the first 1000 steps

jobs simultaneously running on the same processor (higher anomalous peaks), while the other is when the measured time is so small, of the order of 0.01 seconds, that minor variations seem accentuated thereby giving an impression of rather unstable patterns. However, qualitatively, PARDISO gives a constant response at an average of 0.03 seconds per analysis step, while PCG and Woodbury based solvers take lower times. Whenever the Woodbury's identity is restarted (six times up to the 1000th analysis step - brown peaks), the time tends to be equivalent to that of PARDISO. After restarting, the times for the Woodbury approach are reduced to an average of 0.005 seconds. However, in comparison, the performance of PCG is poorer. This is attributed to the fact that the bandwidth of the stiffness matrix is relatively small for 2-dimensional problems. Consequently, backward and forward substitutions are relatively more expensive than a matrix factorisation. Since PCG uses these backward and forward substitutions every analysis step to apply the preconditioner, costs for PCG based method increase quicker in the intermediate steps thereby demanding more frequent restarts in comparison to the Woodbury based solver.

In case of the 3D RC slab, a similar trend is observed in the time patterns of the three solver types, refer Figure 7.6(b). The aforementioned fluctuations are not that apparent here since each analysis step takes times in the order of 0.1 seconds. The only interesting point is that the performance of PCG is a little different compared to the 2D shear wall problem. The times for the intermediate steps do not increase as sharply as for the 2D problem because of the larger bandwidth of the stiffness matrix for 3D problems. This results in the back- and forward substitutions becoming relatively cheap compared to the matrix factorisation. However, over both cases, Woodbury outperforms PCG on a single-threading, because of the relatively lower rate of increase of time in its intermediate steps.

In summary, the total elapsed time to solve the system of equations (SOLVE) decreases by a factor of ~ 5 using the Woodbury solver as against PARDISO for both the shear wall and RC slab cases, whose model sizes are roughly 3400 DOFs and 11100 DOFs respectively.

These problem sizes are extremely small in reference to the range illustrated in Figure 7.1 and therefore, for bigger problem sizes, the gains would be significantly higher. A parametric study on problem sizes for the 3D RC slab is presented in Section 7.3.2. However, the improvement of PCG solver over PARDISO is only by a factor of ~ 2 for both case studies, due to PCG using back- and forward substitutions every analysis step to apply the preconditioner. An interesting point of observation, with regard to the Woodbury solution, is that when the rank-update is very high owing to complete loss of stiffness, the solution time exceeds the direct solution time step. To address this, restarts were prescribed for such unforeseen steps, wherein the rank update in one analysis step is large, i.e. close to the rank of the critical element matrix, in addition to the time-estimation based restarting steps as detailed in Section 7.2.3.
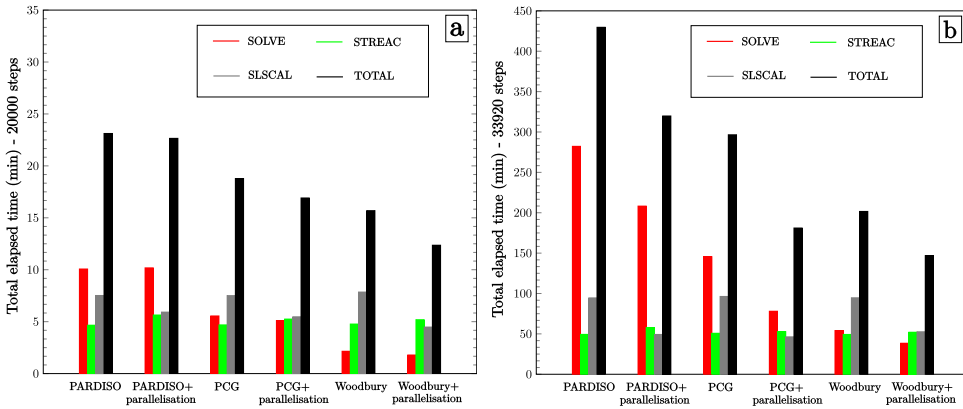
Figure 7.7: Performance of the PARDISO, PCG and Woodbury based direct solution methods, with and without parallelisation, in terms of total elapsed time for the two case studies: (a) Shear wall and (b) RC Slab

Parallel computing   The performance of both the proposed methods have been illustrated, thus far, using 2D and 3D simulations run on a single-thread of a processor. Table 7.1, summarising the times for major operations in the work flow of SLA, indicates that with improved times for solving the system of equations (SOLVE), the SLSCAL and STREAC building blocks become the bottleneck. To address this and further improve the computational performance of SLA, the operations in SOLVE and SLSCAL have been parallelised. Furthermore, the calculation of stresses and strains in STREAC can also be computed in parallel but this is not taken into account in this study. The result of multi-threading on the performance of the PARDISO, PCG and Woodbury solvers for the two case studies, using 4 threads of the AMD processor (Section 7.3.1), is shown in Figure 7.7. Firstly, for the 2D shear wall simulation, the SOLVE blocks of the Woodbury and PCG methods (with multi-threading) improve over PARDISO by the same factors of ~ 5 and ~ 2 respectively, as observed in single-threading. Additionally, PARDISO's performance with multi-threading is similar to its single-threaded counterpart since the problem is 2-dimensional and is small in size. While in the case of SLSCAL, times are reduced with multi-threading owing to the fact that many operations in this block are

otherwise carried out sequentially for each integration point. Secondly, with regard to the 3D RC slab simulation, the SOLVE blocks of the Woodbury and PCG methods (with multi-threading) again improve over PARDISO by factors of ~ 5 and ~ 2 respectively, as observed in single-threading. The effective gains made in SOLVE due to multi-threading is greater for PCG in comparison to the Woodbury solver. This is because in PCG's case the number of restarts is greater, and with multi-threading, the factorisation and repeated back- and forward substitutions become cheaper. Additionally, PARDISO's performance with multi-threading shows an improvement over its single-threaded counterpart as it is highly optimised for parallel computing. The improvement is more apparent compared to the 2D case because the problem is 3-dimensional and is a larger case study. Furthermore, the effect of parallel computing on PARDISO is expected to increase with increasing problem sizes. In case of the SLSCAL block, all three solvers gain by a factor ~ 2 since the number of integration points in this case is higher than the 2D case, and therefore the positive effect of multi-threading is greater. In summary, upon multi-threading, all 4 possible combinations (of Woodbury and PCG - with or without multi-threading) are an improvement over the traditional direct solution method (PARDISO) in terms of the total elapsed times.

7.3.2. SENSITIVITY STUDIES: SAW-TEETH & MESH-SIZE OBJECTIVITY

EFFECT OF NUMBER OF SAW-TEETH ON SOLUTION METHODS

In order to understand the effect of refinement of the saw-tooth law (p-factor) (as shown in Figure 2.2), on the performance of the presented solution strategies in Sections 7.2.1 & 7.2.2 and their corresponding restarting approaches, a parametric study is carried out. Only the 3D RC slab is considered for this study since the total computation time is higher than the 2D example, and is therefore more interesting. The single-threaded response elaborated in Section 7.3 is treated as reference. By adjusting the saw-teeth discretisation parameter (p) for the number of saw-teeth in the tensile softening relation, four cases are considered: 5, 9 (reference), 11 and 13 saw-teeth, while the compressive softening relation is kept unchanged with respect to the reference case (since the compressive failure does not influence the failure mechanism).

   Figure 7.8(a) shows the force displacement relation for the four considered cases, all run on single-threading. It is evident that with increase of the number of saw-teeth (or decrease in p-factor), the peak loads decrease by a small amount. This is attributed to the corresponding shift in strength properties based on the ripple band approach (Figure 2.2). The tail part of the post-failure response, as seen in Figure 7.5(b), is not shown here for the 4 cases because of the small differences between them. However, qualitatively, the onset of brittle failure begins approximately around the same displacement, and a similar ultimate load and failure mechanism are obtained in all the cases. Therefore, in order to objectively compare the computation times of the responses, the onset of brittle failure for each response is treated as the reference point. The number of analysis steps (events) to reach the reference points are 11233, 26202, 38000 and 43051 for the 5, 9 (reference), 11 and 13 tensile saw-teeth cases respectively.

   The total and SOLVE block elapsed times for all four responses, to reach their respective onsets of brittle failure, are illustrated in Figure 7.8(b), and additionally, in Figure 7.9.
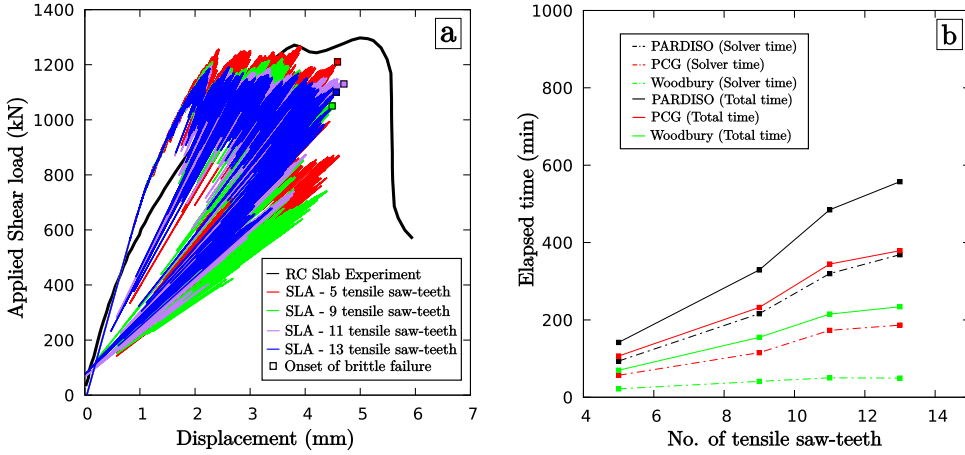
Figure 7.8: (a) Force-displacement curves of 4 FE models with different number of saw-teeth for the tensile softening relation and their corresponding onsets of brittle failure, and (b) the total & SOLVE block elapsed times for these cases with regard to the three types of considered solvers.
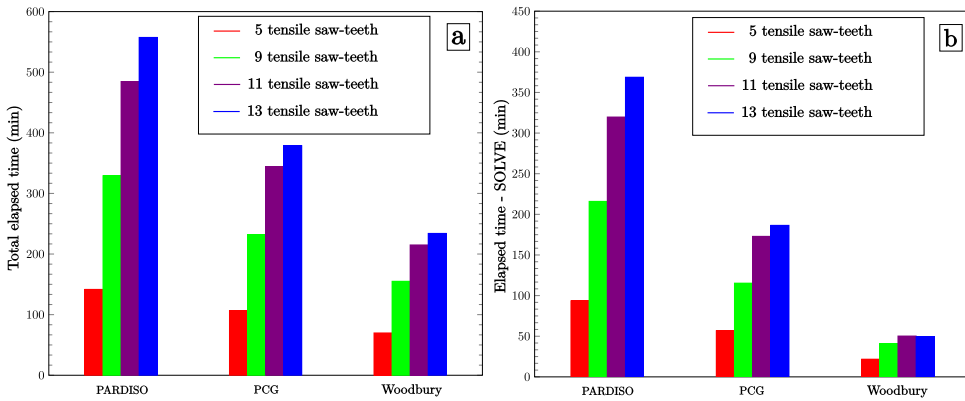

Figure 7.9: Saw-teeth parametric study using the PARDISO, PCG and Woodbury solvers showing (a) Total and (b) SOLVE block elapsed times

When the saw-tooth model is rather coarse, the number of events required to reach the onset of brittle failure is lower as against a finer one. That is, regardless of the solver type, the total number of SLA steps required is anyway lower for a coarser saw-tooth model, and therefore the total analysis time also drops. This is reflected in the trends of Figure 7.9(a),(b) and as expected, both PCG and Woodbury outperform PARDISO. However, the point of interest lies in the amount of gain that Woodbury or PCG make over PARDISO which increases with increasing number of saw-teeth, and this is evident in both Figures 7.8(b) and 7.9. This is attributed to the inherent increase in the number of events required, and also to the fact that the time-estimation based restarting strategy is indirectly related to the rank-update per analysis step in SLA. With increasing number of saw-teeth in the constitutive model, the rank update per analysis step decreases. In
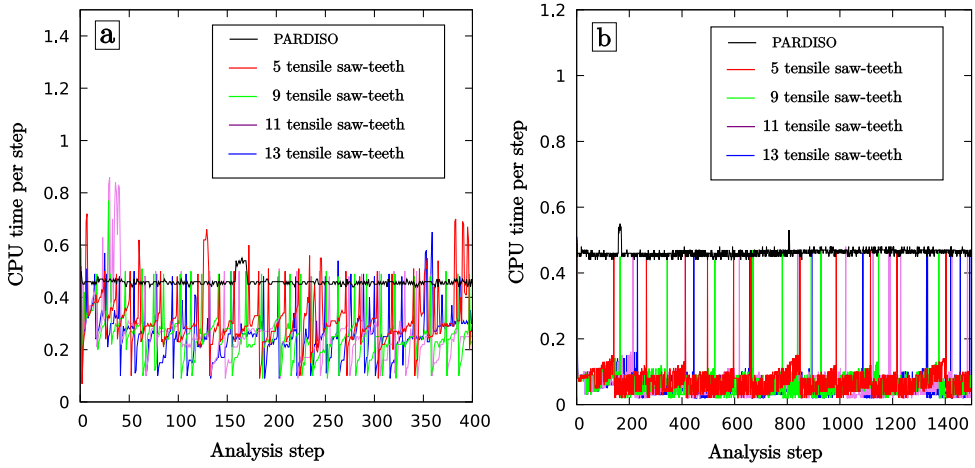
Figure 7.10: (a) Performance of PCG and (b) Woodbury solvers, with respect to PARDISO for the 4 cases in the saw-teeth parametric study

other words, the jump in rank is more abrupt for a coarser saw-tooth law as against a finer saw-tooth law. Therefore, the rate of increase of the times for intermediate steps and the proximity of the restarting steps is influenced by the saw-tooth discretisation which in turn affects the amount of gain.

The typical pattern of expensive steps followed by cheaper steps for all four cases, with Woodbury and PCG based solvers, is illustrated in Figure 7.10, and these patterns are identical to those presented in Figure 7.6(b). Only the first few analysis steps are shown herein, and the variations in the number of restarts needed for the different cases is more evident in the performances of the Woodbury based solver (Figure 7.10) which in turn affects the gain. The performance can be further improved using parallel computing, as detailed in Section 7.3.1, to reduce the total time shown in Figure 7.9(a), but is not presented here owing to triviality.

EFFECT OF PROBLEM SIZE ON SOLUTION METHODS

In order to understand the effect of mesh refinement on the performance of the Woodbury and PCG solvers, another sensitivity study is carried out. Once again, only the 3D RC slab is considered for this study because of the higher computation times involved. The response elaborated in Section 7.3 is treated as reference, wherein the average size of the 20-noded iso-parametric solid brick element is approximately 150 mm. Three other cases with average element sizes of 100 mm, 75 mm and 50 mm are considered. In terms of the total number of degrees of freedom (DOFs), the four cases translate to 11175 (reference), 31443, 56910 and 181182 DOFs. The three new simulations are run with the same parameters as in Table 5.4 except that the saw-teeth discretisation factor (p) is increased to 0.25 to reduce the total number of events, in order to avoid extremely higher computation times. The finite element models of the 4 cases are shown in Figure 7.12(a).

Figure 7.11(a) shows the force displacement relation for the four considered cases, all
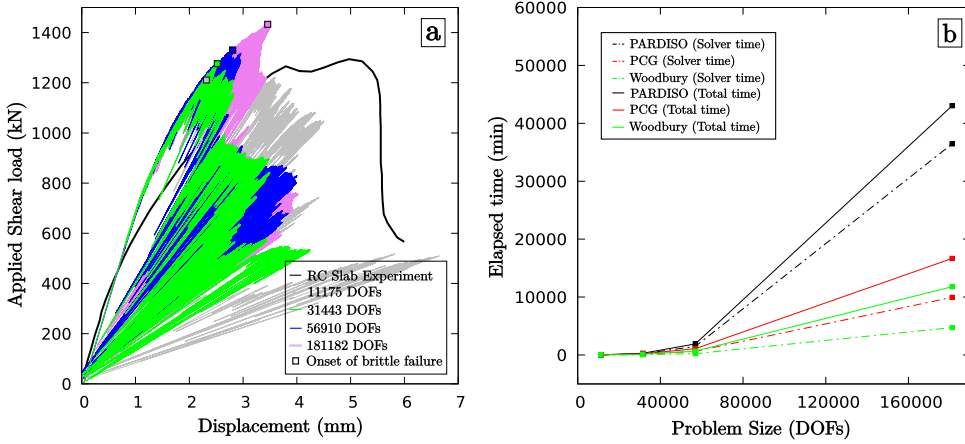
Figure 7.11: (a) Force-displacement curves of 4 FE models with different mesh sizes and the corresponding reference points for comparison, and (b) the total & SOLVE block elapsed times for these cases with regard to the three types of considered solvers.

run on multi-threading (4 cores). It is observed that results are closer to the experimental peak load upon mesh refinement but the finest mesh overshoots the experimental peak load by 150 kN. A similar failure mechanism is observed for the finer meshes but the reference case clearly suffers from mesh objectivity problems, refer Figure 7.12(b). However, this is not a feature just of SLA and is also observed in NLFEA in general, since the brittle shear failure when simulated using 150 mm elements (2 elements over the depth of the slab) instead of 100, 75 or 50 mm elements (3, 4 and 6 elements over depth of slab respectively) could be affected by mesh-directional bias, although the smeared cracking approach based on the traditional crack band theory limits element size dependency. The one way shear failure mechanism is captured better by the finer meshes as shown in Figure 7.12(b). Therefore, in order to objectively compare the computation times of the responses considering the structural response, the peak loads reached in each response (which is followed by the brittle collapse) are treated as the reference points (denoted in Figure 7.11(a)).

It is well known that for a band solver, the calculation of a matrix factorisation scales ($\mathcal{O}(Nb^2)$), and back- and forward substitutions scale ($\mathcal{O}(Nb)$), with respect to the problem size N and bandwidth b (given by ($\mathcal{O}(N^{\frac{(d-1)}{d}})$)) wherein d is the dimension of the problem) [56]. Therefore, for 3D problems, factorisation and back/forward substitution scale ($\mathcal{O}(N^{\frac{7}{3}})$) & ($\mathcal{O}(N^{\frac{5}{3}})$) respectively. The reinforced slab problem is 3-dimensional, and therefore the bandwidth of the stiffness matrix increases significantly faster for increasing problem sizes. Consequently, the number of non-zeros within the bandwidth increases faster, and the number of calculations to be performed on these non-zero elements increase. This manifests as the nonlinear trend observed in Figure 7.11(b) for all three solution methods. For smaller problems, the costs of factorisation and back- and forward substitutions are low. However, most of the performance that is gained with the solution methods is compensated by relatively expensive overhead costs for setting up Woodbury's
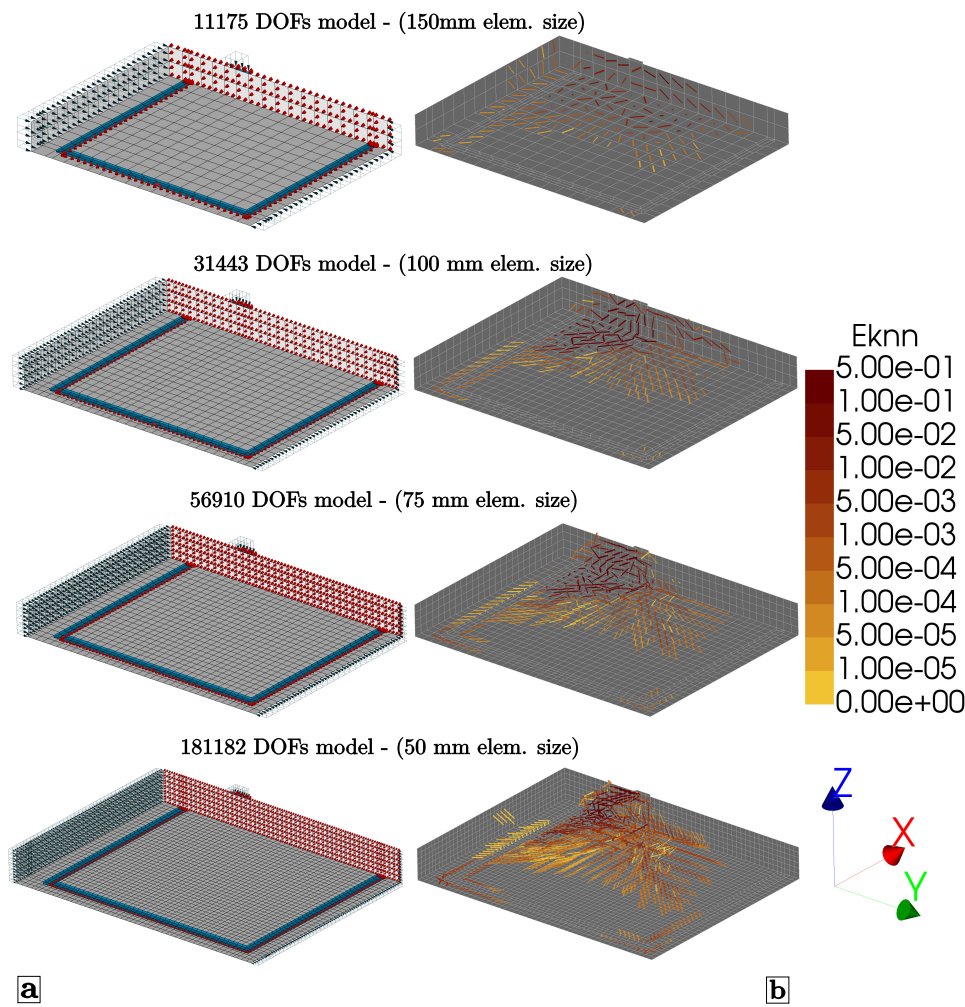
Figure 7.12: (a) Finite element models (halves - using symmetry along global X) for the 4 cases with average element sizes of 150 mm, 100 mm, 75 mm and 50 mm: showing the axial loads (along global Y), concentrated shear loads (along global negative Z), and the boundary conditions (simple supports along blue steel plates and for symmetry along the mid-face), and (b) the corresponding crack pattern plots (Eknn denotes the normal crack strain) at the ends of the respective collapses

identity and PCG; which include allocating memory, creating arrays and initialising the PARDISO interface for the back- and forward substitutions. Since these costs do not depend on the problem size, with increasing problem sizes the influence of the overhead costs on the overall performance drops.

The gains made by the proposed solution methods compared to the PARDISO, all run with 4 threads of the AMD processor (Section 7.3.1), are summarised in Table 7.2 in terms of factors of improvement. The PARDISO performance is treated as unity. SOLVE

Table 7.2: Factors of improvement of Woodbury & PCG methods over PARDISO's performance treated as unity

Problem Size (DOFs)	Analysis steps (events)	SOLVE			TOTAL		
		PARDISO	PCG	Woodbury	PARDISO	PCG	Woodbury
11175	3999	1.0	1.80	4.38	1.0	1.29	1.58
31443	8049	1.0	1.98	5.08	1.0	1.54	2.30
56910	23708	1.0	2.34	6.42	1.0	1.77	2.87
181182	93328	1.0	3.66	7.72	1.0	2.58	3.65

improves by a factor of ~ 8 with Woodbury and ~ 4 with PCG for the largest case of 181182 DOFs. All simulations are run fully except the PARDISO ones, because of the enormous run-times, and the total times for PARDISO necessary to calculate the factors depicted in Table 7.2, are extrapolated based on the average of the first 3000 steps of the simulations for each of the cases.

In case of 2D problems, the factorisation scales ($\mathcal{O}(N^2)$) and back/forward substitutions scale ($\mathcal{O}(N^{\frac{3}{2}})$) for band solvers. Although the influence of problem sizes on the 2D case study is not illustrated here, previous studies [137] show an almost linear scaling of the direct solution, contrary to that of the 3D case. This can be attributed to the relatively small growth in bandwidth due to the problem being 2 dimensional. For 3D problems, the bandwidth of the matrix generally grows significantly faster due to the inherent numbering of the degrees of freedom. Furthermore, as previously pointed out in Section 7.3.1, for 2-dimensional problems the back- and forward substitutions are relatively expensive and therefore, for increasing problem sizes, the performance of PCG was observed to remain largely equal to that of the direct solution method while the Woodbury method gained. Detailed information on the performance of the methods for the 2D case with regard to problem sizes can be found in Reference [137].

7.4. CONCLUDING REMARKS

This chapter addresses the high computational intensity of Sequentially Linear Analysis (SLA), an alternative to NLFEA for civil engineering applications, through two solutions methods that use the favourable event-by-event strategy of the method. Since numerous linear analyses have to be solved, each requiring an expensive stiffness matrix factorisation that only changes locally, the proposed methods reuse the factorisation of a certain analysis step followed by steps involving small matrix and vector manipulations to solve a significantly smaller system of equations. The first method is that of direct solution method, wherein Woodbury's matrix identity is applied which allows for a numerically efficient computation of the inverse of a low-rank corrected matrix. The second method is a preconditioned CG, wherein instead of using an ILU preconditioner, the complete LU factorisation of the stiffness matrix is used as preconditioner for the CG. Due to the quality of this preconditioner, few iterations are required every analysis step. Furthermore, an optimal time-estimation based restarting strategy is derived, for both the approaches, to determine the point at which a new factorisation should be calculated. The restarting strategy is additionally forced to have restarts when there are unforeseen high rank updates, resulting in times higher than that of the PARDISO, contrary to the assumed repeating patterns of time. Additionally, parallel computing is introduced for certain sec-

tions of SLA's algorithm (including those of the proposed solution methods), where there is need for calculations at integration point level, to further improve the computational performance.

Table 7.3: Contribution of the three dominant processes - SLSCAL, STREAC and SOLVE, in %, for the 4 cases of Section 7.3.2

Problem Size (DOFs)	SOLVE			STREAC			SLSCAL		
	PARDISO	PCG	Woodbury	PARDISO	PCG	Woodbury	PARDISO	PCG	Woodbury
11175	63.08	40.9	22.73	17.79	30.21	37.59	16.73	24.84	34.69
31443	73.33	57.15	33.23	14.08	21.47	34.61	11.20	18.28	27.30
56910	77.68	58.72	34.76	12.00	20.86	34.21	9.25	17.41	26.26
181182	84.70	59.71	40.08	7.59	19.02	28.08	7.02	18.52	27.72

Two benchmark cases, involving non-proportional loading (which further increases the computational intensity of SLA due to the additional need for solving quadratic and cubic equations for undamaged integration points), are chosen to elucidate the performance of the proposed solution methods compared against a traditional direct linear solver like PARDISO. The first one is of a masonry wall subject to overburden followed by a lateral load, and the second, a prestressed reinforced concrete (RC) slab subject to axial loads followed by a concentrated shear load, simulated using 2D-plane stress and 3D models respectively. Both the proposed solution methods perform significantly better than PARDISO, especially for 3D problems, and the Woodbury identity based solver seems the better choice of the two proposed methods. Furthermore, numerical experiments on the sensitivity of the proposed methods were performed for the 3D RC slab case. Firstly, the number of tensile saw-teeth in the constitutive model was varied, and as the saw-teeth became finer, the gains made by both the proposed methods over the direct linear solver (PARDISO) increased. The finer the saw-tooth model, the larger the number of events that are required to bring about a similar mechanism as in the response using a coarser saw-teeth model. The proposed time-based restarting strategy used by both methods relies indirectly on the rank update per linear analysis, which in turn depended on the fineness of the saw-tooth model. Since the rank update per analysis step is smaller for finer cases, which results in a lower rate of increase in time for the intermediate steps, the effective number of restarts are lower, and therefore the gains are significant. Secondly, the effect of problem size on solution methods was studied, and both methods gained significantly over PARDISO for increasing problem sizes. SOLVE, the bottleneck as illustrated in Figure 7.1, for large problem sizes is not the constraint anymore as is shown in the drop of contribution to total times from about 85 % to about 40 % in the 181182 DOFs case, refer Table 7.3. However, the remaining two blocks now become equally intensive. There is further scope for improvement as multi-threading is yet to be introduced in STREAC.

In conclusion, to achieve higher speeds for typical FE models used in SLA, the use of Woodbury identity based solver is recommended, in combination with parallel processing. Furthermore, coarser saw-teeth are recommended for faster simulations, and further research is required to find an optimum number of saw-teeth for the best performance with regard to both computational and mechanics aspects.

CONCLUSIONS & OUTLOOK

Sequentially Linear Methods (SLM), of which the Sequentially Linear Analysis (SLA) is a feature, offer a robust alternative to traditional incremental-iterative methods in the finite element analysis of quasi-brittle structures, e.g. those made of concrete and masonry. It helps overcome convergence issues associated with post-peak softening behaviour, due to the combined use of secant-stiffness based discretised constitutive relations and the event-by-event damage-driven approach. This thesis took shape with the main objective of extending the sequentially linear framework to enable typical 3D structural applications, such as pushover analyses on masonry structures and shear strength assessment of reinforced concrete structures/components.

8.1. REVISITING THE OBJECTIVES

In this regard, the following specific objectives were formulated, and the novel contributions of the thesis are summarised accordingly.

1. **Objective**: *"To develop a better understanding of the redistribution mechanism involved in sequentially linear analysis under non-proportional loading conditions"*. The SLA approach combined with the double load multiplier strategy, under non-proportional loading conditions, is directed to an *Intermittent Proportional Loading* when there is no constitutively admissible load multiplier (referred to as *limit point*[*] throughout the thesis) for variable loads on the FE model. Although correctly aimed at avoiding violations of the constitutive law at some integration point in the FE model, it was not clear as to what the origin of this problem was, with the lack of crack-closure algorithm being highlighted as a possible reason in one of the previous structural case studies [55]. Furthermore, the need for multiple failures subsequent to a unique damage increment to bring about the redistribution was also indicated as a possible reason, thereby concluding that the Intermittent Proportional Loading is "a *particular* method to obtain a set of multiple damage increments after which static equilibrium is re-established" [139].

   Scientific Contribution: Chapters 3 & 4 aim to analyse this problem by first assessing all sequentially linear methods, and their approaches to the non-proportional loading problem. The methods are classified as *total*, *incremental* and *combined incremental-total*, and an extensive qualitative review is presented on these methods highlighting the primary differences in load modification, and on how they address the multiple failures. Based on this preliminary understanding and to further extend it to continuum structural applications, in a first of its kind, three case

---

[*]The terminology of *limit point* is not to be confused with the traditional limit point encountered in NLFEA.

studies involving real structural collapse were analysed to exemplify the differences between a *total* approach: SLA with the double load multiplier strategy, and an *incremental* approach: the Force-Release method. The latter is an incremental sequentially linear method that allows for gradual stress redistribution after each damage increment, while simultaneously keeping track of the loading history. The conclusions drawn based on this study are summarised in Section 8.2.

2. **Objective**: *"To extend the constitutive models in SLA and develop the non-proportional loading strategy for full 3D stress states".* Most of the existing constitutive formulations used in SLA were 2-Dimensional. Structural level simulations motivate the need for 3D constitutive formulations with view to non-proportional loading conditions.

   Scientific Contribution: Chapters 5 & 6 aim to address this problem and are summarised in the following.

   - Chapter 5 addresses the lack of a closed form solution for the critical load multiplier in a 3D continuum stress state under non-proportional loading, which hinders the switch from the isotropic to the orthotropic formulation in a fixed smeared cracking framework. Accordingly, two novel strategies are proposed to allow for damage initiation in the 3D Orthogonal smeared fixed cracking model [150] (with additionally possibility of crushing failures) under non-proportional loading conditions. The first approach involves analytically solving two cubic equations in the load multipliers per undamaged integration point (tension and compression failures). This is done by first manipulating the equations into monic trinomials, and subsequently, solving the depressed cubic equations using the *Cardano method* or *trigonometric solutions* (for one or three real roots respectively) depending on the discriminant of the equation. The second approach involves a reformulation of the case as an *optimisation problem*, wherein the load multiplier is expressed as a function of the inclination of a potential failure plane. The approach finds solutions to the inclination of the critical plane, i.e the directional cosines and consequently, determines the critical load multiplier. The conclusions drawn based on this chapter are summarised in Section 8.2.

   - Chapter 6 proposes a simplified compression cap extension to the discretised tension-shear criterion (using the step-wise secant relations for discrete cracking and Coulomb friction [139]) to be used in the sequentially linear framework. This makes it possible to analyse masonry components using the micro-modelling approach, in combination with sequentially linear methods, until structural collapse. The proposed constitutive model is a *composite failure criterion* with: 1) a tension gap criterion coupled with a uniaxial linear tension softening law, 2) an uncoupled step-wise secant Coulomb friction formulation that discards dilatancy effects but allows for cohesion softening, and 3) a simplified compression cut-off criterion coupled with a uniaxial parabolic hardening-softening law. This formulation is presented for line (2D) interfaces, and additionally, for planar interfaces (3D) to enable structural simulations.

8

Furthermore, the formulations are also verified and validated for use with an incremental approach, the Force-Release method. The conclusions drawn from this study are summarised in Section 8.2.

3. **Objective**: *"To develop tailor-made solvers in order to efficiently solve the system of linear equations in an SLA setup".* The event-by-event nature of SLA, which effectively changes the system of linear equations only locally per analysis, is not efficiently utilised by traditional direct solvers.

   Scientific Contribution: Chapter 7 proposes two new solvers namely the *Woodbury-Identity based direct solver* and a *Preconditioned Conjugate Gradient solver* to improve the computational performance of SLA. Both solvers perform the expensive factorisation of the global stiffness matrix only in a few steps. In the first method, the inverse of the low-rank corrected stiffness matrix in the remaining steps is computed using the Woodbury-matrix Identity, which is a generalisation of the *Sherman-Morrison* formula for an arbitrary rank-r correction. Therefore, these steps use the old factorisation, and the equations are solved with minimal matrix-vector manipulations. In the second method, the said factorisation is used as a preconditioner in the traditional Conjugate Gradient method to obtain faster converged solutions in the remaining steps, which involve a range of matrix-vector manipulations. Both solvers use a time-based restarting strategy which invokes factorisation of the stiffness matrix only at certain steps such that the total analysis time is optimal. The performance of both solvers is extensively studied using a 2D and 3D case study, additionally, with saw-teeth refinement and mesh-refinement sensitivity studies to draw the conclusions summarised in Section 8.2.

8.2. CONCLUSIONS

Non-proportional loading

The main conclusions from the study of Chapters 3 & 4 are as follows:

1. Oncoming dynamic failure processes at limit points in an SLA type response for structural level examples can be distinguished into *intermediate local instabilities* or the eventual *collapse* mechanism. Depending on the type of dynamic failure, the interpretation of the SLA results varies. In case of *intermediate local instabilities*, if the intermittent proportional loading allows for a redistribution which helps recover the full value of constant load, the redistribution is deemed acceptable. One such zone is observed around the first peak load of the pushover case study on a masonry facade in Section 4.1.4. However, if the redistribution results in gradual loss of constant loads to extremely low values, much ahead of the actual structural collapse, as observed in the case study of a pushover on a squat masonry wall in Section 4.2, then the results have to be interpreted accordingly. This could either correspond to alternate equilibrium paths of damage propagation that do not culminate in the actual expected collapse mechanism or be interpreted as premature structural failure. On the contrary, in case of the eventual *collapse*, the intermittent propor-

tional loading forces a relaxed mechanism maintaining equilibrium all through
the simulation. In other words, SLA lets the damage progress quasi-statically by
releasing previously applied loads thereby allowing the structure to relax during
a dynamic collapse. Herein, as against overall unloading of the structure, only
the elastic parts on either side of active damage zones unload. This is acceptable
under non-proportional loading conditions *only* if the experiments are controlled
quasi-statically. Since the system as whole is allowed for *an overall* quasi-static
damage propagation, it may be interpreted to be equivalent to CMOD controlled
experiments as in Reference [122] which involve a *unique* damage process zone. In
case of *multiple* cracks developing in the system, SLA does not control a *unique*
damage process zone as in a CMOD experiment, and therefore may incorrectly
decrease it.

2. However, interpretations aside, it is clear from all case studies in Chapters 4 & 6
that the limit point situation, and the associated need for intermittent proportional
loading is not an artefact of the stress locking problem in a typical smeared fixed
model (also verified for smeared rotating model [19]), Coulomb friction model, or
even the discrete cracking model. It means that irrespective of the constitutive
model used, there is a need for multiple failures at certain points in an SLA simula-
tion (as previously concluded [139]). In such a scenario, a problem arises owing to
the inherent *non-proportional unloading & reloading* on a damaged state of the
structure, and therefore intermittent proportional loading follows. Furthermore, it
is exemplified using an example in Section 8.3 that the crack-closure problem is
also an effect of the said non-proportional reloading on the damaged state.

3. Comparative studies between the SLA and Force-Release approaches throughout
the thesis further substantiate the above conclusions on the dynamic propagation
of damage, which is addressed statically by both approaches through a sequence of
failures referred to as the *avalanche of ruptures*. On the one hand, the SLA approach
does so by temporarily releasing existing loads and maintaining equilibrium, while
the Force-Release traverses through disequilibrium states for a constant imposed
displacement. These studies also exemplify the characteristic aspects of both
approaches, at the continuum level, as summarised in the following.

   • In terms of the force-displacement curves, the differences in the Force-Release
     and SLA responses are due to their inherent load modification approaches.
     Since every damaged element's stress is released instantaneously in SLA, the
     neighbouring elements whose stresses are close to their respective allowable
     strengths, subsequently, become critical at a considerably lower load. This is
     possible in SLA only by the temporary release of the load, which essentially
     explains the snap-backs. The Force-Release, on the other hand, releases
     the stresses gradually through disequilibrium states while maintaining all
     previously applied loads (displacement history), and therefore shows drops of
     load for constant displacements.

   • In general, it is observed across all three case studies of Chapter 4, and further-
     more the case study in Chapter 6 that the non-proportional loading strategy

in a *total* approach like SLA, and the *incremental* solution obtained using a Force-Release method result in the qualitatively similar results i.e. damage patterns, despite the aforementioned differences. The contrasting differences observed between the approaches in lattice modelling applications, for e.g. in the elemental failure sequence as in the work of Elias [44], are not observed in structural case studies since the change in stiffness due to a single damage event is not so abrupt and large. Therefore, the redistribution of the energy into the vicinity as is done in the Force-Release method does not cause further failure before attaining equilibrium. In principle, it could also be extended that a very fine saw-teeth formulation would result in near-equivalent responses using the SLA and Force-Release methods.

- The suitability of the two methods depends on the type of experiment being simulated. Force-Release method is suitable for typical displacement controlled experiments which actually exhibit instabilities. On the other hand, it may not be suitable for physical processes which exhibit snap backs or for truly quasi-static experiments. SLA is more preferable when the damage process zone is unique and controlled for quasi-static evolution in an experiment [122]. However, for a CMOD controlled experiment with multiple cracking zones, SLA may not be appropriate. Force-Release method, in this case, may increase the CMOD due to the redistribution. In a quasi-static sequentially linear setup, a truly CMOD controlled experiment with multiple evolving damage zones can be appropriately simulated by the *general* method [43].

Constitutive modelling

The main conclusions from the study of Chapter 5 are as follows:

1. Although successfully validated for 2D plane stress states [106], the reformulated optimisation approach to determine the load multiplier for damage initiation in 3D continuum stress state (under non-proportional loading) is computationally intensive, and also cannot guarantee solutions that match up to the analytical solution. This is owing to the optimisation being 2D (with respect to the 2 directional cosines), which requires multiple restarts to verify the obtained root for convergence. Therefore, the analytical approach is preferred and recommended for further studies using the 3D smeared cracking concept. Nevertheless, the validity of the optimisation concept as such remains.

2. 3D Multi-directional cracking is adequately captured using the smeared fixed cracking model, despite the shear locking issues, as shown in the RC slab study of Section 5.4.2. However, similar to NLFEA, mesh-directional bias is an issue as confirmed by the study on mesh-objectivity in Section 7.3.2. To this end, the crack tracking algorithms proposed by Slobbe [131] or Cook et al. [28] could help if extended to a 3D formulation, and furthermore, make the procedure less intensive by reducing the number of possible computations to deduce each event.

3. A recent study by Bresser [19] successfully uses the analytical approach for damage initiation in the elastic-brittle fraction model for 3D stress states. This further substantiates the validity of the approach.

4. Non-planar 3D curved cracking is also captured well under non-proportional loading situations.

The main conclusions from the study of Chapter 6 are as follows:

1. The proposed composite failure criterion works adequately for both planar and line interface formulations as illustrated by the pushover study on 2D and 3D simulations of a masonry shear wall. This formulation is recommended to realise global softening problems in masonry components analysis. Additionally, the model works well with both the SLA and Force-Release methods.

2. The choice of user-specified shear displacement increment factors a_t or a_s to deduce the stiffness update, during run-time of the analysis, in the uncoupled shear mode has a significant influence on the shear capacity. Previously in the study of Van de Graaf [139], it was shown that increasing the factor a_t makes the response coarser giving it a saw-teeth type appearance. However, this also results in faster loss of shear stiffness leading to larger plastic displacements, and consequently, a quicker drop in the mobilised cohesion.

Computational efficiency

The main conclusions from the study of Chapter 7 are as follows:

1. The Woodbury-Identity based direct solver performs better than the PCG solver over both 2D and 3D problems, because the PCG involves back- and forward substitutions every analysis step to apply the preconditioner, in addition to the several matrix-vector manipulations. Therefore, the growth of elapsed time in intermediate steps is faster in the case of PCG, which necessitates frequent restarts.

2. The proposed solvers perform better than the traditional PArallel DIrect sparse SOlver (PARDISO), and especially for large 3D problems. However, despite the reduction of the contribution of time to solve the system of linear equations from ~ 85 % to around ~ 40% for a 180000 degrees of freedom problem size (as illustrated in Section 7.3.2), the analysis times are still significantly longer. Recommendations to further boost the performance are listed in Section 8.3.

8.3. **Outlook**

The following topics are potential directions for future work in the sequentially linear framework.

- *Adopting biaxial failure criteria to include tension-compression interaction effects.* Considering the complexity of the existing non-proportional loading problem in addressing dynamic failures using the static approach in SLA, the tension (T) compression (C) interaction effects were not investigated in depth in this work. The decision to use a simple Rankine-type failure criterion for damage initiation in the smeared crack/crush framework, both 2D and 3D, was made. However, considering a 2D plane stress state, it is in principle possible to additionally solve two more equations, one each for the T-C and C-T stress states, in the principal stress space using a Mohr-Coulomb type yield surface as proposed in the work of Bresser [19]. Alternatively, an idealised failure surface defined by a number of cones, in the global coordinate space, is also possible [39]. This approach has the added advantage of combinations with different types of surfaces by tuning the coefficients of the characteristic equation. Additionally, it also allows for extensions to anisotropic effects typical of masonry applications. Both these approaches should be investigated further, subject to the non-proportional loading problem and at junctures involving the need for intermittent proportional loading. Furthermore, if the computational intensity of SLA is addressed, these interaction effects could be considered for 3D damage initiation as well.

  All the above options are concerning the primary interaction effects between tension and compression with regard to damage initiation. However, during damage propagation, secondary effects such as the dependence of compressive behaviour on lateral effects of confinement or cracking arise. The effect of lateral cracking, for instance, is crucial in reinforced concrete analysis typified by the compressive strut action in the secondary direction. To this end, in accordance with the models proposed by Vecchio and Collins [146], the a priori defined compressive saw-teeth relations could be updated based on the lateral tensile strains as shown in Figure 8.1. A normal saw-teeth definition by scaling those corresponding to the original curve will be preferable, as against a new ripple bandwidth definition during run-time. For details on the adapted curves, the reader is referred to the work of Vecchio and Collins [146].

- *Computational efficiency of SLA needs to be improved further.* SLA has an advantage over NLFEA in the sense that the man-hours required to run the model and obtain results is not as high. This is due to the significantly large number of trials in obtaining an appropriate scheme of load step-size, iteration scheme, arc-length definitions etc. necessary in NLFEA to obtain converged results. Although the computational performance of SLA has been improved in this study using the tailor-made solvers, the solution times are still high. To this end, a smart damage-tracking algorithm, such as those proposed by Cook et al.[28], is recommended to be developed to distinguish the elements with the potential to be damaged, thereby significantly reducing the number of necessary computations. Furthermore,
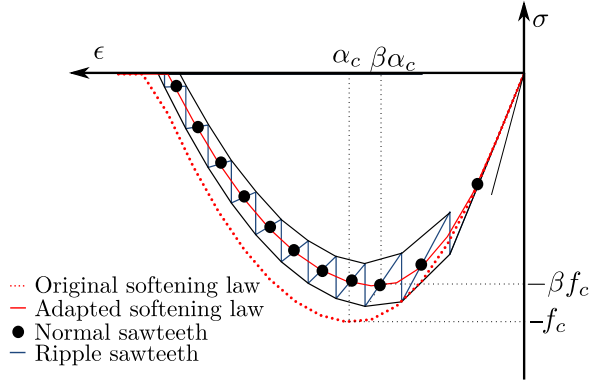
Figure 8.1: The modification of the base compression softening law upon lateral cracking as
proposed by Model-A in Reference [146], and the possible saw-teeth versions

the use of reduced integration schemes, coarser saw-teeth laws, linear elements
instead of quadratic elements, all of which could potentially reduce solution times
is recommended to be investigated systematically, in order to obtain a balance
between computational performance and the mechanics aspects.

- *Dedicated stress reversal event & algorithm, and the move to an incremental approach.* The stress reversal problem is a long-standing one, wherein the uniaxial damage in tensile regime is carried on one-to-one to the compressive regime or vice-versa. As previously proposed in Pari et al. [103] and Elias et al. [45], a dedicated crack-closure or crack-reopening event is also to be considered while determining the critical event. The damage increment in this case will be the appropriate reset of stiffness based on the reversal, and on the damage indicators representative of the saw-teeth numbers in the tension and compression states. An example of such a crack-closure incorrectly captured using SLA is illustrated in Figures 8.2 & 8.3.

  The problem arises because of using a sequentially linear approach during stress redistributions, particularly under non-proportional loading. It has been observed in a recent study [19] that the use of an elastic-brittle sublayer model instead of the saw-toothed fixed cracking model can delay the crack-closure effects. Also, the pushover case study of a squat RC-Wall in Section 4.1.3 suggests that the use of an incremental approach can delay crack-closure effects. These studies essentially imply that crack-closure effects can be postponed but not avoided. Therefore, it could be interpreted that the *non-proportional reloading* on a damaged state, which was previously understood to account for premature tensile/compressive failure problems and the need for intermittent proportional loading, could also potentially cause these crack closure effects which are essentially *premature*. Therefore, in order to relieve the crack-closure event of premature problems, it is suggested to move to an incremental approach which inherently tracks stress history, and then include the stress reversal algorithm.
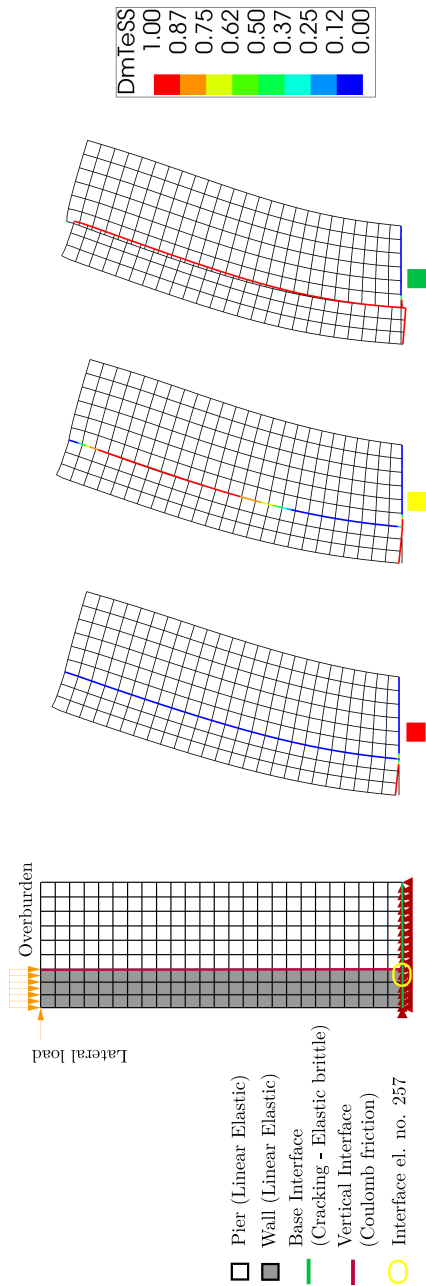
Figure 8.2: Wall-Pier connection subject to overburden followed by a lateral load [32], showing discrete cracking of the base followed by sliding down of the wall, resulting in crack closure along the cracked horizontal base beneath the wall, and the subsequent complete shear failure. The DmTeSS damage plots indicate loss of shear stiffness which is either due to a pure-sliding failure or the damage in shear due to the associated normal cracking.
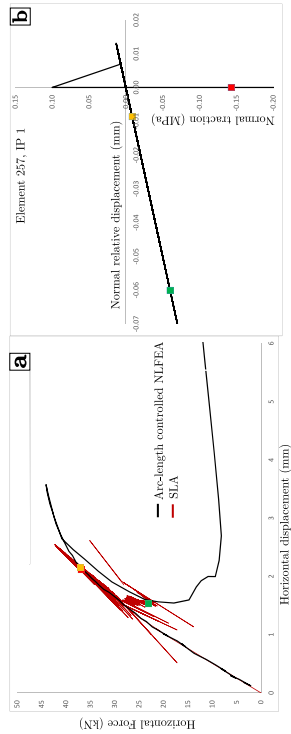
Figure 8.3: (a) Arc-length controlled NLFEA simulation [32] and an SLA simulation for the non-proportionally loaded wall in Figure 8.2, and (b) the stress reversal in integration point 1 of element 257 (marked in Figure 8.2).

8

CHARACTERISTIC EQUATION IN 3D STRESS STATE FOR CONTINUUM

Characteristic equation in the 3D stress states, given by Eq. 5.10, transforms into the following equations by limiting the maximum (σ_1) and minimum principal stresses (σ_3) to the the tensile (f_t) and compressive strengths (f_c) respectively:

$$f_t^3 - I_1 f_t^2 + I_2 f_t - I_3 = 0 \tag{8.1a}$$

$$f_c^3 - I_1 f_c^2 + I_2 f_c - I_3 = 0 \tag{8.1b}$$

The global stresses are expressed as a scaled combination of those due to the non-proportional loads (constant loads depicted by subscript 'con' and variable loads by subscript 'var'), as in Eq. 5.13, and subsequently, substituted in the invariants I_1, I_2 and I_3 of the 3D-stress tensor (Eq. 5.14) to give the following:

$$\sigma_{ij} = \sigma_{ij,\text{con}} + \lambda \sigma_{ij,\text{var}} \tag{8.2}$$

$$
\begin{aligned}
I_1 &= \sigma_{xx} + \sigma_{yy} + \sigma_{zz} \\
&= \left(\sigma_{xx,\text{var}} + \sigma_{yy,\text{var}} + \sigma_{zz,\text{var}}\right)\lambda + \left(\sigma_{xx,\text{con}} + \sigma_{yy,\text{con}} + \sigma_{zz,\text{con}}\right) \\
&= c_1\lambda + d_1
\end{aligned} \tag{8.3}
$$

$$
\begin{aligned}
I_2 &= \sigma_{xx}\sigma_{yy} + \sigma_{yy}\sigma_{zz} + \sigma_{zz}\sigma_{xx} - \sigma_{xy}^2 - \sigma_{yz}^2 - \sigma_{zx}^2 \\
&= \left(\sigma_{xx,\text{var}}\sigma_{yy,\text{var}} + \sigma_{xx,\text{var}}\sigma_{zz,\text{var}} - \sigma_{xy,\text{var}}^2 + \sigma_{yy,\text{var}}\sigma_{zz,\text{var}} - \sigma_{yz,\text{var}}^2 - \sigma_{zx,\text{var}}^2\right)\lambda^2 + \\
&\quad \left(\sigma_{xx,\text{con}}\sigma_{yy,\text{var}} + \sigma_{xx,\text{con}}\sigma_{zz,\text{var}} + \sigma_{xx,\text{var}}\sigma_{yy,\text{con}} + \sigma_{xx,\text{var}}\sigma_{zz,\text{con}} - 2\sigma_{xy,\text{con}}\sigma_{xy,\text{var}} + \right. \\
&\quad \left. \sigma_{yy,,\text{con}}\sigma_{zz,\text{var}} + \sigma_{yy,\text{var}}\sigma_{zz,\text{con}} - 2\sigma_{yz,\text{con}}\sigma_{yz,\text{var}} - 2\sigma_{zx,\text{con}}\sigma_{zx,\text{var}}\right)\lambda + \\
&\quad \left(\sigma_{xx,\text{con}}\sigma_{yy,\text{con}} + \sigma_{xx,\text{con}}\sigma_{zz,\text{con}} - \sigma_{xy,\text{con}}^2 + \sigma_{yy,\text{con}}\sigma_{zz,\text{con}} - \sigma_{yz,\text{con}}^2 - \sigma_{zx,\text{con}}^2\right) \\
&= b_1\lambda^2 + c_2\lambda + d_1
\end{aligned} \tag{8.4}
$$

$$I_3 = \sigma_{xx}\sigma_{yy}\sigma_{zz} + 2\sigma_{xy}\sigma_{yz}\sigma_{zx} - \sigma_{xx}\sigma_{yz}^2 - \sigma_{yy}\sigma_{zx}^2 - \sigma_{zz}\sigma_{xy}^2$$

$$= \Big(\sigma_{xx,\mathrm{var}}\sigma_{yy,\mathrm{var}}\sigma_{zz,\mathrm{var}} - \sigma_{xx,\mathrm{var}}\sigma_{yz,\mathrm{var}}^2 - \sigma_{xy,\mathrm{var}}^2\sigma_{zz,\mathrm{var}}+$$

$$2\sigma_{xy,\mathrm{var}}\sigma_{yz,\mathrm{var}}\sigma_{zx,\mathrm{var}} - \sigma_{yy,\mathrm{var}}\sigma_{zx,\mathrm{var}}^2\Big)\lambda^3+$$

$$\Big(\big(\sigma_{xx,\mathrm{con}}\sigma_{yy,\mathrm{var}} + \sigma_{xx,\mathrm{var}}\sigma_{yy,\mathrm{con}}\big)\sigma_{zz,\mathrm{var}} + \sigma_{xx,\mathrm{var}}\sigma_{yy,\mathrm{var}}\sigma_{zz,\mathrm{con}}-$$

$$\sigma_{xx,\mathrm{con}}\sigma_{yz,\mathrm{var}}^2 - 2\sigma_{xx,\mathrm{var}}\sigma_{yz,\mathrm{con}}\sigma_{yz,\mathrm{var}} - 2\sigma_{xy,\mathrm{con}}\sigma_{xy,\mathrm{var}}\sigma_{zz,\mathrm{var}}$$

$$- \sigma_{xy,\mathrm{var}}^2\sigma_{zz,\mathrm{con}} + 2\big(\sigma_{xy,\mathrm{con}}\sigma_{yz,\mathrm{var}} + \sigma_{xy,\mathrm{var}}\sigma_{yz,\mathrm{con}}\big)\sigma_{zx,\mathrm{var}}+$$

$$2\sigma_{xy,\mathrm{var}}\sigma_{yz,\mathrm{var}}\sigma_{zx,\mathrm{con}} - \sigma_{yy,\mathrm{con}}\sigma_{zx,\mathrm{var}}^2 - 2\sigma_{yy,\mathrm{var}}\sigma_{zx,\mathrm{con}}\sigma_{zx,\mathrm{var}}\Big)\lambda^2+$$

$$\Big(\sigma_{xx,\mathrm{con}}\sigma_{yy,\mathrm{con}}\sigma_{zz,\mathrm{var}} + \big(\sigma_{xx,\mathrm{con}}\sigma_{yy,\mathrm{var}} + \sigma_{xx,\mathrm{var}}\sigma_{yy,\mathrm{con}}\big)\sigma_{zz,\mathrm{con}}-$$

$$2\sigma_{xx,\mathrm{con}}\sigma_{yz,\mathrm{con}}\sigma_{yz,\mathrm{var}} - \sigma_{xx,\mathrm{var}}\sigma_{yz,\mathrm{con}}^2 - \sigma_{xy,\mathrm{con}}^2\sigma_{zz,\mathrm{var}}-$$

$$2\sigma_{xy,\mathrm{con}}\sigma_{xy,\mathrm{var}}\sigma_{zz,\mathrm{con}}+$$

$$2\sigma_{xy,\mathrm{con}}\sigma_{yz,\mathrm{con}}\sigma_{zx,\mathrm{var}} + 2\big(\sigma_{xy,\mathrm{con}}\sigma_{yz,\mathrm{var}} + \sigma_{xy,\mathrm{var}}\sigma_{yz,\mathrm{con}}\big)\sigma_{zx,\mathrm{con}}-$$

$$2\sigma_{yy,\mathrm{con}}\sigma_{zx,\mathrm{con}}\sigma_{zx,\mathrm{var}} - \sigma_{yy,\mathrm{var}}\sigma_{zx,\mathrm{con}}^2\Big)\lambda + \Big(\sigma_{xx,\mathrm{con}}\sigma_{yy,\mathrm{con}}\sigma_{zz,\mathrm{con}}-$$

$$\sigma_{xx,\mathrm{con}}\sigma_{yz,\mathrm{con}}^2 - \sigma_{xy,\mathrm{con}}^2\sigma_{zz,\mathrm{con}} + 2\sigma_{xy,\mathrm{con}}\sigma_{yz,\mathrm{con}}\sigma_{zx,\mathrm{con}} - \sigma_{yy,\mathrm{con}}\sigma_{zx,\mathrm{con}}^2\Big)$$

$$= a_1\lambda^3 + b_2\lambda^2 + c_3\lambda + d_2$$

$$(8.5)$$

For demonstrative purposes, substituting the above equations in only the tensile part of Eqs. 8.1 yields:

$$f_t^3 - (c_1\lambda + d_1)f_t^2 + (b_1\lambda^2 + c_2\lambda + d_1)f_t - (a_1\lambda^3 + b_2\lambda^2 + c_3\lambda + d_2) = 0 \qquad (8.6)$$

Rearranging the above equations in the form of Eq. 5.16:

$$-a_1\lambda^3 + (b_1 f_t - b_2)\lambda^2 + (-c_1 f_t^2 + c_2 f_t - c_3)\lambda + (f_t^3 - d_1 f_t^2 + d_1 f_t - d_2) = 0 \qquad (8.7)$$

Dividing the above equation by $-a_1$, the following depressed cubic equation is obtained.

$$\lambda^3 - \frac{(b_1 f_t - b_2)}{a_1}\lambda^2 - \frac{(-c_1 f_t^2 + c_2 f_t - c_3)}{a_1}\lambda - \frac{(f_t^3 - d_1 f_t^2 + d_1 f_t - d_2)}{a_1} = 0 \qquad (8.8)$$

which is similar to the form as in Eq. 5.17, and the coefficients herein correspond to $\hat{b}, \hat{c}$ and $\hat{d}$ as in Eq. 5.17 in the analytical solution detailed in Section 5.3.1. These coefficients have to be written down hard-code to be able to subsequently solve the cubic equation, using either the Cardano method or the trigonometric solutions.

BIBLIOGRAPHY

[1] AL-SABAH, A. S., AND LAEFER, D. F. Meshfree sequentially linear analysis of concrete. *Journal of Computing in Civil Engineering 30*, 2 (2016), 04015009.

[2] AL-SABAH, A. S., AND LAEFER, D. F. Use of negative stiffness in failure analysis of concrete beams. *Engineering Structures 126* (2016), 187–199.

[3] ALFAIATE, J., AND SLUYS, L. J. On the use of non-iterative methods in cohesive fracture. *International Journal of Fracture 210*, 1-2 (2018), 167–186.

[4] ALNAAS, W. *Nonlinear finite element analysis of quasi-brittle materials.* PhD thesis, Cardiff University, 2016.

[5] AMESTOY, P. R., DUFF, I. S., L'EXCELLENT, J.-Y., AND KOSTER, J. MUMPS: a general purpose distributed memory sparse solver. In *International Workshop on Applied Parallel Computing* (2000), Springer, pp. 121–130.

[6] ANTHOINE, A., MAGONETTE, G., AND MAGENES, G. Shear-compression testing and analysis of brick masonry walls. In *10th European Conference on Earthquake Engineering* (1995), pp. 1657–1662.

[7] ATKINSON, K. E. *An introduction to numerical analysis.* John Wiley & Sons, 2008.

[8] BARENBLATT, G. I., ET AL. The mathematical theory of equilibrium cracks in brittle fracture. *Advances in applied mechanics 7*, 1 (1962), 55–129.

[9] BATHE, K.-J. *Finite element procedures.* Klaus-Jurgen Bathe, 2006.

[10] BAZANT, Z. P. Instability, Ductility, and Size Effect in Strain-Softening Concrete. *ASCE J Eng Mech Div 102*, 2 (1976), 331–344.

[11] BAŽANT, Z. P., AND JIRÁSEK, M. Nonlocal integral formulations of plasticity and damage: Survey of progress. *Journal of Engineering Mechanics 128*, 11 (2002), 1119–1149.

[12] BAŽANT, Z. P., AND OH, B. H. Crack band theory for fracture of concrete. *Matériaux et Constructions 16*, 3 (1983), 155–177.

[13] BELLETTI, B., DAMONI, C., AND HENDRIKS, M. A. N. Development of guidelines for nonlinear finite element analyses of existing reinforced and pre-stressed beams. *European journal of environmental and civil engineering 15*, 9 (2011), 1361–1384.

[14] BELYTSCHKO, T., AND BLACK, T. Elastic crack growth in finite elements with minimal remeshing. *International Journal for Numerical Methods in Engineering 45*, 5 (1999), 601–620.

[15] BELYTSCHKO, T., FISH, J., AND ENGELMANN, B. E. A finite element with embedded localization zones. *Computer Methods in Applied Mechanics and Engineering 70*, 1 (1988), 59–89.

[16] BEVERLY, P. *fib model code for concrete structures 2010*. Ernst & Sohn, 2013.

[17] BIRKHOFF, G., AND MACLANE, S. *A Survey of Modern Algebra*. AK Peters, Ltd., 1997.

[18] BOISSE, P. H., BUSSY, P., AND LADEVEZE, P. A new approach in non-linear mechanics: The large time increment method. *International journal for numerical methods in engineering 29*, 3 (1990), 647–663.

[19] BRESSER, D. Mimicking a rotating crack model within sequentially linear analysis using an elastic-perfectly brittle sublayer model. Master's thesis, Delft University of Technology, 2019.

[20] BUI, T. T., NANA, W. S. A., ABOURI, S., LIMAM, A., TEDOLDI, B., AND ROURE, T. Influence of uniaxial tension and compression on shear strength of concrete slabs without shear reinforcement under concentrated loads. *Construction and Building Materials 146* (2017), 86–101.

[21] CAROL, I., AND BAŽANT, Z. P. Damage and plasticity in microplane theory. *International Journal of Solids and Structures 34*, 29 (1997), 3807–3835.

[22] CERVERA, M., AND CHIUMENTI, M. Mesh objective tensile cracking via a local continuum damage model and a crack tracking technique. *Computer Methods in Applied Mechanics and Engineering 196*, 1-3 (2006), 304–320.

[23] CERVERA, M., AND CHIUMENTI, M. Smeared crack approach: Back to the original track. *International Journal for Numerical and Analytical Methods in Geomechanics 30*, 12 (2006), 1173–1199.

[24] CERVERA, M., PELÀ, L., CLEMENTE, R., AND ROCA, P. A crack-tracking technique for localized damage in quasi-brittle materials. *Engineering Fracture Mechanics 77*, 13 (2010), 2431 – 2450.

[25] CHABOCHE, J. L. Continuous damage mechanics - A tool to describe phenomena before crack initiation. *Nuclear Engineering and Design 64*, 2 (1981), 233–247.

[26] CHOI, H. H., HWANG, S. M., KANG, Y. H., KIM, J., AND KANG, B. S. Comparison of implicit and explicit finite-element methods for the hydroforming process of an automobile lower arm. *The International Journal of Advanced Manufacturing Technology 20*, 6 (2002), 407–413.

[27] COMI, C., AND PEREGO, U. Fracture energy based bi-dissipative damage model for concrete. *International Journal of Solids and Structures 38*, 36-37 (2001), 6427–6454.

[28] COOK, A. C., VEL, S. S., AND JOHNSON, S. E. Pervasive cracking of heterogeneous brittle materials using a multi-directional smeared crack band model. *International Journal of Mechanical Sciences 149* (2018), 459–474.

8

[29] CRISFIELD, M. A. Accelerated solution techniques and concrete cracking. *Computer Methods in Applied Mechanics and Engineering 33*, 1-3 (1982), 585–607.

[30] CRISFIELD, M. A. An arc-length method including line searches and accelerations. *International journal for numerical methods in engineering 19*, 9 (1983), 1269–1289.

[31] CRISFIELD, M. A. Difficulties with current numerical models for reinforced concrete and some tentative solutions. In *Int. Conf. on Computer-Aided Analysis and Design of Concrete Structures* (1984), pp. 331–358.

[32] CUR. Structural masonry: an experimental/numerical basis for practical design rules (English version). Tech. Rep. 171, Dutch Version (1994), J. G. Rots (Ed.), 1997.

[33] DANKS, B. Validation of sequentially linear analysis for quasi-brittle behaviour of reinforced concrete structures under proportional and non-proportional loading. Master's thesis, Delft University of Technology, 2019.

[34] DE BORST, R. Computation of post-bifurcation and post-failure behavior of strain-softening solids. *Computers & Structures 25*, 2 (1987), 211–224.

[35] DE BORST, R., CRISFIELD, M. A., REMMERS, J. J., AND VERHOOSEL, C. V. *Nonlinear finite element analysis of solids and structures.* John Wiley & Sons, 2012.

[36] DE BORST, R., AND MÜHLHAUS, H. B. Gradient-dependent plasticity: Formulation and algorithmic aspects. *International Journal for Numerical Methods in Engineering 35*, 3 (1992), 521–539.

[37] DE BORST, R., REMMERS, J. J., NEEDLEMAN, A., AND ABELLAN, M. A. Discrete vs smeared crack models for concrete fracture: Bridging the gap. *International Journal for Numerical and Analytical Methods in Geomechanics 28*, 7-8 (2004), 583–607.

[38] DEJONG, M. J., BELLETTI, B., HENDRIKS, M. A. N., AND ROTS, J. G. Shell elements for sequentially linear analysis: Lateral failure of masonry structures. *Engineering Structures 31*, 7 (2009), 1382–1392.

[39] DEJONG, M. J., AND HARRISON, S. A biaxial failure criterion for sequentially linear analysis. In *8th International masonry conference, Dresden* (2010).

[40] DEJONG, M. J., HENDRIKS, M. A. N., AND ROTS, J. G. Sequentially linear analysis of fracture under non-proportional loading. *Engineering Fracture Mechanics 75*, 18 (2008), 5042–5056.

[41] DUGDALE, D. S. Yielding of steel sheets containing slits. *Journal of the Mechanics and Physics of Solids 8*, 2 (1960), 100–104.

[42] DVORKIN, E. N., CUITIÑO, A. M., AND GIOIA, G. Finite elements with displacement interpolated embedded localization lines insensitive to mesh size and distortions. *International Journal for Numerical Methods in Engineering 30*, 3 (1990), 541–564.

[43] ELIÁŠ, J. Generalization of load–unload and force-release sequentially linear methods. *International Journal of Damage Mechanics 24*, 2 (2015), 279–293.

8

[44] ELIÁŠ, J., FRANTÍK, P., AND VOŘECHOVSKÝ, M. Improved sequentially linear solution procedure. *Engineering fracture mechanics 77*, 12 (2010), 2263–2276.

[45] ELIÁŠ, J., AND STANG, H. Lattice modeling of aggregate interlocking in concrete. *International journal of fracture 175*, 1 (2012), 1–11.

[46] ENDO, Y., PELÀ, L., AND ROCA, P. Review of different pushover analysis methods applied to masonry buildings and comparison with nonlinear dynamic analysis. *Journal of Earthquake Engineering 21*, 8 (2017), 1234–1255.

[47] ENSINK, S. W. H., VAN DE GRAAF, A. V., SLOBBE, A. T., HENDRIKS, M. A. N., DEN UIJL, J. A., AND ROTS, J. G. Modelling of bond behaviour by means of sequentially linear analysis and concrete-to-steel interface elements. In *Proceedings of the Fourth Bond In Concrete Conference* (2012).

[48] ESPOSITO, R., AND RAVENSHORST, G. J. P. Quasi-static cyclic in-plane tests on masonry components 2016/2017. Tech. Rep. C31B67WP3-4,(1), Delft University of Technology, 2017.

[49] FEENSTRA, P. H. *Computational aspects of biaxial stress in plain and reinforced concrete*. PhD thesis, Delft University of Technology, 1993.

[50] FEENSTRA, P. H., ROTS, J. G., ARNESEN, A., TEIGEN, J. G., AND HOISETH, K. V. A 3D constitutive model for concrete based on a co-rotational concept. In *Computational Modelling of Concrete Structures, Bad Gastein, Austria; Editors : R. de Borst et al.* (1998), pp. 13–22.

[51] FERREIRA, D. Diana user manual. Tech. Rep. Release 10.3, DIANA FEA B.V., 2019.

[52] FERTÉ, G., MASSIN, P., AND MOËS, N. 3D crack propagation with cohesive elements in the extended finite element method. *Computer Methods in Applied Mechanics and Engineering 300* (2016), 347 – 374.

[53] FLETCHER, R. Conjugate gradient methods for indefinite systems. In *Numerical analysis*. Springer, 1976, pp. 73–89.

[54] GEORGIOUDAKIS, M., STEFANOU, G., AND PAPADRAKAKIS, M. Stochastic failure analysis of structures with softening materials. *Engineering Structures 61* (2014), 13–21.

[55] GIARDINA, G., VAN DE GRAAF, A. V., HENDRIKS, M. A. N., ROTS, J. G., AND MARINI, A. Numerical analysis of a masonry facade subject to tunnelling-induced settlements. *Engineering Structures 54* (2013), 234–247.

[56] GOLUB, G. H., AND VAN LOAN, C. F. *Matrix Computations (4th edition)*. John Hopkins University Press, 2013.

[57] GRAÇA-E-COSTA, R., ALFAIATE, J., DIAS-DA-COSTA, D., NETO, P., AND SLUYS, L. J. Generalisation of non-iterative methods for the modelling of structures under non-proportional loading. *International Journal of Fracture 182*, 1 (2013), 21–38.

8

[58] GRASSL, P., AND JIRÁSEK, M. Damage-plastic model for concrete failure. *International Journal of Solids and Structures 43*, 22-23 (2006), 7166–7196.

[59] GRASSL, P., XENOS, D., NYSTRÖM, U., REMPLING, R., AND GYLLTOFT, K. CDPM2: A damage-plasticity approach to modelling the failure of concrete. *International Journal of Solids and Structures 50*, 24 (2013), 3805–3816.

[60] GREEN, A. E., AND HILL, R. The Mathematical Theory of Plasticity. *The Mathematical Gazette 35*, 313 (1951), 208.

[61] GUTIÉRREZ, M. A. Energy release control for numerical simulations of failure in quasi-brittle solids. *Communications in Numerical Methods in Engineering 20*, 1 (2004), 19–29.

[62] HENDRIKS, M. A. N., DE BOER, A., AND BELLETTI, B. Guidelines for nonlinear finite element analysis of concrete structures. *Rijkswaterstaat Technisch Document (RTD), Rijkswaterstaat Centre for Infrastructure, RTD 1016* (2012), 2012.

[63] HENDRIKS, M. A. N., AND ROTS, J. G. Simulation of creep induced cracking based on sequentially linear analysis. In *Proc. of the 8th International Conference on Creep, Shrinkage and Durability Mechanics of Concrete and Concrete Structures; Editors: T. Tanabe et al.* (2009), pp. 579–585.

[64] HESTENES, M. R., AND STIEFEL, E. Methods of conjugate gradients for solving linear systems. *Journal of research of the National Bureau of Standards 49*, 6 (1952), 409–436.

[65] HILLERBORG, A., MODÉER, M., AND PETERSSON, P. E. Analysis of crack formation and crack growth in concrete by means of fracture mechanics and finite elements. *Cement and Concrete Research 6*, 6 (1976), 773–781.

[66] HORDIJK, D. *Local approach to fatigue of concrete.* PhD thesis, Delft University of Technology, 1991.

[67] INGRAFFEA, A. R., AND MANU, C. Stress-intensity factor computation in three dimensions with quarter-point elements. *International Journal for Numerical Methods in Engineering 15*, 10 (1980), 1427–1445.

[68] INGRAFFEA, A. R., AND SAOUMA, V. Numerical Modeling of Discrete Crack Propagation in Reinforced and Plain Concrete. In *Fract Mech of Concr, Struct Appl and Numer Calc* (1985), pp. 171–225.

[69] INVERNIZZI, S., TROVATO, D., HENDRIKS, M. A. N., AND VAN DE GRAAF, A. V. Sequentially linear modelling of local snap-back in extremely brittle structures. *Engineering Structures 33*, 5 (2011), 1617–1625.

[70] JEFFERSON, A. D. Craft - A plastic-damage-contact model for concrete. I. Model theory and thermodynamic considerations. *International Journal of Solids and Structures 40*, 22 (2003), 5973–5999.

8

[71] JÄGER, P., STEINMANN, P., AND KUHL, E. Modeling three-dimensional crack propagation—a comparison of crack path tracking strategies. *International Journal for Numerical Methods in Engineering 76*, 9 (2008), 1328–1352.

[72] JIRÁSEK, M. Comparative study on finite elements with embedded discontinuities. *Computer Methods in Applied Mechanics and Engineering 188*, 1-3 (2000), 307–330.

[73] JIRASEK, M. Modelling of localized inelastic deformation. In *Lecture Notes, Advanced course, CTU Prague* (2018).

[74] JIRÁSEK, M., AND BAŽANT, Z. P. Macroscopic fracture characteristics of random particle systems. *International Journal of Fracture 69*, 3 (1994), 201–228.

[75] KACHANOV, L. M. *Introduction to continuum damage mechanics.* Martinus Nijhoff Publishers, 1986.

[76] KLISINSKI, M., RUNESSON, K., AND STURE, S. Finite element with inner softening band. *Journal of Engineering Mechanics 117*, 3 (1991), 575–587.

[77] KRAJCINOVIC, D., AND FONSEKA, G. U. The continuous damage theory of brittle materials: Part 1: General theory. *Journal of Applied Mechanics, Transactions ASME 48*, 4 (1981), 809–815.

[78] LEFAS, I. D., KOTSOVOS, M. D., AND AMBRASEYS, N. N. Behavior of reinforced concrete structural walls: strength, deformation characteristics, and failure mechanism. *Structural Journal 87*, 1 (1990), 23–31.

[79] LIU, J. X. Simulating quasi-brittle failures including damage-induced softening based on the mechanism of stress redistribution. *Applied Mathematical Modelling 55* (2018), 685–697.

[80] LIU, J. X., AND SAYED, T. E. On the load–unload (l–u) and force–release (f–r) algorithms for simulating brittle fracture processes via lattice models. *International Journal of Damage Mechanics 21*, 7 (2012), 960–988.

[81] LIU, J. X., AND SAYED, T. E. A quasi-static algorithm that includes effects of characteristic time scales for simulating failures in brittle materials. *International Journal of Damage Mechanics 23*, 1 (2014), 83–103.

[82] LOURENÇO, P. B. *Computational strategies for masonry structures.* PhD thesis, Delft University of Technology, 1996.

[83] LOURENÇO, P. B., AND ROTS, J. G. Multisurface interface model for analysis of masonry structures. *Journal of engineering mechanics 123*, 7 (1997), 660–668.

[84] LOURENÇO, P. B., MILANI, G., TRALLI, A., AND ZUCCHINI, A. Analysis of masonry structures: review of and recent trends in homogenization techniques. *Canadian Journal of Civil Engineering: Special Issue on Masonry. 34*, 11 (2007), 1443–1457.

8

[85] MAGENES, G., KINGSLEY, G. R., AND CALVI, G. M. *Seismic testing of a full-scale, two-story masonry building: test procedure and measured experimental response.* Consiglio nazionale delle ricerche, Gruppo nazionale per la Difesa dai terremoti, 1995.

[86] MAZARS, J. A description of micro- and macroscale damage of concrete structures. *Engineering Fracture Mechanics 25*, 5-6 (1986), 729–737.

[87] MESSALI, F., ESPOSITO, R., JAFARI, S., RAVENSHORST, G. J. P., KORSWAGEN, P., AND ROTS, J. G. A multiscale experimental characterisation of dutch unreinforced masonry buildings. In *Proceedings of 16th European Conference on Earthquake Engineering (ECEE), Thessaloniki, Greece* (2018).

[88] MESSALI, F., PARI, M., ESPOSITO, R., ROTS, J. G., AND DEN HERTOG, D. Blind prediction of a cyclic pushover test on a two-storey masonry assemblage: a comparative study. In *16th European Conference on Earthquake Engineering (ECEE), Thessaloniki* (2018).

[89] MOËS, N., DOLBOW, J., AND BELYTSCHKO, T. A finite element method for crack growth without remeshing. *International Journal for Numerical Methods in Engineering 46*, 1 (1999), 131–150.

[90] MOËS, N., STOLZ, C., BERNARD, P. E., AND CHEVAUGEON, N. A level set based model for damage growth: The thick level set approach. *International Journal for Numerical Methods in Engineering 86*, 3 (2011), 358–380.

[91] MUNTENDAM-BOS, A. G., ROEST, J. P. A., AND DE WAAL, H. A. The effect of imposed production measures on gas extraction induced seismic risk. *Netherlands Journal of Geosciences 96*, 5 (2017), s271–s278.

[92] MURAKAMI, S., AND OHNO, N. A Continuum Theory of Creep and Creep Damage. In *Creep in Structures*. Springer, 1981, pp. 422–444.

[93] NANA, W. S. A., BUI, T. T., LIMAM, A., AND ABOURI, S. Experimental and Numerical Modelling of Shear Behaviour of Full-scale RC Slabs Under Concentrated Loads. *Structures 10* (2017), 96–116.

[94] NGUYEN, G. D. *A thermodynamic approach to non-local damage modelling of concrete.* PhD thesis, Oxford University, 2005.

[95] NGUYEN, G. D., AND HOULSBY, G. T. A coupled damage-plasticity model for concrete based on thermodynamic principles: Part I: Model formulation and parameter identification. *International Journal for Numerical and Analytical Methods in Geomechanics 32*, 4 (2008), 353–389.

[96] NGUYEN, V. P., RABCZUK, T., BORDAS, S., AND DUFLOT, M. Meshless methods: A review and computer implementation aspects. *Mathematics and Computers in Simulation 79*, 3 (2008), 763–813.

8

[97] NILSEN-NYGAARD, I. Structural safety assessment of reinforced concrete structures with nonlinear finite element analyses and the significance of the modelling uncertainty. Master's thesis, Norwegian University of Science and Technology, 2015.

[98] NOORU-MOHAMED, M. *Mixed-mode fracture of concrete: an experimental approach.* PhD thesis, Delft University of Technology, 1992.

[99] OLIVER, J. A consistent characteristic length for smeared cracking models. *International Journal for Numerical Methods in Engineering 28*, 2 (1989), 461–474.

[100] OLIVER, J., HUESPE, A. E., AND CANTE, J. C. An implicit/explicit integration scheme to increase computability of non-linear material and contact/friction problems. *Computer Methods in Applied Mechanics and Engineering 197*, 21-24 (2008), 1865–1889.

[101] OMIDI, O., AND LOTFI, V. Continuum large cracking in a rate-dependent plastic-damage model for cyclic-loaded concrete structures. *International Journal for Numerical and Analytical Methods in Geomechanics 37*, 10 (2013), 1363–1390.

[102] OŽBOLT, J., AND BAŽANT, Z. P. Microplane model for cyclic triaxial behavior of concrete. *Journal of Engineering Mechanics 118*, 7 (1992), 1365–1386.

[103] PARI, M., HENDRIKS, M. A. N., AND ROTS, J. G. Sequentially linear analysis on masonry walls - a new crack closure algorithm. In *In Proceedings of the 13th Canadian Masonry Symposium, Halifax* (2017).

[104] PARI, M., HENDRIKS, M. A. N., AND ROTS, J. G. Non-proportional loading in sequentially linear analysis for 3D stress states. *International Journal for Numerical Methods in Engineering 119*, 6 (2019), 506–531.

[105] PARI, M., HENDRIKS, M. A. N., AND ROTS, J. G. Non-proportional loading in sequentially linear solution procedures for quasi-brittle fracture: A comparison and perspective on the mechanism of stress redistribution. *Engineering Fracture Mechanics* (2020), 106960.

[106] PARI, M., ROTS, J. G., AND HENDRIKS, M. A. N. Non-proportional loading for 3-D stress situations in Sequentially Linear Analysis. In *Computational Modelling of Concrete Structures; Editors: G. Meschke et al.* (2018), CRC Press, pp. 931–940.

[107] PARI, M., SWART, W., VAN GIJZEN, M. B., HENDRIKS, M. A. N., AND ROTS, J. G. Two solution strategies to improve the computational performance of sequentially linear analysis for quasi-brittle structures. *International Journal for Numerical Methods in Engineering 121*, 10 (2020), 2128–2146.

[108] PEERLINGS, R. H. J., DE BORST, R., BREKELMANS, W. A. M., AND DE VREE, J. H. P. Gradient enhanced damage for quasi-brittle materials. *International Journal for Numerical Methods in Engineering 39*, 19 (1996), 3391–3403.

[109] PIJAUDIER-CABOT, G., AND BAŽANT, Z. P. Nonlocal damage theory. *Journal of Engineering Mechanics 113*, 10 (1987), 1512–1533.

8

[110] PRAZERES, P. G. C., BITENCOURT, L. A. G., BITTENCOURT, T. N., AND MANZOLI, O. L. A modified implicit–explicit integration scheme: an application to elastoplasticity problems. *Journal of the Brazilian Society of Mechanical Sciences and Engineering 38*, 1 (2016), 151–161.

[111] PRESS, W. H., TEUKOLSKY, S. A., VETTERLING, W. T., AND FLANNERY, B. P. *Numerical recipes 3rd edition: The art of scientific computing.* Cambridge university press, 2007.

[112] RABCZUK, T., AKKERMANN, J., AND EIBL, J. A numerical model for reinforced concrete structures. *International Journal of Solids and Structures 42*, 5-6 (2005), 1327–1354.

[113] RAIJMAKERS, T., AND VERMELTFOORT, A. T. Deformation controlled tests in masonry shear walls. *Report B-92-1156, TNO-Bouw, Delft* (1992).

[114] RAIJMAKERS, T., AND VERMELTFOORT, A. T. Deformation controlled tests in masonry shear walls: Part 2. *Report TUE/BKO/93.08, Eindhoven university of technology* (1993).

[115] REINHARDT, H. W. Fracture Mechanics of an elastic softening material like concrete. *Heron 29*, 2 (1984).

[116] ROTS, J. G. *Computational modeling of concrete fracture.* PhD thesis, Delft University of Technology, 1988.

[117] ROTS, J. G. Sequentially linear continuum model for concrete fracture. *Proc. of Fracture mechanics of concrete structures (FraMCoS) 2* (2001), 831–840.

[118] ROTS, J. G., BELLETTI, B., AND INVERNIZZI, S. Robust modeling of RC structures with an "event-by-event" strategy. *Engineering Fracture Mechanics 75*, 3-4 (2008), 590 – 614.

[119] ROTS, J. G., AND BLAAUWENDRAAD, J. Crack models for concrete: discrete or smeared? Fixed multi-directional or rotating? *Heron 34*, 1 (1989), 3–59.

[120] ROTS, J. G., AND HENDRIKS, M. A. N. Elastic-brittle fraction model for robust post-peak analysis of masonry structures. *Key Engineering Materials 624* (2015), 27–39.

[121] ROTS, J. G., AND INVERNIZZI, S. Regularized sequentially linear saw-tooth softening model. *International Journal for Numerical and Analytical Methods in Geomechanics 28*, 7-8 (2004), 821–856.

[122] ROTS, J. G., INVERNIZZI, S., AND BELLETTI, B. Saw-tooth softening/stiffening-a stable computational procedure for rc structures. *Computers and Concrete 3*, 4 (2006), 213–233.

8

[123] ROTS, J. G., INVERNIZZI, S., BELLETTI, B., AND HENDRIKS, M. A. N. Circumventing bifurcations in structural softening. In *Computational Modeling Workshop on Concrete, Masonry and Fiber-reinforced Composites, Delft, The Netherlands* (2009), pp. 49–52.

[124] ROTS, J. G., MESSALI, F., ESPOSITO, R., JAFARI, S., AND MARIANI, V. Computational modeling of masonry with a view to groningen induced seismicity. In *10th international conference on Structural Analysis of Historical Constructions, SAHC* (2016).

[125] SAAD, Y. *Iterative methods for sparse linear systems*, vol. 82. siam, 2003.

[126] SAAD, Y., AND SCHULTZ, M. H. GMRES: A generalized minimal residual algorithm for solving nonsymmetric linear systems. *SIAM Journal on scientific and statistical computing 7*, 3 (1986), 856–869.

[127] SCHENK, O., AND GÄRTNER, K. Solving unsymmetric sparse systems of linear equations with pardiso. *Future Generation Computer Systems 20*, 3 (2004), 475–487.

[128] SCHLANGEN, E., AND VAN MIER, J. G. M. Experimental and numerical analysis of micromechanisms of fracture of cement-based composites. *Cement and Concrete Composites 14*, 2 (1992), 105 – 118.

[129] SHAH, S. P., SWARTZ, S. E., AND OUYANG, C. *Fracture mechanics of concrete: applications of fracture mechanics to concrete, rock and other quasi-brittle materials*. John Wiley & Sons, 1995.

[130] SLOBBE, A. T. Sequentially linear analysis of shear critical reinforced concrete beams. Master's thesis, Delft University of Technology, 2010.

[131] SLOBBE, A. T. *Propagation and band width of smeared cracks*. PhD thesis, Delft University of Technology, 2014.

[132] SLOBBE, A. T., HENDRIKS, M. A. N., AND ROTS, J. G. Sequentially linear analysis of shear critical reinforced concrete beams without shear reinforcement. *Finite Elements in Analysis and Design 50* (2012), 108 – 124.

[133] SLOBBE, A. T., HENDRIKS, M. A. N., AND ROTS, J. G. Systematic assessment of directional mesh bias with periodic boundary conditions: Applied to the crack band model. *Engineering Fracture Mechanics 109* (2013), 186–208.

[134] SLOBBE, A. T., HENDRIKS, M. A. N., AND ROTS, J. G. Smoothing the propagation of smeared cracks. *Engineering Fracture Mechanics 132* (2014), 147–168.

[135] SOLTANI, B., MATTIASSON, K., AND SAMUELSSON, A. Implicit and dynamic explicit solutions of blade forging using the finite element method. *Journal of Materials Processing Technology 45*, 1 (1994), 69 – 74.

[136] SUKUMAR, N., MOËS, N., MORAN, B., AND BELYTSCHKO, T. Extended finite element method for three-dimensional crack modelling. *International Journal for Numerical Methods in Engineering 48*, 11 (2000), 1549–1570.

8

[137] SWART, W. Methods for improving the computational performance of sequentially linear analsysis. Master's thesis, Delft University of Technology, 2018.

[138] SWENSON, D. V., AND INGRAFFEA, A. R. Modeling mixed-mode dynamic crack propagation nsing finite elements: Theory and applications. *Computational Mechanics 3*, 6 (1988), 381–397.

[139] VAN DE GRAAF, A. V. *Sequentially linear analysis for simulating brittle failure.* PhD thesis, Delft University of Technology, 2017.

[140] VAN DE GRAAF, A. V., HENDRIKS, M. A. N., AND ROTS, J. G. A discrete cracking model for sequentially linear analysis. *Computational Modelling of Concrete Structures; Editors: Nenad Bicanic et al., EURO-C* (2010), 409–418.

[141] VAN MIER, J. G. M. *Fracture processes of concrete.* CRC press, London, 1997.

[142] VAN ZIJL, G., DE BORST, R., AND ROTS, J. The role of crack rate dependence in the long-term behaviour of cementitious materials. *International Journal of Solids and Structures 38*, 30 (2001), 5063 – 5079.

[143] VAN ZIJL, G. P. A. G. *Computational modelling of masonry creep and shrinkage.* PhD thesis, Delft University of Technology, 2000.

[144] VAN ZIJL, G. P. A. G. Modeling masonry shear-compression: Role of dilatancy highlighted. *Journal of Engineering Mechanics 130*, 11 (2004), 1289–1296.

[145] VANDOREN, B., DE PROFT, K., SIMONE, A., AND SLUYS, L. J. A novel constrained large time increment method for modelling quasi-brittle failure. *Computer Methods in Applied Mechanics and Engineering 265* (2013), 148–162.

[146] VECCHIO, F. J., AND COLLINS, M. P. Compression response of cracked reinforced concrete. *Journal of Structural Engineering 119*, 12 (1993), 3590–3610.

[147] VERHOOSEL, C. V., REMMERS, J. J. C., AND GUTIÉRREZ, M. A. A dissipation-based arc-length method for robust simulation of brittle and ductile failure. *International Journal for Numerical Methods in Engineering 77*, 9 (2009), 1290–1321.

[148] VLEK, C. Induced earthquakes from long-term gas extraction in groningen, the netherlands: Statistical analysis and prognosis for acceptable-risk regulation. *Risk Analysis 38*, 7 (2018), 1455–1473.

[149] VOLOKH, K. Y. Characteristic length of damage localization in concrete. *Mechanics Research Communications 51* (2013), 29–31.

[150] VOORMEEREN, L. Extension and verification of sequentially linear analysis to solid elements. Master's thesis, Delft University of Technology, 2011.

[151] VOREL, J., AND BOSHOFF, W. P. Computational modelling of real structures made of strain-hardening cement-based composites. *Applied Mathematics and Computation 267* (2015), 562 – 570.

8

[152] WAWRZYNEK, P. A., AND INGRAFFEA, A. R. Interactive finite element analysis of fracture processes: An integrated approach. *Theoretical and Applied Fracture Mechanics 8*, 2 (1987), 137–150.

[153] WELLS, G. N., AND SLUYS, L. J. A new method for modelling cohesive cracks using finite elements. *International Journal for Numerical Methods in Engineering 50*, 12 (2001), 2667–2682.

[154] XU, W., AND WAAS, A. M. Modeling damage growth using the crack band model; effect of different strain measures. *Engineering Fracture Mechanics 152* (2016), 126–138.

[155] YU, C., HOOGENBOOM, P. C. J., AND ROTS, J. G. Algorithm for non-proportional loading in sequentially linear analysis. In *9th International Conference on Fracture Mechanics of Concrete and Concrete Structures, UC Berkeley* (2016).

[156] YU, C., HOOGENBOOM, P. C. J., AND ROTS, J. G. Incremental sequentially linear analysis to control failure for quasi-brittle materials and structures including non-proportional loading. *Engineering Fracture Mechanics 202* (2018), 332 – 349.

[157] ZHAO, Z., KWON, S. H., AND SHAH, S. P. Effect of specimen size on fracture energy and softening curve of concrete: Part i. experiments and fracture energy. *Cement and Concrete Research 38*, 8 (2008), 1049 – 1060.

[158] ZHOU, Y. Validation of nonlinear finite element analysis on reinforced concrete slab under concentrated out-of-plane load combined with uniaxial in-plane load based on case study. Master's thesis, Delft University of Technology, 2018.

LIST OF PUBLICATIONS

JOURNAL ARTICLES

- M. Pari, A.V. Van de Graaf, M.A.N. Hendriks and J.G. Rots, "A multi-surface interface model for sequentially linear methods to analyse masonry structures", *Engineering Structures* (2020), *Under Review*

- M. Pari, M.A.N. Hendriks and J.G. Rots, "Non-proportional loading in sequentially linear solution procedures for quasi-brittle fracture: A Comparison and perspective on the mechanism of stress redistribution", *Engineering Fracture Mechanics*, 230 (2020): 106960. https://doi.org/10.1016/j.engfracmech.2020.106960

- M. Pari, W. Swart, M.B. van Gijzen, M.A.N. Hendriks and J.G. Rots, "Two solution strategies to improve the computational performance of sequentially linear analysis for quasi-brittle structures.", *International Journal for Numerical Methods in Engineering*, 121.10 (2020): 2128– 2146. https://doi.org/10.1002/nme.6302

- M. Pari, M.A.N. Hendriks and J.G. Rots, "Non-proportional loading in sequentially linear analysis for 3D stress states.", *International Journal for Numerical Methods in Engineering*, 119.6 (2019): 506-531. https://doi.org/10.1002/nme.6060

CONFERENCE PAPERS/TALKS

- M. Pari, J.G. Rots and M.A.N. Hendriks, "Finite element pushover simulations of masonry structures using sequentially linear analysis", *Proceedings of the 17th World Conference on Earthquake Engineering* (17th WCEE), 2021, Sendai, Japan.

- M. Pari, M.A.N. Hendriks and J.G. Rots, "An alternative approach to non-proportional loading in Sequentially Linear Analysis (SLA) & its extension to 3D stress situations", *Presentation at the 6th European Conference on Computational Mechanics (ECCM 6)*, 2018, Glasgow, United Kingdom.

- F. Messali, M. Pari, R. Esposito, J.G. Rots and D. Den Hertog, "Blind prediction of a cyclic pushover test on a two-storey masonry assemblage: A comparative study", *Proceedings of the 16th European Conference on Earthquake Engineering (ECEE)*, 2018, Thessaloniki, Greece.

- M. Pari, J.G. Rots and M.A.N. Hendriks, "Non-proportional loading for 3D stress situations in sequentially linear analysis", *Proceedings of the Conference on Computational Modelling of Concrete and Concrete Structures*, EURO-C 2018, Bad Hofgastein, Austria. https://doi.org/10.1201/9781315182964-108

- M. Pari, S. Jafari, F. Messali, R. Esposito and J.G. Rots, "Computational modeling of the cyclic pushover test on a calcium silicate element masonry assemblage", *4th WTA International PhD symposium*, 2017, Delft, The Netherlands.

- M. Pari, M.A.N. Hendriks and J.G. Rots, "Sequentially Linear Analysis on masonry walls – a new crack closure algorithm", *13th Canadian Masonry Symposium*, 2017, Halifax, Canada.

CURRICULUM VITÆ

20-09-1989   Born in Chennai, India.

2007–2011   Bachelor of Technology (B.Tech) in Civil Engineering.
                    National Institute of Technology (NIT), Warangal, India.

2012–2015   Master of Science (MSc) in Civil Engineering.
                    Specialisation : Structural Mechanics
                    Delft University of Technology (TU Delft), The Netherlands.

2016–2020   PhD in Computational Mechanics.
                    Delft University of Technology (TU Delft), The Netherlands.
                    Thesis: Simulating quasi-brittle failure in structures
                                 using Sequentially Linear Methods
                    Promotors: Prof. dr. ir. Jan G. Rots &
                                 Prof. dr. ir. Max A.N. Hendriks

2020–   Research Engineer
                    Plaxis B.V. (Bentley Systems)
                    Delft, The Netherlands.

ACKNOWLEDGEMENTS

Independence is key to a PhD but maybe overrated, for without collaboration and supervision, or support from family and friends the journey becomes a long forlorn battle. This is to express my sincere gratitude and reverence to people who made this journey possible.

First and foremost, I would like to thank **Nederlandse Aardolie Maatschappij B.V (NAM)** for sponsoring the PhD project, and my promotor **Prof. Jan Rots** for providing me the opportunity to pursue my doctoral research. Right from the moment I was offered the position to the finish, Jan's been nothing short of an exemplary role-model leader. His child-like enthusiasm for the topic and computational mechanics in general, has inspired me to push my boundaries in dire times. I'd like to thank him for valuable remarks on articles, for his ever-positive approach to work and beyond, for the opportunity to visit conferences, and for the beers & football matches that I could never have imagined back home with a professor. His empathetic nature and gregarious personality is something I wish I could emulate. **Prof. Max Hendriks**, who became my promotor a few months into the PhD, was a blessing in disguise considering his expertise on the topic. His practical suggestions, attention to details, and critical remarks on articles were invaluable. I'd like to thank him for bearing with me whenever I dropped by his office, most often uninvited, for a 'short' discussion which ended up being far from short almost every single time. I also learnt a lot from his suggestions on handling tricky situations at work, and I am truly indebted to him in this regard.

Prof. Rathish Kumar, my mentor during under-graduation at NIT Warangal, India, is one name I can't afford to miss at this juncture, for I owe him my interest in research, and the move to TU Delft for post-graduate & doctoral education. His thought provoking way of teaching with special focus on application of concepts, solutions to practical problems, and talks on recent research developments laid the foundations for my research career, and I am grateful to him for this.

I extend my sincere gratitude to the doctoral committee comprising **Dr. Jan Elias, Prof. Gideon van Zijl, Prof. Kalle Høiseth, Prof. Tom Scarpas,** and **Prof. Bert Sluys** for agreeing to take part in the defence process amidst these covid times. Thank you for your time and valuable comments which helped shape up the thesis leading up to the defence.

PhD brings with it the need for collaborations, and I'm happy to have collaborated with some of the brightest minds. I'd like to specially thank **Dr. Gerd-Jan Schreppers** for the opportunity to work at DIANA FEA, and implement all ideas pertaining to this work. I'd also like to thank **Jos Jansen, Wijtze-Pieter, Arno, Anne, Hee-Jeong, Kesio, Angelo, Tanvir,** and **Denise** for their patience in attending to my queries at DIANA FEA. **Wouter Swart**, with his MSc thesis, made a huge contribution in developing the solvers for SLA, and I'm grateful to him for his work and the collaboration to write the research article on it. **Dr. Martin van Gijzen**'s timely and valuable guidance in writing the same is also highly appreciated. Lastly but most certainly, thanks to **Panos Evangeliou** for his assistance with getting started and working around the source code in DIANA. Implementations